Dissertation

submitted to the

Combined Faculties for the Natural Sciences and for Mathematics

of the Ruperto-Carola University of Heidelberg, Germany

for the degree of

Doctor of Natural Sciences

Put forward by

Dipl.-Phys.: Stefan Hoppe

Born in: Cologne, Germany

Oral examination: 3.12.2008

Emitters of VHE γ-radiation as revealed by the H.E.S.S. Galactic plane survey

Referees: Prof. Dr. Werner Hofmann

Prof. Dr. Heinz Völk

Abstract

The High Energy Stereoscopic System (H.E.S.S.) – an array of four Imaging Atmospheric Cherenkov Telescopes located in the Khomas highlands of Namibia – explores the non-thermal universe by means of very-high-energy (VHE; >100 GeV) γ-ray emission. Its high sensitivity and large field-of-view make it the ideal instrument for a survey of the Milky Way in VHE γ-rays. The H.E.S.S. Galactic Plane Scan resulted in the most complete view of our Galaxy achieved so far in this energy regime. The results of this extensive survey will be presented in this work. From the 45 VHE γ-ray sources detected so far within the Galactic Plane, a short summary is given for the 19 sources detected within the framework of this thesis and three representative sources were analyzed in even more detail: HESS J1912+101 was detected in the vicinity of an energetic pulsar, suggesting a pulsar wind nebula origin of the γ-ray emission. A clear signal of VHE γ-ray emission was also detected from RCW 86, a well-known shell-type supernova remnant. And finally, HESS J1708-441 was discovered in the vicinity of the well known pulsar PSR B1706-44, but cannot be clearly associated with this strong counterpart. As the energy spectra of these sources yield most valuable information about the processes at work in the underlying astrophysical objects, extensive studies of the spectral extraction method were performed to ensure their correct determination.

Kurzfassung

H.E.S.S. ist ein Experiment zur Erforschung des nicht-thermischen Universums duch die Detektion sehr hochenergetischer Gamma-Strahlung. H.E.S.S. besteht aus vier abbildenden Cherenkov Teleskopen im Khomas Hochland von Namibia. Die hohe Sensitivität und das grosses Gesichtsfeld befähigen H.E.S.S. zu einer grossflächigen Durchmusterung der Galaktischen Ebene. Dieses Durchmusterung resultierte in der bisher vollständigsten Kartographierung unserer Galaxie in dem Energiebereich zwischen 100 GeV und 100 TeV. Die Ergebnisse werden in dieser Abhandlung vorgestellt. Von der grossen Anzahl an Quellen – 45 an der Zahl – werden die 19 Quellen, welche im Rahmen dieser Arbeit entdeckt wurden, naeher beschrieben und drei representative Quellen gesondert analysiert: Zum einen HESS J1912+101, eine Quelle, die in der Nähe eines hochenergetischen Pulsares entdeckt wurde. Die positionelle Koinzidenz legt eine Assoziation mit einem Pulsar-Wind-Nebel (PWN) nahe. Ebenfalls näher untersucht wird die Emission hochenergetischer Gamma-Strahlung von dem bekannten Supernovaüberrest RCW 86. Als letztes vorgestellt wird HESS J1708-44, eine Quelle in der Umgebung des bekannten Pulsaren PSR B1706-44, die trotz des suggestiven Gegenstücks keine klare Zuordnung erlaubt. Da die Energiespektren der obengenannten Quellen wertvolle Informationen über die zugrundeliegenden Prozesse innerhalb der assoziierten Objekte liefern, werden zusätzlich die Methoden der Spektrumsbestimmung im Detail beschrieben und ausführlichen Tests unterzogen.

Contents

List of Figures

List of Tables

Preface

On a clear night, when we look at the Milky Way with our bare eyes, we see a tranquil universe, consisting mainly of silently burning stars and hot gas. Beyond this "thermal" universe, at wavelengths not observable by human eyes, a violent universe emerges. It contains objects which accelerate particles to energies far beyond what is reachable by man-made particle accelerators. These cosmic accelerators might not be numerous compared to ordinary stars, but the energy contained in the particles they produce is comparable to the total energy in the interstellar magnetic field and the kinetic energy of all the interstellar gas in our Galaxy. Their effect on the evolution of our Galaxy is therefore considerable.

When a massive star ends its life in a supernova explosion, enormous energies are released. Part of this energy is channeled into the acceleration of charged particles. For many years now, supernova remnants have been considered the most likely origin of the cosmic rays, a stream of energetic ions hitting the Earth's atmosphere. But even a hundred years after the discovery of these cosmic rays, this concept for their origin is still not proven unambiguously. While with the detection of synchrotron radiation in the radio and X-ray regime, the acceleration of electrons to GeV and TeV energies was established, ion acceleration in these objects to even higher energies remains still to be proven. Very high energy (VHE; >100GeV) gamma-ray astronomy is considered a promising approach to tackle this problem by observing the gamma-rays produced in collisions of high energy ions with the ambient medium.

Unlike the very high energy regime, detailed surveys carried out at radio/X-ray energies (e.g. by the VLA or ROSAT) are available since a long time. They provide the grounds to study high energy electrons in these and other accelerators through synchrotron radiation. In the GeV range, satellite based gamma-ray observatories such as the Energetic Gamma Ray Experiment Telescope (EGRET) have been used for the detection of gamma-rays originating in protron-protron interactions or being inverse Compton radiation from these objects. A survey of the galaxy at very high energies – an energy range where observations are less hampered by diffuse gamma-ray emission from the Galactic plane – was not possible so far because of lack of sensitivity of ground-based instruments. With the H.E.S.S. experiment, for the first time, a most complete view of the Milky Way in VHE gamma-rays became available.

The High Energy Stereoscopic System (H.E.S.S.) is an array of four Cherenkov telescopes, located in the Khomas Highlands of Namibia. Due to the possibility of detecting the VHE gamma-rays with more than one telescope at a time (stereoscopic approach), it is the most sensitive instrument for VHE gamma-ray astronomy at the moment. With its large field of view and its high sensitivity, it is the ideal instrument for detailed morphological and spectral studies of extended sources. Furthermore, these properties together

with its location in the southern hemisphere make it well suited for a systematic survey of the Galactic plane to search for unknown VHE gamma-ray sources.

When H.E.S.S. started operation in the year 2003, only very few VHE gamma-ray sources were known, which were discovered by the first generation of Cherenkov telescopes. Since then, H.E.S.S. has played a major role to increase the number of sources. It discovered VHE gamma-rays from well-known shell-type supernova remnants like RX J1713.7-3946 (Aharonian et al. (H.E.S.S. collaboration), 2007d) and pulsar wind nebulae like HESS J1825-137 (Aharonian et al. (H.E.S.S. collaboration), 2005b). Due to its good angular resolution, H.E.S.S. was able to resolve the morphology of these sources and perform detailed spectral studies, which added valuable information to the theoretical models describing the underlying processes.

In the first phase of its Galactic plane survey, which mapped the inner 60° in Galactic latitude, 14 additional, previously unknown, VHE gamma-ray sources were discovered (Aharonian et al. (H.E.S.S. collaboration), 2006h). Recently, the Galactic Plane survey has been extended to larger Galactic longitudes (l) and covers now the regions in between l= 280° and l= 60°. The result is the most complete view of the inner Galactic plane achieved so far in VHE gamma-rays. In this work, a detailed analysis of the full survey is presented which resulted in the discovery of additional 19 sources. The possible associations range from pulsar wind nebulae through supernova remnants to more exotic sources like open star clusters. Of these, three sources representative of the typical VHE gamma-ray emitters were analyzed in detail: HESS J1912+101 was detected in the vicinity of an energetic pulsar suggesting a pulsar wind nebula as possible origin of the gamma-ray emission. Other associations were also investigated using additional multi-wavelength data. For RCW 86, a well-known shell-type supernova remnant, the association of the VHE signal is clearer. Detailed morphological studies were performed in an attempt to resolve the shell-like structure also in VHE gamma-rays — ultimately, a task that will have to wait for more data. And finally, HESS J1708-441 nicely illustrates the problems of identification even when strong counterparts like the energetic pulsar PSR B1706-44 exist.

The outline of this thesis is as follows:

- In Chapter 1, the acceleration of charged particles and the different scenarios of photon production are briefly introduced. Furthermore, the properties of VHE gamma-ray emitters identified to date are shortly described.

- An overview of the H.E.S.S. experiment and the underlying working principles of the Imaging Atmospheric Cherenkov technique will be given in Chapter 2 together with a short description of the H.E.S.S. data analysis scheme. The chapter concludes with a short characterization of the H.E.S.S. performance.

- In Chapter 3 the extraction of energy spectra from the H.E.S.S. data is described. As the energy distribution of the parent population is directly related to the energy spectra of the observed gamma-rays, such spectra contain vital information for further interpretation. Two different methods are introduced in detail and their systematics differences are evaluated.

- In Chapter 4 the H.E.S.S. Galactic plane survey is presented. The available data set is introduced together with an overview of all the VHE gamma-ray sources detected along the Galactic plane.

- Chapter 5 deals with the detailed analyses of the three VHE gamma-ray sources: HESS J1912+101, RCW 86 and HESS J1708-441. The morphology and the energy spectrum of each of these sources are measured. Extensive multi-wavelength studies help to interpret the observations. Possible associations of the gamma-rays sources are proposed, constraining the source parameters in the process.
- In Chapter 6 the findings of this thesis are discussed within the context of Galactic VHE γ-ray astronomy ending with a brief outlook into the future of the field.

Chapter 1

Astrophysics Overview

After the detection of a VHE γ-ray source, a basic understanding of the physical processes at work is essential for the interpretation of the observed characteristics. This chapter is intended as a short summary of the relevant processes needed for the individual source analysis presented in Chapter 5. Special emphasis will be placed on the chararctersitics directly related to the observed VHE γ-ray emission, including the acceleration of charged particles, the photon production processes, as well as the basic characteritics of the astrophysical accelerators influencing the efficiency of the particle acceleration.

VHE γ-radiation cannot be produced in thermal processes, but has to be emitted by particles accelerated to very high energies. Thus, VHE γ-ray sources are always related to particle acceleration. Shock fronts, which occur in many astrophysical objects, like supernova remnants and pulsar wind nebulae, are proven to be sites of particle acceleration with sufficiently high maximum energies to generate the VHE γ-ray emission (see e.g. Koyama et al., 1995). The most successful theories to explain the acceleration of charged particles in shock fronts are variations of the first order Fermi process (Fermi, 1949): Charged particles undergo pitch-angle scattering on magnetic inhomogenities in the fluid rest frame on each side of the shock front, thereby cross and re-cross the shock front and undergo acceleration in the process. As the energy gain is proportional to the particle's energy, the resultant energy distribution follows a power law $N(E)\mathrm{d}E \propto E^{-\alpha}\mathrm{d}E$, the index α being aproximately 2 for strong shocks. The exact shape of the energy spectrum and its maximum energy depends strongly on the details of the acceleration process and therefore on the type of accelerator. Supernova remnants shocks, for example, which move with non-relativistic speeds, exhibit characteristics different from the relativistic shocks occurring in pulsar wind nebulae. Especially in the case of non-relativistic shocks, the acceleration can be so efficient – in particular at the highest energies – that the back-reaction of the accelerated particles modifies the structure of the shock front. The process of Fermi-type acceleration in shock fronts will be shortly summarized in the following section. As the expected energy spectra of the accelerated particles differ slightly in shape and maximum energy, the cases of non-relativistic and relativistic shocks will be distinguished.

The accelerated particles produce electromagnetic radiation through their interaction with the ambient matter, with photon and magnetic fields. Protons scatter in-elastically off the nuclei of the surrounding matter. In these interactions, π^0 and η, are produced, which, in turn, decay into photons (hadronic scenario). Electrons and positrons [1] emit

[1] From now on positrons will not be treated separately and simply referred to as electrons.

synchrotron radiation in the presence of magnetic fields or up-scatter ambient photons in an inverse Compton process (leptonic scenario). If the particle (either proton or electron) was energetic enough, the energy of the emitted photons is in the VHE γ-ray regime and therefore detectable by the H.E.S.S. experiment. Details of the hadronic and the leptonic scenarios will be presented in Section 1.2, including a model for the resultant spectral energy distribution (SED).

The efficiency and the maximum energy of the shock acceleration depends strongly on the characteristics of the shock front and its surrounding and these are subject to change following the evolution of the related astrophysical object. The velocity of the expanding shock front in a SNR strongly influences the maximum energy reachable through shock acceleration. This velocity decreases with time in a non-constant manner, while the SNR is living through its different evolutionary stages. A model for the time dependence of the SNR shock velocity and its influence on the maximum particle energy will be summarized, aiding the interpretation of VHE γ-ray emission observed from SNRs.

Besides the shell-type supernova remnants, pulsar wind nebula as sources of VHE γ-ray emission will be introduced, starting with a short summary of the necessary pulsar characteristic. Emphasis, however, will be placed on the structure of the PWN, the particle acceleration occuring within them and the PWN characteristics at VHE energies.

1.1 Shock Acceleration

In astrophysical objects, the occurrence of strong shocks is often accompanied by a population of very energetic particles reaching far beyond the thermal energy domain. In the supernova remnant SN 1006 (Koyama et al., 1995), observations of X-ray synchrotron emission seem to provide proof for the presence of particles with energies of at least 100 TeV. *Diffusive shock acceleration* (DSA) was proposed by many authors as the acceleration mechanism at work within non-relativistic shocks, found e.g. in the expanding shells of supernova remnants (Krymskii, 1977; Axford et al., 1978; Bell, 1978a,b; Blandford & Ostriker, 1978). DSA relies on repeated scattering off magnetic irregularities to confine charged particles for some time close to the shock. The multiple scattering leads to an isotropic particle velocity distribution in the rest frame of the fluid on either side of the shock. The resulting adjustment of a particle's net-momentum to the fluid bulk motion leads to an increase of the particle's energy whenever it crosses the shock, no matter in which direction (from upstream to downstream or vice versa). Shock acceleration by relativistic shocks operates by a similar principle; however, it cannot be called diffusive any more, as upstream particles are in general not isotropically scattered before they are overtaken by a shock which moves at a relativistic speed. Even though the interest in this *relativistic shock acceleration* (RSA) has been sparked by extragalactic sources (Peacock, 1981), it is equally applicable to the standing termination shocks of pulsar driven winds giving rise to VHE γ-ray emitting pulsar wind nebulae (e.g. Achterberg et al., 2001).

Both, DSA and RSA, produce energetic particle populations exhibiting approximately power-law shaped energy distributions $N(E)\mathrm{d}E \propto E^{-\alpha}\mathrm{d}E$, whereby the slope α is determined by the mean energy gain per shock crossing cycle $\beta = \frac{E_\mathrm{f}}{E_\mathrm{i}}$ ($E_\mathrm{i,f}$ = energy before

(i) and after (f) a crossing cycle) and the mean probability $P_{\rm ret}$ per cycle that a particle returns to the shock (Achterberg et al., 2001):

$$\alpha = 1 + \frac{\ln(1/P_{\rm ret})}{\ln \beta} \ . \tag{1.1}$$

Equation 1.1 illustrates the main difference between DSA and RSA. In the case of DSA, the return probability is high, leading to many crossings per particle, while the energy gain per crossing remains low. In the case of RSA the situation is inverted: the particles cross the shock front only a few times, but gain more energy per crossing. Both acceleration scenarios will be discussed in more detail below.

1.1.1 Diffusive Shock Acceleration

In the case of DSA, particles gain the same amount of energy in both crossing directions, as their distribution becomes completely isotropic before the next crossing of the shock front. The average energy gain β per crossing cycle and the return probability $P_{\rm ret}$ are given by:

$$\ln \beta \approx \frac{4}{3}\frac{V_{\rm s} - V_{\rm s}/r}{c} \tag{1.2}$$

$$\ln P_{\rm ret} \approx \ln\left(1 - \frac{4V_{\rm s}}{rc}\right) \tag{1.3}$$

where $r = \rho_{\rm d}/\rho_{\rm u} = \frac{\gamma+1}{\gamma-1+2M^{-2}}$ is the compression factor of the shock front, $\rho_{\rm u,d}$ the density upstream and downstream of the shock, γ the ratio of the specific heats, M the Mach number of the shock and $V_{\rm s}$ is the velocity of the shock front in the laboratory frame. In case of a strong shock ($M \rightarrow \infty$) in a non-relativistic mono-atomic plasma ($\gamma = 5/3$) the compression factor approaches $r \rightarrow 4$. As the shock front moves at non-relativistic speeds ($V_{\rm s} \ll c$), Equation 1.3 illustrates that the escape probability per cycle is very low, but so is the energy gain per cycle. Using Equation 1.1 the slope of the resultant power-law energy distribution is:

$$\alpha = \frac{r+2}{r-1} \tag{1.4}$$

for $r \rightarrow 4$, α approaches 2.

The necessary isotropy for efficient particle acceleration is reached through elastic scattering off magnetic inhomogeneities (Bell, 1978a). On the downstream side of the shock, these inhomogeneities are created either by the advection of turbulence through the shock front or by irregular gas flows in this region. Upstream of the shock they may arise from self excited Alfvén waves, which are created when the streaming velocity of the particles exceeds the Alfvén speed. Through the scattering, the particles' streaming velocity is reduced to the Alfvén speed ($\sim$10 km/s), which makes it inevitable that they are again overtaken by the shock front (Bell, 1978a). The timescale of this acceleration process is given by (Drury, 1983):

$$t_{\rm acc} = \frac{3r}{r-1} \cdot \left(\frac{rD_{\rm d} + D_{\rm u}}{V_{\rm s}^2}\right) \tag{1.5}$$

where $D_{\rm u,d}$ are the upstream and downstream diffusion coefficients, respectively. Equation 1.5 illustrates the dependence of the acceleration efficiency on the randomization of

the particle's velocity distribution: the acceleration timescale is reduced with decreasing diffusion coefficients, which relates to a faster randomization. The magnetic inhomogeneities that are most efficient at scattering particles are those where the length scale is comparable to the particle's gyro-radius. The fastest kind of diffusion, i.e. the one with the smallest diffusion coefficient, is therefore the Bohm diffusion, as it corresponds to a totally random field on all scales. It is often used as a valid approximation due to the existence of self-excited Alfvén waves. The Bohm diffusion coefficient is given as (Parizot et al., 2006):

$$D_{\mathrm{B}} = (3.3 \cdot 10^{23} \mathrm{cm}^2 \mathrm{s}^{-1}) \frac{E}{1\,\mathrm{TeV}} \left(\frac{B}{100\,\mu\mathrm{G}} \right)^{-1} \tag{1.6}$$

Its dependence on the magnetic field leads to a difference between D_{u} and D_{d} even in the Bohm limit. The downstream magnetic field B_{d} is given by the upstream magnetic field B_{u} and the the compression factor r (following Berezhko et al., 2002):

$$B_d \approx \sqrt{\frac{1+2r^2}{3}} B_u \ . \tag{1.7}$$

It should be noted that only particles with high enough initial energy can be accelerated in DSA. The initial energy of the particles injected into the acceleration process must be high enough such that the particles can cross the shock front multiple times unhampered. The necessity of such an initial population of energetic particles (injection problem) is subjection of intensive theoretical research, for a review, see Malkov & O'C Drury (2001).

Non-linear Modifications

The previously mentioned treatment ingnored any back-reaction of the accelerated particles on the shock itself. However, particle acceleration at non-relativistic shocks can be so efficient that the accelerated particle population modifies the shock structure (shock modification) and non-linearly amplifies the magnetic field in the vicinity of the shock (magnetic field amplification). The standard linear treatment alone does not allow for acceleration of protons to energies beyond $\sim 10^{14} \left(\frac{B}{3\,\mu\mathrm{G}} \right)$ eV (see e.g. Lagage & Cesarsky, 1983a,b). To explain particle acceleration to energies beyond $\sim 100\,\mathrm{TeV}$, non-linear effects must also be taken into account.

Magnetic field amplification and streaming instabilities: Accelerated particles traveling upstream of the shock can drive large-amplitude Alfvén-waves with magnetic fields that dominate the background field (McKenzie & Völk, 1982; Lucek & Bell, 2000). The resulting magnetic field strength can be as high as 1 mG, which leads to much faster randomization (see Equation 1.6). In addition to the amplified background magnetic field, the increased scattering may also decrease the diffusion coefficient down to the Bohm limit (an assumption that was already used in the linear treatment, but here it is fully justified). The hypothesis of magnetic field amplification is supported also by observations of thin X-ray synchrotron filaments surrounding SNRs (Bamba et al., 2003b; Vink & Laming, 2003; Völk et al., 2005).

Shock modification: The following description of shock modification follows closely the intuitive explanations by Berezhko & Ellison (1999). The structure of a strongly modified shock is illustrated in Figure 1.1. A shock precursor, both in fluid velocity and magnetic field strength, is formed in the upstream region of the shock. Energetic particles whose

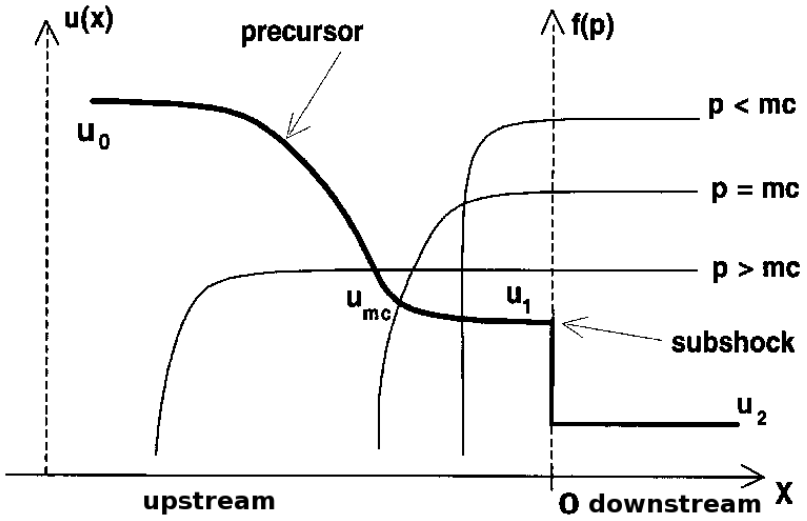

Figure 1.1: Structure of a strong, modified shock. The heavy solid line illustrates the gas velocity u(x) as a function of the position x. The thin lines depict the spatial distribution f(p) of the accelerated particles for different momenta. The figure was taken from Berezhko & Ellison (1999)

diffusion coefficient strongly increases with their momentum, diffuse in front of the shock, and their pressure gradually slows down the upstream fluid. In addition to the precursor, a discontinuous sub-shock forms where the upstream plasma speed is adjusted to the downstream value.

Due to the existence of the precursor region, particles in the upstream region do not experience an overall total compression factor $r_{\rm tot}$, but an effective compression factor $r_{\rm eff}$, depending on how far they diffuse ahead of the shock front. At low energies, the particles do not penetrate far and feel only the low compression factor of the sub-shock $r_{\rm eff} = r_{\rm sub} \approx 3$ (Berezhko & Ellison, 1999). Thus, the expected particle spectrum at lower energies follows a power-law with index $\alpha = \frac{r_{sub}+2}{r_{sub}-1} \approx 2.5$ (Berezhko & Ellison, 1999). At higher energies, the relativistic particles feel an effective velocity jump $u_{\rm p} - u_{\rm d}$, where $u_{\rm d}$ is the downstream fluid bulk velocity and $u_{\rm p}$ the characteristic upstream flow speed where particles of momentum p back-scatter and return downstream. The resultant power-law index is $\alpha = \frac{u_{\rm p}+2u_{\rm d}}{u_{\rm p}-u_{\rm d}} + \frac{{\rm d}\ln(u_{\rm p}-u_{\rm d})}{{\rm d}\ln(p)}$. At the highest energies, the particle momentum spectrum can again be approximated by a power-law with an momentum-independent index

$$\alpha = 1.5 + \frac{1.5 - 0.5 r_{\rm sub}}{2 r_{\rm tot} - r_{\rm sub} - 1} \tag{1.8}$$

where $r_{\rm tot} \approx 1.3 M^{3/4}$ and M is the Mach number of the shock. The resultant particle population no longer exhibits a pure power law energy spectrum, but is rather concave with a particle concentration near the cutoff energy.

It should be noted that the total compression factor $r_{\rm tot}$ can be much higher than 4, as stated in the description of the linear DSA. The first reason is the lowering of the specific heat ratio γ in the downstream region due to the relativistic particle population (γ: 5/3

$\rightarrow 4/3 \Rightarrow r_{\rm tot}$: 4$\rightarrow$ 7), the second is the enhancement of the escaping energy flux, as more particles are concentrated at high energies ($r_{\rm tot} \rightarrow 10$).

Temperature: In addition to the acceleration of particles, shocks traversing the interstellar medium heat the overtaken gas to X-ray emitting temperatures. The efficient energy transfer into accelerated particles, however, leads to cooler post-shock temperatures (Ellison et al., 2004). As a consequence, thermal X-ray emission might be suppressed in e.g. VHE γ-ray emitting SNRs.

1.1.2 Relativistic Shock Acceleration

When the velocity of the shock front approaches relativistic speeds, it becomes comparable to the velocity of the accelerated particles and its motion can no longer be neglected. Energetic particles in the downstream region can only outrun the shock and cross into the upstream region if their momentum is almost parallel to the shock's normal. Thus, all particles crossing from downstream to upstream lie in the so-called *loss cone* which has an opening angle of $\theta < \Gamma_{\rm s}^{-1}$ in the rest frame of the upstream fluid, where $\Gamma_{\rm s}$ is the bulk Lorentz factor of the shock (Achterberg et al., 2001). It may happen that these particles get deflected outside the loss cone and are finally overtaken by the shock. Such small angle deflections can easily be caused by a large scale magnetic field that is not parallel to the shock normal or by the non-resonant sloshing motion of particles in a magnetic wave with wavelength much larger than the particle's gyro-radius (Achterberg et al., 2001). Gyro-resonant scattering by Alfvén waves, which is the dominant randomization mechanism in DSA, is of little importance here as the particles spend less than a gyro-period in the upstream region and the resonance can not be established. None of the mechanisms are fast enough to randomize the particles' direction after the initial deflections and before they are overtaken by the shock front. Thus, the distribution of the accelerated particles near the shock front exhibits a large anisotropy $\theta < \Gamma_s^{-1}$, and the diffusion approximation used in DSA is not applicable anymore. As the particles from the upstream region stay close to the loss cone, and the downstream particles have to return to the loss cone to re-cross the shock, strong magnetic fluctuations must be present in the downstream region to allow for the necessary deflection ($\sim 180^\circ$). Due to the narrow loss cone, the escape probability per crossing cycle is much larger than in the case of DSA. Achterberg et al. (2001) estimated that about 50-60% of all particles escape downstream in each cycle.

The large anisotropy in the upstream angular distribution limits the energy gain per shock crossing cycle to $\beta \sim 1.6 - 2.0$ (Achterberg et al., 2001). Using Equation 1.1, the resultant power-law energy distribution has a slope $\alpha = 2.2 - 2.3$ as independently calculated by Achterberg et al. (2001); Kirk et al. (2000); Bednarz & Ostrowski (1998). Different than in the case of DSA, the injection problem does not arise in RSA, because upstream particles which cross and re-cross the shock for the first time get boosted by a factor Γ_s^2. However, only about 10% of the particles will return to the upstream region after their first scattering (Achterberg et al., 2001).

1.1.3 Maximum Energy

While a power-law energy spectrum is expected for the accelerated particles, a high energy cut-off within the spectrum is anticipated due to the necessary confinement of the particles within the acceleration site. This cut-off is often approximated by an exponential

function (Aharonian et al., 1997). Therefore, for the following discussion the spectrum of accelerated particles is assumed to have the following shape:

$$Q_{\rm i}(E) = A \exp\left(-\frac{E}{E_{\rm c}}\right)\left(\frac{E}{1\,\mathrm{TeV}}\right)^{-\alpha^{\rm i}} \quad . \tag{1.9}$$

The actual position of the cut-off energy $E_{\rm c}$ strongly depends on the charactersitics of the accelerator and will be discussed in detail in Chapter 1.3.1 and 1.3.2.

1.2 Radiation Processes

Charged particles accelerated to very high energies, e.g. by the diffusive or by the relativistic shock acceleration, produce energetic electromagnetic radiation. In the presence of magnetic fields, the spiraling motion of electrons around the field lines give rise to synchrotron radiation. Furthermore, when energetic electrons interact with surrounding photon fields, e.g. with the omnipresent cosmic microwave background (CMB), they can up-scatter these low energy photons to very high energies. When both synchrotron radiation and inverse Compton radiation originate from the same electron population, direct correspondence between the two arise. Furthermore, VHE γ-rays are produced through the decay of π^0s, originating from inelastic interactions of protons with the ambient nuclei. The important characteristics of these three production mechanism of VHE γ-radiation will be shortly summarized in the following. In the context of the aforementioned acceleration mechanisms, emphasis is placed on the connection between an (approximate) power-law of particle energies and the spectrum of the produced radiation.

Synchrotron Radiation

The synchrotron spectrum of a single electron spiraling in a magnetic field of strength B with a pitch angle ψ has the following form (Blumenthal & Gould, 1970):

$$P_{\rm emitted}(\nu) = -\frac{\mathrm{d}E}{\mathrm{d}t}(\nu) = \frac{\sqrt{3}e^3 B \sin\psi}{mc^2}\frac{\nu}{\nu_{\rm c}}\int_{\nu/\nu_{\rm c}}^{\infty} d\zeta K_{5/3}(\zeta) \tag{1.10}$$

where $K_{5/3}(\zeta)$ is the modified Bessel function of the order $\frac{5}{3}$ and $\nu_{\rm c}$ is defined by:

$$\nu_{\rm c} = (3eB\gamma^2/4\pi mc)\sin\psi \ . \tag{1.11}$$

The spectral shape of the synchrotron spectrum is strongly peaked with a tail to higher energies. It suggests a δ-functional approximation (Ginzburg, 1979), where all energy is emitted at the peak frequency $\nu_{\rm max} \simeq \nu_{\rm c}/3$. Assuming further an isotropic distribution of pitch angles ($\sin\psi \rightarrow \sqrt{2/3}$), a population of mono-energetic electrons with energy $E_{\rm e}$ will emit synchrotron photons at an energy $E_{\rm sy}$ with (Aharonian et al., 1997)

$$E_{\rm sy} \simeq= 0.2\left(\frac{B}{10\,\mu\mathrm{G}}\right)\left(\frac{E_{\rm e}}{1\,\mathrm{TeV}}\right)^2 \ \mathrm{eV} \ . \tag{1.12}$$

In the more realistic case where the electron population is not mono-energetic, but follows a power-law shape with index $\alpha_{\rm e}$: $N(E_{\rm e})\mathrm{d}E_e \propto E_{\rm e}^{-\alpha_{\rm e}}\mathrm{d}E_e$, the total synchrotron spectrum is a

convolution of the mono-energetic synchrotron spectrum and the electron distribution. The exact shape can be found in Blumenthal & Gould (1970), Equation 4.59. The differential synchrotron spectrum (in units of $\mathrm{erg}^{-1}\mathrm{cm}^{-2}\mathrm{s}^{-1}$) follows again a power-law with index α_s:

$$\alpha_\mathrm{s} = \frac{\alpha_\mathrm{e}+1}{2}\ . \tag{1.13}$$

This analytical dependence allows one to infer the underlying energy spectrum of the accelerated particles from the observed synchrotron spectrum.

Electrons lose energy while emitting synchrotron radiation depending on their original energy and the strength of the magnetic field. The synchrotron lifetime [2] is given by:

$$\tau_\mathrm{s} = \frac{\gamma m c^2}{\frac{4}{3}\sigma_\mathrm{T} c w_\mathrm{B} \beta^2 \gamma^2} = 3.1 \cdot 10^5 \left(\frac{E_\mathrm{e}}{1\,\mathrm{TeV}}\right)^{-1} \left(\frac{w_\mathrm{B}}{1\,\mathrm{eV\,cm^{-3}}}\right)^{-1}\ \mathrm{yrs}\,, \tag{1.14}$$

where $\sigma_\mathrm{T} = 665\,\mathrm{mb}$ is the Thompson cross section, $w_\mathrm{B} = \frac{B^2}{8\pi} = 2.4\left(\frac{B}{10\,\mu\mathrm{G}}\right)^2\,\mathrm{eV\,cm^{-3}}$ is the magnetic field energy density. It should be noted that the synchrotron lifetime is inversely dependent on the particle energy, i.e. higher-energy particles cool faster.

In the case of continuous injection of accelerated electrons, with an injection spectrum following a power-law with index $\alpha_\mathrm{e}^\mathrm{i}$, the energy dependent synchrotron loss, as given in Equation 1.14, leads to a break in the observed accumulated electron spectrum. The spectral break occurs roughly at the energy $E_\mathrm{e,break}$ where the synchrotron cooling time τ_s becomes equal to the age of the system t_age:

$$E_\mathrm{e,break} \simeq 12 \left(\frac{B}{10\,\mu\mathrm{G}}\right)^{-2} \left(\frac{t_\mathrm{age}}{10^4\,\mathrm{yrs}}\right)^{-1}\ \mathrm{TeV}\,. \tag{1.15}$$

Below $E_\mathrm{e,break}$ the electron spectrum still follows a power-law with index $\alpha_\mathrm{e}^\mathrm{i}$, but above, the index has changed to $\alpha_\mathrm{e}^\mathrm{c} = \alpha_\mathrm{e}^\mathrm{i} + 1$. As a consequence, the synchrotron spectrum exhibits a similar break from a photon index $\alpha_\mathrm{s} = (\alpha_\mathrm{e}^\mathrm{i}+1)/2$ as given by Equation 1.13 to $\alpha_\mathrm{s} = (\alpha_\mathrm{e}^\mathrm{c}+1)/2 = (\alpha_\mathrm{e}^\mathrm{i}+2)/2$. The energy $E_\mathrm{sy,break}$ at which this break occurs in the synchrotron spectrum can be obtained by inserting $E_\mathrm{e,break}$ into Equation 1.12. Figure 1.3 (left curves) shows an exemplary synchrotron spectrum in case of an initial electron spectrum given by Equation 1.9 setting $\alpha_\mathrm{e}^\mathrm{i} = 2$, $E_\mathrm{c} = 1000\,\mathrm{TeV}$, $B = 100\,\mu\mathrm{G}$ and $t_\mathrm{age} = 10^4\,\mathrm{yrs}$. Please note that the exponential cut-off in the electron spectrum also causes a cut-off in the synchrotron spectrum.

Inverse Compton Radiation

High energy electrons interacting with ambient photon fields up-scatter low frequency photons to higher energies via the inverse Compton process. The process is governed by the Klein-Nishina-cross section which is given by:

$$\sigma_\mathrm{KN} = \pi r_\mathrm{e} \frac{1}{\xi}\left(\left[1 - \frac{2(\xi+1)}{\xi^2}\right]\ln(2\xi+1) + \frac{1}{2} + \frac{4}{\xi} - \frac{1}{2(2\xi+1)^2}\right) \tag{1.16}$$

where $r_\mathrm{e} = \frac{e^2}{m_\mathrm{e}c^2}$ is the classical electron radius, $\xi = \frac{E_\mathrm{e}E_\mathrm{ph}}{m_\mathrm{e}^2c^4}$ and E_ph the energy of the target photon. In cases of $\xi \ll 1$, the electron transfers only a small fraction of its energy in each

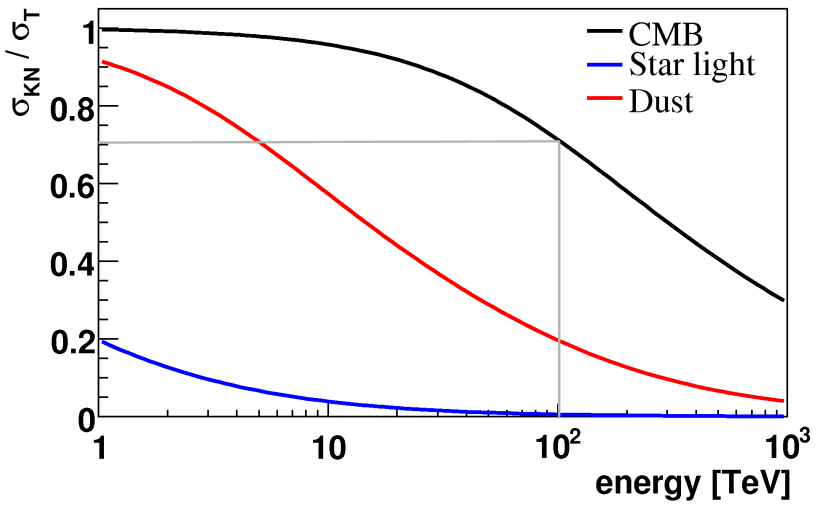

Figure 1.2: Ratio between the full Klein-Nishina cross section $\sigma_{\rm KN}$ and the Thompson cross section $\sigma_{\rm T}$ versus the electron energy $E_{\rm e}$ for three different photon target fields: Cosmic Microwave Background (CMB), diffuse galactic dust background, and starlight photons. The energy of the CMB photons has been approximated by the mean energy of the Planck-distribution: $E_{\rm CMB} = 2.7kT \approx 6 \cdot 10^{-4}$ eV. The energy of the dust and starlight photons was set to the energy at which their intensity distributions reach their maxima: $E_{\rm dust} = 1.24 \cdot 10^{-2}$eV (100 μm) and $E_{\rm dust} = 1.24$eV (1 μm).

Compton scattering event and the cross section becomes roughly independent of energy and equal to the Thompson cross section $\sigma_{\rm T} = 665$ mbarn. Figure 1.2 illustrates the ratio between the Klein-Nishina cross section and the Thompson limit as a function of the electron energy for three different photon target fields: the Cosmic Microwave Background (CMB, T$\simeq$2.7 K), diffuse galactic dust background (far infrared, $\lambda_{\rm FIR} \simeq 100\,\mu$m) and starlight (near infrared/optical, $\lambda_{\rm SL} \simeq 1\,\mu$m). For scattering off the CMB, the Thompson-limit is a good approximation for electron energies up to 100 TeV, with deviations of less than 30%. For higher energy target photons the cross-sections are strongly suppressed relative to the Thompson limit (Klein-Nishina effect). Given the comparable energy densities (with average value $w_{FIR} \sim 0.05\,{\rm eV\,cm^{-3}}$, $w_{SL} \sim 0.5\,{\rm eV\,cm^{-3}}$ Mathis et al., 1983) Aharonian et al. (1997) conclude that inverse Compton scattering off the CMB ($w_{CMB} \sim 0.25\,{\rm eV\,cm^{-3}}$) is the dominant process for the production of VHE γ-rays.

In the Thompson limit, and using a similar δ-approximation as in the case of the synchrotron radiation (Ginzburg, 1979), the relation between electron energy $E_{\rm e}$, energy of the background photon $E_{\rm ph}$ and energy of the up-scattered photon $E_{\rm ic}$ is given by:

$$E_{\rm ic} \simeq \frac{4}{3} E_{\rm ph} \left(\frac{E_{\rm e}}{m_{\rm e}c^2}\right)^2 \simeq 5 \cdot 10^{-3} \left(\frac{E_{\rm ph}}{10^{-3}\,{\rm eV}}\right) \left(\frac{E_{\rm e}}{1\,{\rm TeV}}\right)^2 \ {\rm TeV} \ . \qquad (1.17)$$

[2]The synchrotron cooling time is defined by $\tau = \frac{E_{\rm e}}{-<\frac{{\rm d}E_{\rm e}}{{\rm d}t}>}$

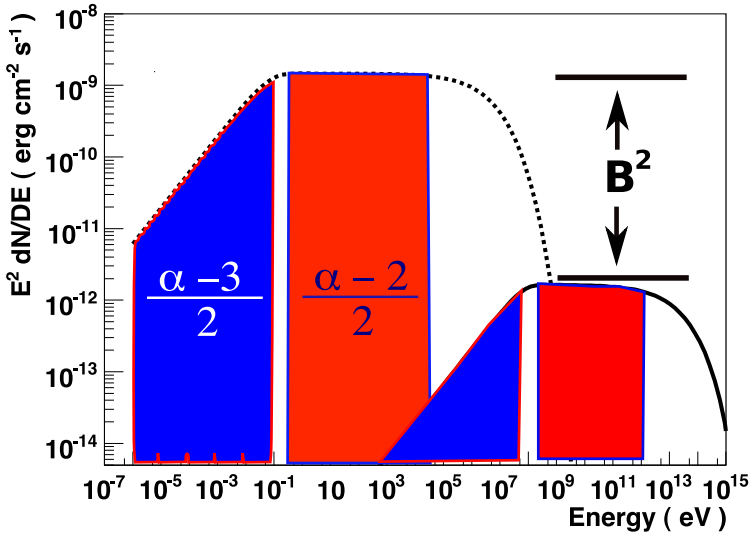

Figure 1.3: Spectral energy distribution (SED) for a $t_{\mathrm{age}} = 10^4$ yrs old system, with an electron injection spectrum following a power-law with index $\alpha_{\mathrm{e}}^{\mathrm{i}} = 2$ and an exponential cut of at $E_{\mathrm{c}} = 1000\,\mathrm{TeV}$, embedded within a magnetic field of $B = 100\,\mu\mathrm{G}$. The spectral indices of the resultant synchrotron (left) and IC (right) spectra before (blue) and after (orange) the cooling break are given.

Considering only scattering off the CMB, with its narrow Planck distribution, the initial photon energy can be approximated by the mean energy of the target photons $E_{\mathrm{ph}} \simeq 2.7\,\mathrm{kT} \simeq 6 \cdot 10^{-4}\,\mathrm{eV}$.

Due to the strong similarities between the synchrotron and the inverse Compton process – e.g. compare Equations 1.12 and 1.17 – both spectra exhibit the same shape. Indeed, Equation 1.14 is equally valid for the IC cooling life time, if the magnetic energy density w_{B} is replaced by the energy density of the background photon field w_{ph}. In the case of the CMB $w_{\mathrm{ph}} = w_{\mathrm{CMB}} = 0.25\,\mathrm{eV\,cm^{-3}}$. Comparing magnetic field density w_{B} and energy density of the CMB w_{CMB}, it becomes apparent that IC cooling by CMB can be safely neglected for magnetic fields larger than $3\,\mu\mathrm{G}$. The energy of the cooling break in the IC spectrum can therefore be obtained by inserting the electron break energy from Equation 1.15 into Equation 1.17. Figure 1.3 (right curve) shows an exemplary IC spectrum for $\alpha_{\mathrm{e}}^{\mathrm{i}} = 2$, $E_{\mathrm{c}} = 1000\,\mathrm{TeV}$, $B = 100\,\mu\mathrm{G}$ and $t_{\mathrm{age}} = 10^4$ yrs.

Relation between Synchrotron and IC

If both synchrotron and IC radiation are emitted by the same population of electrons, their spectra exhibit strong correlations. Considering only the CMB as the dominant target field for the IC process and combining Equation 1.12 and 1.17, the relation between the synchrotron E_{sy} and IC E_{ic} photon energies is given by:

$$\frac{E_{\mathrm{sy}}}{1\,\mathrm{keV}} \simeq 0.07 \frac{E_{\mathrm{ic}}}{1\,\mathrm{TeV}} \frac{B}{10\,\mu\mathrm{G}}\,, \tag{1.18}$$

where B is the strength of the ambient magnetic field. The ratio of the corresponding energy fluxes $f(E)$ at energies related by Equation 1.18 is equal to the ratio of the magnetic field $w_{\rm B}$ and CMB $w_{\rm CMB}$ energy densities:

$$\frac{f_{\rm ic}(E)}{f_{\rm sy}(E_{\rm sy})} = \frac{w_{\rm CMB}}{w_{\rm B}} \simeq 0.1 \left(\frac{B}{10\,\mu{\rm G}}\right)^{-2} \tag{1.19}$$

As apparent from Equation 1.19, synchrotron radiation exhibits a larger energy flux than the IC radiation for all magnetic field strengths above the average interstellar value ($B > 3\mu G$). Figure 1.4(a) to 1.4(c) depict the synchrotron and IC spectra produced by an electron population following a power-law shape with exponential cut-off as described in Equation 1.9. Only in the case of a low magnetic field strengths, close to the average interstellar value of $B \simeq 2-5\mu G$, both synchrotron and IC processes, contribute equally to the total radiated power. For larger magnetic field strengths, however, synchrotron losses clearly dominate over IC losses. Figure 1.4(b) depicts the influence of the exponential cutoff in the electron spectrum. For cutoff-energies beyond 10 TeV, the inverse Compton spectrum peaks in the TeV range, while the synchrotron spectrum reaches its maximum at keV energies. The age dependence of the radiation spectra can be seen in Figure 1.4(c). With increasing age of the system, the synchrotron cooling break shifts to lower energies until it can clearly be distinguished from the exponential cutoff (black curve).

1.2.1 Hadronic Scenario

The inelastic interaction of energetic protons with nuclei of the ambient medium results – amongst others – in the production of π^0- and η-mesons. While nearly 100% of π^0s decay into two photons, the branching ratio of $\eta \rightarrow \gamma\gamma$ is only ∼40% . Due to subsequent decays, however, on average 3.2 photons are produced per η-decay, which carry away approximately 80% of its energy. The total fraction of the energy of the incident proton converted into γ-rays is approximately $\kappa \sim 0.17$, of which the relative contribution of the η-decay chain is ∼25%.

The total γ-ray production rate $\phi_\gamma(E_\gamma) \equiv \frac{{\rm d}N_\gamma}{{\rm d}E_\gamma}$, due to the production and subsequent decay of π^0 and η-mesons can be calculated from:

$$\phi_\gamma(E_\gamma) = c n_{\rm H} \int_{E_\gamma}^{\infty} \sigma_{\rm inel}(E_{\rm p}) J_{\rm p}(E_{\rm p}) F_\gamma(\frac{E_\gamma}{E_{\rm p}}, E_{\rm p}) \frac{dE_{\rm p}}{E_{\rm p}} \ , \tag{1.20}$$

where $n_{\rm H}$ is the ambient density of target protons (mostly provided in form of hydrogen and helium), $\sigma_{\rm inel}$ is the inelastic part of the total p-p interaction cross section, $J_{\rm p}(E_{\rm p})$ the initial proton energy distribution function, $F_\gamma(\frac{E_\gamma}{E_{\rm p}}, E_{\rm p})$ the γ-ray emissivity and $E_{\rm p}$ the proton energy.

In the following, approximate equations for all the necessary quantities needed to calculate the resultant γ-ray spectrum will be given, as originally stated in Kelner et al. (2006):

- The inelastic part of the total p-p interaction cross section:

$$\sigma_{\rm inel}(E_{\rm p}) = (34.3 + 1.88L + 0.25L^2) \cdot \left[1 - \left(\frac{E_{\rm th}}{E_{\rm p}}\right)^4\right] \ {\rm mb}\,, \tag{1.21}$$

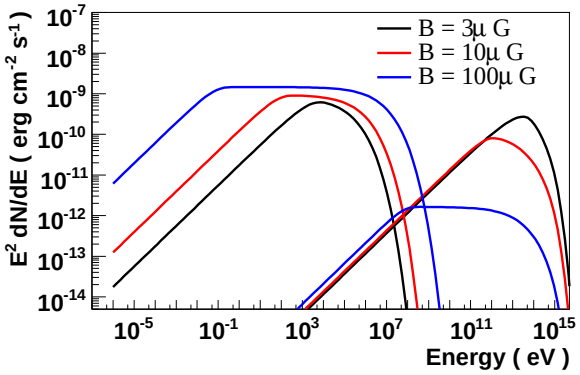

(a)

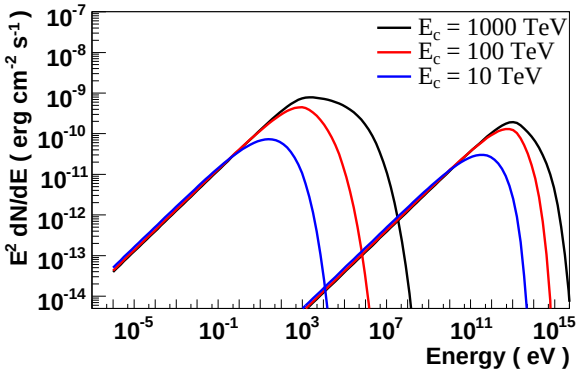

(b)

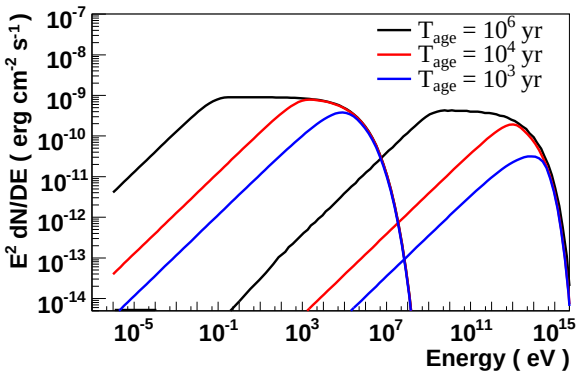

(c)

Figure 1.4: a) Spectral energy distribution (SED) for a $t_{\rm age} = 10^4$ yrs old system, with an electron injection spectrum following a power-law with index $\alpha_{\rm e}^{\rm i} = 2$ and an exponential cut of at $E_{\rm c} = 1000\,{\rm TeV}$. Three different values for the magnetic field B were assumed; b) Same as plot a but with $B = 5\,\mu{\rm G}$ for three different cutoff energies $E_{\rm c}$; c) same as b but for three different values for $t_{\rm age}$ with a fixed position of the exponential cutoff $E_{\rm c} = 1000\,{\rm TeV}$.

where $E_{\rm th} = 1.22\,{\rm GeV}$ is the threshold of pion production and $L = \ln\left(\frac{E_{\rm p}}{1\,{\rm TeV}}\right)$. From the threshold, the cross section rises rapidly to about 30 mb at $E_{\rm p} \sim 2\,{\rm GeV}$. Above this energy it rises only logarithmically with energy.

- The γ-ray emissivity:

$$F_\gamma(x, E_{\rm p}) = B\frac{\ln(x)}{x}\left(\frac{1-x^\beta}{1+kx^\beta(1-x^\beta)}\right)^4 \cdot \Delta \ , \tag{1.22}$$

$$\Delta = \left[\frac{1}{\ln(x)} - \frac{4\beta x^\beta}{1-x^\beta} - \frac{4k\beta x^\beta(1-2x^\beta)}{1+kx^\beta(1-x^\beta)}\right] \ , \tag{1.23}$$

$$B = 1.3 + 0.14L + 0.011L^2 \ , \tag{1.24}$$

$$\beta = \frac{1}{1.79 + 0.11L + 0.008L^2} \ , \tag{1.25}$$

$$k = \frac{1}{0.801 + 0.049L + 0.014L^2} \ , \tag{1.26}$$

  where $x = E_\gamma / E_{\rm p}$.

- The initial proton energy distribution function is assumed to have the following shape:

$$J_{\rm p}(E_{\rm p}) = AE_{\rm p}^\alpha \exp\left[-\left(\frac{E_{\rm p}}{E_{\rm c}}\right)\right] \ , \tag{1.27}$$

  where A is a constant and $E_{\rm c}$ the cut-off energy. Note the similarity to the particle spectrum given in Equation 1.9.

Figure 1.5(a) depicts a γ-ray energy spectrum, calculated using Equations 1.21 to 1.27 with $\alpha = 2$, $E_c = 1000\,{\rm TeV}$ and $n_{\rm H} = 1\,{\rm cm}^{-3}$. It becomes apparent that the shape of the γ-ray energy spectrum away from the threshold and the cut-off regions follows the shape of the parent proton spectrum (both exhibit a power-law with index $\sim$2 in Figure 1.5(a)). This is true for all indices. Figure 1.5(b) illustrates the same γ-ray spectrum, but for a variety of proton indices α. The similarity is due to the nearly energy-independent scattering cross-section in the relevant energy range. As both spectra exhibit a similar power-law shape, the proton spectrum can be approximately infered from the γ-ray spectrum by a simple scaling factor. Consequently, to obtain the energy content of the parent proton spectrum J_p, the γ-ray spectrum is integrated:

$$W_p(10 - 100\,{\rm TeV}) \approx 4.9 \cdot 10^{15}[s]\left(\frac{n}{1{\rm cm}^{-3}}\right)^{-1} L_\gamma(1 - 10\,{\rm TeV}) \ , \tag{1.28}$$

for which the proton spectrum was assumed to follow a pure power-law with index $\alpha = 2.4$. In principle a relation similar to 1.28 holds for each combination of energy ranges (with a different scaling factor), but these specific ranges were chosen because 10-100 TeV protrons give rise to $\sim$1-10 TeV γ-rays. To estimate the energy content within the whole proton population $W_p^{\rm tot}$, the proton spectrum is then extrapolated down to 1 GeV assuming the same spectral shape as the γ-ray spectrum. The result, however, must be considered with caution as possible changes of the spectral shape of the proton spectrum at lower energies are completely neglected. Furthermore, the γ-ray spectrum shows a softer transition in the cut-off region. (see Figure 1.5(a)). Naturally, this deviation cannot be accounted for in a simple scaling of power-laws.

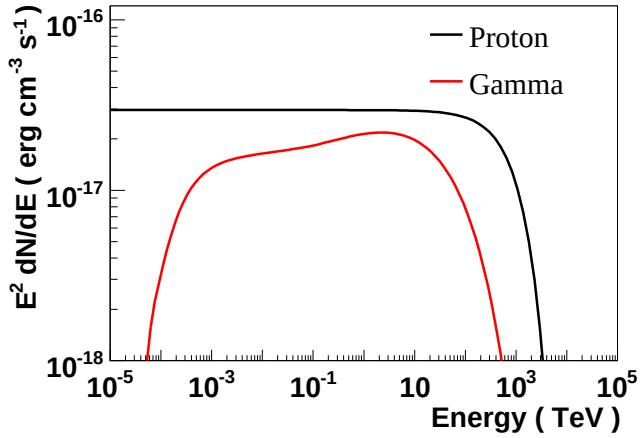

(a)

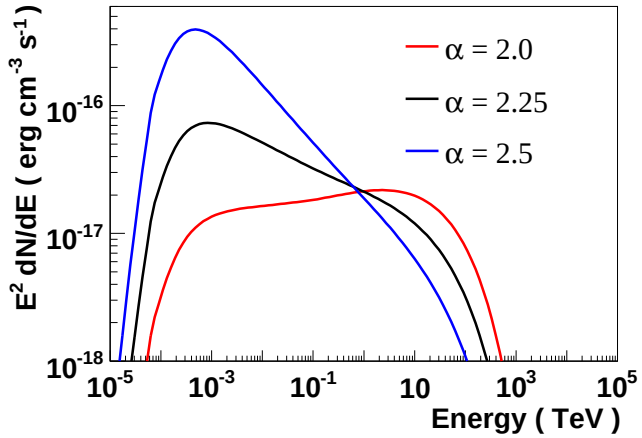

(b)

Figure 1.5: a) SED of γ-ray emission (red curve) produced through inelastic scattering of protons off the ambient medium and subsequent decay of π^0 and η-mesons. The underlying proton spectrum is illustrated by a black line (scaled for illustration purposes, the units on the y-axis are not applicable to this curve). It follows a power-law with index $\alpha = 2$ and exhibits an exponential cutoff at $E_c = 1000\,\mathrm{TeV}$. The assumed density of the ambient medium is $n_H = 1\,\mathrm{cm}^{-3}$. b) Same as *a* but with varying proton spectral indices.

1.3 Accelerators

Shock fronts as sites of efficient particle acceleration are expected in many different astrophysical systems. Within our Galaxy, most of them are related to massive stars, e.g the colliding winds within a close binary consisting of two Wolf-Rayet stars (Bednarek, 2005). At very high energies, the best studied and probably most common of these Galactic objects confirmed to emit VHE γ-rays are the remnants of supernova explosions. This encompasses not only the supernova shock fronts, but also their compact remnants, in particular the pulsars. A short overview of the underlying mechanisms at work within these two source

classes will be given in the following, with emphasis on the source characteristics relevant for VHE γ-ray emission.

1.3.1 Supernova Remnants

When a star ends its evolution in a supernova explosion, an enormous amount of energy is released. These violent deaths of stars belong to the most energetic phenomena known to occur in the universe. Part of the explosion energy is released in the kinetic energy of the progenitor star's ejecta. The expanding material, moving with supersonic speed, drives a shock front into the interstellar medium (ISM). At these shock fronts, particle acceleration is known to occur. Supernova explosions are – so far – the only known phenomena energetic and frequent enough to power the population of (Galactic) cosmic rays up to an energy of 10^{15} eV (Fields et al., 2001).

Many different classes of supernovae can be distinguished. Their defining characteristics are mainly based on the observability of certain line emission and the shape of their light curves. Besides this observational-based taxonomy, only two fundamental classes of supernovae are known: 1.) the thermonuclear disruption of a white dwarf (type Ia) and 2.) the gravitational collapse of the core of a massive star (type II, Ib and Ic). The total supernova rate in our galaxy is about 1.9 ± 1.2 per century (Cappellaro, 2001) from which roughly three-quarters are core-collapse supernovae.

Thermonuclear Supernovae

A white dwarf constitutes the final configuration in the evolution of less massive stars ($M_{\text{initial}} < 8M_{\odot}$). A further gravitational collapse to an even more compact configuration is prevented by the Fermi pressure of the degenerate electron gas. Without further disruption, a white dwarf would cool down on time scales of 10^{10} yr and might become a black dwarf[3]. In a binary system, however, the white dwarf can accrete matter from the companion star. The additional mass increases the gravitational pressure until the white dwarf crosses the Chandrasekhar limit ($M_{\text{cha}} \sim 1.49M_{\odot}$), where the degeneracy pressure of the electrons is overcome. The resultant further compression ignites the next fusion stage and the energy suddenly released leads to the disruption of the white dwarf in a type Ia supernova. The initial conditions of this kind of supernova are inherent to a white dwarf crossing the Chandrasekhar limit and therefore show only little variations. The released energy is of the order of 10^{51} erg, the released ejecta mass close to one solar mass, and the density profile of the expanding ejecta is presumably described by an inner uniform core and an outer power-law envelope region $\rho \propto r^{-n}$ of index $n \sim 7$ (Chevalier, 1982). The inherent similarities result in analog observations from these objects and make them useful as standard candles, e.g. as distance markers in cosmology.

Core-collapse Supernovae

If the progenitor star was more massive ($M_{\text{initial}} > 8M_{\odot}$), the electron degeneracy pressure is not high enough to stop the gravitational driven contraction, and nuclear fusion continues up to iron. Due to the high density and temperature, endothermic processes such as inverse β-decay and photo-disintegration occur. The resulting loss of energy and supporting

[3] No black dwarf has been detected so far.

electron pressure speeds up the gravitational collapse even further. Matter falls nearly freely towards the core and its density rises till the repulsive component of the nuclear force sets in. The initial shock wave which results from outer material crushing onto the higher-density core, however, does not cause the supernova explosion, but fades away due to photo-disintegration and neutrino interactions. Instead, the dense core continues to accrete mass at a high rate ($0.1 M_\odot$ per second). At this stage the core emits neutrinos at a high luminosity which deposit part of their energy into the medium surrounding the core. A large bubble of radiation and electron-positron pairs starts to swell from the inside out, and an outgoing shock front is produced, which causes the explosive ejection of the outer parts of the star (supernova type II, Ib, Ic).

The individual characteristics of such a supernova are by far not as uniform as in the case of a type Ia supernova. The ejected mass can range from one to ten solar masses or even beyond, depending on how massive the progenitor star was and how much mass it had lost prior to the explosion. The kinetic energy of the ejecta covers a large range as well, from about 10^{51} erg (SN1987a Nomoto et al., 1994) to $5 \cdot 10^{52}$ erg in case of a hypernova (Nomoto et al., 2007). The density profile of the ejecta for a type II supernova has been suggested to resemble a combination of a shallow power-law core (index $n < 3$) and a steep power-law envelope (index $n >$ 5 - 14) (Truelove & McKee, 1999; Chevalier & Fransson, 1994).

Supernova Evolution

After the supernova explosion (independent from its type), the ejected stellar mass traverses the ambient medium at supersonic speed and produces a shock front at which charged particles can be accelerated to energies beyond 100 TeV. Because the shock front moves with non-relativistic speed, particles are accelerated by means of *diffusive* shock acceleration. The efficiency and the maximum reachable energy within this DSA process depends strongly on the radius of the shock front and on its speed. These crucial parameters in turn depend on the evolutionary stage of the SNR, which will be briefly summarized below.

Four different stages are distinguished in the evolution of a shell-type supernova remnant: ejecta-dominated phase, Sedov-Taylor phase, snowplow phase and dispersion phase. A more general discussion of these different stages can be found in Woltjer (1972).

- **Ejecta-dominated phase:** In the very first stage of its evolution, the stellar ejecta expands nearly freely into the ambient medium. This phase is also called the free-expansion phase. The velocity of the shock front is constant at $V_\mathrm{S} = \sqrt{\frac{2E_0}{M_\mathrm{ej}}}$, where E_0 is the released kinetic energy and M_ej is the mass of the ejecta. Typical shock velocities are of the order of a few thousand kilometers per second. While the ejecta expands further, it sweeps up the interstellar medium, which decelerates its expansion. A reverse shock forms which travels backwards into the ejecta. The shock velocity V_sh decreases and then follows a power-law (Truelove & McKee, 1999):

$$R^*_\mathrm{sh} = \left[\frac{27}{4\pi}\frac{1}{n(n-3)}\frac{l_\mathrm{ED}^{n-2}}{\phi_\mathrm{ED}}\left[\frac{10}{3}\left(\frac{n-5}{n-3}\right)\right]^{(n-3)/2}\right]^{1/n} t^{*(n-3)/n}, \quad (1.29)$$

$$V^*_\mathrm{sh} = \left(\frac{n-3}{n}\right)\cdot R^*_\mathrm{sh}\cdot t^*, \quad (1.30)$$

where $R^*_{\rm sh}$, $V^*_{\rm sh}$ and t^* are the radius of the shock front $R_{\rm sh}$ scaled by $R_{\rm ch}$, the velocity of the shock front $V_{\rm sh}$ scaled by $V_{\rm ch}$ and the time t since the SN scaled by $t_{\rm ch}$. n is the power-law index of the density profile of the ejecta and $l_{\rm ED}$, $\phi_{\rm ED}$ are given in Table 1.1. $V_{\rm ch}$, $R_{\rm ch}$ and $t_{\rm ch}$ are characteristic scaling variables (Truelove & McKee, 1999):

$$R_{\rm ch} = 3.07 \left(\frac{M_{\rm ej}}{M_\odot}\right)^{1/3} n_0^{-1/3} \ {\rm pc}\,, \tag{1.31}$$

$$t_{\rm ch} = 423\, E_{51}^{-1/2} \left(\frac{M_{\rm ej}}{M_\odot}\right)^{5/6} n_0^{-1/3} \ {\rm yrs}\,, \tag{1.32}$$

$$V_{\rm ch} = 7090\, E_{51}^{1/2} \left(\frac{M_{\rm ej}}{M_\odot}\right)^{-1/2} \ {\rm km/s}\,, \tag{1.33}$$

where $M_{\rm ej}$ is the mass of the ejecta, n_0 is the mean ambient medium number density in units of cm^{-3} and E_{51} is the released kinetic energy in units of 10^{51} erg.

- **Sedov-Taylor phase:** After $t_{\rm ST}$, the amount of material swept up by the outward moving shock front becomes comparable to the original ejecta mass. Most of the energy is transferred to the swept-up material and as radiative losses are still negligible, the result is an adiabatic blast wave. The evolution during this phase is determined only by the originally released kinetic energy, the density of the ambient medium and the time since the supernova event.

$$R^*_{\rm sh} = [R^{*5/2}_{\rm ST} + \eta_0^{1/2}(t^* - t^*_{\rm ST})]^{2/5}\,, \tag{1.34}$$

$$V^*_{\rm sh} = \frac{2}{5}\eta_0^{1/2}[R^{*5/2}_{\rm ST} + \eta_0^{1/2}(t^* - t^*_{\rm ST})]^{-3/5}\,, \tag{1.35}$$

where η_0 is a dimensionless constant determined by the specific heat ratio γ. The originally stated value by (Taylor1950, Sedov1946) is η_0=2.026. The characteristic time $t^*_{\rm ST} = \frac{t_{\rm ST}}{t_{\rm ch}}$ and radius $R^*_{\rm ST} = \frac{R_{\rm ST}}{R_{\rm ch}}$ at which the remnant enters the Sedov-Talyor phase is given in Table 1.1.

- **Snowplow phase:** When the temperature behind the shock front falls below 10^6 K and radiative cooling by line emission of heavy elements starts to be important, the SNR has entered the snowplow phase of its evolution. At the time when the ratio of effective heats approaches unity and the post-shock fluid velocity approaches the shock velocity, the *pressure-driven snowplow* (PDS) stage begins. This stage is characterized by a thin shell of radiatively cooled shocked ambient medium formed behind the blast-wave shock. This thin shell "snowplows" trough the ISM, driven by the hot and isobaric interior of the remnant in addition to its own momentum (Cioffi et al., 1988, and references therein). The onset of this phase occurs roughly at:

$$t_{\rm PDS} = 13,300 E_{51}^{3/14} n_0^{-4/7} \zeta_{\rm m}^{-5/14} \ {\rm yrs}\,, \tag{1.36}$$

$$R_{\rm PDS} = 14 E_{51}^{2/7} n_0^{-3/7} \zeta_{\rm m}^{-1/7} \ {\rm pc}\,, \tag{1.37}$$

$$V_{\rm PDS} = 413 E_{51}^{1/14} n_0^{1/7} \zeta_{\rm m}^{3/14} \ {\rm km/s}\,. \tag{1.38}$$

n	$l_{\rm ED}$	$\phi_{\rm ED}$	$t^*_{\rm ST}$	$R^*_{\rm ST}$
6	1.39	0.39	1.04	1.07
7	1.26	0.47	0.732	0.881
8	1.21	0.52	0.605	0.788
9	1.19	0.55	0.523	0.725
10	1.17	0.57	0.481	0.687
12	1.15	0.60	0.424	0.636
14	1.14	0.62	0.389	0.603

Table 1.1: Values of the numerical parameters used in Equation 1.29, Equation 1.34 and Equation 1.34. The values of $l_{\rm ED}$ and $\phi_{\rm ED}$ originate from Chevalier (1982). The values of $t^*_{\rm ST}$ and $R^*_{\rm ST}$ are taken from Truelove & McKee (1999). n is the power law index of the ejecta density profile.

The evolution of the shock front is governed by (Cioffi et al., 1988):

$$\frac{V_{\rm sh}}{V_{\rm PDS}} = \left(\frac{3}{4}\frac{t}{t_{\rm ch}} - \frac{1}{3}\right)^{-7/10} \tag{1.39}$$

$$\frac{R_{\rm sh}}{R_{\rm PDS}} = \left(\frac{3}{4}\frac{t}{t_{\rm ch}} - \frac{1}{3}\right)^{3/10} \tag{1.40}$$

When even the interior of the remnants has cooled, the momentum-conserving snowplow phase has begun, where the swept-up material carries on, driven mainly by its own momentum. Cioffi et al. (1988), however, argue that unless the ambient density is unusually large, this stage does not occur in the ISM, as the remnant will directly cross over to the next evolutionary stage.

- **Dispersion phase:** At an age $t_{\rm merge}$ the expansion velocity of the shock front becomes sub-sonic , the shock disappears and the SNR mixes with the ISM. Cioffi et al. (1988) estimate $t_{\rm merge}$ to:

$$t_{\rm merge} \sim 57 n_0^{10/49} t_{\rm PDS} \tag{1.41}$$

Figure 1.6 illustrates the dependence of the velocity of the forward shock on the time since the supernova explosion, for two different configurations. The first is thought to be representative of a type Ia supernova; the released energy is estimated to $E = 10^{51}$ erg, the ejected mass to $M_{\rm ej} = 1.4 M_\odot$ and the density profile of the ejecta is approximated by a power-law envelope of index $n = 7$. The second configuration, more likely to resemble a type II supernova, consists of $E = 10^{51}$ erg, $M_{\rm ej} = 10 M_\odot$ and $n = 12$. The mean ambient medium number density is fixed in both cases to $1\,{\rm cm}^{-3}$. In the ejecta dominated phase, a remnant of a type Ia SN expands faster than that of a type II SNR due to the lower mass of its ejecta (given that the released energy is the same). It, however, enters earlier into the Sedov-Taylor phase, as less mass has to be swept up before it dominates over the ejecta mass. As the shock velocity decreases faster in the Sedov-Taylor phase, the two velocities approach each other and are roughly equal when the remnants enter into the pressure-driven snowplow phase. As can be seen from Equation 1.36, the time when the remnants enter this phase is independent of the ejected mass and therefore roughly equal for both types of SNe.

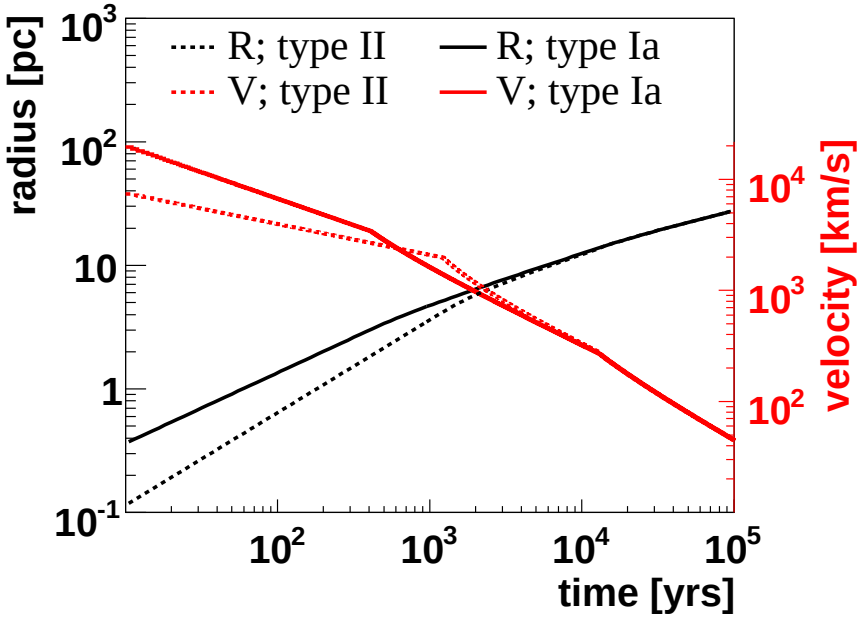

Figure 1.6: Radius and velocity of the SNR forward shock front for two different configurations exemplary for a type Ia supernova ($E = 1{\cdot}10^{51}$erg, $M_{\rm ej} = 1.4 M_{\odot}$, $n = 7$) and a type II SN ($E = 1 \cdot 10^{51}$erg, $M_{\rm ej} = 10 M_{\odot}$ and $n = 12$). The kinks in the curves mark the transition into the next evolutionary stage. They are artificially caused by the over-simplified description which does not take the transition phases into account.

Maximum Energy and γ-Ray Luminosity

Besides the shape of the energy spectrum, the most interesting quantities that determine the visibility of a SNR in VHE γ-rays are the maximum reachable particle energy and the γ-ray luminosity.

The maximum energy particles can reach in the acceleration process at a given time is determined by the energy dependence of the diffusion coefficient (see Section 1.1.1). It can be estimated as (Berezhko et al., 1996):

$$D(E_{\rm max}) = \chi V_{\rm sh} \cdot R_{\rm sh} \ , \tag{1.42}$$

where $\chi \approx 0.04$. Assuming Bohm diffusion and using Equation 1.6, the resultant maximum energy is given by:

$$E_{\rm max}^{\rm Bohm} = (940\,{\rm TeV}) \frac{B}{100\,\mu{\rm G}} \cdot \chi \frac{V_{\rm sh}}{1000\,{\rm km/s}} \cdot \frac{R_{\rm sh}}{1\,{\rm pc}} \, . \tag{1.43}$$

As apparent from Equation 1.43, the maximum reachable energy depends linearly on the magnetic field strength in the vicinity of the shock. Using the normal interstellar value of 2-5 μG, however, would underestimate $E_{\rm max}^{\rm Bohm}$, since self-excited Alfvén-waves generate strong random magnetic fields with amplitudes on the order of a few hundred μG, especially at high shock velocities. This magnetic field enhancement, however, is limited by wave-wave interactions (non-linear effect) or by wave dissipation due to ion-neutral collisions

(linear effect), which strongly damp the Alfvén waves' amplitudes at lower shock velocities (Kulsrud & Cesarsky, 1971; Bell, 1978a; O'C Drury et al., 1996; Voelk et al., 1988; Fedorenko et al., 1990). Ptuskin & Zirakashvili (2003) estimated the maximum reachable proton momentum in the presence of cosmic-ray streaming instabilities with Kolmogorov-type non-linearities (non-linear wave damping) and with collisional wave dissipation (linear wave damping). In the case of non-linear wave damping, the maximum proton momentum is given by (Ptuskin & Zirakashvili, 2003):

$$p^{\mathrm{p}}_{\mathrm{max}} \approx 17\,\mathrm{TeV} \left(\frac{\zeta_{\mathrm{cr}}}{0.5}\right) n^{1/2} \left(\frac{V_{\mathrm{sh}}}{1000\,\mathrm{km/s}}\right)^2 \left(\frac{R_{\mathrm{sh}}}{1\,\mathrm{pc}}\right) \,, \tag{1.44}$$

for high shock velocities $V_{\mathrm{sh}} \gg 800\,\mathrm{km\,s^{-1}}$. For low shock velocities $V_{\mathrm{sh}} \ll 700\,\mathrm{km\,s^{-1}}$ (expansion into hot, ionized gas), $V_{\mathrm{sh}} \ll 400\,\mathrm{km\,s^{-1}}$ (expansion into warm, partly ionized gas), p_{max} is determined by (Ptuskin & Zirakashvili, 2003):

$$p^{\mathrm{p}}_{\mathrm{max}} \approx 0.24\,\mathrm{TeV} \left(\frac{\zeta_{\mathrm{cr}}}{0.5}\right)^2 n^2 \left(\frac{V_{\mathrm{sh}}}{100\,\mathrm{km/s}}\right)^7 \left(\frac{R_{\mathrm{sh}}}{1\,\mathrm{pc}}\right) \left(\frac{B_0}{1\,\mu\mathrm{G}}\right)^{-3} \,, \tag{1.45}$$

where ζ_{cr} is the ratio of the cosmic ray pressure at the shock and the upstream momentum flux entering the shock front, n is the inter-cloud gas number density and B_0 is the regular (non-amplified) magnetic field.

In the case of collisional wave dissipation in partly ionized warm gas, the maximum momentum is estimated to (Ptuskin & Zirakashvili, 2003):

$$p^{\mathrm{p}}_{\mathrm{max}} \approx 60\,\mathrm{TeV} \left(\frac{\zeta_{\mathrm{cr}}}{0.5}\right) n^{-1/2} \left(\frac{V_{\mathrm{sh}}}{1000\,\mathrm{km/s}}\right)^3 \,. \tag{1.46}$$

Note the strong dependence of the maximum energy on the velocity of the shock front, especially in Equation 1.44 to 1.46, but also in Equation 1.43. A careful analysis of this shock parameter is therefore of uttermost importance for the possible association of an observed VHE γ-ray emission with a SNR.

Figure 1.7 illustrates the aforementioned equations in the case of a SNR in the Sedov-Taylor phase (Ptuskin & Zirakashvili, 2003). The kinetic energy of the explosion is set to 10^{51} erg. The other parameters are set to ζ_{cr}=0.5, $n = 0.1 \cdot 10^{-3}\mathrm{cm}^{-3}$ and $B_0 = 5\,\mu$G. At lower shock velocities, equivalent to an older SNR, the linear and non-linear wave damping effects reduce the maximum energy below the Bohm-limit. If these effects are important, no proton acceleration beyond 1 TeV occurs, if the shock velocity drops below a few hundred km/s. Using Equation 1.35, this velocity is reached somewhere in the last third of the Sedov-Taylor phase.

These aforementioned equations only hold in the absence of additional energy losses. In the case of electrons, synchrotron losses are more likely to be the limiting factor for the maximum reachable energy. E_{max} can be estimated by comparing the acceleration timescale with the synchrotron colling timescale. Combining Equation 1.5 and 1.7 and assuming $D_{\mathrm{d}} \approx D_{\mathrm{B}}$, the acceleration time scale reads as (Parizot et al., 2006):

$$\tau_{\mathrm{acc}} \approx 1.83\, \frac{D_{\mathrm{B}}}{V^2_{\mathrm{sh}}} \frac{3r^2}{r-1} \,. \tag{1.47}$$

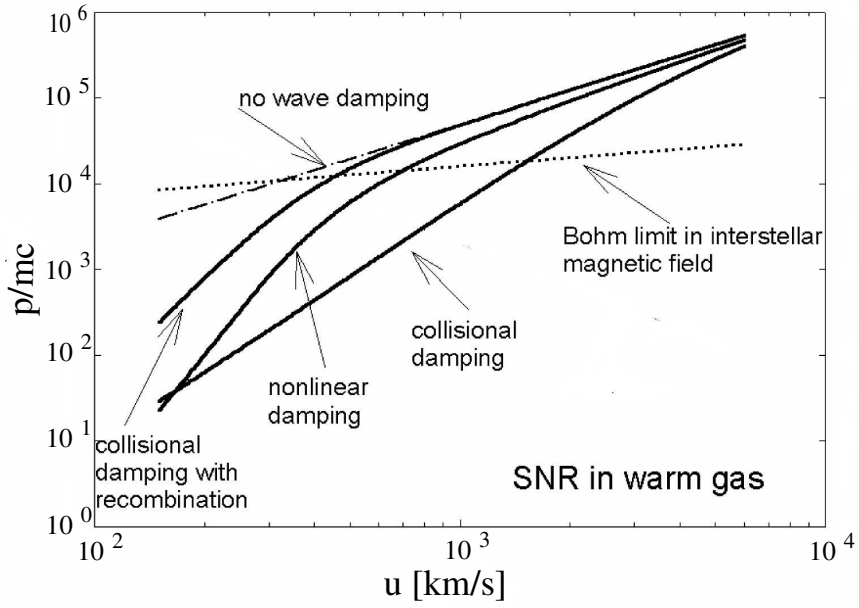

Figure 1.7: Maximum momentum of accelerated protons $p_{\rm rm}$ in units of mc as a function of the shock velocity $u_{\rm sh}$. The assumed SNR is in the Sedov-Taylor stage of its evolution and expands into warm interstellar gas ($T = 8 \cdot 10^3\,\mathrm{K}$, $n = 0.1\mathrm{cm}^{-3}$, $B_0 = 5\,\mu\mathrm{G}$). The parameter of the SNR are: $E_{51} = 1$, $M_{\rm ej} = M_\odot$, $\zeta_{\rm cr} = 0.5$. The figure was adopted from Ptuskin & Zirakashvili (2003)

The mean synchrotron cooling timescale (upstream and downstream) as described in Equation 1.14 is given by:

$$< \tau_{\rm synch} > \approx (1.25 \cdot 10^3 \mathrm{yr}) \left(\frac{E_{\rm e}}{1\,\mathrm{TeV}} \right)^{-1} \left\langle \left(\frac{B}{100\,\mu\mathrm{G}} \right)^2 \right\rangle^{-1} , \tag{1.48}$$

with $< B^2 > \approx 0.59 B_{\rm d}^2 = 0.59 B_{\rm B}^2$. Comparing Equation 1.47 with 1.48 gives the maximum electron energy $E_{\rm e,max}$ (Parizot et al., 2006):

$$E_{\rm e,max} \approx (8.3\,\mathrm{TeV}) \cdot \bar{f}(r) \left(\frac{B}{100\,\mu\mathrm{G}} \right)^{-1/2} \frac{V_{\rm sh}}{1000\,\mathrm{km/s}} , \tag{1.49}$$

where $\bar{f}(r) = \frac{f(r)}{f(4)}$ and $f(r) = \frac{\sqrt{r-1}}{r}$.

Besides the maximum energy, it is the evolution of the VHE γ-ray luminosity which determines the visibility of a SNR in a certain evolutionary stage. Figure 1.8(a) illustrates the fraction of the total explosion energy converted into the energy of the accelerated particles (Drury et al., 1994). The assumed ejecta mass of the SNR is $1.4\,M_\odot$, the ambient medium density is $0.3\,\mathrm{cm}^{-3}$. During the free-expansion phase the fraction is still low, but it increases constantly and reaches a maximum of $\sim$0.5 in the late Sedov-phase. The corresponding integral γ-ray flux above 1 TeV is shown in Figure 1.8(b), increases quickly in the free expansion phase, and becomes roughly constant during the Sedov-Taylor phase.

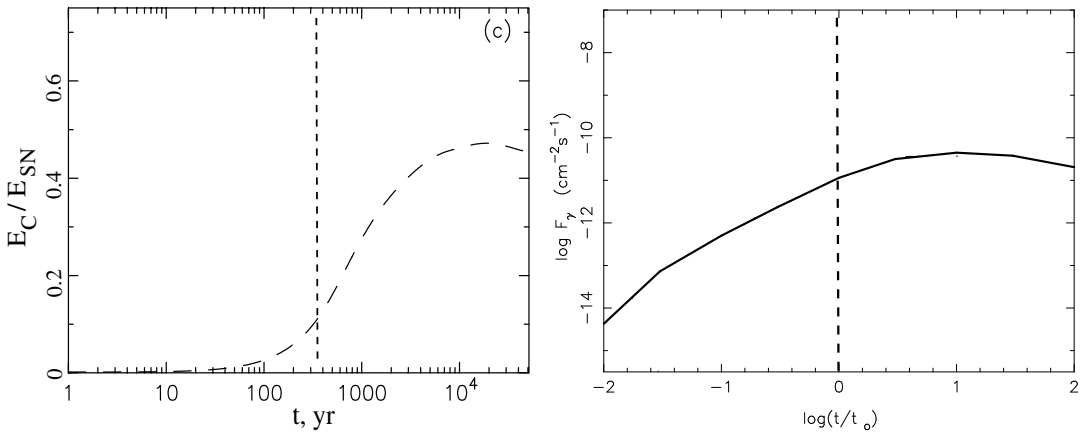

(a) (b)

Figure 1.8: a) Ratio of the explosion energy channeled into accelerated particles depending on the time since the explosion; The explosion energy is set to 10^{51} erg, the ISM gas number density is set to $0.3\,\mathrm{cm}^{-3}$. The ejecta mass is $1.4\,\mathrm{M}_\odot$ and the power-law index of the density profile is set to $n = 7$. The injection rate is 10^{-4}. The figure was taken from Berezhko & Völk (2004). The vertical line illustrates the time t_0=368 yrs when the SNR enters the Sedov-Taylor phase; b) Integral TeV γ-ray flux, normalized to a distance of 1 kpc as a function of time. The same parameters as in a) were used. The figure was taken from Berezhko & Völk (2000).

1.3.2 Pulsars and Pulsar Wind Nebulae

A large fraction of the Galactic VHE γ-ray sources are related to high-energy pulsars, the compact remnants of core-collapse supernovae of very massive stars. The VHE γ-radiation, however, normally does not originate directly from the pulsar. Only in the case of the Crab nebula, pulsed VHE γ-ray emission was observed above 25 GeV (Teshima, 2008). Instead, the pulsar drives a wind of energetic particles into the surrounding SNR ejecta. At the resulting shock front, particles are re-accelerated and form the pulsar wind nebula (PWN) which expands into the surround medium. It is this inflating bubble filled with energetic particles that emits the observed VHE γ-radiation. For a recent review on PWNe see Gaensler & Slane (2006)

After a short introduction of the necessary pulsar characteristics, the main emphasis will be placed on the description of pulsar wind nebulae, including their structure, their evolutionary stages and the dominant γ-ray production mechanisms. The Section will conclude with a short summary of the observational characteristic of these objects as seen in VHE γ-rays.

Pulsars

Due to magnetic freeze-out and angular momentum conservation, a neutron star formed in a core-collapse SN can be highly magnetized and rapidly rotating. Typical rotation periods are of the order of 1-10 ms. The magnetic field on the surface of the neutron star is of the order of 10^{12} G, while the mass ranges from $0.1M_\odot$ to $2M_\odot$ concentrated within a radius of

$\sim$10 km. When there is a misalignment of the magnetic and the rotation axis, the magnetic axis precesses around the rotation axis, and with it a beam of highly energetic radiation which is emitted near the magnetic poles. If this beam happens to sweep past the observer, a periodic signal of energetic radiation is measured from the neutron star, which then is called a pulsar. The first pulsars were detected in the radio waveband (Hewish et al., 1968) and so far $\sim$1700 of them are known (Manchester et al., 2005).

Over time, the rotation of the pulsar slows down as rotational energy is converted into other forms of energy. The typical spin-down rate is of the order of $\frac{\dot{P}}{P} \sim 10^{-15}\,\mathrm{s}^{-1}$, where P is the pulsar's spin period. The converted energy per time (spin-down luminosity) can be estimated from the spin-down rate:

$$\dot{E} = 4\pi^2 I \frac{\dot{P}}{P^3} = I\dot{\Omega}\Omega \tag{1.50}$$

where $I \approx 10^{45}\mathrm{g\,cm}^2$ is the moment of inertia of the pulsar and Ω its angular frequency. The slow down of the rotation can be characterized by:

$$\dot{\Omega} = k\Omega^n \tag{1.51}$$

where k is a constant and n is the braking index, the value of which depends on the energy loss mechanism. In the case where all energy is lost due to magnetic dipole radiation, i.e. pure magnetic braking, $n = 3$. If the second derivative of the rotational period is known, $\ddot{\Omega} = nk\dot{\Omega}^{n-1}$, the braking index can be directly inferred. In the four cases in which the braking index could be confidently measured, it falls in the range $2 < n < 3$ (Gaensler & Slane, 2006, and references therein), indicating that magnetic dipole braking is not the only energy loss mechanism at work.

The age of the pulsar can be estimated from

$$\tau = \frac{P}{(n-1)\dot{P}}\left[1 - \left(\frac{P_0}{P}\right)^{n-1}\right] \tag{1.52}$$

where P_0 is the pulsar's period at birth (Manchester & Taylor, 1977). Assuming $n = 3$ and $P_0 \ll P$, Equation 1.52 reduces to

$$\tau_\mathrm{c} \equiv \frac{P}{2\dot{P}} \tag{1.53}$$

where τ_c is called the *characteristic age*. τ_c often overestimates the true age of the system (e.g. Migliazzo et al., 2002), indicating that P_0 is not negligible compared to P.

Pulsar Wind Nebulae

Pulsars are known to drive powerful winds consisting of electromagnetic energy and highly relativistic particles. The interaction of this pulsar wind with the ambient medium gives rise to a complex structure known as pulsar wind nebula. Kennel & Coroniti (1984), in their pioneering spherically symmetric MHD[4] model for the Crab nebula, subdivided the structure of the pulsar/PWN/SNR complex into six parts. Their original structure is illustrated in Figure 1.9. Even though alterations to the model were necessary to account for e.g. the observed anisotropy of the Crab nebula, the original six-fold structure is still valid and will be used in the following.

[4]Magnetohydrodynamic

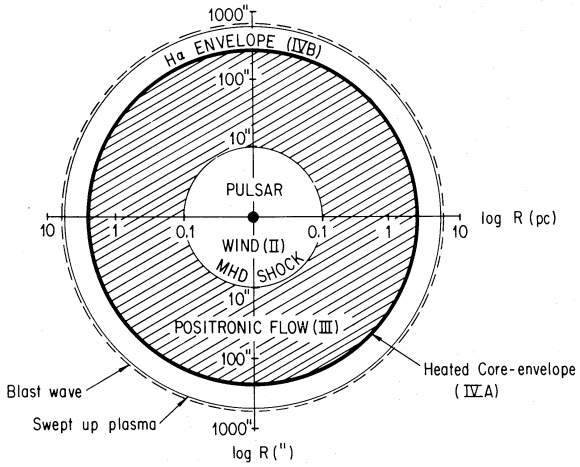

Figure 1.9: Idealized sketch of the Crab nebula and the parent SNR. Region I: pulsar and magnetosphere, outer boundary is the light cylinder; Region II: un-shocked ultra-relativisitc wind terminated by a standing MHD shock; Region III: actual PWN; RegionIV: Region outside the PWN, but still within the parent SNR, region (A) has been shock heated in its interaction with the pulsar flow, region (B) contains a cooler hydrogenic envelop; Region V: Contains the material, swept up by the SNR forward shock front; Region VI: The interstellar medium. The figure was taken from Kennel & Coroniti (1984).

Region I: The first region is called the pulsar's magnetosphere. The magnetic field lines at its boundary surface, which originate from the pulsar and co-rotate with it, are torn as their track speed reaches the speed of light. The radius of the light cylinder is of the order of 10^8 cm. The region is indicated in by the small spot at the center of Figure 1.9 and 1.10. The pulsar wind consisting of electromagnetic energy and highly relativistic particles originates from this region. However, how (and especially where) these particles are accelerated is still not settled. The currently best guess is that the particle acceleration occurs in the collapse of charge-separated gaps, either close to the pulsar at the polar caps (polar cap model), in gaps further out and close to the light cylinder (outer gap model) or somewhere in between (sliding gap model). For more details on acceleration models within pulsar magneto-spheres, see Harding (2001).

Region II: The pulsar wind leaves the light cylinder and traverses outward at highly relativistic speed, with a bulk Lorentz factor of the order of 10^4 to 10^6. Where the wind is decelerated to match the velocity of the more slowly-expanding ambient material, a standing termination shock is formed — visible as an inner ring structure in Figure 1.10 (right). In the Crab nebula case, the radius of the termination shock is estimated to $\sim$0.1 pc (Kennel & Coroniti, 1984).

The nature of the pulsar wind changes somewhere in this region. Close to the pulsar it is dominated by the energy flux of the magnetic dipole radiation, thus the magnetization σ (ratio between electromagnetic and particle energy density) is very large ($\sigma \gg 1$). At the shock front, the situation has changed and the pulsar wind is highly particle dominated ($\sigma < 1$). Thus, the energy has been transferred from electro-magnetic fields to the bulk of the particle population, by which mechanism is still unknown. The problem is directly related

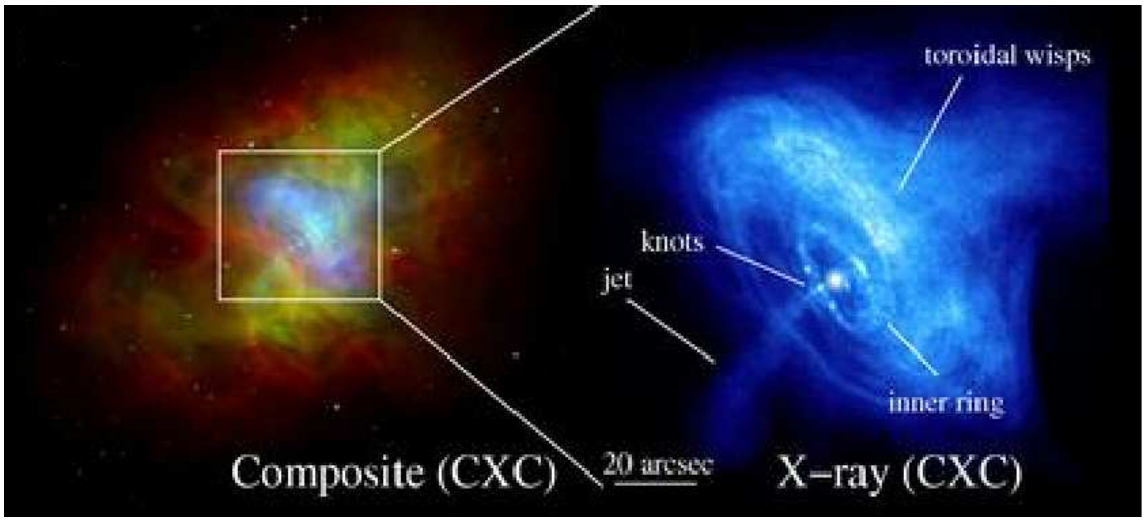

Figure 1.10: Image of the Crab nebula. *left:* Composite image of radio (red), optical (green) and X-ray emission (blue). *right:* X-ray synchrotron emission showing the termination shock (inner ring), the wind downstream of the shock and the jets. The Figure was taken from Gaensler & Slane (2006).

to the nature of the wind's particle content. Models of pair-creation in the magnetosphere fail to produce the necessary number of leptons to explain all the nebula's emission. An additional contribution of ions would soften the requirement on the lepton production, but ions are even harder to extract from the pulsar (Kirk et al., 2007).

The particle-dominated wind from the pulsar is not isotropic, but most of its energy is concentrated into an equatorial belt. As the plasma flows between the light cylinder and the termination shock is along the magnetic field lines, this region appears under-luminous in synchrotron radiation, see region within the inner ring in Figure 1.10 (right).

Region III: This region constitutes the actual pulsar wind nebula. At the shock front, the particles of the pulsar wind are thermalized and re-accelerated. As the wind's energy is concentrated into an equatorial belt, a torus, visible through its synchrotron radiation at X-ray energies (Weisskopf et al., 2000), is formed perpendicular to the pulsar's rotation axis, see Figure 1.10 (right). In addition, jets and counter-jets are visible, but these – most likely – do not originate directly from the pulsar, but consist of shocked plasma collimated by azimuthal magnetic fields (Kirk et al., 2007).

Further out – far beyond the torus – the re-accelerated particles form an expanding bubble, which often exhibits slight elongation along the pulsar spin axis, see Figure 1.10 (left). Despite the elongation of the bubble, the bulk particle flow has still a large radial component, which is orthogonal to the toroidal field lines. Diffusion is therefore suppressed and the PWN expands convectively (de Jager & Djannati-Ataï, 2008). Thus, the expansion velocity and thereby the size of the PWN is determined by the bulk flow velocity of the energetic particles. Together with the magnetic field within the PWN, the flow velocity depends on the distance to the pulsar and the magnetization parameter σ. Figure 1.11 illustrates the radial dependence of both quantities. Note that the magnetization is very low for the Crab nebula ($\sigma \sim 0.03$ Kennel & Coroniti, 1984). The average flow speed within the Crab neb-

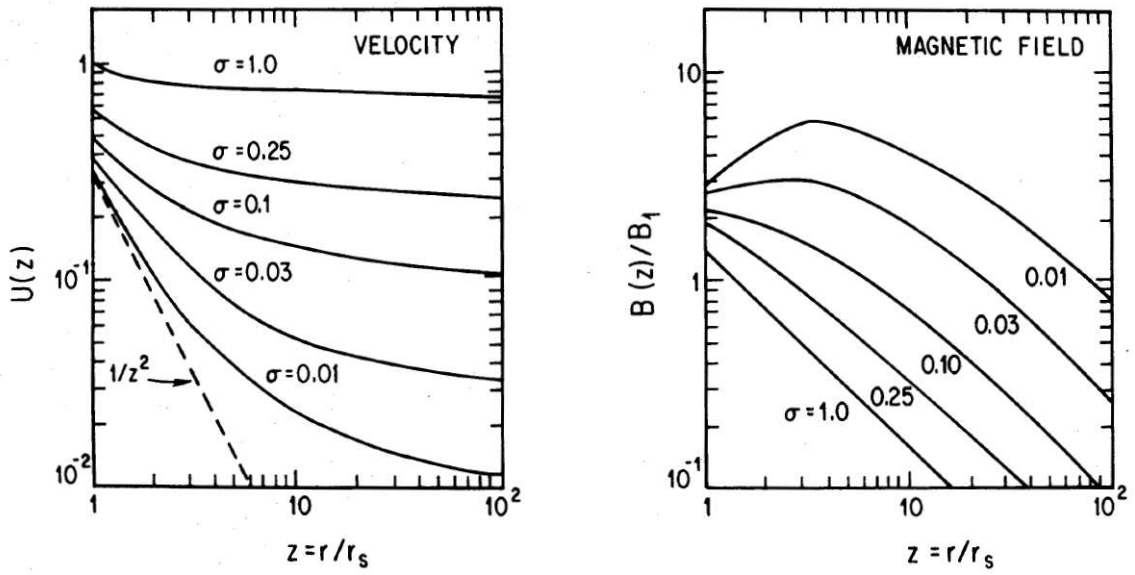

Figure 1.11: *left:* Post-shock flow velocity within the Crab PWN in units of c against $z = r/r_{\rm s}$ where r is the distance to the pulsar and $r_{\rm s} \sim 0.1\,{\rm pc}$ is the radius of the termination shock front. *right:* Magnetic field within the Crab PWN relative to its upstream value. The figure was taken from Kennel & Coroniti (1984).

ula is therefore estimated to $\sim 2000\,{\rm km/s}$, the maximum magnetic field strength is of the order of $200 - 300\,\mu{\rm G}$. The Crab nebula magnetic field strength is particularly high. More evolved and consequently more extended nebula show much lower magnetic field strength of $B \sim 10\,\mu{\rm G}$, as in the case of PSR B1823-13 (Aharonian et al. (H.E.S.S. collaboration), 2005b, 2006e).

Region IV, V and VI: These regions are located outside the PWN. Region IV (A) in Figure 1.9 constitutes the interaction zone of the inflating PWN and the SNR ejecta. The PWN expands supersonically into the ejecta and thus produces a termination shock. Region IV (B) hosts a cooler hydrogenic envelope (McKee, 1974). Region V contains the material swept up by the SNR forward shock front and Region VI is the ambient interstellar medium.

PWN Evolution

Since a PWN is typically embedded into a SNR, its early evolution is strongly coupled to the SNR evolution. Four evolutionary stages can be distinguished (van der Swaluw et al., 2004):

- Supersonic expansion stage: The PWN bubble, inflated by the wind particles thermalized and re-accelerated at the termination shock, expands supersonically and thereby drives a shock into the ejecta of the SNR.
- Reverse shock interaction phase: When – typically after a few thousand years – the reverse shock of the SNR arrives at the boundaries of the inflating bubble, the PWN is crushed by the shock front. This initial interaction leads to an oscillation

of the PWN extension, which last typically for a time span of few thousand years. Due to the crushing, Rayleigh-Taylor instabilities form, which lead to a mixing of thermal and non-thermal material and a strengthening of the magnetic field within the PWN. If the reverse shock did not arrive simultaneous at the PWN from all sides, the resulting PWN may exhibit a strong asymmetry after the oscillation have faded and might even be offset from the actual pulsar position. Reasons discussed to explain a deferred arrival of the reverse shock are a high kick velocity of the pulsar and a density gradient in the surrounding of the SNR (van der Swaluw et al., 2004; Blondin et al., 2001). A high velocity of the pulsar might offset the PWN from the SNR center before the reverse shock arrives. A density gradient in the ambient medium would lead to a deferred creation of the reverse shock in the low density region compared to the region of higher density.

- Subsonic expansion stage: After the oscillations have faded the pulsar will steadily inflate its nebula around its current position. The expansion of the PWN is now subsonic because the surrounding SNR ejecta has been heated by the reverse shock. If the original PWN, created before the interaction with the reverse shock, is far offset from the current pulsar position, it is not energized anymore by the pulsar and becomes a *relic* PWN.

- Bow shock stage: This stage only occurs if the pulsar was born with a high kick velocity. As it approaches the edge of the SNR, the sound speed in the shocked ejecta decreases and the pulsar starts to drive a cometary bow shock. At some point it might leave its SNR and traverse the interstellar medium, still creating the bow shock PWN until its power-output decreases to a point where it can no longer power a PWN.

γ-Radiation from PWN

The regions of a pulsar/PWN complex (Region I, II and III in Figure 1.9) differ substantially in their astrophysical properties, and thus, in their dominant production mechanisms for γ-radiation. Their characteristics are illustrated in Figure 1.12, and are summarized in the following:

Region I: Pulsed γ-radiation is expected in the GeV energy range dominantly created by the curvature radiation of the ultra-relativistic electrons within the pulsar magnetosphere. Both, the polar cap and the outer gap model, predict an exponential cut-off of the curvature radiation spectrum around 10 GeV. However, the model predictions differ in the TeV energy range: The outer gap model predicts an additional multi-TeV component due to IC scattering of the energetic electrons on the ambient photon fields, like the thermal emission from the pulsar. The polar gap model, however, predicts no such component, because the TeV γ-rays do not leave the magnetosphere. They are absorbed in pair-production processes within the strong magnetic field at their production site close to the pulsar.

Region II: The bulk Lorentz-factor of the un-shocked wind is of the order of 10^4-10^7. Even though the wind is magnetized, it does not emit synchrotron radiation, because the electrons move with the magnetic field lines frozen into the wind. Therefore the region appears under-luminous in Figure 1.9. However, Aharonian & Bogovalov (2003) suggested that the un-shocked ultra-relativistic wind can produce non-negligible high energy

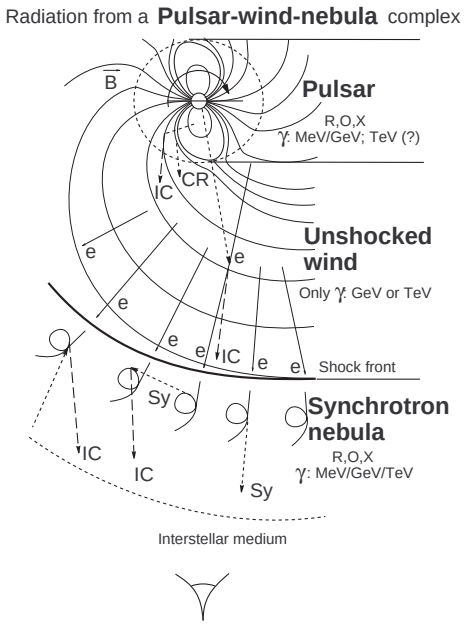

Figure 1.12: Sketch of the sites and radiation mechanisms of non-thermal emission within a pulsar/PWN complex: The three regions correspond to Region I, II and III in Figure 1.9. R, O, X and γ stand for radio, optical, X-ray and γ-rays. CR, IC and Sy are abbreviations for curvature, inverse Compton and synchrotron radiation. The orientation of the magnetic field lines is also shown. The figure was taken from Aharonian & Bogovalov (2003).

γ-radiation via IC scattering. Suitable target photon field would be e.g. the thermal emission from the pulsar or non-thermal radiation from the magnetosphere. Depending on the Lorentz factor of the wind, the IC γ-radiation is expected in the energy range from 10 GeV to 10 TeV.

Region III: At the termination shock front, the particles of the pulsar wind are thermalized and re-accelerated. The energetic electrons then emit synchrotron and IC radiation. It is this particle population which contributes most to the VHE γ-radiation observed by H.E.S.S.. Therefore, its characteristics will be addressed in a bit more detail below:

The nature of the acceleration process, occurring at the termination shock front, is still under debate. It seems that at least two different processes are necessary. The first dominates at low energies (100 MeV-1 TeV). Possible candidates are the resonant absorption of coherently emitted ion cyclotron waves and the annihilation of magnetic flux in the shock front (Hoshino et al., 1992; Amato & Arons, 2006). The second process, believed to be responsible for the high energy particles (>1 TeV), is most likely Fermi-type relativistic shock acceleration (Kirk et al., 2007). The spectrum expected from RSA, as shortly described in Section 1.1.2, is a power-law $N(E) \propto E^{-s}$ with an index of $s = 2.2-2.3$ (Achterberg et al., 2001).

Equivalent to the case of SNR shock acceleration, the maximum reachable energy of the accelerated particles is of great interest also for PWNe, as it determines the detectability of an individual object at very high energies. Originally proposed by Harding & Gaisser

(1990), the maximum energy is limited by the requirement that the highest energy particles must still be contained in the shock to participate in the acceleration process. The necessary requirement writes as:

$$E_{\rm max} = Ze\epsilon B_{\rm s} R_{\rm s} \ , \tag{1.54}$$

where Z is the charge number of the accelerated particles, $B_{\rm s}$ is the post-shock magnetic field strength, $R_{\rm s}$ the radius of the shock front and $\epsilon < 1$ is the fractional size of $R_{\rm s}$ required for containment (de Jager & Djannati-Ataï, 2008). Relating $B_{\rm s}$ to the pulsar spin-down power $\dot{E}$ and to the characteristics of the termination shock, de Jager & Djannati-Ataï (2008) arrive at the following expression for the maximum energy:

$$E_{\rm max} = (110\,{\rm TeV})\kappa \left(\frac{\epsilon}{0.2}\right) \left(\frac{\sigma}{0.1}\frac{\dot{E}}{10^{36}{\rm erg/s}}\right)^{1/2} \ , \tag{1.55}$$

where $1 < \kappa < 3$ (Kennel & Coroniti, 1984) is the magnetic compression ratio and σ is the wind magnetization parameter. This relation only holds in the case where additional losses, such as synchrotron cooling, can be neglected. Thus Equation 1.55 is applicable to ion acceleration or electron acceleration in a low ambient magnetic field.

In the case of electron acceleration in strong magnetic fields, the maximum energy can be approximated by balancing the acceleration rate with the synchrotron loss rate. de Jager et al. (1996) estimate the acceleration rate $t_{\rm acc}^{-1}$ to be close to the particle's gyro-frequency $\nu_{\rm g}$: $t_{\rm acc}^{-1} = \alpha\nu_{\rm g}$, where $\alpha \leq 1$, and arrive at the following expression for the maximum energy:

$$E_{\rm max} \simeq (200\,{\rm TeV}) \left(\frac{\alpha}{< \sin^2\theta >}\right)^{1/2} \left(\frac{B}{100\,\mu{\rm G}}\right)^{-1/2} \ , \tag{1.56}$$

where θ is the electron's pitch angle.

Observational Characteristics

A significant fraction of all Galactic VHE γ-ray sources are likely associated with PWNe of very energetic pulsars. Two classes seem to emerge within this important population. On the one hand, there area the young plerions, like G 21.05-0.9 or Kes 75 (Djannati-Atai et al., 2007a), which are still at the beginning of their evolution and appear point-like to IACTs like H.E.S.S.. The other class consists of middle-aged and more evolved PWNe like HESS J1825-137 (Aharonian et al. (H.E.S.S. collaboration), 2005b, 2006e) or VelaX (Aharonian et al. (H.E.S.S. collaboration), 2006f). As two of the VHE γ-ray sources analyzed in this work might belong to the class of evolved PWNs, a few observational characteristics of this class will be summarized below. A more detailed discussion will be given in the individual analysis in Section 5.

- The VHE PWNe of middle aged pulsars (older than a few thousand years) are often largely extended. The necessarily long cooling time of the parent electron population hints at a low magnetic field strength within the VHE PWN, with values not much higher than the Galactic average of 2-5 μG.
- The center of gravity of the VHE emission region is often offset from the current pulsar position. As described in the Section *PWN Evolution* 1.3.2 such asymmetries

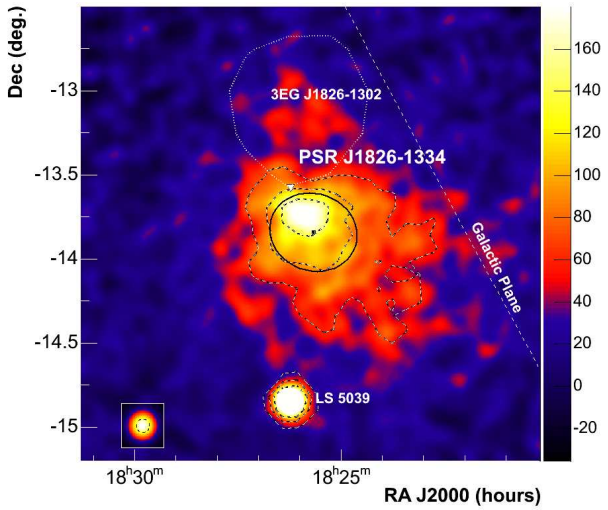

Figure 1.13: Smoothed VHE γ-ray excess map of HESS J1825-137(Aharonian et al. (H.E.S.S. collaboration), 2006e). The position of the pulsar is marked by a white triangle, as well as the best-fit position (black rectangle) and the extension (black ellipse) after accounting for the point-spread function of the instrument.

can be attributed either to a high kick velocity of the pulsar or to an inhomogeneity in the ambient interstellar medium.

- The energy content within the large VHE PWNe can be rather high and might account for a large fraction of the pulsar's spin-down power. Due to the low magnetic field, relic electrons accelerated since the birth of the pulsar might be stored in the PWN reservoir. The observed VHE γ-ray flux would then be relative to the time integrated spin-down power, including the epochs of much higher power output. Naturally, this is only possible if the strong magnetic field, as expected at the pulsar's birth, drops fast due to a rapid expansion of the PWN in the supersonic expansion phase.

- The VHE PWN are often much larger than their synchrotron counterparts visible at X-ray energies. The radially decreasing magnetic field limits the size of the synchrotron emission region. Additionally, the electrons emitting synchrotron radiation in the X-ray regime are, in magnetic fields of 2-5 μG, more energetic than the VHE γ-ray producing electrons, see Equation 1.18. The result is a longer synchrotron lifetime of the later electron population, which, assuming energy independent convection speeds, leads to a larger size of the VHE PWN as well. Furthermore, an energy dependent morphology was observed even within the PWN regime. It becomes manifest in the spectral steepening of the VHE γ-ray spectrum with increasing distance to the pulsar.

- X-ray counterparts have not been detected for all VHE PWN candidates. If the magnetic field strength is low enough, the X-ray synchrotron radiation might be below detectable levels. Not even the pulsar might be detectable through its thermal X-ray component, since the lifetime of the VHE γ-ray emitting electrons

may even exceed the neutron star's cooling and non-thermal radiation time scales (de Jager & Djannati-Ataï, 2008). The result would be a VHE PWN without X-ray counterpart.

Figure 1.13 depicts the VHE γ-ray excess of HESS J1825-137, which is securely associated with the PWN of the high spin-down luminosity pulsar PSR B1823-13 (Aharonian et al. (H.E.S.S. collaboration), 2005b, 2006e). It is one of the prime examples of a VHE PWN and exhibits all of the aforementioned characteristics.

Chapter 2

H.E.S.S. and its Data Analysis Scheme

When high-energy γ-rays enter the earth's atmosphere they interact with atmospheric nuclei and induce large cascades of secondary particles – known as *air showers* – in the process. Thus, their direct detection is only possible above the atmosphere and satellite-based experiments such as EGRET (Hartman et al., 1999), INTEGRAL (Winkler et al., 2003) and FGST [1] (Ritz et al., 2007) dominate the field of γ-ray astronomy up to energies of $\sim$100 GeV. At even higher energies, the detection area of these satellite experiments (on the order of m^2) is not sufficient to measure the strongly declining particle flux. At these energies, only the indirect detection of the primary γ-rays by means of their induced air showers can provide the necessary instrumented volume. The Imaging Atmospheric Cherenkov Technique is currently the most successful approach for the detection of VHE γ-rays at energies between 100 GeV and 100 TeV. It uses the Cherenkov light emitted by the secondary particles to image the air shower and deduce from it the properties of the primary γ-ray. The characteristics of air showers and their emitted Cherenkov light will be shortly summarized in Section 2.1. The general principle of the Imaging Atmospheric Cherenkov Technique will be explained in Section 2.2. The chapter will conclude with a description of the H.E.S.S. (High Energy Stereoscopic System) experiment, an array of four IACTs, which currently dominates the field of VHE γ-ray astronomy. The telescope array itself is presented in Section 2.3. The standard analysis scheme applied to the H.E.S.S. data is summarized in Section 2.4. Finally, some basic performance properties of the H.E.S.S. experiment will be given in Section 2.5.

2.1 Air Showers

The stream of cosmic rays impinging onto the earth atmosphere consists mainly of protons (87%), α-particles (12%) and a small fraction of heavier atomic nuclei. Electrons, γ-rays and high energy neutrinos constitute only a minor fraction (0.2%). When these particles enter the atmosphere, the first interaction with an air molecule initiates a cascade of secondary particle production and further interactions. The air shower propagates through the atmosphere until the initial energy of its primary particle is exhausted by particle

[1] Fermi Gamma-ray Space Telescope, originally named GLAST

creation and ionization. The characteristics of the air shower depend strongly on the nature of the primary particle. In case of a γ-ray or an electron, the shower is purely electromagnetic. If the incident particle was a nucleus – most likely a proton – a hadronic component will emerge, further producing electromagnetic sub-showers. If the incident particle's energy is high enough, the secondary particles within the shower traverse the atmosphere at velocities higher than the local speed-of-light. The consequently emitted Cherenkov light can be used for their detection.

Electromagnetic Air Showers

If the incident particle interacts purely via the electromagnetic interaction, the resulting air shower will be of electromagnetic nature as well. Successive bremsstrahlung and pair production processes sustain the electromagnetic cascade: a high energy γ-ray converts into an electron-positron pair when traversing the Coulomb-field of an atmospheric nucleus (pair production); the leptons created in turn are deflected by close-by nuclei and thereby emit high energy photons (bremsstrahlung). These two processes dominate the propagation of the air shower mainly along the primary particle's initial course as the secondary particles are emitted with minimal transverse momentum. Some lateral spread, however, arises from multiple Coulomb scattering of the $e^{\pm}$-pairs in the atmosphere. The total number of secondary particles rises exponentially at first. Its increase, however, recedes when the average particle energy falls below $\sim$80 MeV as the shower particles start to lose their energy mainly through ionization of air molecules instead of photon creation via bremsstrahlung. The maximum number of particles is directly proportional to the energy of the primary particle. The height at which this maximum is reached, however, depends only logarithmically on the primary particle energy. The evolution of such an electromagnetic shower from the first interaction to its extinction occurs on a timescale microseconds. For a 1 TeV γ-ray the full shower cascade develops within $\sim$50 μs, the first interaction occurs at about 25 km and the maximum shower height is $\sim$10 km. Figure 2.1(a) illustrates the geometry of an electromagnetic air shower.

Hadronic Air Showers

In the case where the energetic primary particle is a hadron, it scatters in-elastically off the air nuclei and gives rise not only to secondary mesons like pions and kaons but also hyperons and nucleons. As these particles interact via the strong interaction, a hadronic particle cascade develops. At each interaction, however, about one sixth of the shower's energy is channeled into electromagnetic sub-showers via the decay of neutral and charged mesons. Furthermore, additional energy loss occurs in the form of penetrating muons and high energy neutrinos generated in the decay of the charged $\pi^{\pm}$. The shower geometry of a hadron-induced air shower is illustrated in Figure 2.1(b).

Due to the distinct interaction processes, hadronic showers exhibit different characteristics than their electromagnetic counterparts:

- Due to the large transverse momentum of secondary particles produced in strong interactions, hadronic showers exhibit a far greater lateral spread than electromagnetic showers.
- While complex multi-particle processes occur in hadronic shower, electromagnetic showers are dominated mainly by simple three-particle processes. As a result,

hadronic showers are less regular and exhibit larger fluctuations than electromagnetic showers.

- The mean free path within the atmosphere is far greater for protons than for γ-rays (about a factor of 2). Consequently, hadronic showers penetrate deeper into the atmosphere.

- A large fraction of the primary hadron energy is lost from the hadronic shower through the production of long-lived muons and neutrinos as well as from dissipation in nuclear interactions. Despite the efficient energy transfer from the hadronic to the electromagnetic component, a hadronic shower contains three times less particles in the electromagnetic component than a γ-ray induced one, given the same primary particle energy.

Cherenkov Light from Air Showers

When the primary particle is energetic enough, the velocity of the secondary particles within the induced air shower may exceed the local speed-of-light. Under these circumstances, the charged particles will emit Cherenkov radiation. The peak of the Cherenkov emission lies in the UV region. Strong absorption in the atmosphere, however, shifts it to a wavelength of $\sim$330 nm. The Cherenkov photons are emitted into a narrow cone along the particle course. The opening angle is of the order of 1°-2° , depending on the refraction index of the surrounding medium and the particle velocity.

In the case of an electromagnetic shower, which itself shows only a small lateral spread, the Cherenkov light is emitted into a narrow cone. Figure 2.1(a) depicts the lateral projections of the Cherenkov light pool emitted from a simulated, γ-ray-induced air shower. The initial energy is 300 GeV. The narrow and homogeneous distribution of the Cherenkov-light emitting particles is clearly visible. Additionally, the increasing refraction index with decreasing height, leads to a slight focusing of the Cherenkov light onto the outer rim of the cone, which is merely smeared out by further scattering processes. The resulting light distribution on the ground is a rather homogeneous circle of radius 80 to 120 m around the shower axis, which is slightly fainter towards the center, see Figure 2.1(c). Even though the whole development of an electromagnetic shower takes about $\sim$50 μs, the front of the Cherenkov light is only visible for $\sim$10 ns at the ground as the cascade develops nearly along the light path. The Cherenkov light intensity on the ground is low. Due to further scattering (Mie and Rayleigh scattering) and additional absorption by ozone, only 100 ph/m^2 reach the ground in the case of a 1 TeV γ-ray primary particle.

In the case of a hadron-induced shower, the distribution of particles is more widely spread and exhibist stronger fluctuations, and the same is true for the emitted Cherenkov light. As the energy necessary to produce Cherenkov photons depends linearly on the mass of the particle, low mass particles, such as electrons, dominate the Cherenkov emission. It is, therefore, mostly the electromagnetic component within the hadron-induced showers that gives rise to the observed Cherenkov radiation. As a consequence, the Cherenkov emission from a hadron-induced shower is even more irregular than the shower itself. Due to the smaller number of particles in the electromagentic component, it is also three times fainter than that observed from a γ-ray induced shower, given the same primary particle energy. Figure 2.1(b) depicts the lateral projection of the Cherenkov light emitted by a hadronic air shower initiated by a proton with an energy of 1 TeV. The irregularity of

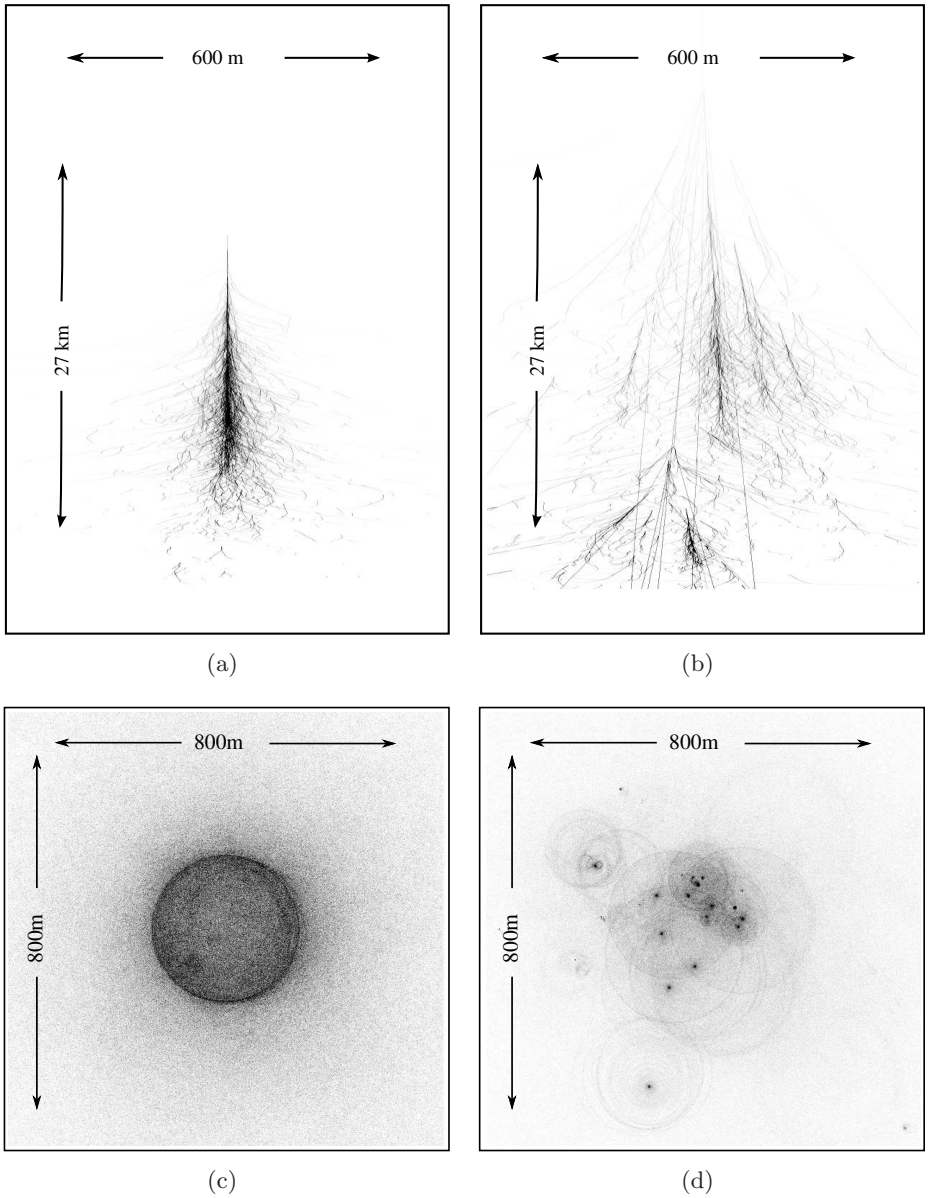

Figure 2.1: Cherenkov emission of a simulated air shower initiated by a 300 GeV γ-ray (a+c) or by a proton with an initial energy of 1 TeV (b+d); depicted are the projection on the (x,z)-plane (a+b) and the (x,y)-plane (c+d), where the x-axis and y-axis are parallel to the ground and the z-axis is orthogonal to both. The images were kindly provided by Konrad Bernlöhr.

the distribution compared to a γ-induced air shower (shown on the left) is clearly visible. The multiple sub-showers are also apparent in the light distribution on the ground, shown in Figure 2.1(d). An additional component of the hadron-induced air showers are the penetrating muons, which are – even close to the ground – still energetic enough to emit Cherenkov light in a narrow cone around their path.

2.2 Imaging Atmospheric Cherenkov Technique

Imaging atmospheric Cherenkov telescopes (IACTs) are currently the most sensitive instruments for VHE γ-ray astronomy in the energy range above 50-100 GeV. The technique was pioneered by the Whipple collaboration which operated a single 10 m diameter IACT and achieved an energy threshold of $\sim$350 GeV. They detected the Crab nebula, the first VHE γ-ray source, in 1989 (Weekes et al., 1989). In the successive generation of IACTs, significant improvements in sensitivity were achieved through the integration of multiple telescopes into arrays to allow for stereoscopic imaging. Prominent examples are the HEGRA (Fonseca, 1998) and the Cangaroo (e.g. Kubo et al., 2000) experiments. As the stereoscopic approach proved to be very successful, it was adopted in all instruments of the consequent third generation: H.E.S.S. (Hinton, 2004), Veritas (Weekes, 2005), Cangaroo-III (Kubo et al., 2004). As an exception, the MAGIC instrument (Cortina, 2005) employs only one IACT so far, but will take a second telescope into operation at the beginning of 2009 (Goebel, 2007). Compared with the previous generation instruments, the energy threshold was significantly lowered towards $\sim$100 GeV through the use of larger mirror areas.

Working Principle

VHE γ-rays incident on the earth's atmosphere, generate air showers of secondary particles which in turn emit Cherenkov radiation. A telescope located in the light pool, can collect the Cherenkov radiation using a large mirror and image the shower onto a sensitive camera. In this way the atmosphere acts as an integral part of the instrument and large detection areas of up 50,000 m^2 can be achieved surpassing by far the instrumented area of satellite-based experiments. As the Cherenkov flashes from air showers last only for a few ns, fast cameras are needed, suggesting the use of photo-multiplier arrays. The resulting image constitutes a two-dimensional projection of the shower into the camera plane. Figure 2.2(a) and 2.2(b) illustrates schematically the imaging geometry. The distance on the ground between the reflector mirror and shower influences the position of the shower image. The angle under which the shower is observed determines the length of the image, while the shower's lateral extent corresponds to the image's width. For the narrow γ-ray induced showers, the image's width is usually much smaller than its length, such that the shower image resembles an ellipse. Most hadron-induced showers exhibit a larger lateral spread and can thereby be distinguished from the γ-ray induced showers by the larger width of their images. The major axis of the elliptical images points on one side towards the direction of the primary γ-ray, and on the other side towards the shower impact point on the ground. Even though both parameters can be determined from a single shower image, the angular resolution is greatly improved if multiple images of the shower have been recorded from different viewing angles. This stereoscopic approach also improves the hadron rejection since the inconsistency between reconstructed shower directions can be utilized. The energy of the primary particle can be estimated from the intensity of the shower image and the distance between the telescope and the shower impact point on the ground.

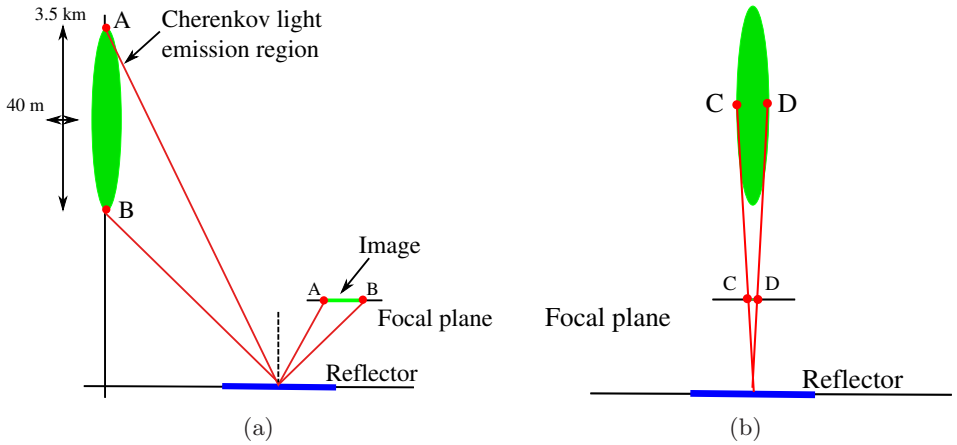

Figure 2.2: Sketch of the imaging geometry to illustrate the dependencies between shower morphology and the resultant image in the camera. a.) View on the plane spanned by the shower axis and the telescope position. The position of the image is determined by the distance of the shower from the telescope, its length additionally depends also on the longitudinal extend of the shower. b.) View from the telescope towards the shower, distance to the telescope and the lateral spread of the shower determines the width of the image.

Data Taking

Imaging atmospheric Cherenkov telescopes are normally operated only during *astronomical darkness*, when the moon is below the horizon, as the detection of the faint Cherenkov flashes is otherwise hampered by the additional light source. In H.E.S.S. data taking, the available time is sub-divided into observations of 28 minutes duration. During these *observation runs* a single astronomical object or a certain position in the sky is tracked and the data are taken continuously. The original observation strategy consists of consecutive *on-off* observations, in which data are taken first on the actual target (*on*-run) and then on an empty part of the sky (*off*-run), which serves to estimate the background. To keep the conditions for the two runs as constant as possible, both are taken at the same elevation.

Since modern IACTs are built with a larger field-of-view, *wobble*-mode observations are now more common. In this observation mode, the telescopes are aimed at a point slightly offset from the actual target (0.5° to 1.0°) which allows the simultaneous taking of *on*- and *off*-data. The background estimate is then obtained from the same field-of-view as the *on*-data, e.g. from a region with a similar offset from the camera center. The advantage of this observation scheme is, beside the doubling of the *on*-source time, that the *off*-data is taken under the exact same conditions.

2.3 The H.E.S.S. Experiment

The High Energy Stereoscopic System (H.E.S.S.) is an array of Imaging Atmospheric Cherenkov telescopes, dedicated to the observation of VHE γ-rays in the energy range between $\sim$100 GeV and a few tens of TeV. It started observation in summer 2002, when

the first telescope went into operation. The other telescopes were then gradually completed and the whole array is routinely operated since December 2003. The H.E.S.S. array is shown in Figure 2.3.

The Site

The H.E.S.S. array is located at 1800 m above sea level in the Khomas Highlands of Namibia (23°16'17"S, 16°29'58"E). A site chosen for its good observation conditions (Wiedner, 1998). In about 60% of all moonless nights, the sky above the H.E.S.S. array is completely cloud-less, allowing for unhampered imaging of the air showers. Furthermore, in almost all of these nights the relative humidity is below 90%, conditions easing the operation of the H.E.S.S. cameras. Finally, the location in the southern hemisphere permits the observation of the inner part of the Galactic Plane at low zenith angles, resulting in a maximum sensitivity coverage of this interesting region.

The Telescopes

The H.E.S.S. array consists of four identical telescopes placed on a square of 120 m side length to allow for stereoscopic imaging of the air showers. The spacing was chosen as a compromise between a maximum baseline for stereoscopic imaging and the number of telescopes able to observe the same shower. Each telescope consists of a camera, a reflector dish and a support structure. The reflector dish has a diameter of 13 m. It is equipped with 382 round mirrors each having a diameter of ∼60 cm. They are arranged in a Davies-Cotton design with a focal length of ∼15 m. The total mirror area is ∼107 m^2. The reflectivity of the mirrors at a wavelength of 330 nm is about 80%. After alignment of the individual mirrors, the optical point spread function lies between 0.25 mrad on-axis and 2.8 mrad off-axis at the edge of the field-of-view. The reflector dish is placed in an altitude mount on a supportive steel structure which itself can be rotated on a circular steel track to allow for movement in the azimuth direction. The slewing speed in both directions is about 100° per minute. Both mount and dish, are built for maximum rigidity and weigh together 60 tons. Nevertheless, the pointing accuracy of about ∼20" is limited by the bending of the camera

Figure 2.3: The H.E.S.S. telescope array.

Figure 2.4: One of the H.E.S.S. telescopes.

arm and deformation within the supportive frame. One of the H.E.S.S. telescopes is shown in Figure 2.4.

The Camera

The camera of a H.E.S.S. telescope is positioned in the focal plane of the reflector dish. It weights about 800 kg and is comprised of a hexagonal array of 960 photo multiplier tubes (PMT). The quantum efficiency of the PMTs is ∼25%. They were nevertheless favored above their alternatives like CCD cameras due to their fast response time, as the Cherenkov flashes from air shower last only a few ns. The camera is built in a modular design: each group of 16 PMTs is integrated into one of 60 drawers; each drawer houses the necessary trigger and readout electronics as well as the high voltage supply for its PMTs. The dynamical range of the data acquisition ranges from 1 to 1600 photo electrons. The front of the camera is equipped with a layer of Winston cones to funnel the incident light into the closest PMT, which reduces the area insensitive to light to less than 5%. Each PMT corresponds to an area of 0.16°, a pixelation small enough to resolve the details of the shower images. The total field-of-view of the camera in the sky is ∼5° in diameter.

The Trigger

The H.E.S.S. experiment employs a two-level trigger. While the first-level trigger is based on the single telescopes only, the second level requires a coincidence of at least two telescopes to provide the desired stereoscopic imaging. For the first-level trigger decision, the camera is subdivided into 64 overlapping trigger sectors each containing 8×8 pixels. A single telescope is triggered when 5 pixels within such a sector detect a signal of more than ∼4 photo-electrons within a time window of 1.5 ns. In a typical observation run, such single telescope triggers occur at a rate of approximately 250 Hz. Once an individual telescope is triggered, a signal is sent via optical cable to the *central trigger* located in the control building near the telescope array. A trigger for the whole system is generated only if at least two of the four telescopes are coincidentally triggered within a time window of 50 ns. It is only in this case that the data of the individually triggered telescopes are read out and stored. The central trigger thereby drastically reduces the random triggers due to night

sky background as well as single telescope triggers by muons. In a normal observation run, the central trigger rate is approximately 200-250 Hz.

2.4 The Standard Data Analysis Scheme

In this section the standard analysis scheme as applied to the H.E.S.S. data is briefly summarized. The different stages are introduced in the order they occur in the real data processing, from the calibration of the raw data, via the event reconstruction and gamma-hadron separation to the estimation of the remaining background. At the end, a short description is given of the statistical tools employed to quantify the extracted γ-ray signal.

Preparatory Steps

In the first step the raw data of each observation run, which is distributed into multiple files, has to be merged. In the process, the stereoscopic events are time-ordered. The raw data is then calibrated. A detailed description of the individual calibration steps is given in (Aharonian et al. (H.E.S.S. collaboration), 2004a). As the atmosphere is used as an integral part of the detector, only observation runs taken with properly working hardware during good and stable weather conditions can be used in the analysis. Requirements on the absolute value and the RMS of the trigger rate are used to reject observations with clouds in the field-of-view. Furthermore, the number of photo multipliers turned-off due to bright stars, technical problems and meteorites needs to be less than 10%. Beside the assurance of stable conditions, the time varying characteristics of the array must be taken into account. The optical response of each telescope, which is slowly decreasing on timescales of years due to diminishing mirror reflectivity, is extracted from the data. No additional calibration runs are necessary for this task, as the optical efficiency can be extracted from muon images found in the recorded data. Isolated muons normally trigger only one telescope and are therefore rejected by the central trigger. However, they are regularly recorded as part of hadron-induced air showers. They produce ring-shaped images, which greatly differ from the rest of the air shower image and are therefore easily identified. The expected light yield from these muons assuming 100% optical efficiency can be estimated from the geometrical parameters of their images. In comparison with the measured light yield, the actual optical efficiency can be extracted. For a detailed description see Bolz (2004).

Event Reconstruction

After the calibration, the individual shower images are cleaned to remove noisy pixels, whose intensities are unrelated to the Cherenkov image and are likely caused by night sky background and/or photomultiplier noise. Only pixels which contain more then 10 (5) photo electrons (p.e.) and have a neighboring pixel with at least 5 (10) p.e. are kept. The procedure results in a selection of extended features consisting of multiple, spatially connected pixels. Additionally, a varying threshold is applied to exclude pixels suffering from bright star light: the pixel intensity in the image must exceed 3σ of its pedestal RMS from the rest of the observation run. For each of the cleaned images, the *Hillas parameters* are calculated to characterize the image's intensity distribution. They constitute the first and second moments of the distribution and represent a parametrization of an ellipse, a shape motivated by the larger longitudinal then lateral extend of the air showers. They

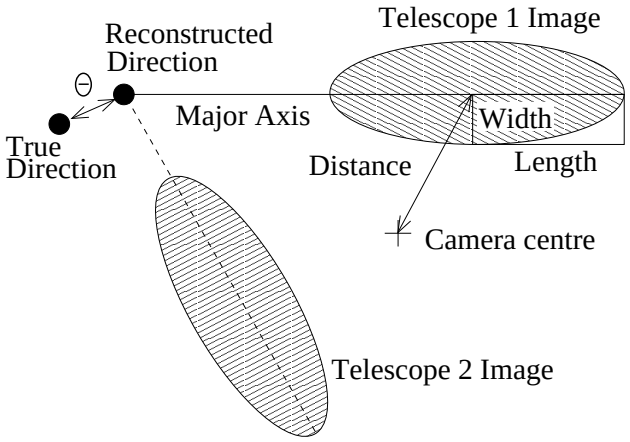

Figure 2.5: Hillas parametrization of the γ-ray induced shower images. The distance of the center-of-gravity to the camera center, the width and the length of the Hillas ellipses are used in the event selection. The intersection of the major axes in the correct coordinate system determines the origin of the primary particle and the impact position of the shower core on the ground. For simulated showers: The distance between the simulated and the reconstructed shower direction is called θ and determines the angular resolution of the instrument. Image taken from Aharonian et al. (H.E.S.S. collaboration) (2006g).

consist of the center-of-gravity, the length of the major axis, the length of the minor axis, the orientation and the image size, i.e. the total number of p.e. in the cleaned image. An illustration of the parameters is shown in Figure 2.5.

The Hillas parameters contain all the necessary information of the shower geometry to reconstruct the arrival direction, the impact point of the shower axis on the ground and the energy of the primary particle. As the H.E.S.S. array is operated with a two telescope multiplicity requirement, each shower is observed with at least two cameras. Using a simple stereoscopic approach, the origin of the primary particle is inferred from the intersection point of the major axis of the Hillas ellipses, superimposed in a common coordinate system. A sketch of the method is shown in Figure 2.5. The accuracy of the direction reconstruction, which determines the angular resolution of the instrument, is better than 0.1° for an individual event. A more detail description of the resulting point-spread function of the H.E.S.S. instrument will be given later in this chapter. The impact point on the ground is obtained in a similar way, intersecting the major axis in an array-wide coordinate system, starting from the telescope locations. Its reconstruction accuracy is better than 10 m for the showers which impact within 200 m from the center of the array. The impact distance is an important parameter for the reconstruction of the primary particle energy. It determines how many Cherenkov photons from the shower arrive at the telescopes. Unlike the direction reconstruction, which could be performed on the basis of the shower images only, the energy reconstruction needs further input from Monte Carlo simulations. Look-up tables, generated from γ-ray Monte Carlo simulations, are used to determine the primary particle energy according to the integrated image amplitude and the reconstructed impact parameter. As the Monte Carlo simulations were produced for a fixed optical efficiency, the energy read from the look-up tables has to be corrected to

account for the difference between simulated and actual optical efficiency of the telescopes during the data taking. The correction is applied in the form of a simple scaling of the energy by the ratio of the optical efficiencies. The average energy resolution estimated using the same Monte Carlo simulations is ∼15%.

Event Selection

Various selection cuts are applied on the image parameters to reject badly reconstructed images and enrich γ-ray induced air showers. First, a minimum requirement on the image amplitude after cleaning ensures a meaningful Hillas parametrization (*size cut*). To avoid images merely partly contained in the camera, only ellipses with a center-of-gravity within 2° of the camera center are used for reconstruction (*nominal-distance cut*). For stereoscopic reconstruction, at least two of the camera images have to fulfill the aforementioned requirements. As the numerically dominant hadron-induced air showers are less elliptical than the γ-ray induced showers, their difference in shape can be exploited to suppress the hadronic background. The width and length of the shower images are compared to the mean values expected from γ-ray Monte Carlo simulations, given their image amplitude, impact distance, zenith angle and offset from the system pointing direction. The difference is then scaled by the spread of the simulated distribution and averaged over all participating telescopes to yield the *mean reduced scaled width* (MRSW) :

$$\mathrm{MRSL} = \frac{1}{N_{\mathrm{tel}}} \sum_{i=1}^{N_{\mathrm{tel}}} \frac{\mathrm{width}_i - < \mathrm{width} >_i}{\sigma_{\mathrm{w,i}}} \ . \tag{2.1}$$

and similarly the MRSL. Figure 2.6(a) and 2.6(b) depict the distributions of MRSW and MRSL for simulated γ-ray induced shower and hadron-induced shower from simulations and real data. Selecting a certain range for the values of MRSL and MRSW leads to an enrichment of γ-ray induced air showers. Furthermore, since the hadronic background arrives isotropically, a restriction on the angular distance θ between reconstructed shower direction and the source position can be used to further suppress the residual hadronic background.

The optimum values of the aforementioned selection requirements were simultaneously optimized to the yield the maximum significance per hour of observations for two different source classes. First, the *hard*-cuts were optimized for faint point-sources, with a flux of 1% of the Crab nebula flux and a hard power-law spectrum with index $\Gamma = 2$. They are mostly used for source detections and morphology studies, as they provide a superior sensitivity and angular resolution. The *standard*-cuts were optimized for more luminous sources with a flux of 10% of the Crab nebula flux and a similar energy spectrum (Γ=2.6). They are mostly used for spectral analysis, as they feature a lower energy threshold than the *hard*-cuts. Table 2.1 summarizes the different cut values. It should be noted that the sizes of the on-source regions stated in Table 2.1 were optimized for point-sources. In case the VHE γ-ray source to be analysed is extended beyond the point-spread-function of the instrument, larger on-source regions can be used to fully incorporate the source.

Background Estimation

After the application of the image shape selection cuts, the remaining events appear γ-ray like, in the sense that they can not easily be distinguished from the signal events by means of

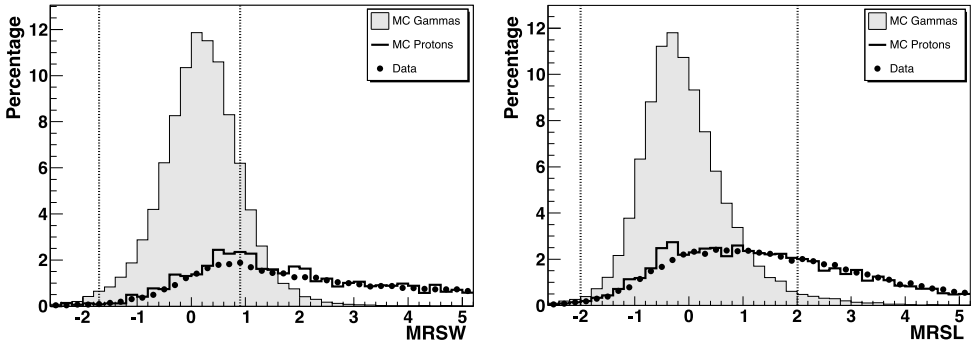

(a) (b)

Figure 2.6: Distribution of a.) mean reduced scaled width (MRSW) and b.) mean reduced scaled length (MRSL) for Monte Carlo γ-ray simulations, Monte Carlo proton simulations and real off-data. The simulated energy spectrum of γ-rays and protons follows a pure power-law with an index of Γ=2.59 and Γ=2.70, respectively. All distributions were produced for a zenith angle of 20°. The cut-values for γ-ray selection used in the *standard*-cuts are illustrated by the vertical lines. The figure was taken from Benbow, W. (for the H.E.S.S. Collaboration) (2005).

set	MRSW min	MRSW max	MRSL min	MRSL max	θ degr.^{2}	size min p.e.
standard	-2.0	0.9	-2.0	2.0	0.0125	80
hard	-2.0	0.7	-2.0	2.0	0.01	200

Table 2.1: Optimized values for the γ-ray selection cuts, for two different configurations. Additionally, a minimum of two camera images passing the size and nominal distance cuts are required.

the aforementioned parameters. Even though the signal events are enriched in this sample, hadron-induced γ-ray-like events are still present. To extract a signal of γ-ray induced events (N_γ) from a certain position in the sky, it is necessary to estimate the underlying background component of non-γ-ray events (N_{Bg}). The signal is then determined by $N_\gamma = N_{\mathrm{On}} - N_{\mathrm{Bg}}$, where N_{On} is the total number of γ-ray-like events within the signal region, commonly defined as a circular region of radius θ around the source position. Three different methods of background modeling are used in this work. They all determine the background level from control regions hosting no γ-ray signals: $N_{\mathrm{Bg}} = \alpha N_{\mathrm{Off}}$. Here, N_{Off} is the number of events within the control regions and α is a normalization factor to account for differences in area and acceptance between signal and control regions. The three methods will be briefly described in the following, emphasizing their strengths and weaknesses that determine their different fields of application.

In the *ring-background method*, the control region is a ring which is centered on the signal region. Its inner radius is chosen far greater than the extent of the *On*-region to avoid a contamination with signal-events. Its area is much larger then the area of the *On*-region

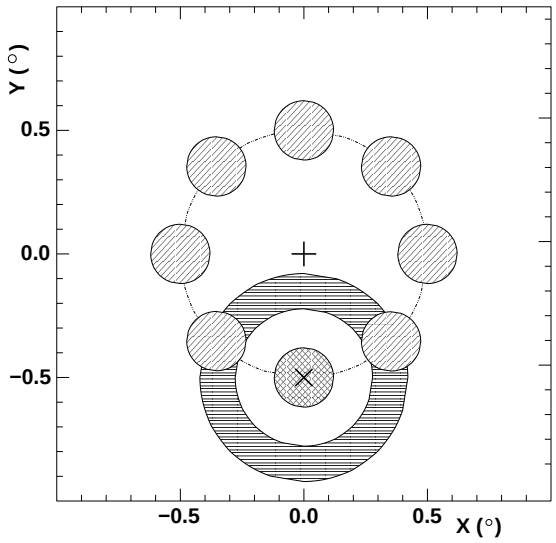

Figure 2.7: Sketch of the *on*- and *off*- region for the different background estimation methods. The *on*-region is cross hatched, the *off*-regions for the reflected region method is filled by diagonal lines and the ring-background region is filled by horizontal lines. The image was taken from Aharonian et al. (H.E.S.S. collaboration) (2006g).

(by a factor of ∼7), to minimize the statistical fluctuations in the background estimate. Figure 2.7 illustrates the ring-shaped *Off*-region. As the *On*- and *Off*-regions have vastly different offsets from the camera center, the normalization factor α has not only to account for the different areas but also for the different background acceptances within the camera. As the model uses an energy-averaged model for the camera acceptance, it cannot easily be used for spectral extraction. However, as the background can be derived for each point in the field of view, the method is well suited for 2D image generation and morphology studies. It should be noted, that the method inherently generates a correlation of the background estimates even for spatially separated sky positions.

To avoid the strong dependence on the camera acceptance model, the *reflected-region background method* uses control regions with the same size and offset from the camera center as the signal region. The background regions are illustrated in Figure 2.7. As the camera acceptance is roughly radially symmetric with respect to the camera center, all regions have the same background acceptance. Consequently, the normalization factor α is then merely the ratio of the number of *On*- and *Off*-regions. The method is ideally suited for the analysis of data taken in wobble-mode observations, and is the default method for spectral analysis.

Inherently, the *reflected-region background method* requires the *On*-region to be offset from the camera center. Consequently it can not be used if the observation position is within the emission region. In this case, the *On-Off background method* is applied, which determines the background level from off-observations which do not have a γ-ray signal in the field-of-view and are taken at the same elevation as the on-source observations. Only one *Off*-region is used. It is placed at the same position relative to the camera center as the *On*-region. Therefore, no assumptions have to be made on the shape of the camera acceptance, aside from it being the same for both observations. Nevertheless, the

background estimate extracted from the off-observation has to be normalized to account for different durations of the observations and different trigger rates. The total number of γ-ray like events outside the emission region is used for that purpose.

Signal Evaluation

Having extracted the number of *On*- and *Off*-events, as well as the corresponding normalization factor α, the number of excess events is given by:

$$N_\gamma = N_{\mathrm{On}} - \alpha N_{\mathrm{Off}} \ , \tag{2.2}$$

and its error:

$$\Delta N_\gamma = \sqrt{N_{\mathrm{On}} + \alpha^2 N_{\mathrm{Off}}} \ . \tag{2.3}$$

The statistical significance of the γ-ray signal is evaluated using the approach by Li & Ma (1983):

$$S_\gamma = \sqrt{2}\left(N_{\mathrm{On}} \ln\left(\frac{(1+\alpha)N_{\mathrm{On}}}{\alpha(N_{\mathrm{On}} + N_{\mathrm{Off}})} \right) + N_{\mathrm{Off}} \ln\left(\frac{1+\alpha)N_{\mathrm{Off}}}{N_{\mathrm{On}} + N_{\mathrm{Off}}} \right) \right)^{1/2} \ . \tag{2.4}$$

Due to some false detections claimed in the early years of the field as well as the large number of trials anticipated in the search for VHE γ-ray sources, it became common practice in γ-ray astronomy to require a significance of at least 5 standard deviations for the reliable detection of a source. The probability for such a signal to be caused by statistical fluctuations is merely $\sim 6{\cdot}10^{-5}$.

2.5 Basic Performance of H.E.S.S.

The basic parameters of the H.E.S.S. instrument that are essential for the observation of extended sources and the survey of the Galactic Plane are its large field-of-view, its good angular resolution and its superior sensitivity compared to other third generation IACTs. These key characteristics will be summarized in the following.

Angular Resolution

The angular resolution of the instrument is of uttermost importance for the sensitivity for point-sources as well as for morphology studies of extended VHE γ-ray sources and their association with astrophysical objects known from other wavebands (especially in the crowded region along the Galactic Plane). It can be derived from point-source γ-ray Monte Carlo simulations by means of the point-spread function (PSF) of the instrument. The PSF is given by the distribution of squared angular distances between the simulated and the reconstructed arrival directions. The angular resolution is then defined as the 68% containment radius of this distribution. Figure 2.8(a) depicts the PSFs for the two different sets of cuts described in Section 2.4 for observations taken at a zenith angle of 20° and 0.5° offset from the camera center. For these parameters, the angular resolution using *hard*-cuts is 0.07°, while it degrades to 0.1°, when *standard*-cuts are used. Due to the superior angular resolution hard cuts are usually used for morphology studies.

Field-of-view

When the object of interest is extended far beyond the PSF or, even more in the case of large area surveys, the off-axis performance is of great importance. Figure 2.8(b) depicts the detection efficiency for γ-ray like events against the angular offset of their arrival directions from the observation position. The curve was generated from *Off*-observations taken at a zenith angle of $\sim$25°. The radial acceptance curve is relatively flat for the inner 1° and then drops quickly mostly due to the *nominal distance* cut presented in Section 2.4. It reaches 50% of its maximum at $\sim$2°. It should be noted that the acceptance is strongly energy dependent. It becomes much flatter for higher energies, e.g. above 5 TeV the acceptance curve reaches beyond 3° without any significant drop at larger offsets.

Sensitivity

Together with the angular resolution and the field-of-view, it is the sensitivity of the instrument which is most important for its performance. Figure 2.8(c) shows the observation time necessary for a 5σ detection of a point-source at a zenith angle of 20° versus the source flux expressed as fraction of the Crab nebula flux. The assumed underlying source spectrum follows a pure power-law with a photon index of 2.5, the background was taken from *Off*-observations with zenith angles ranging from 15° to 25°. The curves illustrate the different optimizations for *hard*- and *standard*-cuts.: *hard*-cuts provide the better sensitivity for the detection of weak sources with flux levels of less than 10% of the Crab nebula flux and *standard*-cuts are optimized for the more luminous sources. In summary, the H.E.S.S. array can detect point sources at flux levels of about 1% of the Crab Nebula flux near zenith with a statistical significance of $5\,\sigma$ in 25 hours of observations.

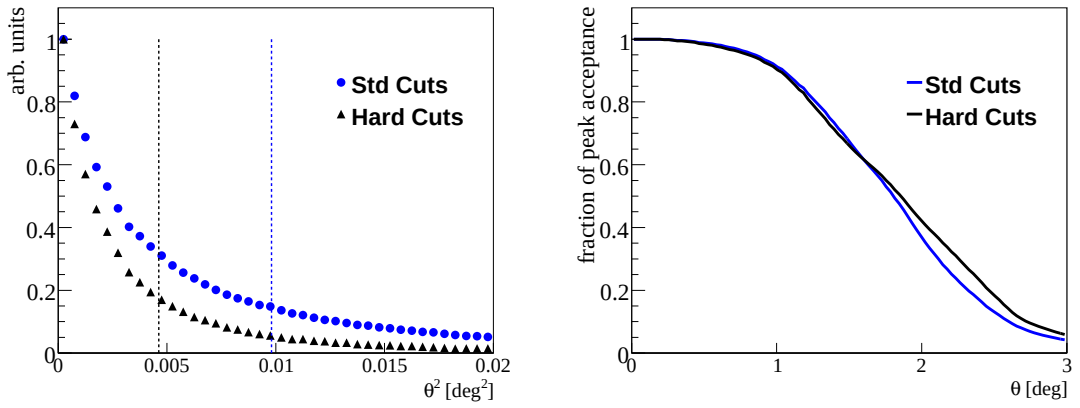

(a)

(b)

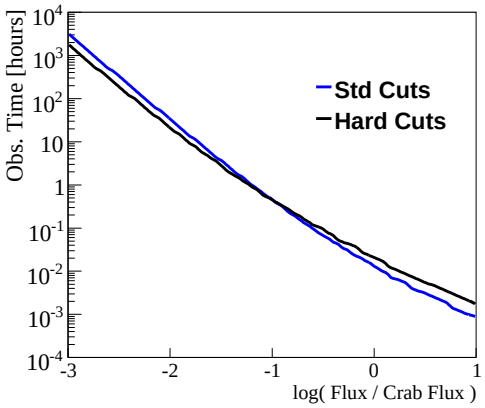

(c)

Figure 2.8: Basic performance parameters of the H.E.S.S. experiment: a.) Point-spread-function of the instrument, shown are the distributions of squared angular distance between the simulated and the reconstructed arrival directions for the two sets of selection cuts. The curves were obtained from point-source MC simulations assuming a zenith angle of 20° and an offset of the source from the pointing direction of 0.5°. b.) Energy-averaged radial acceptance curve for the two sets of selection cuts, shown is the detection efficiency for γ-ray like events against the angular offset of their arrival direction from the observation position. c.)Sensitivity curve: observation time necessary for a $5\,\sigma$ detection versus the source flux expressed in units of the Crab nebula flux. Again a zenith angle of 20° and an offset of 0.5° was assumed. The necessary off-data was taken from and analysis of the AGN PKS 2155-304.

Chapter 3

Spectral Analysis

Along with the morphology of a VHE γ-ray source, it is the energy distribution of it's emitted γ-rays which adds the most valuable information to the theoretical models describing the underlying processes at work in these accelerators. Thus, one of the key quantities in the study of a VHE γ-ray source is its differential energy spectrum, $F(E)$, conventionally defined as the measured number of γ-rays, N_γ, per unit time dt, area dA and energy dE:

$$F(E) = \frac{dN_\gamma}{dEdtdA} \quad . \tag{3.1}$$

The quantity measured by H.E.S.S., which is directly related to the source's γ-ray spectrum is the differential γ-ray rate after event selection and background subtraction in bins of reconstructed energy E_r:

$$\frac{dN_\gamma}{dE_\mathrm{r}dt} = \int_0^\infty P(E, E_\mathrm{r}, \theta_\mathrm{z}, \psi, \nu_\mathrm{az}) \tilde{A}_\mathrm{eff}(E, \theta_\mathrm{z}, \psi, \nu_\mathrm{az}) \epsilon(E, \theta_\mathrm{z}, \psi, \nu_\mathrm{az}) F(E) dE \quad , \tag{3.2}$$

where $P(E, E_\mathrm{r}, \theta_\mathrm{z}, \psi, \nu_\mathrm{az})$ is the probability density function (PDF), which expresses the probability of a γ-ray with energy E to be reconstructed to have an energy E_r. $\tilde{A}_\mathrm{eff}(E, \theta_\mathrm{z}, \psi, \nu_\mathrm{az}) = \int 2\pi\, r\, dr P_\gamma$ is the effective collection area of the instrument and P_γ the γ-ray detection probability. $\epsilon(E, \theta_\mathrm{z}, \psi, \nu_\mathrm{az})$ represents the efficiency of the γ-ray selection. θ_z is the zenith angle of the observation, ν_az its azimuth angle and ψ the offset of the γ-ray source from the pointing direction of the instrument. The PDF, the effective collection area and the cut efficiencies have to be determined using Monte Carlo simulations. In the process, $\tilde{A}_\mathrm{eff}$ and ϵ are usually derived in a combined manner as $A_\mathrm{eff} = \tilde{A}_\mathrm{eff} \cdot \epsilon$.

Equation 3.2 can not be inverted analytically to obtain the underlying source spectrum. In this chapter two different approaches will be presented to circumvent this problem and determine the source spectrum from the measured differential γ-ray rate. In the first method – from now on referred to as 'Method A' – the energy smearing and the energy bias, described by the PDF $P(E, E_\mathrm{r})$, are combined with the effective area $A_\mathrm{eff}(E)$. The resulting quantity is again an effective area $A_\mathrm{eff}(E_\mathrm{r})$, but is expressed in terms of reconstructed energy E_r. Similar to $A_\mathrm{eff}(E)$, it is determined using MC simulations. However, to correctly describe the migration in energy caused by the reconstruction bias (see Section 3.2), the MC γ-rays have to be produced following a typical source spectrum (commonly used is a power law with a photon index of 2.0). The actual source spectrum is then calculated following

$$F(E_\mathrm{r}) = \frac{1}{A_\mathrm{eff}(E_\mathrm{r}, \theta_\mathrm{z}, \psi, \nu_\mathrm{az})} \frac{d^2 N_\gamma}{dE_\mathrm{r} dt} \; . \tag{3.3}$$

The source spectrum assumed in the production of the effective areas can then be adjusted to the reconstructed source spectrum and the procedure repeated iteratively. As will be shown later-on such an iteration is only necessary for large deviations between reconstructed and assumed source spectrum and is normally ommited.

The second method – Method B – is based on a forward folding technique. The expected distribution of reconstructed energies is calculated for a given spectral shape using Equation 3.2. The actual source spectrum is then measured by comparison of the expected and the measured energy distribution.

3.1 Effective Gamma-Ray Collection Area

The effective γ-ray collection area $A_{\rm eff}$ is a product of the the energy-dependent $\gamma-$ray selection efficiency ϵ and the effective area $\tilde{A}_{\rm eff} = \int 2\pi\, r\, dr P_\gamma$, where P_γ the γ-ray detection probability of the intrument. $A_{\rm eff}$ therefore depends on the details of the γ-hadron separation, the characteristics of the instrument, e.g. the trigger conditions, as well as the zenith $\theta_{\rm z}$, offset ψ and azimuth $\nu_{\rm az}$ angles of the actual observation. Well above the trigger threshold, the effective area is of the same order as the Cherenkov light pool on the ground.

Effective areas are determined using Monte Carlo simulations for distinct sets of zenith angles ($\theta_{\rm z} = 0°$, 20°, 30°, 40°, 45°, 50°, 55°, 60°, 63°, 65°), offset angles ($\psi = 0°$, 0.5°, 1°, 1.5°, 2°, 2.5°), azimuth angles ($\nu_{\rm az} = 0°$, 180°) and γ-ray selection cuts. $N_\gamma^{\rm MC}$ events are thrown homogeneously on an area $A_{\rm MC}$. The effective areas are then determined as:

$$A_{\rm eff}(E, \theta_{\rm z}, \psi, \nu_{\rm az}) = \frac{N_\gamma^{\rm sel}}{N_\gamma^{\rm MC}} A_{\rm MC} \ , \tag{3.4}$$

where $N_\gamma^{\rm sel}$ is the number of events which trigger the array and pass the γ-ray selection cuts. The detailed procedure is as follows:

- A γ-ray point source is simulated at a fixed zenith and azimuth angle
  - The development of the electromagnetic shower within the atmosphere induced by the incident γ-ray is simulated using the CORSIKA package (Heck et al., 1998). The atmospheric model used is optimized for a desert-like atmosphere without aerosol pollution (Anderson et al., 1996).
  - The detector response is modeled using the simulation package "SimHESSArray" [designed by Konrad Bernlöhr for the H.E.S.S. array]. The detector response depends strongly on the optical efficiency of the telescopes which in turn depend on the mirror reflectivity. As the reflectivity degrades on the timescale of years, the simulations have to be repeated on the same timescale with up-to-date values for the mirror reflectivity. The effective areas used in this work were produced with a reflectivity of 70% for all telescopes.
  - The source offset within the simulation is determined by the pointing direction of the instrument. Thus, effective areas with different offsets ψ can be obtained with the same simulated showers.
  - The most calculation-intensive part of the simulation is the shower development. Simulated showers are therefore used more than once (∼10 times on average) by shifting the H.E.S.S. array relative to the nominal core position.

  - The incident events are generated with a power law of photon index Γ=2. It should be noted that the weighting with a typical source spectrum is only necessary to determine the effective areas depending on the reconstructed energy $A_{\rm eff}(E_{\rm r})$ as used in Method A.

- The generated Monte Carlos are processed by the same analysis chain as used for the data (see Section 2.4). The effective areas are therefore valid only for the analysis configuration used in this step, including the γ-ray selection cuts and the size of the On-source region.

- The Monte Carlo events are binned in true and reconstructed energies and the effective areas $A(E)$ and $A(E_{\rm r})$ are calculated using Equation 3.4.

- The histograms are fitted with high-order polynomial functions to overcome step-like behavior at bin edges caused by limited event statistics, especially at higher energies.

  - $A(E)$ is fitted with a sixth-order polynomial.
  - $A(E_{\rm r})$ is fitted with a seventh-order polynomial plus an exponential, necessary to describe the more irregular shape of the $A(E_{\rm r})$ close to the threshold which is caused by the energy reconstruction bias, described in Section 3.2.

- The effective areas are created for distinct sets of zenith, offset and azimuth angles. To obtain an effective area for an arbitrary set ($\theta_{\rm z}$, ψ and $\nu_{\rm az}$), a bilinear interpolation in $\cos(\theta_{\rm z})$ and ψ is performed. No interpolation is done for the (rather weak) azimuth dependence.

It should be noted that the effective areas are only valid for the analysis configuration they have been produced with. This is especially important for the size of the on-source region (a circle with the radius θ). Two different kinds of effective areas are used: the *point-source* effective areas and the *full-enclosure* effective areas. The point-source effective areas are produced with a value of θ optimized for the analysis of point sources. The corresponding values for *hard-* and *standard*-cuts are stated in Table 2.1. As can be seen in Figure 2.8(b), the size of the on-source region is then smaller than the extend of a point-source which is caused by the limited angular resolution of the instrument. The point-source effective areas correct for this leakage of source flux outside of the on-source region. Thus, a flux calculated using these effective areas corresponds to the point-source and not just to the emission within the on-source region. Full-enclosure effective areas, on the other hand, are produced with an infinitely large on-source region and therefore do not include this correction factor. Therefore, a flux calculated with these effective areas corresponds only to the emission within the on-source region chosen for the source analysis.

Figure 3.1 to 3.3 show some representative effective areas to illustrate their basic dependencies. Figure 3.1(a) depicts the effective areas for a medium zenith angle of 20° and an offset angle of 0.5° versus reconstructed (blue) and true MC energy (red). Both the histograms and the fitted analytic functions are drawn. As the fit functions describe the histograms reasonably well, they will be solely used in the following. The two effective areas appear very similar. Both rise steeply above the trigger threshold. With increasing energy the rise levels off, until the effective area starts to drop again at even higher energies,

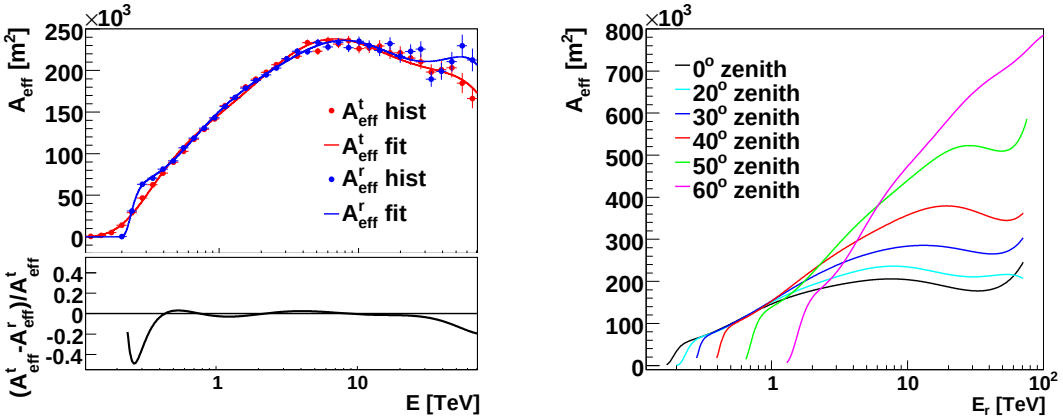

(a) (b)

Figure 3.1: a.) top: Effective areas versus reconstructed (blue) and true MC (red) energy for a medium zenith angle θ_z of 20°, an offset angle ψ of 0.5°and *standard*-cuts for γ-hadron separation. The histograms directly obtained from MC simulations are illustrated by the markers, the analytic functions fitted to the histograms are shown as solid lines. a.) bottom: Residuals between the effective areas versus true MC and reconstructed energy. b.) Effective areas versus reconstructed energies for various zenith angles. The offset and azimuth angle is fixed to $\psi = 0.5°$ and $\nu_{az} = 180°$, respectively.

where the decrease in cut-efficiency starts to dominate[1]. Only at very low and very high energies, where the energy bias becomes dominant over the energy resolution, the effective areas versus true and reconstructed energy deviate, visible in the residuals shown at the bottom of the figure.

Figure 3.1(b) illustrates the zenith angle dependence of the effective areas. The first effect apparent is the increase of the energy threshold with increasing zenith angles. Larger zenith angles result in larger distances between the shower maximum and the telescopes, which on the one hand decreases the photon density on the ground and on the other hand increases the optical column depth the Cherenkov light has to traverse before detection. Thus, the larger zenith angle results in a dimmer Cherenkov light pool on the ground, increasing the energy threshold of the instrument. The second effect visible in Figure 3.1(b) is the increase of the effective areas for fixed energies (well above the energy threshold) and increasing zenith angles. The inclined impact of the Cherenkov cone leads to a larger footprint of the shower on the ground (Cherenkov cone radius: $R_c \sim \frac{1}{\cos(\theta_z)}$) which directly translates into an increase of the collection areas.

Figure 3.2(a) illustrates the dependence of the effective areas from the offset angle between pointing direction and source position (ψ). At a medium zenith angle of 20°, the effective areas for a fixed set of reconstructed energies (0.6, 1, 10, 30 TeV) are shown for offset angles ranging from 0° to 2.5° in steps of 0.5°. For these distinct offset values Monte Carlo simulations exist. The effective areas for all other offset angles are obtained by linear interpolation. Naturally, the curves resemble the radial acceptance curves shown

[1]The drop in cut-efficiency at larger energies is mainly caused by the *nominal distance cut*, because at these energies distant events produce images far away from the camera center.

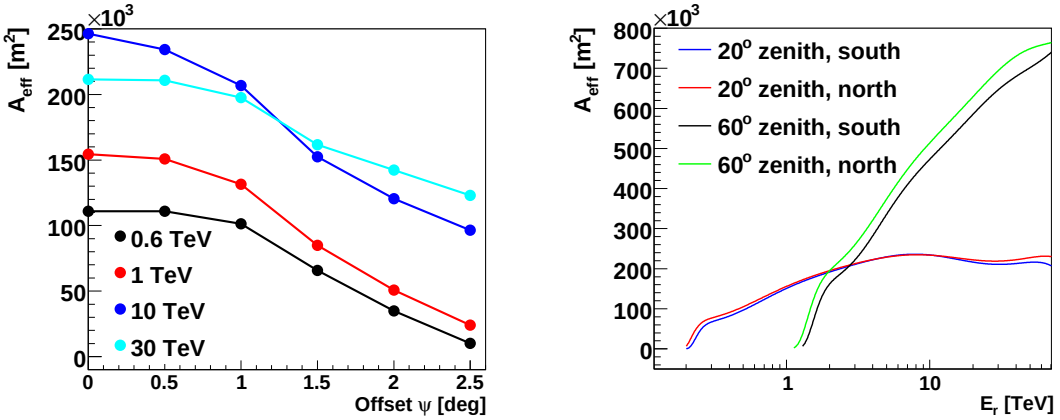

(a) (b)

Figure 3.2: a.) Effective areas for four different reconstructed energies versus the offset of the simulated γ-ray source from the pointing direction of the instrument. The effective areas are obtained at a zenith angle of θ_z=20°, an azimuth angle of ν_{az}=180° and standard γ-ray selection cuts. b.) top: Effective areas for two different zenith angles versus reconstructed energy for azimuth angles of $\nu_{az} = 0°$ (North) and $\nu_{az} = 180°$(South).

in Figure 2.8(b). They are reasonable flat up to 1° and then start to deteriorate at larger offset angles, an effect which is less pronounced at higher energies (see Section 2.5).

So far, all effective areas shown were calculated for an azimuth angle of 180°, e.g. for the H.E.S.S. instrument pointing South. However, the development of an air shower depends on its orientation relative to the Earth's magnetic field, and so does the effective area. The electron and positron pairs created during pair production spiral diametrically in opposite directions in a plane perpendicular to the Earth's magnetic field. At the H.E.S.S. site, the angle between the magnetic field lines and the shower axis is larger when pointing South. The resulting larger angular spread leads to a shift of the effective areas to higher energies. Figure 3.2(b) compares the effective areas for azimuth angles of 0° and 180° for two different zenith angles ($\theta_z = 20°$, 60°). The effective areas are larger for ψ=0° than for ψ=180°. For energies well above the energy threshold, the difference can reach up to 20%. The effect becomes more pronounced for larger zenith angles, due to the longer distance that the shower particles travel through the magnetic field.

Figure 3.3(a) depicts two further dependencies of the effective areas: telescope multiplicity and γ-ray selection cuts. In the case where one of the H.E.S.S. telescopes has a technical problem, the array is operated with only 3 telescopes. This results in a decrease of the effective area of ∼20% for energies well above the trigger threshold. Because the γ-ray cut-efficiency was folded into the effective area, the decrease depends on the set of selection cuts used for γ-hadron separation (including the size of the On-source region). Figure 3.3(a) shows the effective areas for *hard*- and *standard*-cuts as introduced in Section 2.4. As the γ-ray selection efficiency of the *standard*-cuts is 35% and 13% for *hard*-cuts (for point sources, see Benbow, W. (for the H.E.S.S. Collaboration), 2005), the effective areas for *standard*-cuts are ∼5-10% above those for *hard*-cuts at energies far above the trigger thresholds. Also visible is the increase of the energy threshold caused mainly

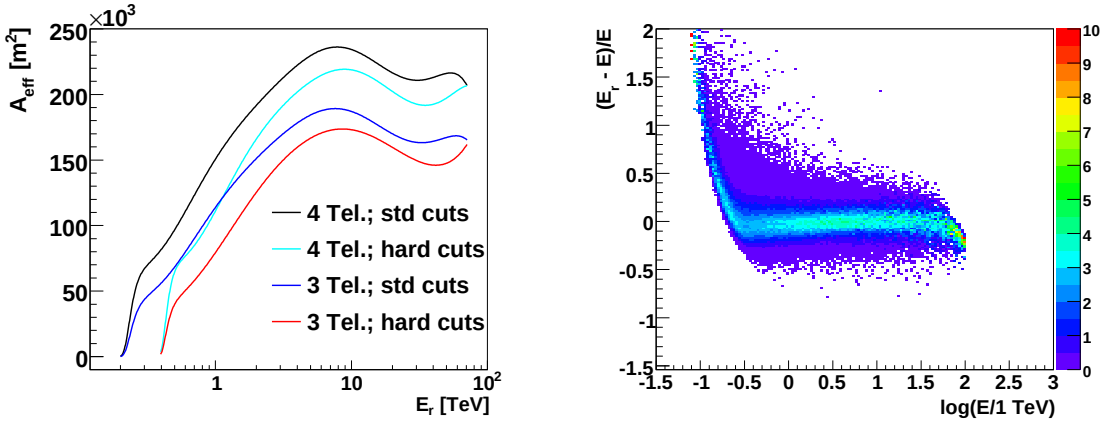

(a) (b)

Figure 3.3: a.) Effective areas obtained at $\theta_z = 20°$ and $\psi = 0.5°$ for *hard* and *standard* γ-ray selection cuts using the full H.E.S.S. array (4 tel) and excluding one telescope (3 tel). b.) PDF to reconstruct an event with true MC energy E to have an energy E_r. The depicted PDF was obtained with $\theta_z = 20°$, $\psi = 0.5°$ and *standard*-cuts.

by 200 photo electrons per shower image required by the *hard*-cuts (in comparison to 80 p.e. for *standard*-cuts, see Section 2.4).

3.2 Probability Density Function

The probability density function $P(E, E_\mathrm{r}, \theta_\mathrm{z}, \psi, \nu_\mathrm{az})$ (see Equation 3.2) determines the probability for an event with true MC energy E to be reconstructed with an energy E_r. The PDF is directly related to the energy resolution and the energy reconstruction bias, which are defined as the spread and the mean value of the PDF for each MC energy, see Figure 3.4(b). For energies close to the threshold there is an inevitable bias in the energy reconstruction due to the sharp requirement on the minimum image amplitude. Due to this cut, only upwards fluctuations are considered and events with a too high reconstructed energy are preferentially selected. The PDF displays the same dependencies as the effective areas, such as the zenith angle, the azimuth angle, the offset angle, as well as the γ-ray selection cuts.

Analogous to the effective area, the PDF is determined from Monte Carlo simulations, following a similar procedure:

- The same γ-ray simulations used for the effective area production are used to derive the PDF. It should be noted that the PDF does not depend on the simulated γ-ray spectrum.
- The MC events are binned in a 2D histogram: $\frac{E_\mathrm{r}-E}{E}$ vs. $\log(E)$
- Each column (E=const.) is normalized such that

$$\sum_{j=0,E=\mathrm{const}}^{\infty} \left(\frac{E_\mathrm{r}-E}{E}\right)_j d\left(\frac{E_\mathrm{r}-E}{E}\right) = 1 \ . \tag{3.5}$$

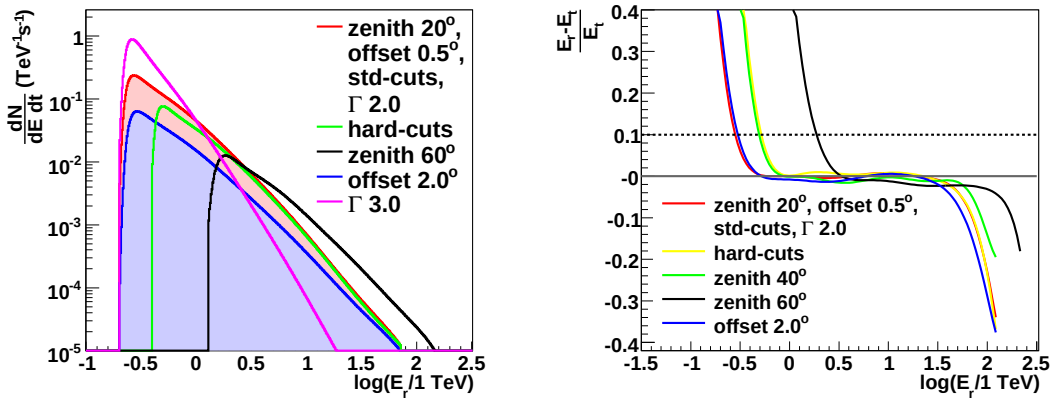

(a) (b)

Figure 3.4: a.) Differential γ-ray rate in units of $\mathrm{TeV}^{-1}\mathrm{s}^{-1}$. The red curve was obtained at a zenith angle of θ_z=20°, an offset angle of ψ=0.5°, an azimuth angle of 180° using *standard*-cuts for γ-hadron separation. The underlying source spectrum follows a power law with photon index Γ=2. All other curves were obtained with similar configurations, only variations are stated in the corresponding legend. b.) Energy reconstruction bias versus true MC energy. The energy bias of 10% as used in the definition of the spectrum energy threshold is illustrated by a black dotted line.

Note that the result is a PDF depending on $\left(\frac{E_r - E}{E}, E\right)$.

- The resulting 2D histograms are directly used as PDF look-ups. No further smoothing or fitting is applied.
- Such PDFs are created for the same sets of zenith, offset and azimuth angles as the effective areas. To obtain a PDF for an arbitrary set of these input variables, the same interpolation as introduced for the effective area is applied.

As an example, Figure 3.3(b) shows the 2D histogram used as a PDF look-up for a zenith angle of 20°, an offset of 0.5° and an azimuth angle of ν_{az} of 0°.

3.3 Energy Threshold

Two different kind of energy thresholds occur in the analysis of the H.E.S.S. data: The first is the *analysis threshold*, defined as the energy at which the differential γ-ray rate (after selection cuts) reaches its maximum. The differential rates are calculated by folding the effective area (obtained from simulations) with a power law source spectrum with a photon index of Γ=2. The analysis threshold exhibits thereby the same dependencies as the effective area (vs. E_r): zenith and offset angle, analysis cuts and the assumed γ-ray spectrum. Figure 3.4 depicts the differential γ-ray rate for various sets of input parameters. Even though the differential rate decreases with increasing offset angle, its maximum remains at roughly the same energy, which results in the analysis threshold to be only weakly dependent on the offset. The dependence on the zenith angle, however,

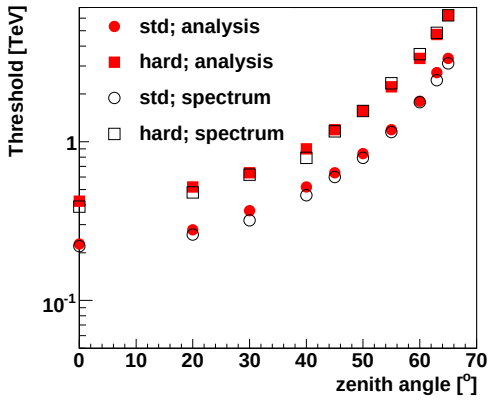

Figure 3.5: Zenith dependence of the analysis threshold and the spectrum energy threshold for *hard* and *standard* γ-ray selection cuts. The thresholds were obtained for a zenith angle of θ_z=20°, an offset angle of ψ=0.5°, an azimuth angle of 180° and an underlying source spectrum following a power law with photon index Γ=2.

is much stronger (see Figure 3.5): the trigger threshold increases (for *standard*-cuts) from ∼200 GeV at a zenith angle of 0° to ∼3 TeV at 65°. Which analysis cuts are applied to the data makes a big difference as well. At a zenith angle of 20° the analysis threshold for *standard*-cuts is ∼ 260 GeV, but it increases to 480 GeV for *hard*-cuts. From the γ-ray selection cuts, it is dominantly the requirement on the image amplitude (see Section 2.4) that determines the trigger threshold. It should be noted that the analysis threshold is the relevant energy threshold for image generation in the H.E.S.S. analysis framework.

The second threshold is the *spectrum energy threshold*, applied to the data for spectral extraction. It is defined as the minimum energy for which the energy bias is less than 10%. There are two reasons for such an additional energy cut. The first is to avoid the strongly rising part of the effective areas just above the analysis threshold, which is easily affected by a non-perfect MC description. The second reason is the large reconstruction bias at these energies, which leads to systematic errors if the measured source spectrum deviates significantly from the spectral shape ($\sim E^2$) used in the simulations. Figure 3.5 illustrates the zenith angle dependence of the spectrum energy threshold. A second spectrum energy threshold is applied at the highest energies. This threshold accommodates for the high-energy end of the derived effective areas. As the energy distribution of the simulated events follows a power-law, the event statistics at energies beyond this threshold is not sufficient to derive a meaningful value for the effective area. For the common data set, the available statistics drops below a useful level long before the upper spectrum energy threshold.

3.4 Differential Gamma-Ray Spectrum: Method A

The aim of the spectral analysis is to calculate the differential γ-ray flux (in units of $\mathrm{TeV}^{-1}\mathrm{cm}^{-2}\mathrm{s}^{-1}$). In Method A, the energy smearing and the energy migration caused by the reconstruction bias are absorbed into the effective areas and the differential γ-ray rate is calculated using Equation 3.3. The detailed procedure is as follows:

- For each observation run, the ON-events and the OFF-events are filled into finely binned histograms (24 bins per decade (bpd)) with $\log(E_\mathrm{r})$ on the abscissa.
- The mean effective area curve (vs. E_r) is calculated on the basis of the zenith and offset angle distribution of the ON-events, for each run individually, taking the number of participating telescopes into account. The run-wise effective area curve is then multiplied by the dead-time corrected duration (livetime) of the corresponding observation. The resulting curve has the units $\mathrm{m}^2\mathrm{s}$ and is referred to as $(TA_\mathrm{eff})_\mathrm{run}$ from now on. It should be noted that the same effective areas are used for the ON- and OFF events, assuming that both share the same system acceptance. The OFF effective areas are merely multiplied by the background normalization factor $1/\alpha$ (see Section 2.4).
- The upper and lower spectrum energy threshold for each individual run is determined on the basis of the zenith and offset angle of the pointing position. The energy thresholds are applied by zeroing all bins within the 3 previously filled histograms (ON-events, OFF-events and $(TA_\mathrm{eff})_\mathrm{run}$), that are not fully included in the range between the energy thresholds.
- The run-wise histograms are summed to obtain the combined histograms valid for the whole data set. In this step, observations with 3- and 4-telescopes are naturally combined. As an example, the resulting histograms in the spectral analysis of HESS J1745-290 – located at the Galactic Center – are depicted in Figure 3.6(a) and 3.6(b).
- Usually the initial binning of 24 bins per decade is too fine for the available statistics. A merging of the fine bins is therefore necessary. Two different methods are used to determine a suitable bin size:
  - Adaptive Binning: An initial coarser binning is chosen on the basis of the statistical significance σ of the whole source (>30 σ: 12 bpd, >12 σ: 6 bpd, <12 σ: 4 bpd). The smallest bin size (12bpd) is chosen such that it is larger than the energy resolution of $\sim 15\%$ (see Section 2.4). Then, starting from the smallest energies, proceeding to higher energies, the initial binning is kept till the significance of a bin is less then 2σ, then the bin width of this and all consequent bins is doubled. The procedure continues till the minimum requirement of 2σ can not be fulfilled anymore.
  - Fixed binning: A fixed size for all bins is chosen as a compromise between the total number of bins and the significance of the highest energy bins. This procedure is not automated but is adjusted to the individual data set by hand.

  The fine bins are then merged into the coarser bins: The numbers of ON- and OFF-events are merely added while the life time weighted effective areas are averaged using an arithmetic mean. It should be noted that the simple arithmetic mean is an approximation. For very large bins a weighting with the expected event distribution within the bin would be more appropriate.
- The ON- and OFF-event numbers (N_on, N_off) are divided by (TA_eff) and the width of the energy bin (dE) to obtain the corresponding differential fluxes (see Figure 3.6(c), with the initial fine binning of 24 bpd).

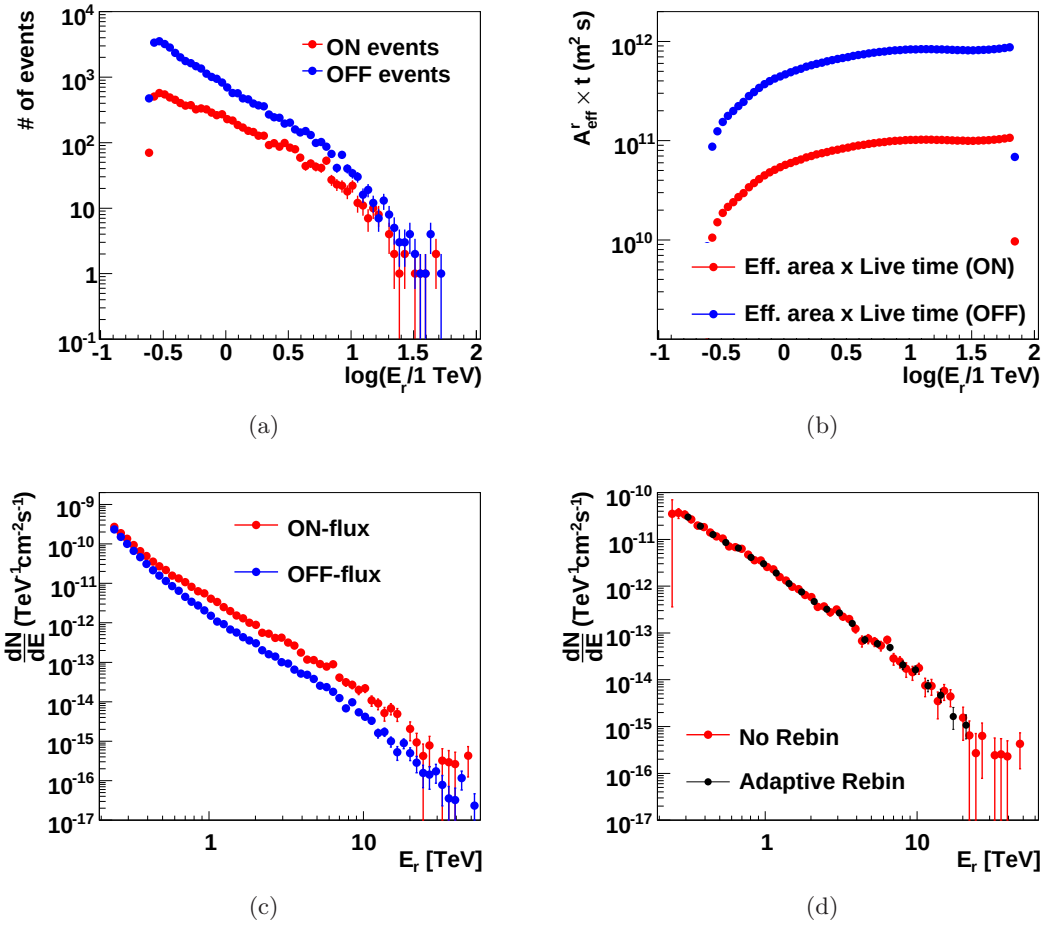

Figure 3.6: Illustration of the various steps in Method A to calculate the differential energy spectrum, taken from the spectral analysis of HESS J1745-290, the VHE γ-ray source at the Galactic Center. a) Reconstructed energy distribution of the ON- and OFF-events finely binned with 24 bins per decade. b) Livetime weighted effective area curve versus reconstructed energy, the same effective area curve is used for ON- and OFF-events. The OFF-events effective area is merely multiplied by the background normalization factor $1/\alpha$. c) ON- and OFF- differential flux. d) Source differential flux in fine bins and after the adaptive re-binning procedure was applied. The re-positioned final flux points are depicted.

- The differential source flux is calculated as the difference between the ON- and OFF-flux.

$$\left(\frac{dN}{dE}\right)_i = \frac{N_{\mathrm{on},i}}{\Delta E_i}\sum_{\mathrm{runs}}(TA_{\mathrm{eff}})_i^{-1}(\theta_z,\psi) - \frac{N_{\mathrm{off},i}}{\Delta E_i}\sum_{\mathrm{runs}}\frac{1}{\alpha_{\mathrm{run}}}(TA_{\mathrm{eff}})_i^{-1}(\theta_z,\psi)\ . \qquad (3.6)$$

  The result is a differential flux point for each of the coarse energy bins (see Figure 3.6(d), with the initial fine binning of 24 bpd).

- The error on each differential flux point is determined assuming that its fractional error equals the fractional error on the corresponding excess. The error on the energy is not taken into account.

- Similar to the re-binning procedure, two different approaches exist to decide which flux points are used in the determination of the source spectrum:

  - When the adaptive binning is used, only flux points which fulfill the minimal requirement of 2σ on the statistical significance and which have a fractional error of less than 100% are used.
  - When "fixed binning" is applied, all flux points within the spectrum energy thresholds are used, regardless of their significance. Only flux points with less than 4 On(Off)-region events are rejected to avoid extreme deviations from Gaussian statistics. Flux points with a significance of less than 1σ are plotted as 2σ upper limits (see Section 2.4).

- To extract the characteristics of the source spectrum, the spectral points are fitted with analytical functions using a minimum χ^2 procedure. Among others, the following spectral shapes are used:

  - Pure power law: $\phi_{\text{fit}} = \phi_0 \cdot \left(\frac{E}{E_0}\right)^{-\Gamma}$, where ϕ_0 is the flux normalization at the reference energy E_0, and Γ the photon index.
  - Power law with exponential cut-off: $\phi_{\text{fit}} = \phi_0 \cdot \left(\frac{E}{E_0}\right)^{-\Gamma} \cdot \exp(\frac{-E}{E_C})$, where E_C is the cut-off energy.

- After the first iteration, the flux points are repositioned within their corresponding bins. So far, they were placed at the arithmetic bin center, a position which results in a systematic shift of the fit results (Lafferty & Wyatt, 1995). Following the approach by Lafferty & Wyatt (1995), the flux points are now placed at the energy $\tilde{E}$ where the expected number of excess events is equal to its mean value over the wide energy bin, e.g. where

$$\phi_{fit}(\tilde{E}_i) = \frac{\int_{E_i}^{E_{i+1}} (TA_{eff})\phi_{fit} dE}{\overline{(TA_{eff})}(E_{i+1} - E_i)} \tag{3.7}$$

  After the repositioning, the flux points are re-fitted. This is an iterative procedure, but one iteration is normally sufficient. The resulting flux points are shown in Figure 3.6(d).

3.5 Differential Gamma-Ray Spectrum: Method B

Method B follows a completely different approach: The expected number of ON- and OFF-events in each bin of reconstructed energy is derived assuming an underlying source spectrum and taking the system performance into account. In comparison with the measured event numbers the most likely spectrum of the source at hand is derived. The detailed procedure is as follows:

- For each observation run, the reconstructed energies of the ON- and OFF- events are filled into finely binned histograms (24 bpd) with $\log(E_\mathrm{r})$ on the abscissa. The number of ON- and OFF-events within each bin is given by N_on and N_off

- The spectrum energy thresholds are applied by setting all bins in the 2 previously filled histograms to zero, if they are not fully contained in the region between the energy thresholds.

- The run wise histograms are then summed.

- The number of expected excess events n_γ within each bin of reconstructed energy is calculated, given the zenith and offset distribution of each run:

$$\begin{aligned} n_\gamma|_{E_\mathrm{r,i}}^{E_\mathrm{r,i+1}} &= \sum_{\mathrm{runs},\theta,\psi} t_{\theta,\psi} \int_{E_\mathrm{r,i}}^{E_\mathrm{r,i+1}} dE_\mathrm{r} \\ &\int_0^\infty dE \cdot \phi_\mathrm{fit}(E) A_\mathrm{eff}(E,\theta,\psi) P(E_\mathrm{r},E,\theta,\psi) \end{aligned} \tag{3.8}$$

  where $E_\mathrm{r,i}$ and $E_\mathrm{r,i+1}$ are the bin edges of the corresponding energy bin, $t_{\theta,\psi}$ the livetime of the observation spent at a zenith angle θ_z and an offset angle ψ[2]. The underlying source spectrum is given by ϕ_fit. $A_\mathrm{eff}(E,\theta,\psi)$ and $P(E_\mathrm{r},E,\theta,\psi)$ have been introduced in Section 3.1 and 3.2. In the sum, only runs are considered in which the corresponding energy bin was within the spectrum energy thresholds.

  Observation runs with only 3 operating telescopes can easily be incorporated in the above summation, when the corresponding effective areas and probability density functions are used.

- The probability of observing a certain number of ON-events (N_{on}) and OFF-events (N_{off}), when n_γ excess events and n_h background events are expected, is given – according to Poisson statistics – by:

$$\begin{aligned} P(N_\mathrm{on},N_{off}|n_\gamma,n_h) &= \frac{(n_\gamma+\alpha n_h)^{N_\mathrm{on}}}{N_\mathrm{on}!}\exp(-(n_\gamma+\alpha n_h)) \\ &\cdot\frac{n_h^{N_{off}}\exp(-n_h)}{N_{off}!} \end{aligned} \tag{3.9}$$

  where α is the background normalization factor.

[2]The actual integration is performed in logarithmic steps and the PDF obtained from the look-up is valid for $\left(E,\frac{E_\mathrm{r}-E}{E}\right)$, the actually performed integral is therefore:

$$\begin{aligned} n_\gamma|_{E_\mathrm{r,i}}^{E_\mathrm{r,i+1}} &= \sum_{\mathrm{runs},\theta,\psi} t_{\theta,\psi} \int_{\log E_\mathrm{r,i}}^{\log E_\mathrm{r,i+1}} \ln(10) E d\log(E_\mathrm{r}) \\ &\int_{-\infty}^{+\infty} \ln(10) E d\log(E)\cdot\phi_\mathrm{fit}(E) A_\mathrm{eff}(E,\theta,\psi)\frac{1}{E}P(\frac{E_\mathrm{r}-E}{E},E,\theta,\psi) \end{aligned}$$

- The best background estimate in the energy bin ($E_{\mathrm{r,i}}$, $E_{\mathrm{r,i+1}}$,), n_h, given N_{on}, N_{off} and n_γ is obtained by maximizing the probability P. The analytical solution is given by:

$$C = \alpha(N_{on} + N_{off}) - (1+\alpha)n_\gamma \quad (3.10)$$

$$D = C^2 + 4\alpha(\alpha+1)N_{off}n_\gamma \quad (3.11)$$

$$n_h|_{E_{\mathrm{r,i}}}^{E_{\mathrm{r,i+1}}} = \frac{C+D}{2\alpha(\alpha+1)} \quad (3.12)$$

  The number of expected excess and background events, together with the actually measured numbers are depicted in Figure 3.7(a) and 3.7(b).

- The underlying source spectrum $\phi_{\mathrm{fit}}(E)$ (for the different spectral shapes see Section 3.4) is then varied to minimize the negative log-likelihood (-L):

$$-L = -log(P) \sim N_{on}\cdot\log(n_\gamma + \alpha n_h) + N_{off}\cdot\log(n_h) - ((1+\alpha)n_h + n_\gamma) \quad (3.13)$$

  The terms independent of n_γ and n_h have been omitted. The minimization is performed using MIGRAT, which is a part of the MINUIT package[3]. Figure 3.8(c) illustrates the log-likelihood plane spaned by the two fit parameters phi_0 and Γ of a pure power-law fit function.

- In contrast to the approach followed in Method A, the underlying source spectrum is determined directly from the ON- and OFF-counts. Thus, no calculation of flux points is necessary for the actual derivation of the fit function. The flux points can, therefore, be determined subsequently:
  - To obtain the size and position of the flux bins in reconstructed energy, the same procedure as described in Section 3.4 is applied.
  - For each broad bin in reconstructed energy, the flux points are positioned at the mean energy $\overline{E}$ derived from the previously obtained fit function and $A_{\mathrm{eff}}(E_{\mathrm{t}})$[4].
  - The flux in each bin of reconstructed energy is calculated from the ratio of excess events to the expected number of signal events:

$$F(\overline{E}) = \frac{(N_{on} - \alpha N_{off})\cdot\phi(E)}{n_\gamma} \quad (3.14)$$

  - The error on the flux in each bin is calculated in the same way as described in Section 3.4.

It should be noted that this approach takes the energy reconstruction bias correctly into account, even for a source spectrum different from the one used in the simulations (see

[3]Part of of PACKLIB: http://cernlib.web.cern.ch/cernlib/packlib.html

[4]The mean energy per bin in reconstructed energy is given by:

$$\overline{E_i} = \frac{\sum_{runs,\theta,\psi} t_{\theta,\psi}\int_{E_{r,i}}^{E_{r,i+1}} dE_r \int_0^\infty dE_{\mathrm{t}}\cdot\phi_{fit}(E)\cdot E\cdot A_{eff}(E,\theta,\psi)PDF(E_{\mathrm{r}},E,\theta,\psi)}{n_\gamma}$$

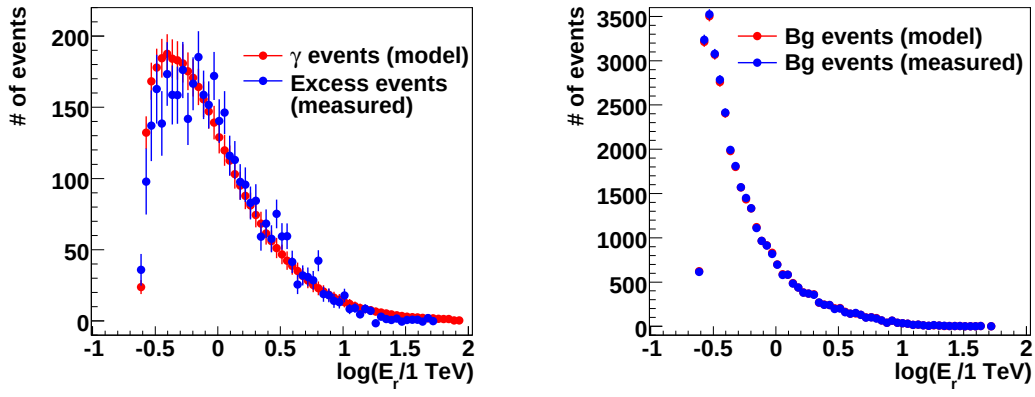

(a)

(b)

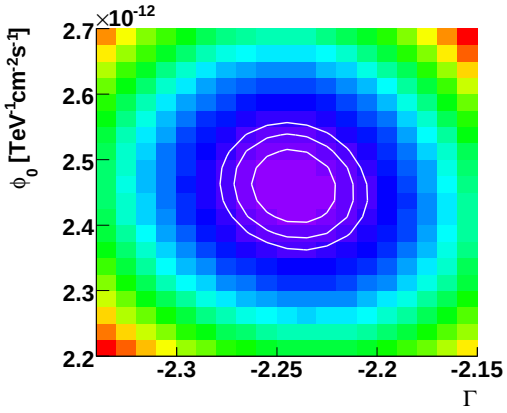

(c)

Figure 3.7: Illustration of the various steps in Method B to calculate the differential energy spectrum. The data was taken from the analysis of HESS J1745-290, the VHE γ-ray source at the Galactic Center. a) Reconstructed energy distribution of the excess events (blue) in comparison to the expected number of signal events (red) after the Log-Likelihood minimization assuming a pure power-law spectral shape. b) Reconstructed energy distribution of the OFF-events, measured (N_{off}) and expected (n_{h}). c) Log-likelihood plane – as given by Equation 3.13 – spanned by the fit parameters ϕ_0 and Γ for a pure power law fit. Contours are given at Min+0.5, Min+1 and Min+1.5, where Min is the Log-Likelihood at the best fit position in parameter space.

Section 3.1 and 3.2). Therefore, it is in principle possible to increase the acceptable energy reconstruction bias and thereby lower the spectrum energy threshold. The possibly non-perfect description of the system response in the region close to the analysis threshold, however, persists, so that the same analysis threshold as in Method A is applied here.

3.6 Systematic Studies

To test the two methods for spectral reconstruction and evaluate their inherent systematic uncertainties, a Toy Model Monte Carlo simulation is deployed. Such simulations have the advantage that multiple data sets for varying input parameters can be produced with little computational time. The production of simulated data sets in great quantities is necessary to study systematic biases and test the error calculation on a statistical basis. As such a Toy Model does not test the whole analysis chain, a consistency check of the two models using real data is performed at the end.

3.6.1 Toy Model MC

The Toy Model Monte Carlo (MC) simulation is used to produce data sets for a fixed zenith angle of 45° and an offset angle of 0.5° following the data set characteristics of the Crab nebula, as published in Aharonian et al. (H.E.S.S. collaboration) (2006g). Input parameters are the underlying source spectrum, the live time of the observations and the signal to noise ratio. The total number of signal events to be simulated is determined from the integral of the corresponding effective area $A_{\text{eff}}(E)$ convolved with the source spectrum and multiplied by the live time. The true MC energy of each signal event is extracted from the same curve $(A_{\text{eff}}(E) \times \phi(E))$. The reconstructed energy for each event is then extracted following the probability density function introduced in Section 3.2. The total number of background events is obtained from the number of signal events above the spectrum energy threshold, the signal to noise ratio and the background normalization factor (here $\alpha = 0.2$). Their reconstructed energy is directly sampled from the energy distribution of real OFF-events obtained from a spectral analysis of the Crab Nebula, restricted to observations taken at a zenith angle of $\sim$45° and an offset $\sim$0.5°.

For 6 different sets of input parameters, 10,000 Toy Model MC data sets are produced and their underlying source spectra reconstructed using Method A and Method B. Apart from Set 4 and 5, all sets have been reconstructed with an allowed energy reconstruction bias of 0.1, which directly determines the spectrum energy threshold. Due to the necessary automation, both methods have been applied with the adaptive binning procedure. Table 3.1 summarizes the different input parameters, while Figure 3.8(a) - 3.9(c) depict the mean deviations of the reconstructed spectral parameters from the simulated values. The corresponding error bars illustrate the mean reconstruction uncertainties. A deviation of the reconstructed parameters beyond the error bars therefore indicates systematic shifts dominating over the statistical uncertainty.

Set 1 is designed to investigate the index dependence of the spectral reconstruction for a very high statistics data set, similar to the one available for the Crab Nebula. A source spectrum following a pure power law was simulated with a reasonable livetime of $\sim$23 h, a flux normalization at 1 TeV of $\phi_0 = 3 \cdot 10^{-11}$ cm^{-2}s^{-1}TeV^{-1} and a signal to noise ratio of 8. Figure 3.8(a) shows the mean absolute deviation of the reconstructed spectral index Γ from the simulated value, while Figure 3.8(b) depicts the mean relative reconstruction deviation of the flux normalization $\phi_0(1\,\text{TeV})$. For a photon index of $\Gamma = 2.0$ the reconstruction of both parameters is close to perfect, but with increasing indices Method A tends to reconstruct the photon index too low and the flux normalization too high. The reconstruction performance of Method B, however, is almost unaffected by the simulated spectral index. The increasing deviations of Method A arise from the effective areas $A_{\text{eff}}(E_{\text{r}})$, which implic-

Set	Γ	$\phi_0(1\,\mathrm{TeV})$ $[\mathrm{cm}^{-2}\mathrm{s}^{-1}\mathrm{TeV}^{-1}]$	E_C [TeV]	livetime [h]	S/N	bias
1	2...4	$3{\cdot}10^{-11}$	–	22.8	8	0.1
2	2...4	$5{\cdot}10^{-13}$	–	34	0.3	0.1
3	2	$3{\cdot}10^{-11}$	3-15	22.8	8	0.1
4	2...3	$3{\cdot}10^{-11}$	–	22.8	8	0.1-0.25
5	2...3	$5{\cdot}10^{-13}$	–	34	0.3	0.1-0.25
6	2...3	$3.2{\cdot}10^{-11}/2^i$ (i=0,..,6)	–	34	$19.2/2^i$	0.1

Table 3.1: Summary of the different source spectra and data sets simulated with the Toy Model Monte Carlo simulation. The source spectra are characterized by the photon index Γ, the flux normalization ϕ_0 at 1 TeV and, in case an exponential cut-off is simulated, by the cut-off energy E_C. The livetime of the simulated data set is given together with the signal to noise ratio S/N and the maximally allowed energy reconstruction bias which determines the position of the spectrum energy threshold.

itly include the energy migration caused by the energy reconstruction bias and therefore depend on the spectral shape of the observed γ-ray source. The effective areas used are produced with a pure power law and a photon index of 2.0. If the source spectrum to be analyzed is much softer (i.e. has a larger photon index), the energy migration is not taken into account properly, which causes a reconstruction bias to smaller photon indices. It should be noted that for photon indices between 2 and 3, a range which includes all energy spectra observed from Galactic γ-ray sources, both methods show equally good agreement between simulated and reconstructed spectra. Only for softer photon indices, $\Gamma > 3$, does Method A show a reconstruction bias, which can be as large as $\Delta\Gamma = -0.15$ and $\Delta\phi_0 =$ 4% for Γ=4.

Set 2 was designed to investigate the same index dependence as Set 1 but with a much weaker source. The characteristics of the simulated γ-ray source ($\phi_0 = 5 \cdot 10^{-13}\mathrm{cm}^{-2}\mathrm{s}^{-1}\mathrm{TeV}^{-1}$) and the data set (livetime = 34 h, signal to noise ratio of 0.3) follow the data set of Kes 75, a weak point source presented in Section 4.5. The reconstruction bias of Method A for very soft spectra is also apparent in this set, see Figure 3.8(c) and 3.8(d). However, as the bias seems to be independent of the statistics of the data set, it is much smaller than the mean statistical reconstruction error and is therefore of no consequence.

Set 3 is designed to study the reconstruction performance of Method A and B for a power law spectrum with an exponential cut-off:

$$\phi(E) = \phi_0 \left(\frac{E}{E_0}\right)^{-\Gamma} \cdot \exp(\frac{-E}{E_\mathrm{C}}) \quad . \tag{3.15}$$

Only a high statistics data set similar to Set 1 is simulated. A fit of 3 free parameters (one more than for a pure power law fit), out of which 2 are strongly correlated (E_C and Γ) is not reasonable for a low statistics data set. A low statistics case similar to Set 2 is therefore omitted. The simulated photon index is 2.0. Figures 3.9(a) to 3.9(c) illustrate the reconstruction performance of Method A and B for the photon index Γ, the flux normalization ϕ_0 and the cut-off energy E_C. Both methods perform equally well,

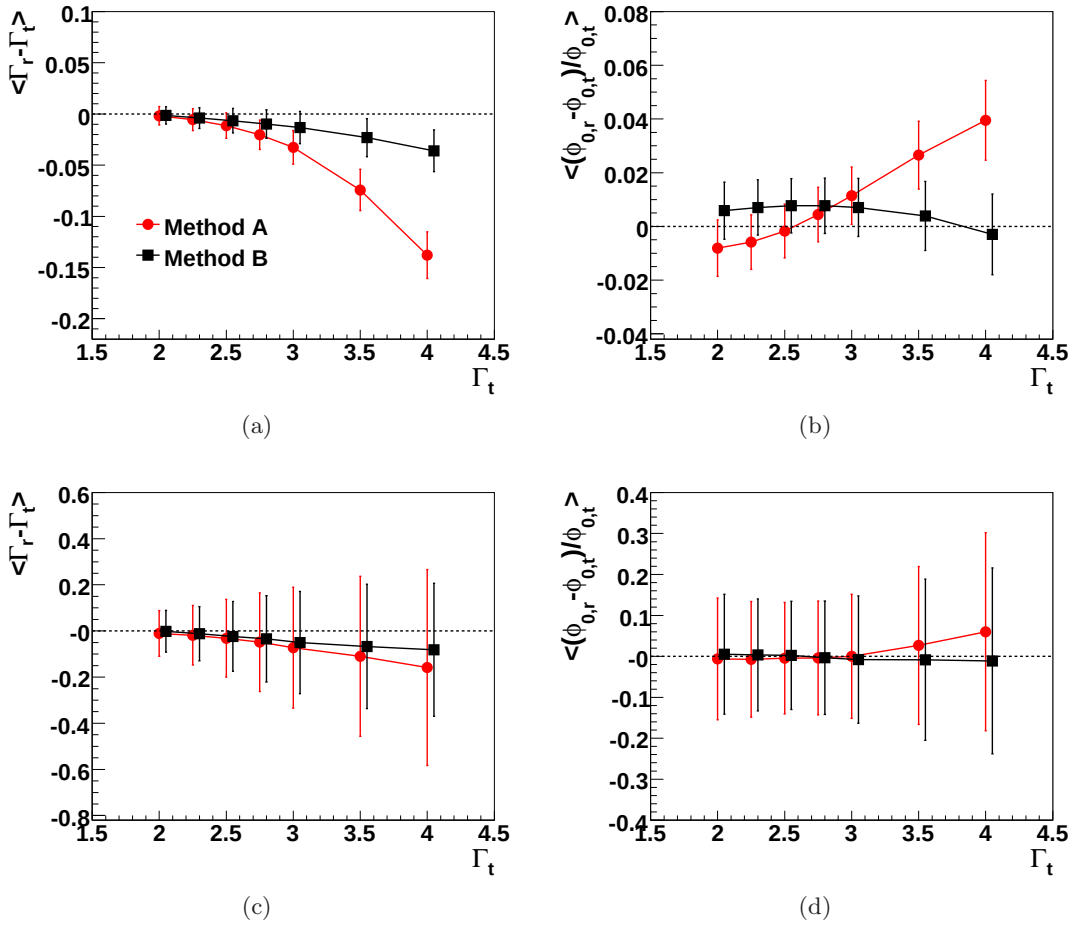

Figure 3.8: Spectral reconstruction performance of Method A and Method B for Set 1 (a+b) and 2 (c+d). Shown are the mean absolute deviation of the reconstructed photon index from the simulated value (a+c) and the mean relative deviation of the flux normalizations at 1TeV (b+d) for varying values of the simulated photon index. The error bars depict the mean statistical reconstruction error of the corresponding parameter. Note that the scale on the y-axis differs between the plots.

however for the flux normalization, Method B shows a smaller reconstruction bias then Method A, which itself is only ∼2%. The bias for the photon index is always below 0.03 and for the cut-off energy below 0.5 TeV even for E_C=15 TeV. Figure 3.10 depicts the pull[5]-distributions obtained for Set 3 with a cut-off energy of E_C=7 TeV. Shown is the distribution of the absolute deviations between reconstructed and simulated spectral parameter (ϕ_0, Γ and E_C) divided by the statistical error for all 10,000 MC simulated data sets. The mean of these distributions are already shown in Figure 3.9(a) to 3.9(c). All three distributions follow a Gaussian shape with width σ ∼1, meaning that the statistical errors are correct and represent the statistical spread of the fit results. The pull-distributions for

[5]Difference between reconstructed and simulated parameter in units of the 1σ error of the reconstructed parameter.

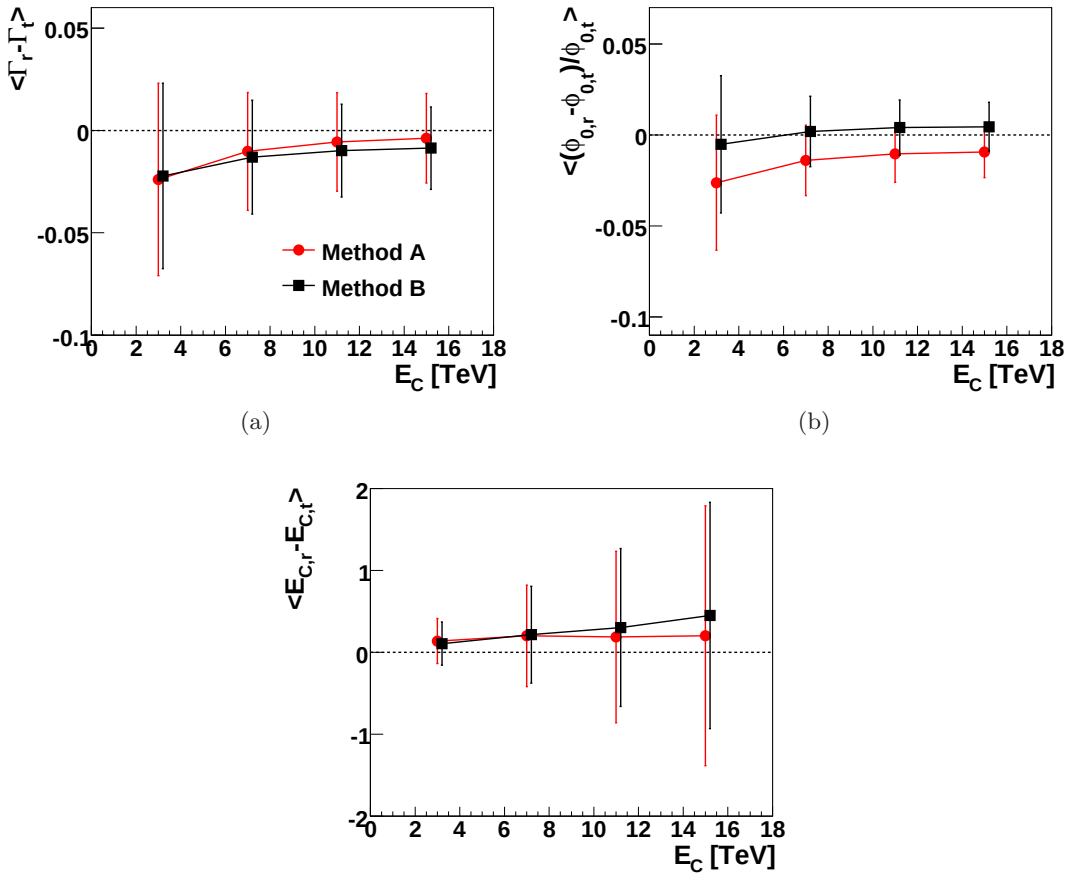

Figure 3.9: Spectral reconstruction performance of Method A and Method B for Set 3. Shown are the mean absolute deviation of the reconstructed photon index from the simulated value (a), the mean relative deviation of the flux normalizations at 1TeV (b) and the mean absolute deviation of the cut-off energy for varying values of the simulated cut-off energy. The error bars depict the mean statistical reconstruction error of the corresponding parameter.

all other sets and spectral parameters are checked as well and their width are also found to be correct.

Set 4 and 5 are equal to Set 1 and Set 2, but the Toy Model data sets were reconstructed with increasingly smaller spectrum energy thresholds (452 GeV, 422 GeV, 393 GeV, 367 GeV for a zenith angle of 45°, an offset angle of 0.5° and *standard* γ-ray selection cuts), corresponding to an allowed energy reconstruction bias of 0.1, 0.15, 0.2 and 0.25. Figures 3.11 to 3.11(d) depict the corresponding construction performance of Method A and B for 2 different photon indices ($\Gamma = 2, 3$). As Method B takes the energy reconstruction bias correctly into account, its performance is largely independent of the spectrum energy threshold. Method A, however, which correctly accounts for the energy reconstruction bias only for a photon index of 2.0, shows increasing deviations for softer

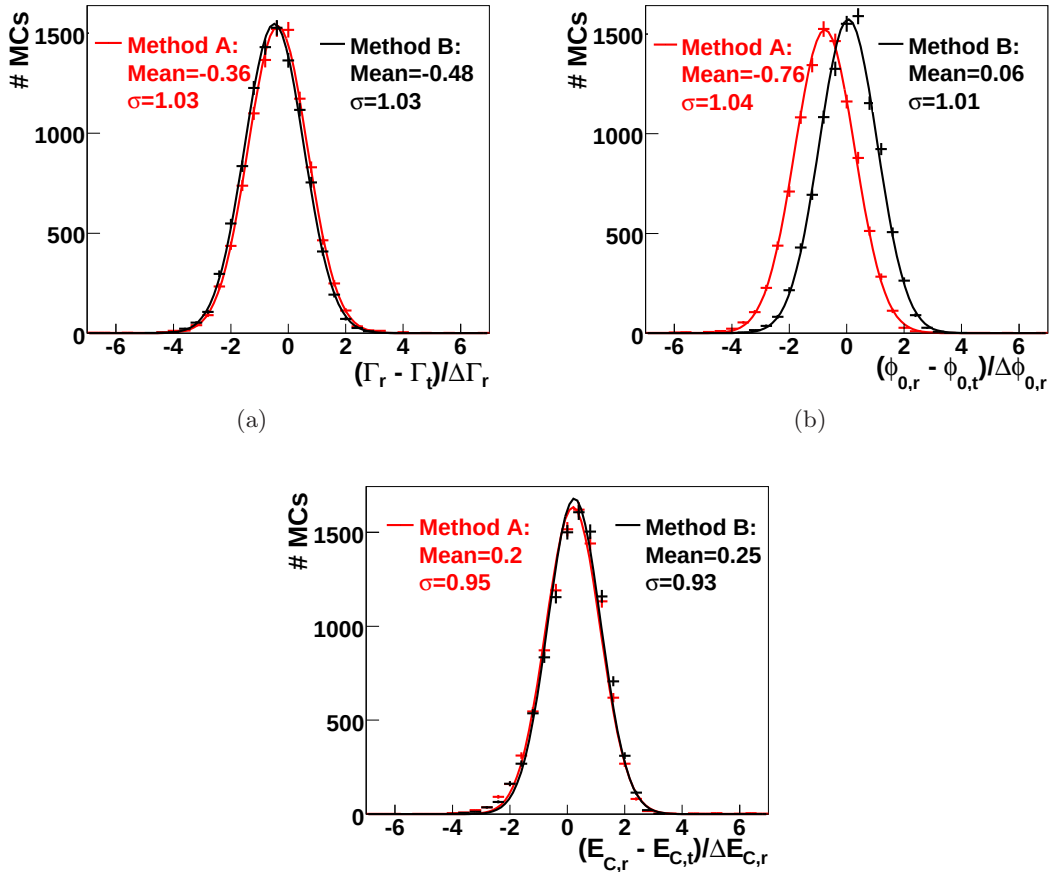

Figure 3.10: Pull distributions of the spectral parameters: photon index Γ (a), flux normalization at 1 TeV $\phi_0(1\,\text{TeV})$ (b) and exponential cut-off energy E_C (c) obtained from Set 3 with a simulated cut-off energy of 7 TeV. Depicted are the distributions of the deviations between simulated and reconstructed parameter values, divided by the corresponding statistical error obtained from the spectral fit. The results for Method A (black) and Method B (red) are shown.

spectra ($\Gamma > 3$) when the allowed energy bias reaches 0.25. As apparent in Figure 3.11(c) and 3.11(d), these biases carry no importance for low statistics sources. For a photon index of 2.0, or smaller energy reconstruction biases, the performance of Method A is equivalent to Method B.

Finally, **Set 6** is designed to verify the impression that potential systematic biases in the spectral reconstruction are independent of the source statistics. Seven different source strengths have been simulated, starting with a flux normalization of $\phi_0 = 3.2 \cdot 10^{-11}\text{cm}^{-2}\text{s}^{-1}\text{TeV}^{-1}$ and a signal to noise ratio of 19.2, consequently dividing both by a factor of 2 from one source strength to the next, keeping the background rate constant. As visible in Figures 3.12(a) to 3.12(b), the reconstruction performance is largely independent of the statistics of the data set. The reconstruction bias of Method A for indices much larger

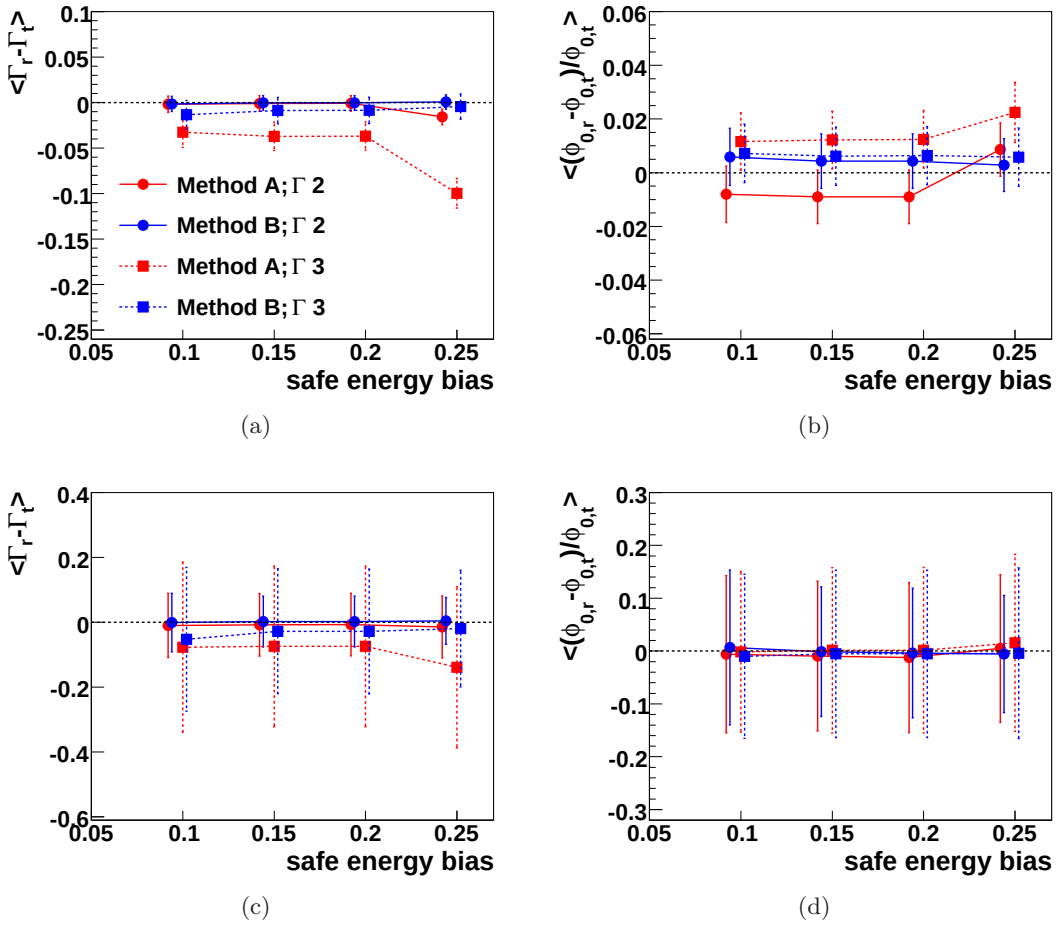

(a) (b)

(c) (d)

Figure 3.11: Spectral reconstruction performance of Method A and B for Set 4 (a+b) and Set 5 (c+d). Shown are the mean absolute deviation of the reconstructed photon index from the simulated value (a+c) and the mean relative deviation of the flux normalizations at 1 TeV (b+d) for varying values of the allowed energy reconstruction bias. The error bars depict the mean statistical reconstruction error of the corresponding parameter.

than 2 becomes of the same order as the statistical uncertainties for a flux normalization of $\phi_0 = 8 \cdot 10^{-12}\text{cm}^{-2}\text{s}^{-1}\text{TeV}^{-1}$, a signal to noise ratio of ~ 5 and a lifetime of 34 h. This corresponds roughly to a statistical significance of 88 standard deviations for a source with a photon index of Γ=3.

In summary, the systematic studies performed using a Toy Model Monte Carlo have led to the following conclusions:

- The statistical error bars on the spectral shape parameters extracted with Method A and B represent correctly the statistical spread of the fit parameters.
- Spectra with indices ranging from $\Gamma = 2$-3 are correctly reconstructed with a potential reconstruction bias smaller than the statistical uncertainties (with the exception of Method A, $\Gamma = 3$ and a very high statistics data set, see Figure 3.8(a)).

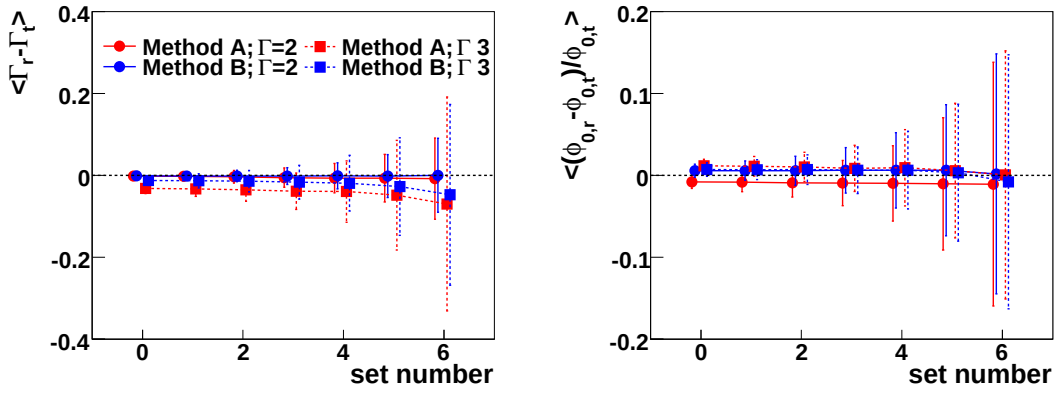

(a) (b)

Figure 3.12: Spectral reconstruction performance of Method A and B for Set 6. Shown are the mean absolute deviation of the reconstructed photon index from the simulated value (a) and the mean relative deviation of the flux normalizations at 1 TeV (b) for decreasing source strength. With each set number, the sources strength decreases by a factor of 2, starting with $\phi_0(1\text{TeV}) = 3.2 \cdot 10^{-11}\,\text{cm}^{-2}\text{s}^{-1}\text{TeV}^{-1}$. The error bars depict the mean statistical reconstruction error of the corresponding parameter.

- For softer spectra, Method A shows a systematic bias towards steeper spectra and larger flux normalizations. But the reconstruction biases are small – with the exception of Γ=4 – and can be neglected for all but the highest statistic sources. Method B shows no reconstruction biases independent of the photon index.

- Source spectra with exponential cut-offs are reconstructed correctly, with reconstruction biases smaller than the statistical uncertainties, even for high statistics data sets.

- The observed reconstruction biases are independent of the source statistics.

It should be noted that the Toy Model MC simulation is far from describing the full analysis chain. Important aspects like the background identification are not tested. The above statements about the performances of the spectral reconstruction is therefore limited to the aspects testable by the Toy Model, i.e. usage of the effective areas, integration accuracy (Method B), binning (Method A), fit procedure etc..

3.6.2 Real Data

The final test the two spectral reconstruction methods (A+B) have to pass is how they perform with real data. Contrary to the previous systematic tests, the "true" source spectrum is not known. Consequently, a correct reconstruction of the underlying source spectrum can not be confirmed with 100% certainty. But the agreement of both methods serves as a last consistency check. For this purpose spectra of two different sources within the Galactic Plane are measured using Method A and B. The first source, chosen as a

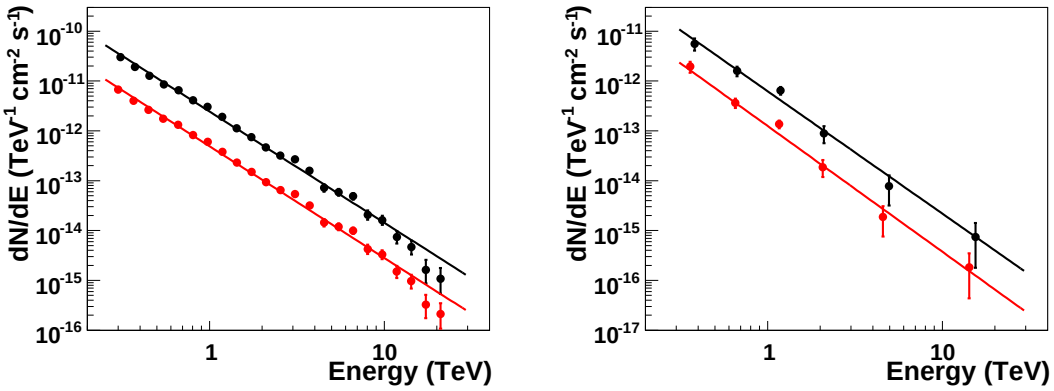

(a) (b)

Figure 3.13: Differential energy spectra of HESS J1745-290 (a) and HESS J1846-029 (b), obtained with Method A (red) and Method B (black). The red curve has been scaled with a factor 0.2 for illustrational purposes.

prime example for a strong source with good observational coverage, is the Galactic Center source HESS J1745-290 located at l=359.94° Galactic longitude and b=-0.04° Galactic latitude. The full available data set of 113 hours of dedicated observations was used in the analysis. The zenith angles of the observations range from 5° to 60°, with a mean of 19°, the mean offset from the pointing direction to the source is 0.7°. The fraction of 3-telescope observations is negligible (3%) and is not used here. The standard H.E.S.S. analysis scheme as described in Section 2.4 was applied to the data. Due to their lower energy threshold, *standard*-cuts are used for gamma-hadron separation. The background is estimated using the reflected-region background method. Even though there is a hint for curvature in the spectrum, the spectrum was fitted with a pure power law. Both spectral reconstruction methods give consistent results. Using Method A the reconstructed spectral parameters are $\phi_0 = (2.44 \pm 0.06) \cdot 10^{-12}$ cm^{-2}s^{-1}TeV^{-1} and $\Gamma = 2.23 \pm 0.02$. For Method B the corresponding values are: $\phi_0 = (2.46 \pm 0.06) \cdot 10^{-12}$ cm^{-2}s^{-1}TeV^{-1} and $\Gamma = 2.24 \pm 0.02$. Both spectra with their spectral flux points and the corresponding fits are shown in Figure 3.13(a). For visibility, the spectrum obtained with Method B was scaled by a factor of 0.2.

The same consistency check was performed with another source, Kes 75, which serves as an example of a weak source, also with sufficiently good H.E.S.S. coverage. The source is – like the Galactic Center – a point-like source, and is located at l =29.70° and b=-0.24°. The data set consists of 33 hours of good quality observations, with a mean zenith angle of 27° and mean offset of 1°. The same analysis procedure as described above is applied to the data. The source spectra measured by Method A and B are again found to be consistent. Using Method A the reconstructed parameters are $\phi_0 = (6.2 \pm 0.7) \cdot 10^{-13}$ cm^{-2}s^{-1}TeV^{-1} and $\Gamma = 2.46 \pm 0.13$. For Method B the corresponding values are $\phi_0 = (6.3 \pm 0.7) \cdot 10^{-13}$ cm^{-2}s^{-1}TeV^{-1} and $\Gamma = 2.52 \pm 0.12$. The two spectra are also shown in Figure 3.13(b).

The good agreement of the two methods in genuine data analysis supports the impression received from the Toy Model MC tests. Both methods give consistent results in all tested cases. For simplicity, only the results obtained with Method A will be shown in the following chapters, eventhough all results have been confirmed using Method B.

Chapter 4

The H.E.S.S. Galactic Plane Survey

Most of the Galactic objects expected to emit VHE γ-rays are related to the evolution of massive stars, either to their wind outflows or to PWNs and SNR shells formed after their collapse. These potential γ-ray sources are therefore expected to cluster along the Galactic plane. A systematic survey of this region is thereby the best means of investigating the properties of these source classes and of searching for yet unknown types of Galactic VHE γ-ray emitters.

At very high energies, the HEGRA instrument was the first system of Imaging Atmospheric Cherenkov telescopes that surveyed at least parts of the Galactic plane, reaching from l=-2° to 85°(Aharonian et al. (HEGRA collaboration), 2002). Due to its location in the northern hemisphere, HEGRA could observe the inner part of the Galactic plane only at large zenith angles and therefore with reduced sensitivity. Consequently, no VHE γ-ray sources were discovered in the survey. Upper limits on the VHE γ-ray flux were derived, ranging from 15% of the Crab nebula flux for $l > 30°$ to more than 30% for -2° $< l <$ 30°. The more southern part of the Galactic plane $l > 0°$ remained effectively unobserved.

The H.E.S.S. experiment, with its improved sensitivity, its larger field-of-view (5°) and its location in the southern hemisphere is better equipped for a survey of the Galactic plane. The first stage of the H.E.S.S. survey started in the year 2004 and was conducted in the Galactic longitude band $l = \pm 30°$ around $l = 0°$. It resulted in the discovery of 14 new sources with a statistical significance of more than 4σ, increasing the number of Galactic VHE γ-ray sources from 3 to 17 (Aharonian et al. (H.E.S.S. collaboration), 2006h). The region was observed with varying sensitivity, reaching down as far as 3% of the Crab nebula flux at the Galactic Center. In the years 2005/2006, the survey region was extended further along the Galactic plane and now reaches from $l = 280°$ to 60°.

This Chapter is devoted to the H.E.S.S. Galactic plane survey to date the most sensitive view of the Galactic plane in VHE γ-rays. The data analysis, the detection procedure of new γ-ray sources, as well as the details of the data set are described. The results of the Galactic plane survey are presented, including the detection of 45 VHE γ-ray sources as well as flux and sensitivity maps of the whole survey region. The Chapter concludes with a brief description of 19 new Galactic VHE γ-ray sources discovered in the years 2006/2007. Three more will be described in more detail in Chapter 5.

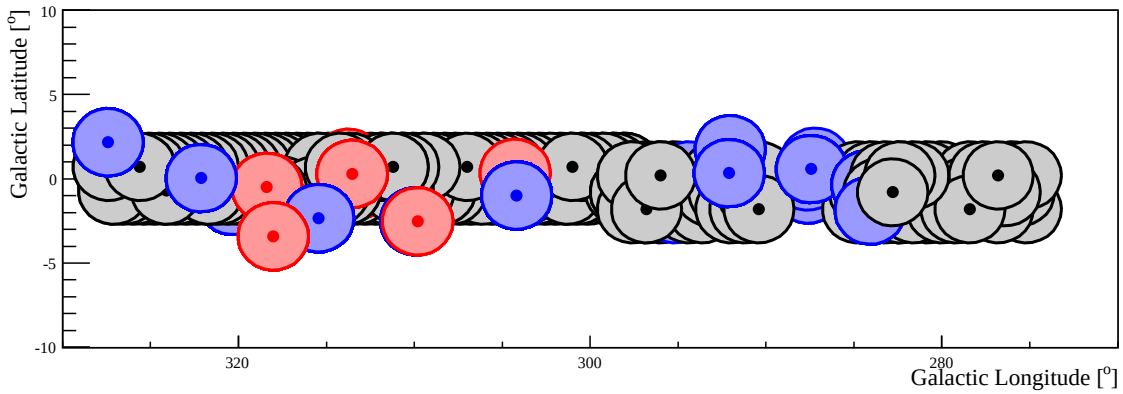

Figure 4.1: Illustration of the observation pointings within the region l=270° - 330°. Each observation of 28 minutes duration is represented by a circle of 4° diameter with the array pointing at their centers. Raster scan observation are depicted in black, the two strips along b=±0.7° are apparent. The red circles correspond to re-observations of promising source candidates discovered in the survey data. The blue circles illustrate dedicated observations of predicted γ-ray emitters known from other wavelengths.

4.1 The General Principle

The H.E.S.S. telescope array is usually operated by taking pointed observation runs in which it tracks a single astrophysical object in the sky. Given the effective field-of-view of the instrument of 4°, such observation runs cover around $12(^\circ)^2$ on the sky. To search for unknown VHE γ-ray sources within such a large region as the Galactic plane, many such observation runs targeted on a grid pattern are necessary to cover the whole survey region. The observation scheme applied is shown in Figure 4.1, where the survey observations are depicted in black. Each observation run is analyzed individually following the standard analysis chain as presented in Chapter 2.4, and the results obtained from all runs are combined to form a continuous map of the whole survey region. Consequently, the resulting map is then used to search for statistically significant signals of VHE γ-ray emission along the Galactic plane. If a VHE γ-ray source was detected, a dedicated and more detailed analysis, including spectral and morphological studies, is performed on the much smaller data set.

4.2 The Data Set

4.2.1 Observation Scheme

The H.E.S.S. Galactic plane survey started in April 2004. The survey of the inner 60° was completed in the years 2004/2005. In the years 2005/6, the survey region was extended further along the plane and now reaches from l=280° to 60°. In addition to further follow-up observations, the region l=1°-4° was re-observed in a deep coverage program in the year 2007. Table 4.1 summarizes the amount of data taken in the different years.

Year	T [h]			ϵ
	Scan	Re-Obs.	Ded. Obs.	%
2004	92	45	179	87
2005	82	73	184	86
2006	81	51	120	76
2007	23	110	174	75

Table 4.1: Description of the survey data set. The observation time T in hours is given for the years 2004-2007, scan raster observations, re-observations of putative sources found in the survey data and dedicated observations of predicted γ-ray sources are differentiated. The efficiency ϵ of data taking, defined the ratio of observation time passing the quality selection and total observation time is stated as well.

To cover the large area of the Galactic plane, a raster scan was performed, consisting of individual observations of 28 minute duration. The observations were taken at pointings with a spacing of 0.7° in Galactic longitude and varied latitude spacing along the Galactic plane. The resulting overlap leads to a continuous coverage. Within the inner 60°, the survey was conducted in three strips in Galactic latitude centered on b = -1°, b = 0° and b = +1°. Based on the experience that most sources were found very close to the Galactic plane, only two strips were used in the following years, centered at b=±0.7° for best sensitivity at b=0°. Consequently, the area covered along the Galactic plane has an approximate width of 6°. Figure 4.1 illustrates the applied observation scheme. In total 277 hours of quality selected data were taken in scan mode. Promising source candidates were re-observed in dedicated observations which yield the same amount of good-quality data. In addition, pointed observations of predicted γ-ray emitters located within the Galactic plane were also conducted. The total data set including all observations within the survey region accounts for 1219 hours of quality-selected data. Most of the observations were taken with the full H.E.S.S. array. Only 58 hours, which comprises merely 5 % of the whole data set, were taken with only 3 or 2 telescopes.

Due to the large number of dedicated observations, the exposure within the survey region is very non-uniform. Figure 4.4 (top) illustrates the exposure along b=0° as equivalent observation time taken at the center of the camera. The large peaks arise from accumulation of dedicated observations of known γ-ray sources, e.g. the Galactic Center at l=0°.

4.2.2 Zenith Angle of Observations

To conduct observations with the best instrumental performance, the observations have to be carried out close to zenith. However, depending on the declination of the region of interest, the culmination of the Galactic plane occurs at the H.E.S.S. site at larger zenith angles. The black line in Figure 4.2(b) illustrates the zenith angle at culmination for b=0° as a function of Galactic longitude. This position-dependent minimum zenith angle leads to a non-uniform sensitivity and energy threshold even in case of a homogeneous coverage. In the worst case, regions can not be observed at all, e.g. $l > 80°$.

Figure 4.2(a) shows the time period within one year at which the Galactic plane can be observed at reasonable zenith angles. The red line illustrates the time of year when the

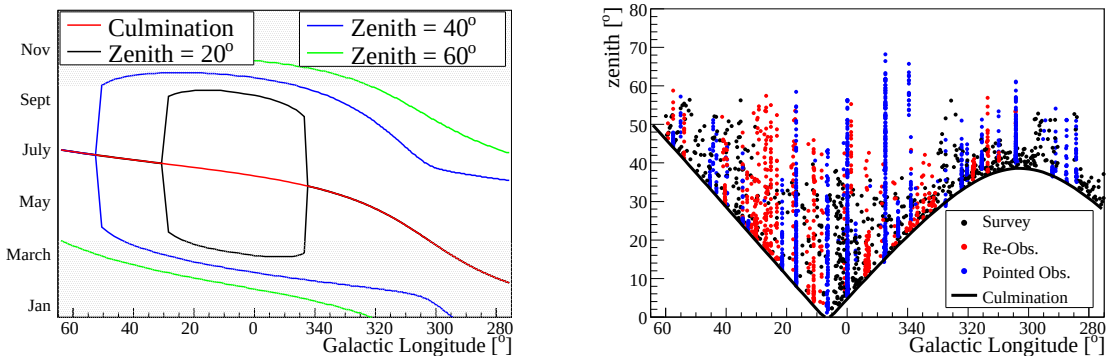

(a) (b)

Figure 4.2: a.) Observability of the Galactic plane for the H.E.S.S. site. The red curve shows the time of the year when the Galactic plane (b=0°) culminated at midnight. No statement is made about the zenith angle at which the culmination occurs. The green and blue curves delimit the ranges in position and season at which observations at zenith angles smaller than 40° and 60° respectively can be taken. b.) Zenith angle distributions of the observations taken within the survey region. The black line illustrates the minimum zenith angle at which the corresponding position along the Galactic plane can be observed from the H.E.S.S. site.

corresponding part of the Galactic plane culminates at midnight, maximizing the time when the region can be observed close to culmination. At which zenith angle this culmination occurs can be read from the black line in Figure 4.2(b). The black, green and blue curves in Figure 4.2(a) border the time of year in which the Galactic plane can be observed at zenith angles smaller than 20°, 40° and 60° respectively. Note that the amount of time, the corresponding region can be observed at these zenith angles is not stated and can be as small as a few minutes per night. The shaded regions in Figure 4.2(a) depict the rainy season in Namibia, especially the data taking in the region l<300° is hampered by bad weather conditions.

Figure 4.2(b) shows the zenith angles at which the observations within the survey region were taken. As can be seen, the correlation between Galactic longitude and zenith angle is not very strong apart from the restiction imposed by the minimum possible zenith angle. However, it is the strongest for scan-mode observations, not counting the deep survey around l=2°. The dedicated observations were taken at all zenith angles — ranging up to 65° — accepting for the resulting decline of sensitivity and energy threshold.

Energy Threshold

The energy threshold is strongly dependent on the zenith angle at which the observation was taken. The details are described in Chapter 3.3. Figure 4.4 (middle) shows the average energy threshold at b=0° along the Galactic plane for the standard survey analysis as described in Section 4.3. The energy thresholds of all observations pointed within 2° were averaged using a simple arithmetic mean. The average threshold ranges from 600 GeV to almost 2 TeV. The maximum is reached at l=340° where very large zenith angle (>55°)

observations were taken (see Figure 4.2). Due to the strong dependence on the zenith angle, the general trend of the energy threshold follows the culmination curve as seen in Figure 4.2. The biggest deviation from the trend occurs again at l=340°.

Sensitivity

The sensitivity reached at each point of the survey region depends predominantly on the amount of time the position has been observed and the zenith angles of the observations. In the following, the sensitivity is defined as the flux necessary to detect a point source with a pre-trials significance of 5σ. The gamma-ray spectrum of the putative source is expected to follow a power law with index 2.5. Figure 4.3 shows the resultant point-source sensitivity in units of the flux of the Crab Nebula (Aharonian et al. (H.E.S.S. collaboration), 2006g) within the survey region. Figure 4.4 (bottom) depicts a slice through the sensitivity map at b=0° and b=1.5°. The sensitivity reached at b=0° ranges from 0.5% of the Crab Nebula flux at the position of the Galactic Center to 3.5% of the Crab Nebula flux at higher longitudes. As the observation pointings were optimized for b=0° and the sensitivity is strongly dependent on the distance to the camera center, the off-plane sensitivity is almost everywhere lower than the on-plane sensitivity. The dependence on the zenith angle of the observations is washed out in these curves by the much stronger dependence on the observation time.

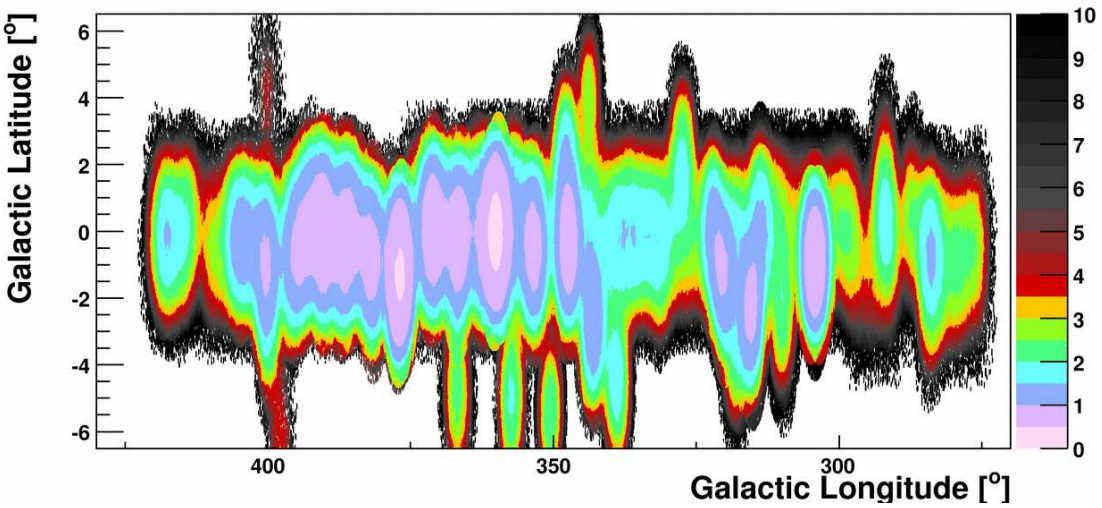

Figure 4.3: Sensitivity map of the survey region in percent of the flux of the Crab nebula (Aharonian et al. (H.E.S.S. collaboration), 2006g). The sensitivity depicted here is defined as the flux necessary to detect a point source with a pre-trial significance 5σ. The gamma-ray spectrum of the putative source is assumed to follow a power law with photon index 2.5. The best sensitivity is reached at the Galactic Center with ~ 5 mCrab flux equivalent.

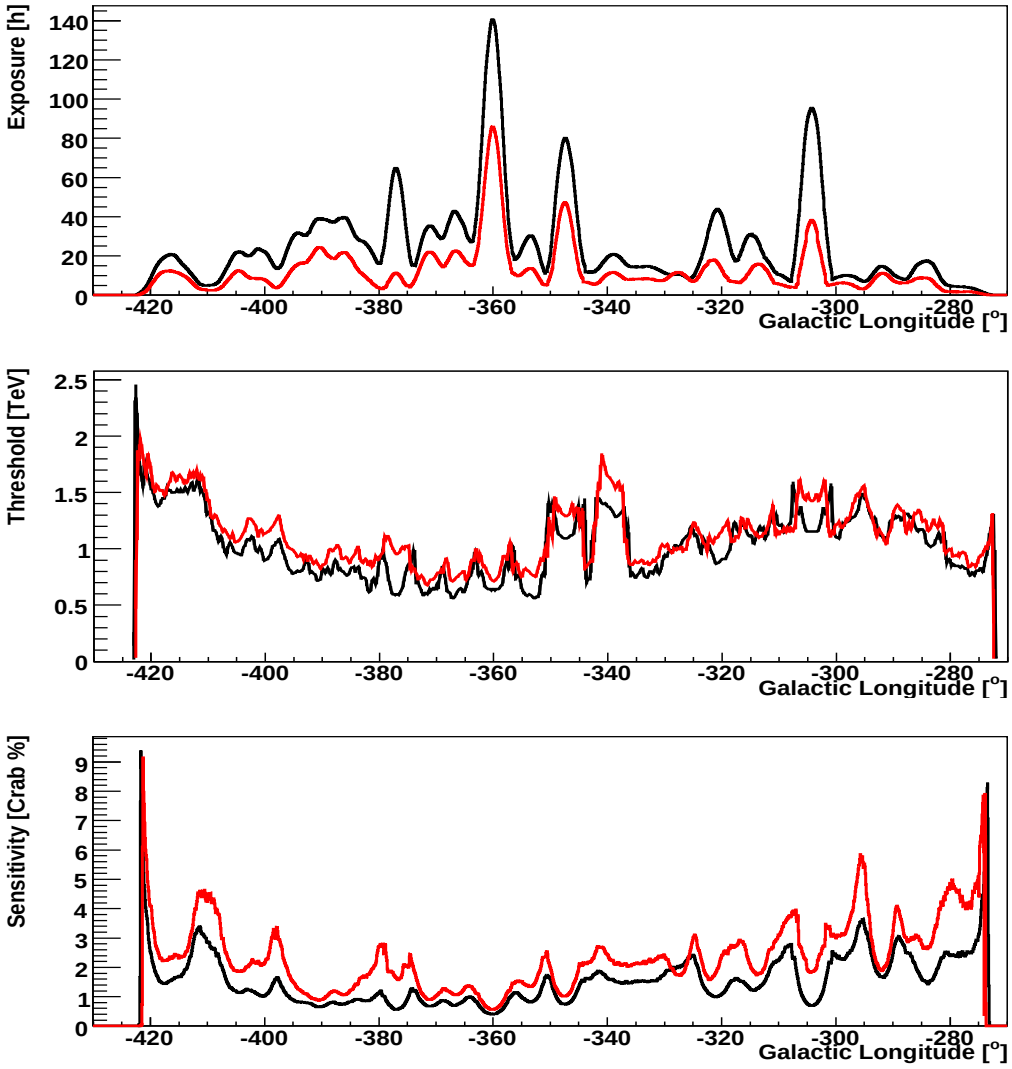

Figure 4.4: *Top:* Acceptance corrected exposure along the Galactic plane expressed as equivalent observation time at the center of the field-of-view. The black curve was extracted at b=0°, the red curve at b=1.5°. The strong contribution of dedicated observations results in a very inhomogeneous exposure. *Middle:* Analysis energy threshold using hard-cuts for γ-ray selection as described in Section 2.4. The threshold is averaged over all observations with exposure at the corresponding position. The increase in threshold with the offset from the camera center is taken into account. The same color coding as in the top figure is used. Due to the strong dependence of the energy threshold on the zenith angle, the curves show general agreement with the minimum reachable zenith angle depicted in Figure 4.2(a). The peak at l=340° arises from dedicated observations taken at very large zenith angles. *Bottom:* Sensitivity for the detection of a point source in units of the flux of the Crab nebula (Aharonian et al. (H.E.S.S. collaboration), 2006g) for b=0° (black) and b=1.5° (red). For the definition of sensitivity see caption of Figure 4.3.

4.3 The Survey Analysis

The analysis of the survey data is almost identical to the data analysis chain described in Chapter 2.4. However, the large number of observation runs to be considered (2665), necessitates a splitting between run-wise operations and the combination of their results later on. The survey analysis can be subdivided into 3 distinct steps.

- Pre-processing of the individual observation runs.
- Combination of the run-wise results to large overview maps spanning the whole survey region.
- Search for statistically significant signals of VHE γ-ray emission within the combined data set.

4.3.1 Processing the Individual Observations

Each individual observation run is pre-processed using the analysis procedure described in Chapter 2.4. Two maps centered on the pointing position are created for each run.

- A raw count map containing all events passing the event-selection with a bin size of 0.04°. The map is centered on the observation position. For gamma-hadron separation, *hard-cuts* (see Section 2.4) are usually used due to their superior separation power. To avoid systematic effects related to the acceptance curve at larger distances from the camera center, only events detected within 3.0° of the pointing direction of the instrument are considered.
- An acceptance map, filled by rotating a one-dimensional acceptance template around the observation position. The acceptance template was obtained from off-runs which were taken at a similar zenith angle as the observation run. The acceptance map, as well, is truncated at a distance of 3° from the observation position.

After the raw count map is filled, the event-wise information is lost and the subsequent analysis is based on the maps only.

4.3.2 Combination of Run-wise Information

In the next step, the maps of all observations are added up to large maps encompassing the whole survey region in Galactic Longitude and Latitude. To minimize binning effects during the adding process, the bin size of the overview maps is adjusted to the binning of the run-wise maps (0.04°). As the center positions of the small maps are chosen independently of each other and independently of the large map, the bins of the small maps have to be shifted within the coordinate frame to coincide with the bins of the large map. The maximum shift in each coordinate is 0.02°, which is much less than the PSF of the instrument and has a negligible effect on the subsequent signal determination. The raw count maps are merely added. The acceptance maps, however, need to be scaled relative to each other to account for different observation times and weather conditions during data taking. The total number of background events not originating from the position of known VHE γ-ray sources are used for this scaling. A third large map is produced indicating the position and extension of the known VHE γ-ray sources within the survey region. This "exclusion

Set	$\theta[^\circ]$	$R[^\circ]$	$\Delta R[^\circ]$	ζ
1	0.1	0.9	0.2	1/32
2	0.22	0.9	0.2	1/7
3	0.4	1.2	0.46	1/7

Table 4.2: Different parameters for the significance maps used to search for new VHE γ-ray sources. θ is the radius of the on-source region, R and ΔR denote the mean radius and the width of the ring from which the background was estimated, ζ is the area factor between on-source and off-source region. The area factor for Set 1 is made much smaller than for the other sets to avoid binning effects from a too thin ring.

map" is used as a mask and no background estimate is taken from a region marked within this map.

4.3.3 Detection of Sources

Significances

The three resulting large maps, the raw count map, the acceptance map and the exclusion map, are fed back into the standard analysis chain. To search for statistical significant signals from various sized VHE γ-ray sources, three large significance maps are produced with varying correlation radii. For all maps, the *ring background method* (Section 2.4) is used to estimate the background at each sky position. Table 4.2 summarizes the different parameters used to create the significance maps.

Trials

The pre-trials significance S_{pre} stated within the maps denotes the probability P that the signal within the corresponding bin is not to an upward fluctuation in the cosmic-ray background. Because the significance follows a Normal Distribution in the absence of a signal, the probability P is given by:

$$P = \frac{1}{\sqrt{2\pi}} \int_{-\infty}^{S} \exp\left(-\frac{t^2}{2}\right) dt \ . \tag{4.1}$$

However, the blind-search for a possible γ-ray signal within the three significance maps introduces a large number of statistical trials. The important point is therefore to evaluate the probability P_N of finding a fake source with a pre-trials significance S_{pre} anywhere within the maps. This probability increases with the total number of independently tested sky positions, or, more generally, with the total number of statistical trials N, and is given by

$$1 - P_N = (1-P)^N \quad \rightarrow P_N = 1 - (1-P)^N \ , \tag{4.2}$$

while $1 - P_N$ is the probability of not having reached the pre-trials significance corresponding to P even once in N trials. The probability P_N can then be translated back into a post-trials significance using Equation 4.1. It is this post-trials significance which measures the authenticity of a source found in the survey. As a conservative estimate,

Significance	
Pre-trials	Post-trials
5.0	0.4
6.0	3.0
7.0	4.6
7.5	5.3
8.0	6.0
9.0	7.3
10.0	8.5

Table 4.3: Detection significances before and after accounting for $1.575{\cdot}10^6$ trials.

the total number of bins tested within the three significance maps is used to estimate the number of trials. Each map spans the whole survey region with $\Delta l \sim 140^\circ$ and $\Delta b \sim 60^\circ$. The bin sizes are $0.04^\circ \times 0.04^\circ$. The total number of bins in each map is then 525,000. As three different maps have been used in the search, the total number of statistical trials is assumed to be $1.575{\cdot}10^6$. This number is surely an overestimate, as the summation within the on- and the off-regions which span across many bins, has lead to a strong correlation of neighboring bins. Furthermore, the three significance maps are obtained from the same events and only differ in the sizes of the on- and off-regions. This results in a correlation of the bins at the same sky position in the different maps. Table 4.3 summarizes the mapping of pre- and post-trials significances assuming $1.575{\cdot}10^6$ trials.

Detection Thresholds

Two different thresholds on the post-trials significance are set a-priori. If an agglomeration of bins exceeds $3\,\sigma$, but is below $5\,\sigma$, it is considered a hint for a new source and proposed for re-observation. If the peak significance within such an agglomeration is beyond $5\,\sigma$, the detection of a new VHE γ-ray source is regarded as solid.

4.4 Results

4.4.1 Source Detection

One of the three significance maps used within the search is shown in Figure 4.5. The depicted map is produced with parameter set 2 from Table 4.2. The color scale was saturated at 15 σ for visibility. The transition from blue to red occurs at ~ 7 σ pre-trials which corresponds to ~ 5 σ post-trials, the threshold set for a solid source detection. The other two maps can be found in Appendix A.1. In total, 45 VHE γ-ray sources are detected by H.E.S.S. within the survey region, their characteristics are summarized in Table 4.4 and 4.5. All but HESS J1507-622, which is at slightly larger latitude, are visible in Figure 4.5. Some are better visible with smaller (e.g. HESS J1833-105) or larger (e.g. HESS J1908+062) correlation radii due to their intrinsic angular sizes. Twenty of these 45 sources were discovered within the framework of this work and are individually introduced in Chapter 4.5.

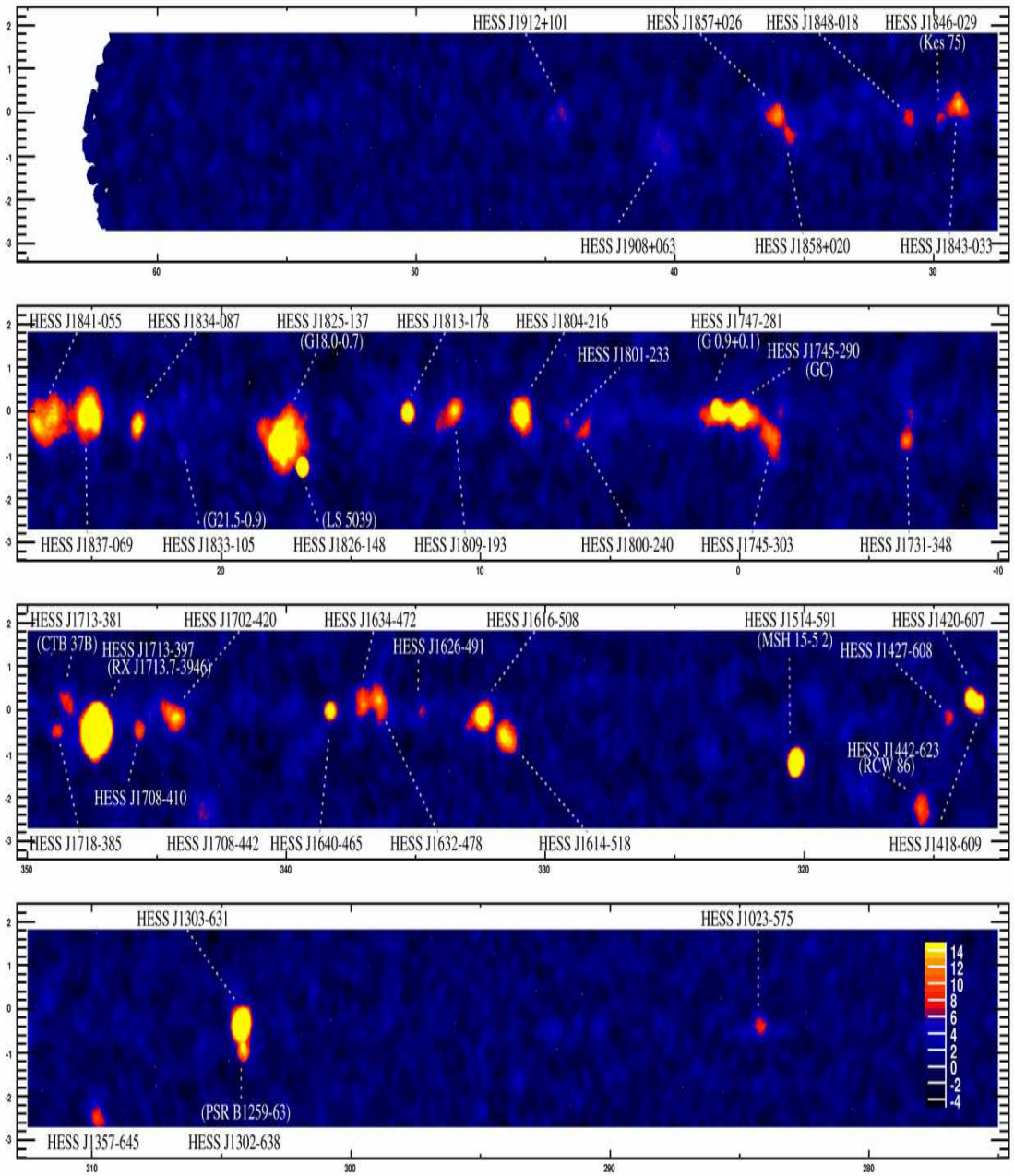

Figure 4.5: Significance map of the H.E.S.S. Galactic plane survey region. The on-source counts are summed from a circle of radius 0.22° around each bin. The background is estimated from a ring with mean radius of 0.9° and an area 7 times as large as the on-source region. The γ-hadron separation was done using hard-cuts. The mean energy threshold and the sensitivity varies strongly throughout this map. A slices along b=0° can be found in Figure 4.4. All VHE γ-ray source from Table 4.4 and 4.5 are labeled. The color scale is truncated at 15 σ for visibility. The other two maps used in the search for new VHE γ-rays sources can be found in Appendix 4.5

4.4.2 Flux Measurements

The significance maps are merely used to gage the authenticity of a potential source. The significance itself strongly depends on observation time and performance of the instrument and therefore does not constitute a physical measurement of the sources' characteristics. The most meaningful way to represent the Galactic plane as seen in VHE γ-rays is with the number of photons detected per second per unit detection area from each point within the survey region. These flux maps depict the actual brightness of the detected sources in VHE γ-rays.

In the following, the procedure to calculate flux maps is introduced. Figure 4.7 then depicts the flux measured from all the detected sources within the survey region using the parameter set 2 from Table 4.2.

The Calculation of Flux Maps

The calculation of the flux maps is directly incorporated into the survey analysis and therefore shares its general design as descibed in Section 4.3:

- During the processing of the individal observations, an additional exposure map is calculated:
  - The zenith angle (θ_z) distribution of all events after γ-ray selection is stored in a histogram of 20 bins ranging from 0° to 60°. The histrogram is normalized such that its integral is equal to the livetime of the observation. The result is an event-weighted distribution of livetime t_{θ_z} effectively spent at a certain zenith angle.
  - Given the zenith distribution, the exposure for the observation at hand is calculated for six different offsets from the camera center $\psi = 0°, 0.5°, 1.0°, 1.5°, 2.0°, 2.5°$. Assuming the differential source spectrum follows a pure power-law with index Γ, the exposure Ξ is given by:

$$\Xi(\psi) = \sum_{\theta_z} t_{\theta_z} \cdot \int_{\tilde{E}_{\min}}^{\tilde{E}_{\max}} \left(\frac{\tilde{E}}{\tilde{E}_0}\right)^{-\Gamma} A_{\text{eff}}(\tilde{E}/\mu, \theta_z, \psi) \mathrm{d}\tilde{E} \tag{4.3}$$

    where $\tilde{E}_0$ is the reference energy for the differential power-law spectrum, $\tilde{E}_{\min}$ and $\tilde{E}_{\max}$ are the minimum and maximum energies between which events were filled into the survey maps, μ is the muon energy correction factor for the observation and $A_{\text{eff}}(\tilde{E}/\mu, \theta_z, \psi)$ is the effective area.
  - The value for each bin within the run-wise exposure map is then determined by linear interpolation from the offset of the bin to the camera center.
- The run-wise exposure maps are added up to produce large overview maps in the same way as the raw count maps within the survey analysis. Figure 4.6(a) depcits the exposure map for the 1.6°×1.6° region surrounding the Crab Nebula.

- From the exposure map and the correlated excess map, which is obtained in the same way as the significance maps shown in Figure 4.5, the flux $F|_{E_1}^{E_2}$ within an energy range $[E_1, E_2]$ for each bin i of the flux map is calculated:

$$F^i|_{E_1}^{E_2} = \int_{E_1}^{E_2} \frac{\text{excess}^i}{\Xi^i} \left(\frac{\tilde{E}}{E_0}\right)^{\Gamma} \mathrm{d}\tilde{E} \ . \tag{4.4}$$

  It should be noted that E_1 and E_2 can be chosen independently of $\tilde{E}_{\text{min}}$ and $\tilde{E}_{\text{max}}$, the necessary extrapolation, however, makes the result dependent on the assumed source spectrum. For the following maps, E_1 is set to 200 GeV and $E_2 = \infty$. Figure 4.6(b) depicts the flux map of the $1.6° \times 1.6°$ region surrounding the Crab Nebula. Figure 4.6(c) shows the corresponding close-up of the Crab Nebula, only the signal exceeding a statistical significance of $5\,\sigma$ is shown.

- When the statistical significance of the VHE γ-ray signal is below a pre-determined threshold (typical value is $5\,\sigma$), flux upper-limits can be calculated in the same manner using Equation 4.4. The measured number of excess events is then replaced by its upper limit value, determined using e.g. the unified approach by Feldman & Cousins (1998).

A few choices have to be made when calculating the flux maps, concerning the effective areas $A_{\text{eff}}(\tilde{E}/\mu, \theta_z, \psi)$ and the energy range $[\tilde{E}_{\text{min}}, \tilde{E}_{\text{max}}]$ used in Equation 4.3. The different possibilities will be shortly addressed as well as the consequences for the interpretation of the obtained flux values.

Effective Areas

The first choice concerns the effective areas used in Equation 4.3. If point-source effective areas are used, the calculated flux value is corrected for the leackage of a point-source's signal outside of the on-source region, see Section 3.1. The obtained flux value then has to be interpreted as the flux of a putative point-source located at the bin center. It should be noted that, in this case, the excess map has to be correlated with the same radius as the on-source region used to produce the effective areas. Point-source effective areas have been used to produce the flux maps of the Crab nebula shown in Figure 4.6
In the case where a larger size of the on-source region is chosen for the correlation of the excess map, full-enclosure effective areas (as described in Section 3.1) must be used. The effective areas then do not account for a possible leackage of source flux outside the on-source region and the obtained flux value corresponds to a celestial region (the On-source region) rather than to a putative point-source. The flux maps of the Galactic plane shown in Figure 4.7 were produced using full-enclosure effective areas.

Energy Range

Similarly, two choices arise for the energy range $[\tilde{E}_{\text{min}}, \tilde{E}_{\text{max}},]$ used in Equation 4.3. The first possibility is to use no energy cuts ($\tilde{E}_{\text{min}} = 0$ and $\tilde{E}_{\text{max}} = \infty$) and to fill all events into the survey maps. The effective areas A_{eff} versus the true MC energy $\tilde{E} = E$ can then be used. In the second approach, the minimum and maximum energies are set to the spectrum energy thresholds described in Section 3.3. In this case, the effective areas generated using

the reconstructed energy $\tilde{E} = E_{\mathrm{r}}$ must be used, since the event selection then depends this quantity. The first approach has the advantage that all event statistics are preserved; thus the flux maps are consistent with the significance maps. In the second approach, the underlying event statistics are the same as used in the spectrum determination. Both approaches give similar results, as will be shown below.

Testing of the Flux Maps

The flux maps are tested unsing the Crab nebula. Three flux measurements have been performed:

1. As a reference measurement, the VHE γ-ray flux above 200 GeV is derived using the standard analysis chain with the reflected region background method and the spectral reconstruction Method A as described in Section 3.4. The size of the on-source region is set to $\theta = 0.1°$, which is suitable for a point source. *Hard*-cuts are used for gamma-hadron separation. The spectrum obtained together with the fit of a pure power-law function is shown in Figure 4.6(d). The measured flux is $F(> 200\,\mathrm{GeV}) = (3.46 \pm 0.22) \cdot 10^{-10}\,\mathrm{cm}^{-2}\mathrm{s}^{-1}$.

2. A corresponding flux map is produced without additional energy cuts ($\tilde{E}_{\mathrm{min}} = 0$ and $\tilde{E}_{\mathrm{max}} = \infty$) and point-source effective areas. The assumed source spectrum was set to be the same as the differential energy spectrum obtained with the standard analysis chain, described in 1.). The map is shown in Figure 4.6(c). The maximum flux value at the position of the Crab nebula is $F(> 200\,\mathrm{GeV}) = (3.38 \pm 0.22) \cdot 10^{-10}\,\mathrm{cm}^{-2}\mathrm{s}^{-1}$.

3. A second flux map was produced applying the spectrum energy thresholds described in Equation 4.3. The maximum flux value at the position of the Crab nebula is $F(> 200\,\mathrm{GeV}) = (3.48 \pm 0.22) \cdot 10^{-10}\,\mathrm{cm}^{-2}\mathrm{s}^{-1}$

The difference of 1.) and 2.) to 3.) is merely 2% and 5‰, respectively.

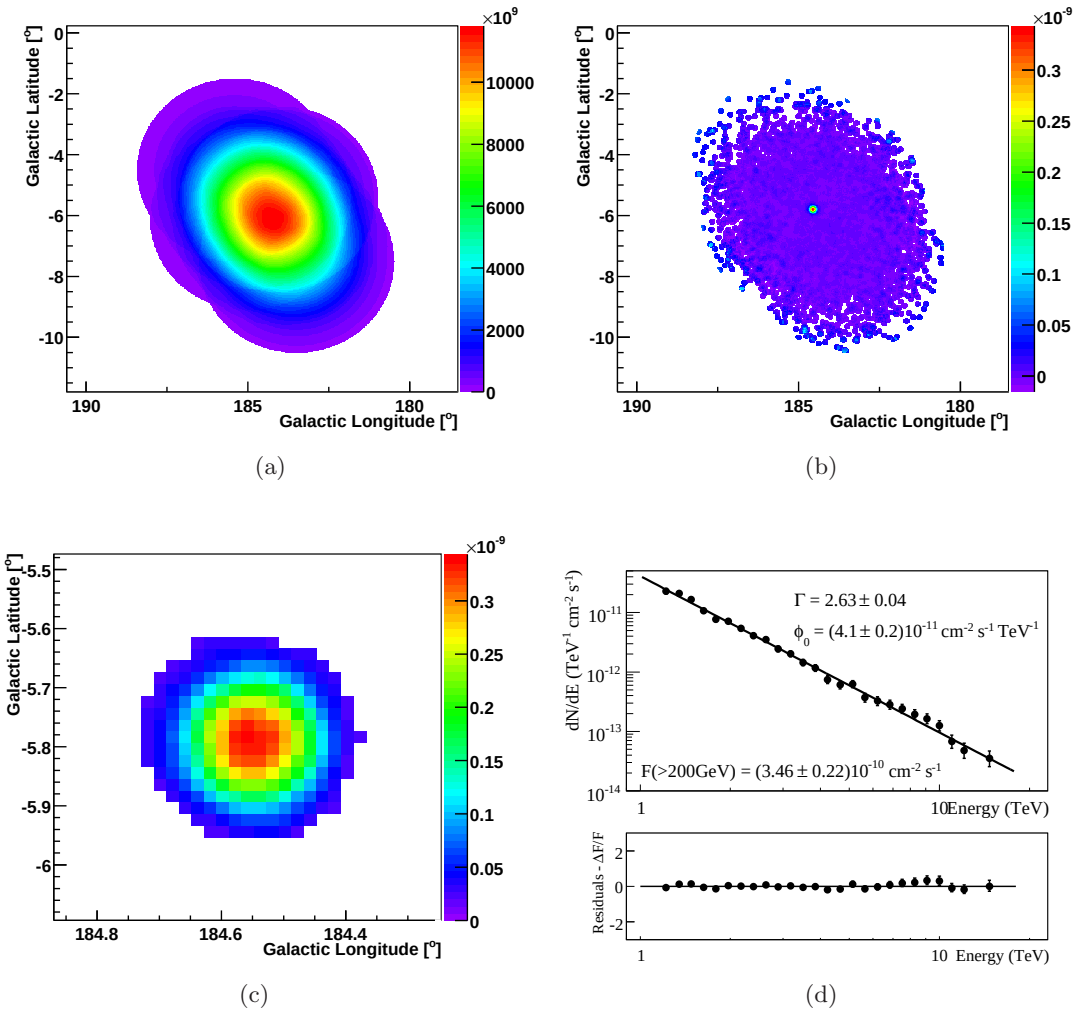

Figure 4.6: Flux map and spectral analysis of the Crab nebula: a.) Exposure map for the 1.6°×1.6° region surrounding the Crab nebula. The exposure is calculated using Equation 4.3 with point-source effective areas and no additional energy cuts ($\tilde{E}_{\mathrm{min}} = 0$ and $\tilde{E}_{\mathrm{max}} = \infty$). The effective areas versus the true MC energy are used. b.) Map of the integral VHE γ-ray flux above 200 GeV. The flux was calculated using Equation 4.4 and the exposure map shown in a.). c.) Same flux map as shown in b.) but zoomed onto the Crab nebula. Only the signal exceeding a statistical significance of $5\,\sigma$ is shown. d.) Differential spectrum of the Crab nebula as obtained with the standard analysis chain, *hard*-cuts for gamma-hadron separation and the *reflected region background method*. The fit with a pure power-law function is also depcited.

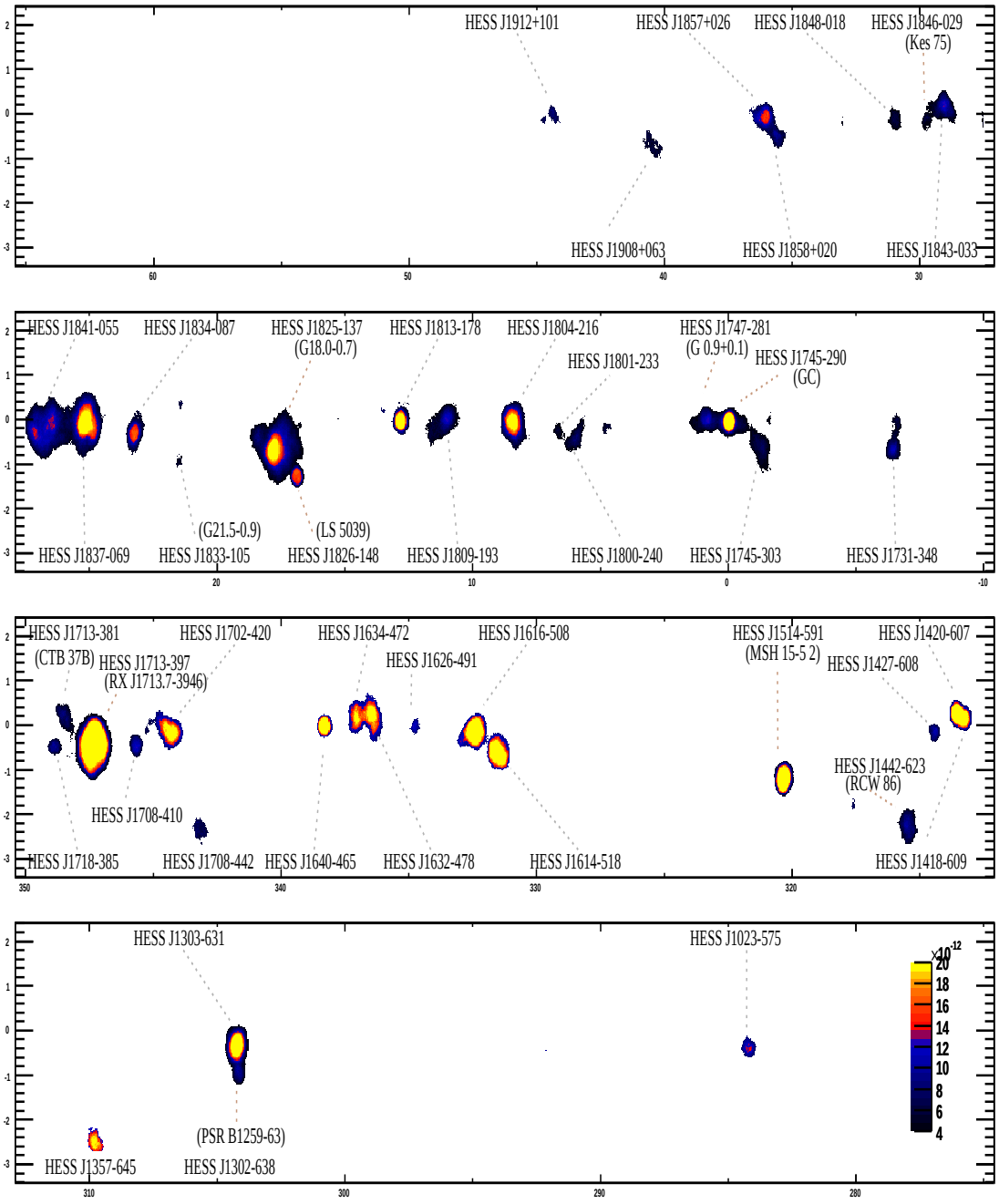

Figure 4.7: Flux map of the H.E.S.S. Galactic plane survey region in units of $\mathrm{cm}^{-2}\ \mathrm{s}^{-1}$. The signal and background estimation was performed equivalent to Figure 4.5. For the flux calculation full enclosure effective areas as described in Chapter 3 were used. The assumed source spectrum follows a power law with a photon index 2.5. The flux is calculated above an energy of 200 GeV. Only the flux values are shown which correspond to a VHE γ-ray signal with a statistical significance of more than 5σ.

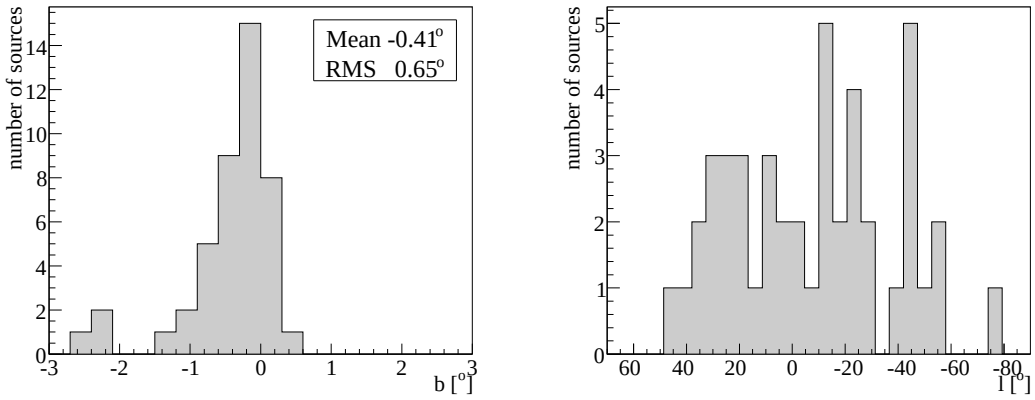

(a) (b)

Figure 4.8: Position parameters of all sources within the survey region. The parameters were extracted using a Gaussian brightness fit to the source morphology. a) Galactic latitude coordinate of the center of gravity of the VHE γ-ray source; the distribution has a mean of -0.41°and a rms of 0.65°. b) Galactic longitude coordinate of the center of gravity of the VHE emission.

4.4.3 Source Characteristics

After the detection of a new VHE γ-ray source within the survey analysis, a detailed analysis of the source using the full analysis chain presented in Chapter 2.4 must be performed. The following source characteristics, summarized in Table 4.4, have been determined within such an individual analysis and most of them were already published by the H.E.S.S. collaboration:

Morphology

The latitude distribution of all sources within the survey region is shown in Figure 4.8(a). Most of the sources cluster closely to the Galactic plane ($b = 0°$), only HESS J1356-645 ($b = -2.5°$), RCW 86 ($b = -2.3°$) , HESS J1507-622 ($b = -3.5°$) and HESS J1708-442 ($b = -2.35°$) are located at slightly lower latitude. The mean of the latitude distribution is -0.41°with a rms of 0.65°. The longitude distribution is shown in Figure 4.8(b). The distribution does not seem uniform, however a statement about accumulation points seem premature.

From the 45 detected sources, only 6[1] are point-like; all others extend beyond the point-spread function of the H.E.S.S. instrument. Figure 4.10(b) shows the distribution of intrinsic sizes resulting from a Gaussian fit to the source morphology. The mean intrinsic size is 0.13° and the spread of the distribution is 0.09°.

[1]HESS J1303-638, HESS J1745-290, HESS J1747-281, HESS J1826-148, HESS J1833-105 and HESS J1846-029

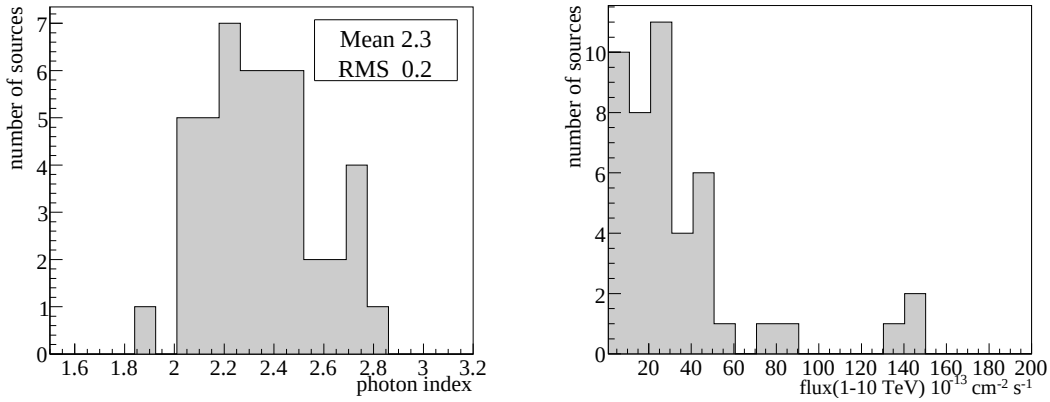

(a) (b)

Figure 4.9: Key parameters of the γ-ray spectra measured from all sources within the survey region. The energy spectra were extracted from a region individually selected to fully enclose the source. a) Index of a power law fit to the γ-ray energy spectrum of the source; the mean of the distribution is 2.3, its rms is 0.2; b) Flux between 1 and 10 TeV (in units of cm^{-2} s^{-1}).

Spectrum

The VHE γ-ray spectrum of all the sources can be fitted reasonably well with a power law. The resulting photon indices range from 1.9 to 2.8 with a mean of 2.3 and a rms of 0.2; see Figure 4.9(a). The range of fluxes between 1-10 TeV measured from these sources spans almost two orders of magnitude from the faintest sources: HESS 1713-381 with a flux of $(3.85\pm\ 0.77)\cdot 10^{-13}$ $\mathrm{cm}^{-2}\mathrm{s}^{-1}$ to the brightest RX J1713.7-3946 with a flux of $(1.48\pm\ 0.03)\cdot 10^{-11}$ $\mathrm{cm}^{-2}\mathrm{s}^{-1}$, see Figure 4.9(b). As shown in Figure 4.10(a), no correlation between source strength and photon index is observed, not even at the lowest fluxes. In Figure 4.10(c), however, a correlation between intrinsic source size and source flux is apparent. The observed correlation illustrates the decrease of sensitivity with increasing source size which results in a detection bias. The sensitivity decrease originates in the still limited field-of-view of the H.E.S.S. experiment and the standard background subtraction procedure which estimates the background level from within the same field-of-view.

Figure 4.10(d) shows the number of sources with fluxes above a certain value as a function of that value. The plot illustrates that an improvement in sensitivity from 50% of the Crab Nebula flux to 5% Crab resulted in a detection of 33 sources. The flattening below $\sim$ 3% of the flux of the Crab Nebula is not due to a thinning out of the source population, but due to the decreasing area observed with the necessary sensitivity.

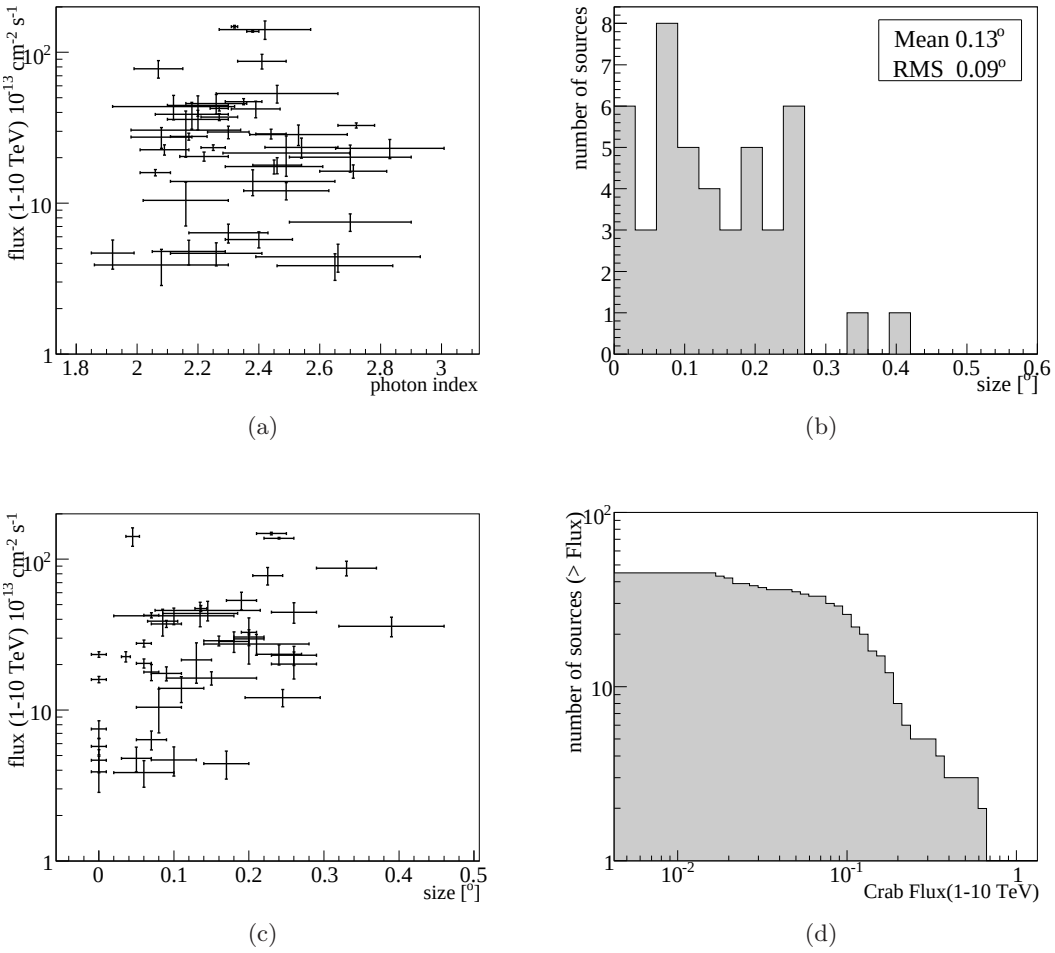

Figure 4.10: Key parameters of the γ-ray spectra and the source size measured from all sources within the survey region. The energy spectra were extracted from a region individually selected to fully enclose the source. a.) Photon index vs. flux between 1 and 10 TeV; no correlation is visible. b.) Intrinsic source size σ: For elongated sources, the arithmetic mean of the major and minor axis was used; for the shell type SNR RX J1713.7-3946, the intrinsic size of a Gaussian with the same rms was used. The distribution has a mean of 0.13° and a rms of 0.09°. c.) Intrinsic source size like in b vs. flux between 1 and 10 TeV; a hint for a detection bias is visible. d.) Number of sources with fluxes (1-10 TeV) above a certain value as a function of that value (in units of the flux of the Crab Nebula in the same energy range).

Table 4.4: Key parameters of all VHE γ-ray sources detected in the H.E.S.S. Galactic plane survey region. The best fit positions assuming a Gaussian brightness profile are given in degrees of Galactic Longitude, l, and Latitude, b. The width of the underlying Gaussian σ and σ' and its orientation counterclockwise relative to the Galactic Latitude axis are given in degrees. The photon index Γ of a power law fit to the source spectrum is given together with the inferred flux F between 1-10 TeV (in units of 10^{-14} cm^{-2} s^{-1}). T denotes the acceptance corrected exposure at the source position in hours. S denotes the peak significance of the source having accounted for $\sim$1.5 million trials. The number of stars denotes the on-source correlation radius with which the significance was calculated: † 0.1° , ‡ 0.22° and $^{\wr}$ 0.4°. Only the largest peak significance is given. In case a well known astronomical object is identified as a likely counterpart its name is stated. The last column gives the reference to the publication from which the morphological and spectral information stated in this table was taken. The errors on the last relevant digits are given in brackets.

Name	Source Position		Extension			Γ	F(1-10 TeV)	T	S	Counterpart
	l[°]	b[°]	σ°	σ'°	w [°]		[$\cdot 10^{-14}$cm^{-2}s^{-1}]	[h]	[σ]	
HESS J1023-575	284.19(3)	-0.38(3)	0.18(2)			2.53(16)	285(44)	18.7	8.0‡	Westerlund 2
HESS J1303-638	304.180(5)	-0.980(5)	0			2.7(2)	75(10)	105.7	14.9†	PSR B1259
HESS J1303-631	304.230(9)	-0.3(3)	0.16(2)			2.44(5)	288(21)	104.9	48.1$^{\wr}$	
HESS J1356-645	309.79(3)	-2.48(3)	0.20(2)			2.2(2)	211(76)	10.6	9.7$^{\wr}$	PSR J1357-6429
HESS J1418-609	313.24(1)	0.15(1)	0.06(1)			2.22(8)	204(14)	25.1	23.5$^{\wr}$	Rabbit
HESS J1420-607	313.550(9)	0.260(9)	0.06(1)			2.17(6)	277(14)	26.0	24.8‡	Kookaburra
HESS J1427-608	314.40(5)	-0.14(5)	0.04(2)	0.08(3)	11(17)	2.16(14)	104(34)	34.3	7.4‡	
HESS J1442-623	315.40(2)	-2.30(2)	0.41(3)[1]			2.54(12)	235(36)	44.9	13.5$^{\wr}$	RCW 86
HESS J1507-622	317.96(3)	-3.49(3)	0.13(2)			2.49(21)	215(64)	18.6	8.4‡	
HESS J1514-591	320.330(3)	-1.19	0.11(1)	0.040(8)	-18(13)	2.27(3)	425(17)	46.3	48.4‡	MSH 15-5 2
HESS J1614-518	331.52(3)	-0.58(3)	0.23(2)	0.15(2)	49(10)	2.46(2)	532(71)	13.8	22.8$^{\wr}$	
HESS J1616-508	332.39(2)	-0.13(1)	0.136(8)			2.35(6)	471(22)	14.6	26.5$^{\wr}$	
HESS J1626-491	334.77(5)	0.04(5)	0.07(2)	0.10(5)	-40(40)	2.18(12)	388(78)	14.6	5.0‡	
HESS J1632-478	336.38(3)	0.19(3)	0.21(5)	0.06(4)	21(13)	2.12(20)	437(81)	15.4	17.8$^{\wr}$	
HESS J1634-472	337.11(5)	0.21(4)	0.11(3)			2.38(27)	139(27)	17.2	15.4$^{\wr}$	
HESS J1640-465	338.310(7)	-0.020(7)	0.045(9)			2.42(15)	1416(198)	20.6	20.6†	
HESS J1708-442	343.12(5)	-2.35(5)	0.26(3)			2.20(10)	445(69)	18.4	8.4$^{\wr}$	
HESS J1702-420	344.30(5)	-0.18(5)	0.30(2)	0.15(1)	30(07)	2.07(8)	778(104)	24.7	19.2$^{\wr}$	
HESS J1708-410	345.68(5)	-0.46(5)	0.06(1)	0.08(1)	-57(23)	2.46(8)	179(21)	57.7	10.5†	

[1] Here the radius of a 2-dimensional shell is stated

Table 4.5: Continuation of Table 4.4

Name	Source Position		Extension			Γ	F(1-10 TeV)	T	S	Counterpart
	l[°]	b[°]	σ°	σ'°	w [°]		[$\cdot 10^{-14}$cm^{-2}s^{-1}]	[h]	[σ]	
HESS J1713-397	347.33	-0.472	$\sim$0.4[1]			2.32(1)	1479(30)	81.2	70.3$^{\wr}$	RX J1713.7-3946
HESS J1714-385	348.38(2)	0.107(2)	0.07(2)			2.30(13)	64(09)	68.5	10.9$^{\wr}$	CTB 37A
HESS J1713-381	348.64(3)	0.39(3)	0.06(4)			2.65(19)	39(08)	60.1	8.3$^{\wr}$	CTB 37B
HESS J1718-385	348.83(3)	-0.49(3)	0.15(3)	0.07(2)	$\sim$ -2	1.92(7)	47(10)	61.7	8.0‡	PSR J1718-3825
HESS J1731-347	353.56(5)	-0.622(5)	0.18(7)	0.11(3)	-122(21)	2.26(10)	458(67)	31.6	11.3‡	
HESS J1745-303	358.71(4)	-0.64(5)	0.21(6)	0.09(4)	54(07)	2.71(11)	163(16)	106.7	16.9$^{\wr}$	
HESS J1745-290	359.940(3)	-0.040(3)	0			2.25(4)	234(10)	140.5	68.8†	Sgr A
HESS J1747-281	0.870(5)	0.070(5)	0			2.40(11)	58(07)	127.8	24.5$^{\wr}$	G 09+0.1
HESS J1800-240	5.96(2)	-0.38(2)	0.32(5)	0.17(3)	-30	2.49(14)	121(15)	42.0	10.0$^{\wr}$	W 28
HESS J1801-233	6.66(3)	-0.26(3)	0.17(3)			2.66(27)	44(09)	43.0	5.7$^{\wr}$	W 28
HESS J1804-216	8.40(2)	-0.03(2)	0.20(1)			2.72(06)	328(12)	33.2	29.4$^{\wr}$	
HESS J1809-193	11.18(3)	-0.08(3)	0.53(7)	0.25(4)	$\sim$ 21	2.20(10)	359(53)	35.3	16.3$^{\wr}$	PSR J1809-1917
HESS J1813-178	12.810(5)	-0.030(5)	0.036(6)			2.09(8)	226(17)	31.9	25.6†	
HESS J1826-148	16.870(3)	-1.280(3)	0			2.06(5)	159(08)	83.0	42.2†	LS 5039
HESS J1825-137	17.71(1)	-0.69(1)	0.24(2)			2.38(2)	1375(17)	78.5	78.5$^{\wr}$	PSR J1826-1334
HESS J1833-105	21.51(2)	-0.87(2)	0			2.08(22)	39(10)	26.2	4.7†	G21.5-0.9
HESS J1834-087	23.24(2)	-0.32(2)	0.09(2)			2.45(16)	175(19)	29.2	16.4$^{\wr}$	
HESS J1837-069	25.17(1)	-0.11(2)	0.12(2)	0.05(2)	149(10)	2.27(6)	373(20)	38.0	39.6$^{\wr}$	
HESS J1841-055	26.79(5)	-0.19(5)	0.41(4)	0.25(2)	13(6)	2.41(8)	872(98)	40.0	25.3$^{\wr}$	
HESS J1843-033	29.08(2)	0.15(2)	0.20(2)			2.30(7)	296(28)	38.6	16.1$^{\wr}$	
HESS J1846-029	29.70(1)	-0.24(1)	0			2.26(15)	47(08)	38.8	8.2†	Kes 75
HESS J1848-018	30.96(4)	-0.14(4)	0.26(3)			2.83(18)	231(34)	38.9	8.8$^{\wr}$	
HESS J1858+020	35.57(5)	-0.58(5)	0.08(2)	0.02(4)	-24(17)	2.17(12)	48(09)	28.3	8.6$^{\wr}$	
HESS J1857+026	35.97(5)	-0.05(5)	0.11(8)	0.08(3)	-30(49)	2.39(8)	421(53)	24.9	15.5$^{\wr}$	
HESS J1908+062	40.45(6)	-0.80(5)	0.21(7)			2.08(10)	275(43)	26.6	9.1$^{\wr}$	MGRO 1908+06
HESS J1912+101	44.39(5)	-0.07(5)	0.26(3)			2.70(20)	202 (41)	22.4	6.8$^{\wr}$	PSR J1913+1011

[1] Here the radius of a 2-dimensional shell is stated

4.5 New Galactic VHE γ-ray Sources

This section contains a brief description of the new VHE γ-ray sources discovered during the H.E.S.S. Galactic plane survey in the years 2006/2007. A description of the sources discovered before this date can be found either in Aharonian et al. (H.E.S.S. collaboration) (2006h) or in the publication summarized in Table A.1. Many of the sources presented have been published already elsewhere, the corresponding references are also stated in Table A.1. The sources are grouped according to their most likely associations. It should be noted, however, that in most cases alternative interpretations of the VHE γ-ray emissions are also possible. Three new sources (HESS J1912+101, RCW 86 and HESS J1708−443) are ommited in this section, they have been analyzed in depth in the context of this thesis and will be presented in more detail in Chapter 5.

4.5.1 Pulsar Wind Nebulae and Plerions

HESS J1356-645

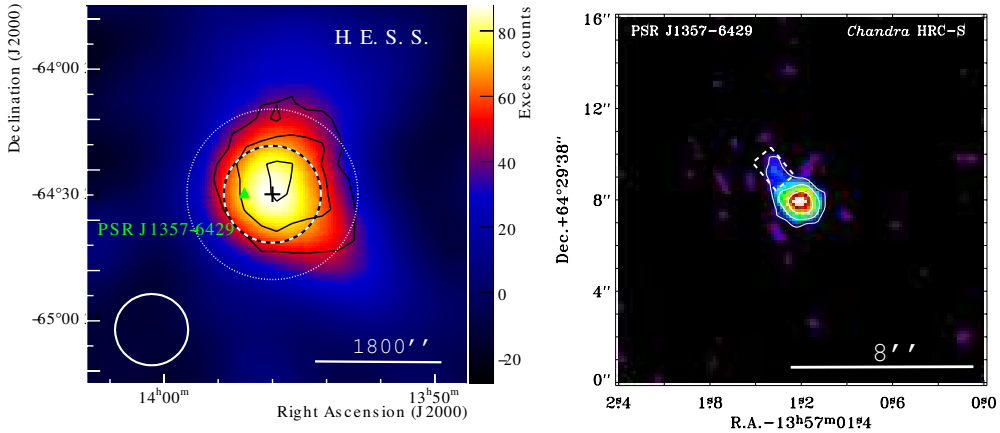

(a) (b)

Figure 4.11: a) Image of the VHE γ-ray excess of HESS J1356-645, smoothed with a Gaussian brightness profile of σ=0.13° along each axis. Significance contours calculated for an integration radius of $\theta_{\rm cor}$=0.22° are shown in black at 5,7 and 9 σ.The black cross indicates the best fit position of the source centroid together with its statistical errors. The intrinsic source rms is shown by the dashed circle. The position of the pulsar PSR J1357-6429 is marked with a green triangle. The Figure was taken from Aharonian et al. (H.E.S.S. collaboration) (2008e) b) Chandra HRC-S 16"×16" image of PSR J1357-6429 smoothed with 0."4 FWHM Gaussian. The image shows the pulsar surrounded by an extended structure elongated in the east-north direction (indicated by a white dashed box). White contours indicate the intensity values of 0.17, 0.55 and 1.74 counts arcsec^{-2} ks^{-1}. The Figure was taken from Zavlin (2007).

HESS J1356-645 was discovered in the vicinity of the energetic pulsar PSR J1357-6429. The emission region is extended to 0.2°and the integral flux between 1 and 10 TeV is ∼11% of the Crab Nebula flux in the same energy range. The differential energy spectrum

is well described by a power law with photon index Γ=2.2±0.2$_{\rm stat}$ ± 0.2$_{\rm sys}$. The most likely association of the VHE emission is with the PWN of the close by energetic pulsar. PSR J1357-6429 is a middle-aged Vela-like pulsar with a characteristic age of $\tau_{\rm c} = 7.3\,$kyr, its spin-down luminosity is as high as $\dot{E} = 3.1 \cdot 10^{36}\,$erg s^{-1} and its rotational period is 166 ms. It was discovered during the Parkes multibeam survey (Camilo et al., 2004). The distance estimate obtained from dispersion measurements is ∼2.5 kpc. The pulsar has been intensively studied at X-ray energies: Esposito et al. (2007) reported a 3σ marginal evidence of diffuse X-ray emission surrounding the pulsar using the XMM-Newton instrument, while Zavlin (2007) reported a faint tail-like emission to be visible in Chandra observations, see Figure 4.11(b). The centroid of the VHE emission is offset from the pulsar position by $\sim 5\frac{\rm d}{2.5{\rm kpc}}$ pc in the direction opposite to the faint X-ray tail (d is the assumed distance to the pulsar). The H.E.S.S. source is positionally coincident with the extended radio emission G309.8-2.6. Even though G309.8-2.6 was originally cataloged as a supernova remnant candidate, a rather flat radio spectrum (Aharonian et al. (H.E.S.S. collaboration), 2008e) suggests a different interpretation as the relic radio nebula of PSR J1357-6429, a conclusion which supports the association of the H.E.S.S. source with the PWN of PSR J1357-6429. At the pulsar distance, the projected size of the VHE emission is ∼9pc. The implied effective conversion efficiency from rotational energy to VHE γ-ray with energies between 1 and 10 TeV is 0.2%.

HESS J1718-385

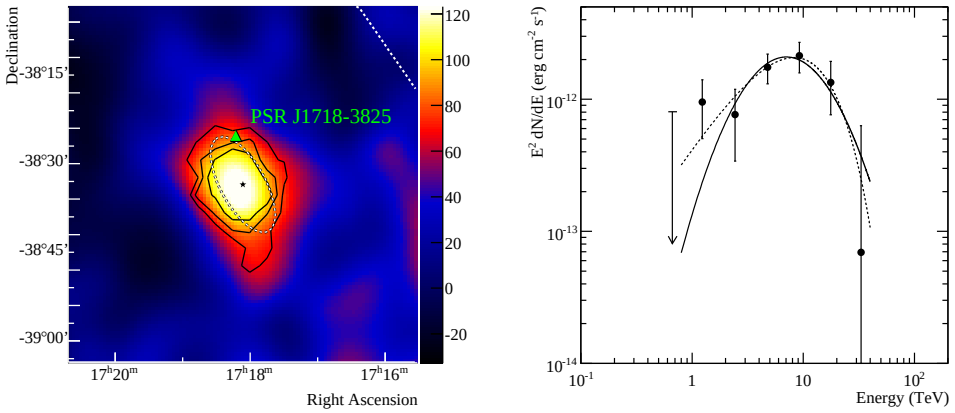

(a) (b)

Figure 4.12: a) VHE γ-ray excess smoothed with a Gaussian profile of width 0.06°. The black contours are 4, 5, 6 σ significance contours obtained using a 0.11° correlation radius. Position of the pulsar is marked with a green triangle. The best fit position of HESS J1718-385 is marked with a black star and the fit ellipse with a dashed line. b.) Spectral energy distribution of HESS J1718-385. The fit with a curved power law is shown by a solid line. The dashed line indicates the fit of an exponentially cut-off power law. Both figures were taken from Aharonian et al. (H.E.S.S. collaboration) (2007b).

This source is located 1.6° north-east of the well known shell-type SNR RX J1713.7-3946. It is extended beyond the PSF of the instrument, see Figure 4.12(a). The intrinsic widths of a two-dimensional Gaussian profile fitted to the VHE γ-ray signal are 0.15°±0.03° for the major axis and 0.07°±0.02° for the minor axis (with the effect of the PSF removed, Aharonian et al. (H.E.S.S. collaboration), 2007b). The energy spectrum is well described by a curved profile exhibiting a peak at ∼7 TeV, see solid line in Figure 4.12(b). Such a peak in the VHE spectrum has to date only be resolved for one other source, VelaX Aharonian et al. (H.E.S.S. collaboration) (2006f). The integrated flux between 1-10 TeV is about 2% of the flux of the Crab nebula in the same energy range. The centroid of the VHE emission is located ∼0.14° south of the energetic pulsar PSR J1718-3825. The pulsar appears Vela-like with comparable age (90 kyr) and spin-period (75ms) (Manchester et al., 2005; Morris et al., 2002). The distance to the pulsar is estimated to 4.2 kpc. Its spin-down luminosity is $1.3{\cdot}10^{36}$ erg/s. So far, no PWN has been detected at radio or X-ray energies. Nevertheless assuming an association with a PWN of PSR J1718-3825, the projected size of the VHE emission region is 11 pc. The apparent conversion efficiency from rotational energy to 1-10 TeV γ-rays is ϵ_γ=0.5%.

HESS J1809-193

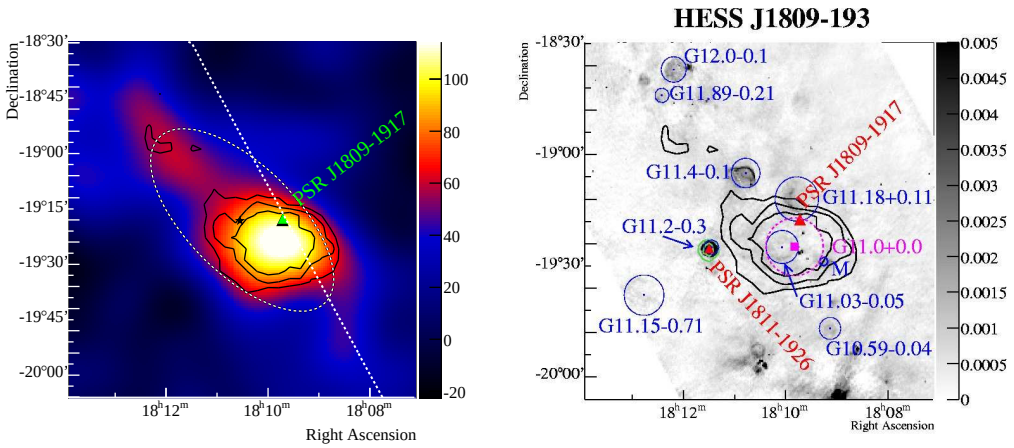

(a) (b)

Figure 4.13: a) VHE γ-ray excess smoothed with a Gaussian profile of width 0.11°. The black contours are 4, 5, 6 σ significance contours obtained using a 0.19° correlation radius. The position of the pulsar is marked with a green triangle. The best fit position of HESS J1809-193 is marked with a black star and the fit ellipse with a dashed line. b.) Radio image from the MAGPIS survey at 1.4 GHz (Helfand et al., 2006) in units of Jy/beam. The H.E.S.S. significance contours are depicted in black. The positions of close-by pulsars are marked with red triangles. Green contours depict the adaptively smoothed ROSAT hard-band data (Voges et al., 2001). Cataloged position and sizes of nearby SNRs (Green, 2004) and SNR candidates (Brogan et al., 2006) are shown in blue. The location of the ASCA source G11.0+0.0 is indicated in magenta. Both figures were taken from Aharonian et al. (H.E.S.S. collaboration) (2007b).

This source is very similar to the aforementioned HESS J1718-385. It is as well extended, see Figure 4.13(a); a fit with a two-dimensional Gaussian profile leads to an intrinsic length of the major/minor axis of $0.53^\circ \pm 0.07^\circ$ and $0.25^\circ \pm 0.03^\circ$(Aharonian et al. (H.E.S.S. collaboration), 2007b). The energy spectrum is well described by a power law with photon index $2.2 \pm 0.1_{\mathrm{stat}} \pm 0.2_{\mathrm{sys}}$. Its integral flux is about 14% of the Crab nebula flux in the same energy range. The source is detected $\sim 0.2^\circ$ east of the energetic pulsar PSR J1809-1917. The pulsar — similar to PSR J1718-3825 — resembles the characteristics of the Vela pulsar: a characteristic age of 51 kyr, a spin-period of 83 ms and a spin-down luminosity of $1.8 \cdot 10^{36}$ erg/s (Manchester et al., 2005; Morris et al., 2002). The distance to the pulsar is estimated to 3.7 kpc. The multiwavelength picture for HESS J1809-193 is more complex than in the case of HESS J1718-385: The diffuse ASCA source G11.0+0.0 (Bamba et al., 2003a; Brogan et al., 2004, 2006) which is coincident with the peak of the VHE emission (see Figure 4.13(a)), constitutes a possible X-ray counterpart. Bamba et al. (2003a) suggested a plerionic SNR as possible origin based on the X-ray spectrum of G11.0+0.0. Even though the estimated distance of G11+0.0 of 2.6 kc is compatible with the pulsar's distance, an association with PSR J1718-3825 is still uncertain given its spatial offset from the pulsar position. A PWN origin of HESS J1809-193 is supported as well by the finding of Sanwal et al. (2005), which detected a PWN around PSR J1809-1917 using the Chandra instrument. The PWN exhibits a cometary tail structure on a much smaller scale than the γ-ray emission. Assuming an association of HESS J1809-193 with the PWN of PSR J1718-3825, the project size of the former is 13 pc. The apparent conversion efficiency is ϵ_γ=1.2%.

HESS J1833-105

HESS J1833-105 is one of the very few Galactic sources where the extension cannot be resolved by the H.E.S.S. instrument; it therefore appears point-like in Figure 4.14(a). It's energy spectrum is again well described by a power law; the fitted photon index is $\Gamma = 2.1 \pm 0.2_{\mathrm{stat}} \pm 0.1_{\mathrm{sys}}$ (Djannati-Atai et al., 2007a). The integral flux is of the order of $\sim$2% of the Crab nebula flux. The H.E.S.S. source is positionally coincident with the composite SNR G21.5-0.9. Figure 4.14(b) depicts the plerion/SNR complex as seen with the Chandra instrument (Bocchino et al., 2005). The non-thermal X-ray PWN has a radius of 40". It shows a significant steepening of the X-ray spectrum with increasing distance to the pulsar. In addition a synchrotron X-ray halo is apparent reaching out to a radius of 140" from the pulsar. Bocchino et al. (2005) argue that the X-ray halo consists of 3 components: 1.) a diffuse component which has been subtracted to yield Figure 4.14(b). Dust scattering of the X-rays from the plerion has been suggested as possible origin. 2.) a bright limb which traces the particle acceleration in the forward shock front of the SNR and 3.) a bright spot ("North Spur") that might originate from a knot of ejecta in adiabatic expansion. The plerion is powered by the very energetic pulsar PSR J1833-1034 which was just recently discovered (Gupta et al., 2005; Camilo et al., 2006). It has a characteristic age of 4.9 kyr, a spin-down power of $3.3 \cdot 10^{37}$ erg/s. Its distance is estimated to 4.7 ± 0.4 kpc. The most likely association of the VHE emission is with the PWN of PSR J1833-1034. However, given the evidence of synchrotron emission in the SNR shell, a possible origin of the VHE γ-ray from the forward shock front of the SNR can not be excluded (Djannati-Atai et al., 2007a).

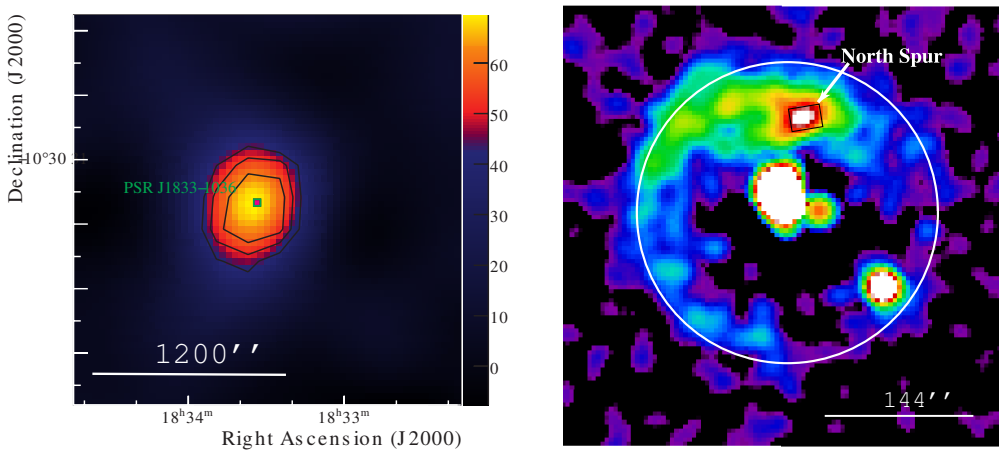

(a) (b)

Figure 4.14: a) VHE γ-ray excess smoothed with a Gaussian profile of width 0.07°. The black contours are 4, 5, 6 σ significance contours obtained using a 0.1° correlation radius. The position of the pulsar is marked with a green square. b.) Chandra ACIS-S image of G 21.5-0.9 in the 2-8 keV band. A model for the dust scattering component of the X-ray halo has been subtracted. The figure was taken from Bocchino et al. (2005). Note the different scale of the image compared to *a*: The white circle has a radius of 0.04°.

HESS J1846-029

This source is very similar to HESS J1833-105. It appears point-like and has a hard energy spectrum following a power law with photon index $\Gamma = 2.3 \pm 0.2_{\rm stat} \pm 0.1_{\rm sys}$ (Djannati-Atai et al., 2007a). The total flux between 1 and 10 TeV is again on the level of 2% of the Crab nebula flux. HESS J1846-029 is spatially coincident with the composite SNR Kes 75 (SNR G29.7-0.3). Similar to the case of G 21.5-0.9, the complex consists of a 3'.5-diameter radio shell surrounding a flat-spectrum radio PWN approximately 30" across (Becker & Helfand, 1984). The PWN is also visible in X-rays having a slightly smaller extension of 25"×20" (Helfand et al., 2003). Unlike G21.5-0.9, the X-ray PWN in Kes 75 does not show any evidence of cooling. At its center lies the high energy pulsar PSR J1846-258 (Gotthelf et al., 2000). With a characteristic age of 723 yrs, its is the youngest pulsar discovered so far. It's spin-down luminosity is $8.1{\cdot}10^{36}$ erg/s. The distance of Kes 75 is somewhat uncertain: Becker & Helfand (1984) used neutral hydrogen absorption measurements and estimated the distance to be close to 21 kpc. Leahy & Tian (2008), however, used HI and ^{13}CO measurements in combination to revise this estimate. They place Kes 75 at a distance of 5.1 to 7.5 kpc. Assuming a distance of 5.1 kpc for the pulsar and an association with HESS J1846-029 the conversion efficiency from rotational energy to 10-10 TeV γ-rays is ϵ_γ=0.07%.

HESS J1857+026

HESS J1857+026 is an extended and approximately radially symmetric source that exhibits a slight extension toward the north (see Figure 4.15(a)). The extension

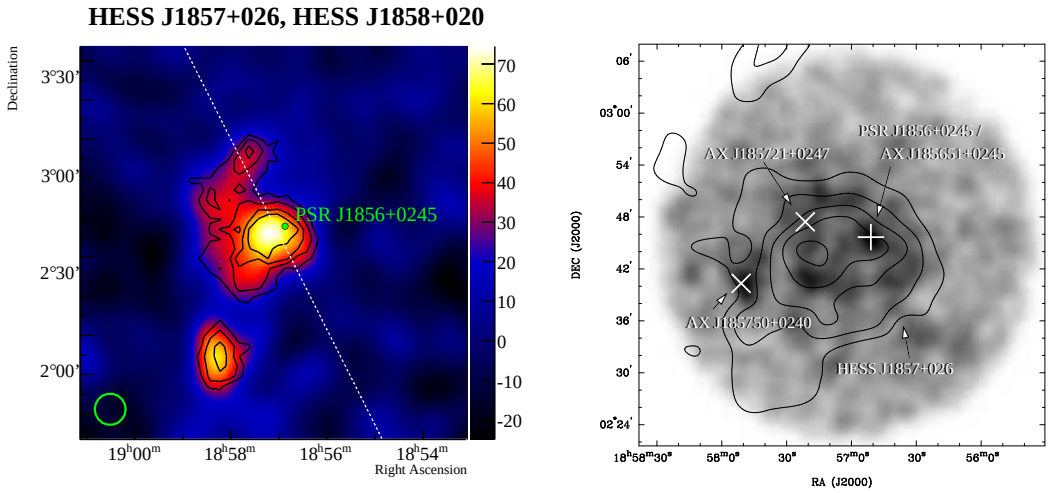

(a) (b)

Figure 4.15: a) VHE γ-ray excess smoothed with a Gaussian profile of width σ=0.8°. The black contours are 4, 5, 6 and 7 σ significance contours. The position of the pulsar is marked with a green dot. The figure was taken from Aharonian et al. (H.E.S.S. collaboration) (2008g). b) ASCA GIS image (2-10 keV) of the region containing HESS J1857+026. The image is smoothed with a 0.03° (FWHM) Gaussian. The contours show significance levels of 5-9 σ of the VHE γ-ray excess depicted in *a*. The position of the pulsar PSR J1856+0245 and the coincident X-ray source AX J185651+0245 are marked with a plus sign. The positions of two further ASCA sources detected by Sugizaki et al. (2001) are also shown.

might indicate a more extended morphology or the presence of a weaker nearby source (Aharonian et al. (H.E.S.S. collaboration), 2008g). Fitting the γ-ray excess with a 2D asymmetric Gaussian profile results in an intrinsic width of $\sigma_1 = 0.11 \pm 0.08°$ and $\sigma_1 = 0.08 \pm 0.03°$. The source has a differential spectral index of $2.4 \pm 0.1_{\mathrm{stat}} \pm 0.2_{\mathrm{sys}}$. Its flux between 1-10 TeV corresponds to $\sim$19% of the Crab nebula flux in the same energy range.

When the source was discovered in VHE γ-rays, no counterpart in other wavebands was known. Triggered by the initial detection, a Vela-like pulsar PSR J1856+0245 was found in the Arecibo PALFA survey data (Hessels et al., 2008). PSR J1856+0245 has a spin-period of 81 ms, a characteristic age of 21 kyr. Its distance is estimated from dispersion measurements to be close to $\sim$9 kpc. The spin-down luminosity is measured as $4.6{\cdot}10^{36}$erg/s. The inferred conversion efficiency from rotational energy to VHE γ-rays in the energy range between 1 and 10 TeV is $\epsilon_\gamma \approx 3\%$. The association of the VHE γ-ray source with the PWN of this energetic pulsar is supported by the detection of the faint X-ray source AX J185651+0245 at the pulsar's position (Sugizaki et al., 2001). The ASCA source might be the X-ray PWN of PSR J1856+0245 and thereby constitute the synchrotron counterpart of HESS J1857+026.

4.5.2 Supernova Remnants

HESS J1800-240 / HESS J1801-233

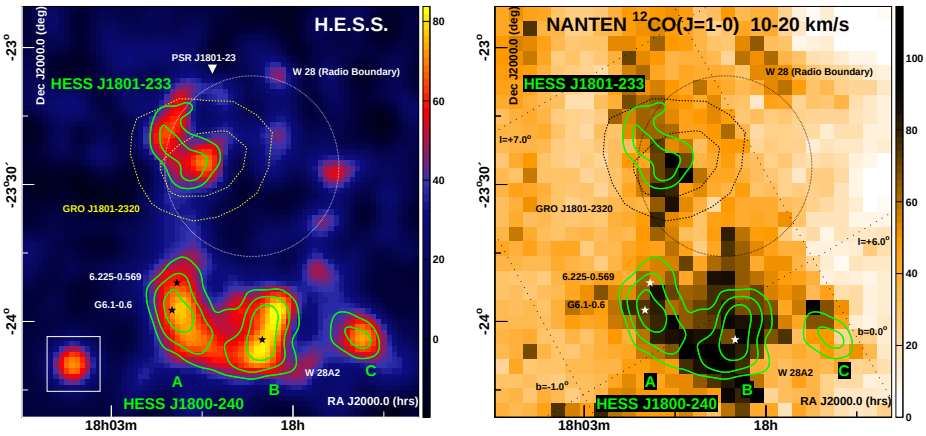

(a) (b)

Figure 4.16: a) Image of the VHE γ-ray excess in the W 28 field smoothed with a Gaussian of 0.07° standard deviation. The green contours are 4, 5 and 6 σ significance contours after integrating events within an oversampling radius of 0.1°. The white thin-dashed circle illustrates the approximate radio boundary of W 28 (Dubner et al., 2000; Brogan et al., 2006). Identified are two VHE emission regions: HESS J1801-233 to the northeast and the more complex region HESS J1800-240 (A, B and C) to the south of W 28. The 68% and 95% location contours of the EGRET source GRO J1801-2320 are illustrated by the yellow dashed lines. b) NANTEN ^{12}CO(J=1-0) image of the W 28 region (in units of K km s^{-1}) for the velocity range 10 to 20 km s^{-1}. The shown contours are identical to Figure *a*. Both figures were taken from Aharonian et al. (H.E.S.S. collaboration) (2008c).

Both VHE γ-ray sources, HESS J1800-240 and HESS J1801-233, have been discovered in the vicinity of the supernova remnant W 28 (Aharonian et al. (H.E.S.S. collaboration), 2008c). HESS J1801-233 is spatially coincident with the northeastern boundary of W 28, while the complex emission region HESS J1800-240 has been found ∼0.5° south of W 28 within the Galactic plane (see Figure 4.16(a)). HESS J1800-240 displays several peaks on the 2σ level (A, B and C), but a clear separation between them could not be established on the basis of the available statistics. The differential photon spectra of these VHE γ-ray sources are well described by a power law with photon indices $2.49 \pm 0.14_{\mathrm{stat}} \pm 0.20_{\mathrm{sys}}$ (HESS J1800-240) and $2.66 \pm 0.27_{\mathrm{stat}} \pm 0.20_{\mathrm{sys}}$ (HESS J1801-233). The spectral slopes measured from the different regions within HESS J1800-240 (A, B and C) are consistent within statistical errors. All emission regions are extended with an intrinsic width of ∼10', except for HESS J1800-240C, which appears point-like.

W 28 belongs to the class of old-age mixed-morphology supernova remnants. The position and extension of its 50'×45' shell are illustrated by a white circle in Figure 4.16(a). The distance estimates range between 1.8 and 3.3 kpc (see e.g. Goudis, 1976; Lozinskaya, 1981), the estimates of its age range from 35,000 to 150,000 yrs (e.g. Kaspi et al., 1993). It is thought to have entered into the radiative phase of its evolution (e.g. Lozinskaya, 1981).

HESS J1800-240 and HESS J1801-233 are positionally coincident with molecular clouds revealed in NANTEN ^{12}CO(J=1-0) data, see Figure 4.16(b). Aharonian et al. (H.E.S.S. collaboration) (2008c) argue for an association of the VHE γ-ray emission with the molecular clouds overtaken by the forward shock of W 28. At least in the northern region (HESS J1801-233) the scenario is supported by a high concentration of 1720 MHz OH masers (Frail et al., 1994a; Claussen et al., 1997, 1999) and the presence of shocked ^{12}CO(J=3-2) molecular gas (Arikawa et al., 1999). Furthermore, the shell-like radio emission detected from the SNR (Brogan et al., 2006) exhibits a peak along its north and northeastern boundaries (e.g. Dubner et al., 2000), which also hints at the ongoing interaction with molecular clouds. Such an association with molecular clouds could indicate a hadronic origin of the VHE γ-ray emission. Aharonian et al. (H.E.S.S. collaboration) (2008c) estimated the necessary cosmic-ray density enhancement to explain the VHE γ-ray emission to $\sim$10-30, depending on the distance to the source. It should be noted that particle acceleration might also occur in several cataloged SNRs and SNR candidates (like G5.71-0.08 which overlaps well with HESS J1800-240C, see Figure 4.16), the energetic ultra compact HII region W 28A2, and the HII regions M 8 and M 20 (Aharonian et al. (H.E.S.S. collaboration), 2008c).

HESS J1714-385

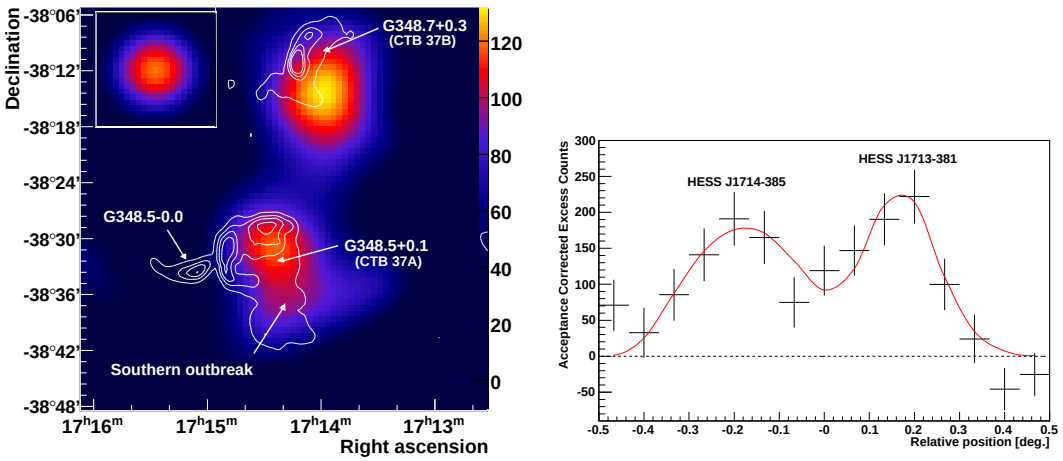

(a) (b)

Figure 4.17: a) Image of the VHE γ-ray excess smoothed with a Gaussian of 0.05° width. The white contours are radio (843 MHz) contours at 0.1, 0.5, 0.9 and 1.4 Jy/beam obtained in the Molonglo Galactic Plane survey (Green et al., 1999). b) Emission profile along the axis connecting HESS J1714-385 and HESS J1713-381. The best fit with two separated Gaussians is shown as a red curve. Both figures were taken from Aharonian et al. (H.E.S.S. collaboration) (2008b).

A further VHE γ-ray source possibly associated with a SNR overtaking a molecular cloud is HESS J1714-385, which was discovered in the supernova remnant complex

CTB 37. The source lies between the well-known SNR RX J1713.7-3946 and the VHE γ-ray source HESS J1713-381 (Aharonian et al. (H.E.S.S. collaboration), 2006h). Even though HESS J1714-385 and HESS J1713-381 lie close together, Figure 4.17(b) supports the separation into two sources. HESS J1714-385 is only slightly extended beyond the PSF of the H.E.S.S. instrument (intrinsic width of a Gaussian profile, σ=0.07±0.02). It's differential energy spectrum follows a power law with a photon index of 2.30 $\pm 0.13_{\mathrm{stat}} \pm 0.20_{\mathrm{sys}}$ (HESS Collaboration: F Aharonian, 2008). The integral flux above 1 TeV is of the order of 3% of the Crab nebula flux in the same energy range.

The complex CTB 37 consists of three SNRs: G348.5+0.1 (CTB 37A), G348.5-0.0 and G348.7+0.3 (CTB 37B). While HESS J1713-381 is positionally coincident with CTB 37B (see HESS Collaboration: F. Aharonian, 2008, for a detailed discussion), HESS J1714-385 coincides with CTB 37A. The position and extension of CTB 37A (9.5'×8') is consistent with the association of the VHE γ-ray emission with the whole shell. However, the VHE emission is also consistent with the molecular gas distribution around the SNR (HESS Collaboration: F Aharonian, 2008). Thus, an association with the molecular clouds overtaken by the SNR forward shock is also possible. The additional presence of 1720 MHz masers as in the case of the aforementioned SNR W 28 supports this scenario. HESS Collaboration: F Aharonian (2008) estimate the necessary conversion efficiency of mechanical energy into cosmic rays to 4%-30% to explain the observed VHE γ-ray emission.

An alternative scenario is the association with the extended non-thermal X-ray source CXOU J171419.8-383023 discovered in the north-western part of the remnant (HESS Collaboration: F Aharonian, 2008). A possible interpretation of the X-ray source is the PWN of an as of yet undiscovered pulsar. Judging from the X-ray luminosity, the pulsar's spin-down energy luminosity would be $1.9 \cdot 10^{37}$ erg/s. Since the necessary conversion efficiency is merely 0.1%, such a pulsar would be energetic enough to power the H.E.S.S. source.

HESS J1731-347

This source is another example where the discovery of a VHE γ-ray source precedes the detection of a possible counterpart in other wavebands. HESS J1731-347 is detected at the $\sim 8\sigma$ level (see Figure 4.18(a)). It exhibits a significant tail extending westwards in RA, which might indicates the presence of more than one source. The differential energy spectrum is well described by a power law with photon index $2.3 \pm 0.1_{\mathrm{stat}} \pm 0.2_{\mathrm{sys}}$. The integral flux between 1 and 10 TeV corresponds to ∼20% in units of the Crab nebula flux in the same energy range.

After the publication of the source discovery in Aharonian et al. (H.E.S.S. collaboration) (2008g), Tian et al. (2008) discovered a new faint radio shell (G353.6-0.7) in 1420 MHz continuum data taken within the Southern Galactic Plane Survey (Haverkorn et al., 2006). The nearly-circular shell structure has an angular size of 0.5° and is positionaly coincident with the main part of HESS J1731-347 in the east (see Figure 4.18(b)). Furthermore, a diffuse X-ray enhancement coincident with the lower half of the shell was found in the ROSAT data taken during the all-sky survey in 1993. Tian et al. (2008) argue for an association of the HESS source with the radio shell and the diffuse X-ray emission. They account the morphological mismatch at X-ray energies to an increase of column density, and thereby absorption of X-rays, in the regions closer to the Galactic plane. Given the shell-like structure and the lack of thermal

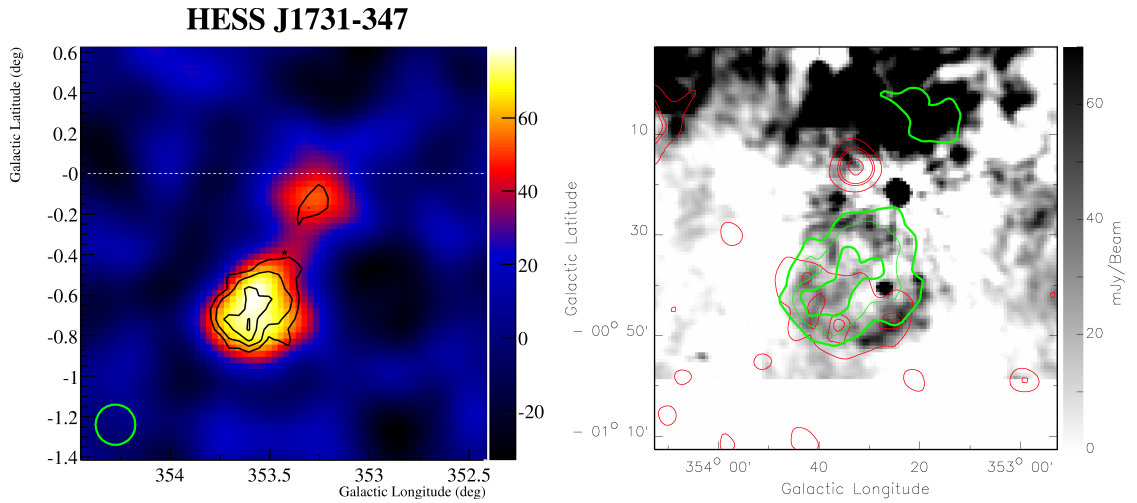

(a) (b)

Figure 4.18: a) Image of the VHE γ-ray excess of HESS J1731-347 smoothed with a Gaussian of σ=0.1°. The black contours illustrate the 4, 5 and 6 σ significance levels. The figure was taken from Aharonian et al. (H.E.S.S. collaboration) (2008g). b) 1420 MHz image of the SNR G353.6-0.7. X-ray contours of constant count rate as measured by the ROSAT instrument are shown in red. The contours correspond to 0.11, 0.19, 0.23 and 0.8 counts in units of 10^{-3}s^{-1}pixel^{-1}. The green contours correspond to the black contours shown in *a*. The figure was taken from Tian et al. (2008).

emission in 8 μm GLIMPSE data, Tian et al. (2008) favor an SNR as possible origin. The large angular size and the faint radio and X-ray emission suggest that the SNR is in its radiative phase and has an age of ∼27,000 yrs, which is rather old for a VHE γ-ray emitting SNR.

Given the radio shell as possible counterpart for the eastern part of HESS J1731-347 the initial assumption that the VHE emission might be due to more than one source is further strengthened.

4.5.3 Unidentified Sources

A significant number of the VHE γ-ray sources discovered in the H.E.S.S. Galactic plane survey could not be identified with any astrophysical objects so far, despite extensive counterpart searches using multi-wavelength data in the radio through X-ray wavebands (Aharonian et al. (H.E.S.S. collaboration), 2008g). These "dark" sources are depicted in Figure 4.19. Their morphological and spectral information are summarized in Table 4.4 and 4.5.

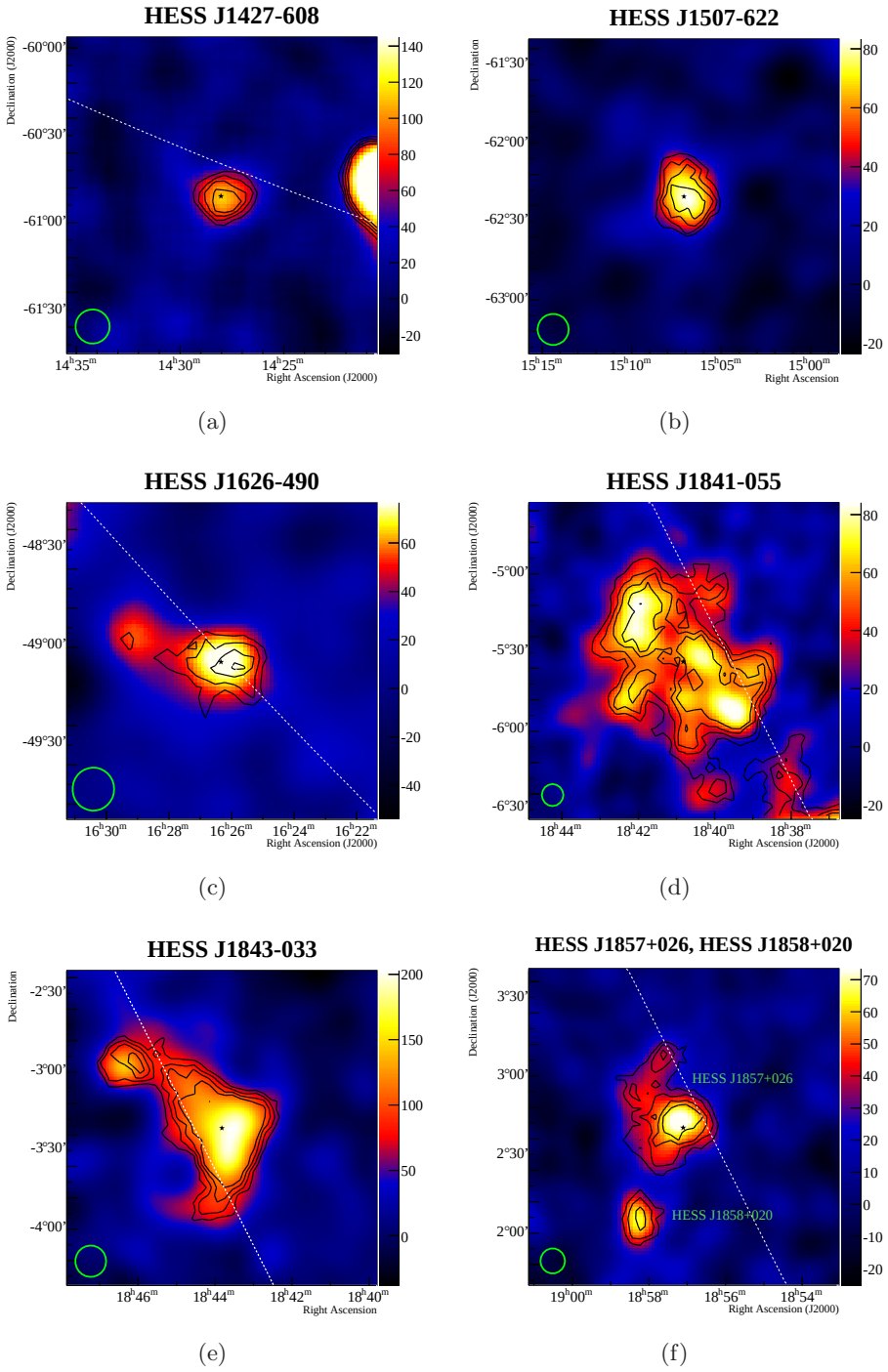

Figure 4.19: VHE γ-ray images of the Galactic H.E.S.S. sources without identified counterparts. The images are smoothed with a Gaussian profile to suppress statistical fluctuations. Overlaid on the image are the significance contours starting at 4σ in 1σ steps. The Figures, except for *b* and *e*, were taken from Aharonian et al. (H.E.S.S. collaboration) (2008g).

4.5.4 Miscellaneous

HESS J1908+063

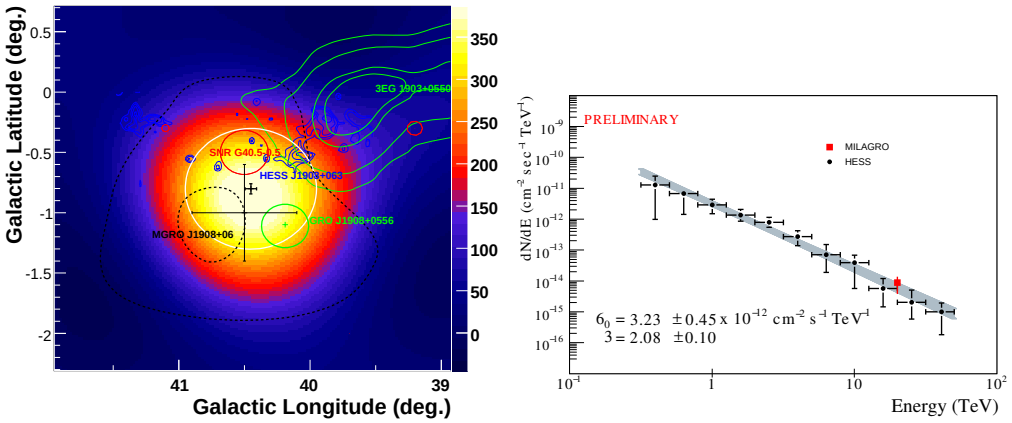

(a) (b)

Figure 4.20: a) VHE γ-ray image of the $1.5° \times 1.5°$ region around HESS J1908+063 smoothed with a Gaussian brightness profile ($\sigma = 0.5°$). The dotted black line illustrates the 5 and 8σ significance contours of MGRO J1908+06. The position of the EGRET GeV source GRO J1908+0556 is marked in green together with its 68% confidence region. The 99, 95, 68 and 50% confidence levels of 3EG J1903+0550 are also shown in green. The red circle marks the position and size of the SNR G040.5-00.5. b) Differential energy spectrum of HESS J1908-063. The 1σ-confidence region is shown in gray. The differential flux of MGRO J1908+06 at 20 TeV is shown in red. Both figures were taken from Djannati-Atai et al. (2007b).

HESS J1908+063 was discovered with a post-trials significance of 5.7σ (Djannati-Atai et al., 2007b). It is extended with an intrinsic width of $0.21° \pm 0.07°$. It exhibits a hard spectrum with a power law photon index of $2.08 \pm 0.1_{\mathrm{stat}} \pm 0.2_{\mathrm{sys}}$ and a flux above 1 TeV of 14% of the Crab nebula flux above that same energy.

HESS J1908+063 is positionally coincident with the Milagro source MGRO J1908-06 (see Figure 4.20(a)) the detection of which was announced after seven years of operation of the Milagro experiment with a pre-trials significance of 8.3σ (Abdo et al., 2007). The extension of the Milagro source remains unknown due to the rather poor angular resolution of the instrument. However, an upper limit of 2.6° on its diameter could be determined. Assuming a power law shape of the differential energy spectrum and a photon index of 2.3, the differential flux of MGRO J1908-06 at the median energy of 20 TeV is quoted as $(8.8 \pm 2.4_{\mathrm{stat}} \pm 2.6_{\mathrm{sys}}) \cdot 10^{-15} \mathrm{TeV}^{-1} \mathrm{cm}^{-1} \mathrm{s}^{-1}$. The positional match as well as the quite good agreement with the H.E.S.S. spectrum shown in Figure 4.20(b) strenghten the association of the two sources. Furthermore, the consistency in measured flux implies the absence of any other significant contribution to the Milagro flux.

A possible association to the nearby SNR G040.5-00.5 and the EGRET source 3EG J1903+0550 are unlikely given the relative positions and sizes, see Figure 4.20(a).

However, a connection to the EGRET source GRO J1908+0556, detected within an analysis of the highest energy photons (>1GeV) detectable by EGRET might be possible.

HESS J1023-575

HESS J1023-575 was discovered within the Galactic plane survey with a statistical significance of more than 9σ (pre-trials), the source is extended beyond a point-like object within the H.E.S.S. PSF with an intrinsic Gaussian width of $\sigma = 0.18^\circ \pm 0.02^\circ$; the differential energy spectrum follows a power law with a moderately hard spectrum of $\Gamma = 2.53 \pm 0.16_{\rm stat} \pm 0.20_{\rm sys}$, the total flux above 1 TeV corresponds to 13% of the Crab nebula flux above the same energy (Aharonian et al. (H.E.S.S. collaboration), 2007a).

The possible associations of this VHE γ-ray source, however, distinguish this new detection from other Galactic H.E.S.S. sources: HESS J1023-575 is positionally coincident with the well-known giant HII region RCW 49 and its ionizing stellar cluster Westerlund 2 (see Figure 4.21(a) and Rodgers et al., 1960). Westerlund 2 (Westerlund, 1961) contains an exceptional ensemble of hot and massive stars including a Wolf-Rayet star WR 20b and a very massive WR-star binary WR 20a (Shara et al., 1991; Rauw et al., 2004). With a mass of $2\times80\,M_\odot$ WR 20a is the most massive binary system in our Galaxy known to-date (Rauw et al., 2004; Bonanos et al., 2004). Radio continuum observations indicate wind-blown bubbles in the core of RCW 49, one surrounding Westerlund 2 (diameter $\sim$7.3') (Whiteoak & Uchida, 1997) and the other around WR 20b (diameter $\sim$4') (Shara et al., 1991). Furthermore, Figure 4.21(b) illustrates the extent of a blister on the western side of the bubble around Westerlund 2 (Whiteoak & Uchida, 1997), which hints at a rapid expansion into a low density medium outside the wind-blown bubble.

The detection of VHE γ-ray emission from this complex region indicates the existence of an extreme high-energy particle acceleration process. Multiple acceleration scenarios have been discussed in Aharonian et al. (H.E.S.S. collaboration) (2007a) (and references therein):

- Emission from the colliding wind zone of WR 20a. The supersonic stellar winds of both WR stars collide producing a reverse and a forward shock at the stagnation point. This scenario is disfavored as it fails to explain the extension of the VHE emission, since the WR 20a binary system, including its colliding wind zone, would appear as a point source.

- Particle acceleration by the collective stellar winds from the hot and massive stars in the stellar cluster Westerlund 2. This scenario predicts an extension of the γ-ray source similar to Westerlund 2. Comparing the extension of HESS J1023-575 and Westerlund 2, the cluster itself appears too compact to account for the observed VHE emission. Furthermore, the stellar cluster appears offset from the center-of-gravity of the γ-ray emission (see Figure 4.21(a)).

- Magneto-hydrodynamic particle acceleration in the wind-blown bubbles around WR 20b and Westerlund 2.

- Diffusive shock acceleration from supersonic winds breaking out into the interstellar medium. The particle acceleration would then occur at the boundaries of the blister shown in Figure 4.21(b). This scenario is supported by the good match in position and extend of the blister with HESS J1023-575.

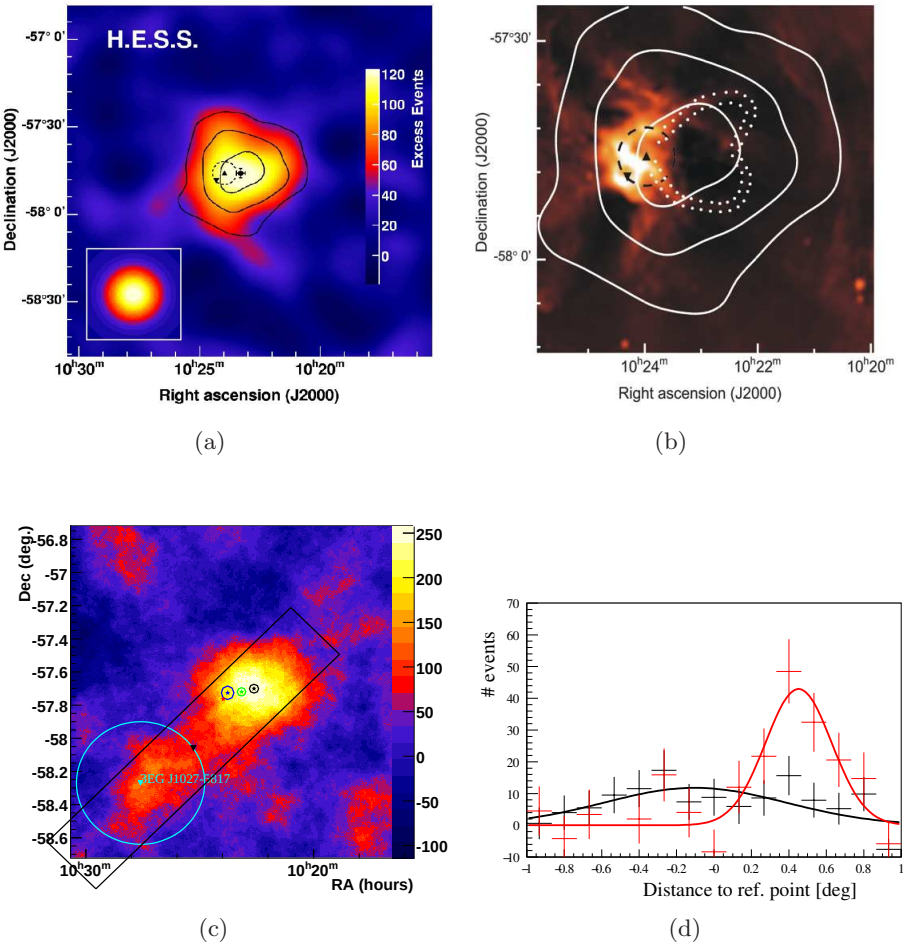

Figure 4.21: a) Correlated excess map of the region containing HESS J1023-575, oversampled with a radius of 0.12°. Additionally, the map has been smoothed with a 2-dimensional symmetric Gaussian brightness profile ($\sigma = 0.04°$). The black contours correspond to statistical significances of 5, 7 and 9 σ determined using an oversampling radius of 0.22°. The cross illustrates the best fit position of the VHE γ-ray excess. The position of the WR binary WR20a is depicted by an upright triangle, the extension of the Westerlund 2 is indicated by a dashed circle. The reverse triangle illustrates the location of WR 20b. b.) 843 MHz image from the Molonglo Observatory Synthesis Telescope. The contours and the symbols are identical to Figure *a*. The blister is indicated by white dots as shown in Whiteoak & Uchida (1997). Both figures (*a, b*) are taken from Aharonian et al. (H.E.S.S. collaboration) (2007a). c.) Correlated excess map (correlation radius 0.22°) for energies above 1 TeV. The black box illustrates the region in which the slice shown in *d* has been taken. The black marker illustrates the reference point used to center the slice shown in *d*. The green marker shows the best fit position for all energies, black for E>1 TeV and blue for E<1 TeV. The colored circles illustrate the corresponding fit errors. The red marker is at the position of WR 20a. The 95% error circle of the EGRET source 3EG J1027-5817 is also shown.

Even tough a clear identification with one of the aforementioned scenarios could not be established, the convincing association of HESS J1023-575 with the massive HII region RCW 49 and its ionizing stellar cluster Westerlund 2 represents the first case of a new type of VHE γ-ray source.

Early hints of energy-dependent morphology have been found in the detailed analysis of this source. Figure 4.21(c) shows the correlated VHE γ-ray excess above an energy of 1 TeV. A different morphology becomes apparent at these higher energies which exhibits a tail that is coincident with the EGRET source 3EG J1027-5817, see also Figure 4.21(d). The visual impression is supported by a shift of the best fit position for different energy ranges illustrated by the colored markers in Figure 4.21(b). This hint of energy dependent morphology still has to be varified and re-observations of this source have been proposed.

HESS J1848-018

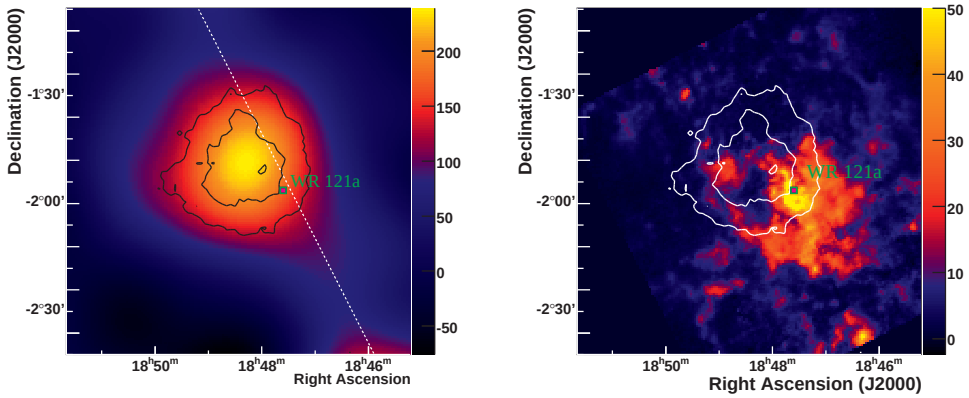

(a) (b)

Figure 4.22: a) VHE γ-ray image of HESS J1848-018 smoothed with a Gaussian brightness profile ($\sigma = 0.17°$). The dotted black line illustrates the 5, 7 and 9σ significance contours obtained with a correlation radius of 0.3°. The position of the Wolf-Rayet star WR 121a is marked in green. b) Image of the ^{13}CO emission measured within the Boston University Galactic Ring Survey (Jackson et al., 2006) integrated over the velocity range: v = 85 − 105 km/s. The contours are the same as in Figure *a*.

HESS J1848-018 might be a second example of an association with a star-forming region, similar to the case of Westerlund 2. It was discovered with a statistical significance of 9 standard deviations (pre-trials). The intrinsic rms is determined to $0.32 \pm 0.2_{\mathrm{stat}}$. The power law photon index of the differential energy spectrum is $2.8 \pm 0.2_{\mathrm{stat}} \pm 0.2_{\mathrm{sys}}$, the integrated flux above 1 TeV corresponds to 2% of the Crab nebula flux above the same energy.

HESS J1848-018 is partially coincident with the star-forming region W 43 located at a distance of 6.2±0.6 kpc (Russeil, 2003). W 43 contains the giant HII region G30.8-0.2, which hosts at least two O-type super-giants and a Wolf-Rayet star (WR 121a) in a dense and young stellar cluster at its center (Blum et al., 1999; van der Hucht, 2001).

Furthermore, W 43 also contains a $10^6 M_\odot$ giant molecular cloud, visible in the $^{13}CO(J = 1 - 0)$ Boston University Galactic Ring Survey (Jackson et al., 2006, see Figure 4.22(b)).

Given the morphological mismatch visible in Figure 4.22, the association of HESS J1848-018 with the star-forming region has to be considered less likely than in the case of HESS J1023-575.

Chapter 5

Individual Source Analysis

Forty-five VHE γ-ray sources were discovered within the H.E.S.S. Galactic plane survey region. With the increased number of sources it is now possible to associate astronomical objects with VHE γ-ray sources on a statistical basis, which was nicely illustrated for pulsar wind nebulae by Carrigan et al. (2007). But these studies make statements only on populations of sources. To identify an individual VHE γ-ray source as a certain type of accelerator, extensive morphological and spectral studies of the source are necessary. Only in comparison with data taken in other energy bands, can a clear identification of the source type be established. However, in many cases no clear connection between the VHE γ-ray emission and any astronomical object known in its vicinity can be made. Further observations in other wavebands, such as radio and X-rays, are then triggered by the VHE γ-ray detection, and if an association is established, the source's characteristics observed at very-high energies add valuable information about the enviromental conditions and underlying processes at work in these particle accelerators.

The majority of the VHE γ-ray sources that have been identified with some confidence are related to supernova remnant shells (e.g. RX J1713.7-3946 Aharonian et al. (H.E.S.S. collaboration), 2004b, 2006b, 2007d) or pulsar wind nebulae (e.g. HESS J1825-137 Aharonian et al. (H.E.S.S. collaboration), 2005b, 2006e). This chapter is devoted to the detailed analysis of three objects selected from the large number of VHE γ-ray sources detected in the H.E.S.S. Galactic plan survey presented in the previous chapter. The sources were chosen as a representative sample of the typical VHE γ-ray emitters, containing a plausible PWN association (HESS J1912+101), a clearly identified supernova remnant (RCW 86) and a VHE γ-ray source for which a clear identification proves to be rather difficult (HESS J1708-443).

Detailed morphological and spectral analysies are performed for all of the three sources, as well as extensive multi-wavelength studies to evaluate all possible associations, and to combine the available information to an increasingly complete picture of the conditions prevailing in these objects.

5.1 HESS J1912+101

In the extension of the H.E.S.S. Galactic plane scan towards lower longitudes, a new extended VHE γ-ray source was discovered in the vicinity of the energetic pulsar PSR J1913+1011. In this chapter the morphological and spectral analysis of the new VHE γ-ray source HESS J1912+101 is presented. Its possible association with a putative pulsar wind nebula of PSR J1913+1011 is discussed. Possible connections of the VHE emission with an as yet unconfirmed SNR candidate, proposed from low frequency radio observation and/or with molecular clouds found in ^{13}CO data, are also examined. This Chapter is adapted from a paper that the author has written on behalf of the H.E.S.S. collaboration. It was published in Aharonian et al. (H.E.S.S. collaboration) (2008d).

5.1.1 Observations and Results

The region of interest, roughly $2^\circ \times 2^\circ$ around the position of HESS J1912+101, includes the microquasar GRS 1915+105 (Rodriguez et al., 1995), the Integral source IGR J19140+0951 (Hannikainen et al., 2004), the high spin-down luminosity pulsar PSR J1913+1011 (Morris et al., 2002), as well as the SNR candidate 44.6+0.1 (Kassim, 1988). It was first targeted in 2004 as part of the observational programme on GRS 1915+105. In 2005, dedicated observations were taken on the supernova remnant W 49B (Harris & Roberts, 1960); some of the pointings also cover the field-of-view of interest. In 2006, the region was observed again, as part of the extended H.E.S.S. Galactic Plane Survey and with dedicated observations of IGR J19140+0951. PSR J1913+1011 was selected for dedicated observations as part of a systematic study of high spin-down luminosity pulsars, but was not observed due to the planned coverage of this region in other programmes. The combined data set was investigated using the standard survey analysis (a radius of the on-source region of $\theta_{\rm cut}$=0.22°, a ring background region of radius 0.8° and *hard* cuts, which include a minimum requirement of 200 photo electrons per shower image, for γ-ray selection) as described in Section 2.4.

The analysis presented here considers only observations pointed within 3° of the original source candidate found within the Galactic plane survey analysis. The mean pointing offset is 1.1°. After quality selection to remove data affected by unstable weather conditions or hardware issues, the data set has an acceptance corrected live time (equivalent time spent at an offset of 0.5°) of 20.8 h at the centre of the emission. The zenith angles of the observations range from 33° to 54°, leading to a typical energy threshold of $\sim$800 GeV. Figure 5.1 shows the excess count map of the $1.6^\circ \times 1.6^\circ$ region around the source smoothed with a Gaussian profile of width 0.13° to reduce statistical fluctuations. A clear excess of VHE γ-rays is observed with a peak statistical significance of 7.5 σ for an integration radius of $\theta_{\rm cut}$=0.22°. As the source was discovered as part of the H.E.S.S. Galactic Plane Survey, the statistical trials associated with this survey must be taken into account (see Section 4.3.3). A very conservative estimate of the number of trials which accounts for the large number of sky positions probed ($\sim 5\times10^5$) leads to a post-trials significance of 5.5 σ. Fitting the uncorrelated excess count map with a symmetric Gaussian profile convolved with the point spread function of the instrument leads to a best fit position of α_{2000}=$19^h12^m49^s$, δ_{2000}=+10°09′6″, with a 3′ statistical error in each coordinate, as indicated by the black cross in Fig. 5.1. HESS J1912+101 is clearly extended with an intrinsic Gaussian width of $\approx 0.26^\circ \pm 0.03^\circ_{\rm stat}$, with a fit probability for a Gaussian source

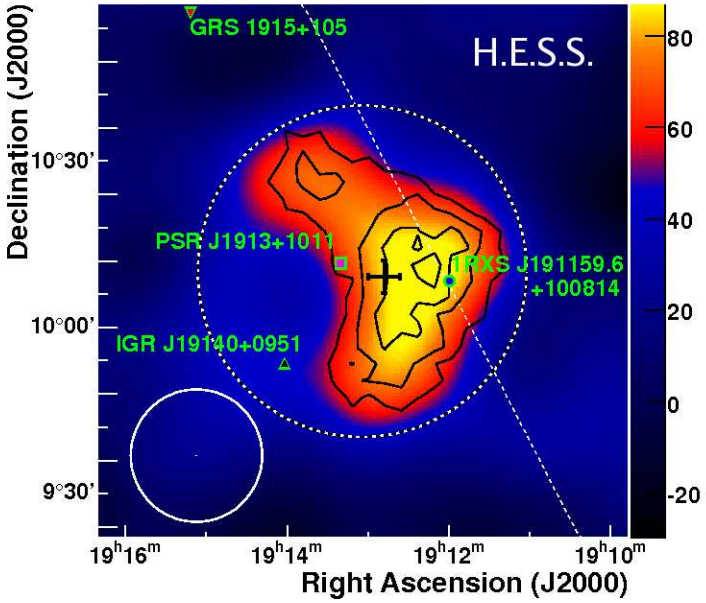

Figure 5.1: Image of the VHE γ-ray excess from HESS J1912+101, smoothed with a Gaussian profile of σ=0.13° along each axis. Significance contours calculated for an integration radius of $\theta_{\rm cor}$=0.22° are shown in black at 3.5, 4.5, 5.5 and 6.5 σ. The black cross indicates the best fit position of the source centroid together with its statistical errors. The dashed circle indicates the region from which the spectrum shown in Fig. 5.5 has been extracted. The positions of the pulsar PSR J1913+1011, the ROSAT source 1RXS J191159.6+100814, the INTEGRAL source IGR J19140+0951 and the microquasar GRS 1915+105 are marked. The Galactic plane is indicated by a white dotted line. The white solid circle illustrates the 68% containment radius of the Gaussian brightness profile used for smoothing convolved with the point spread function of the instrument.

profile of 9%. Ellipsoidal fits do not improve the fit probability. No further statements about the morphology are possible at the level of statistics available at the moment.

For the spectral analysis, only observations pointed within 2.0° of the centre of the source were used, to remove events with large uncertainties in reconstructed energy. The live time of the remaining dataset is 18.7 h. The spectrum was determined within a circular region of 0.5° radius (indicated by a dashed circle in Fig.5.1), which represents an $\sim$90% enclosure of the excess, chosen as a compromise between optimal signal to noise ratio and independence of source morphology. To minimise spectral uncertainties, the background was estimated from regions with equal offset from the centre of the field-of-view as described in Section 2.4. The dataset contains a large fraction of observations targeted at other possible sources within the field-of-view (e.g. GRS 1915+105) and was taken over a time period of three years. Furthermore, due to the source extension, the observations of HESS J1912+101 have rather uneven exposure across the region and coverage over time. Consideration of only nearby H.E.S.S. pointing positions, use of the reflected-region background model and the estimation of the time-dependent optical response of the system, help correct for these variations. However, these factors lead to somewhat increased systematic errors with respect to typical H.E.S.S. results. Within the large integration circle,

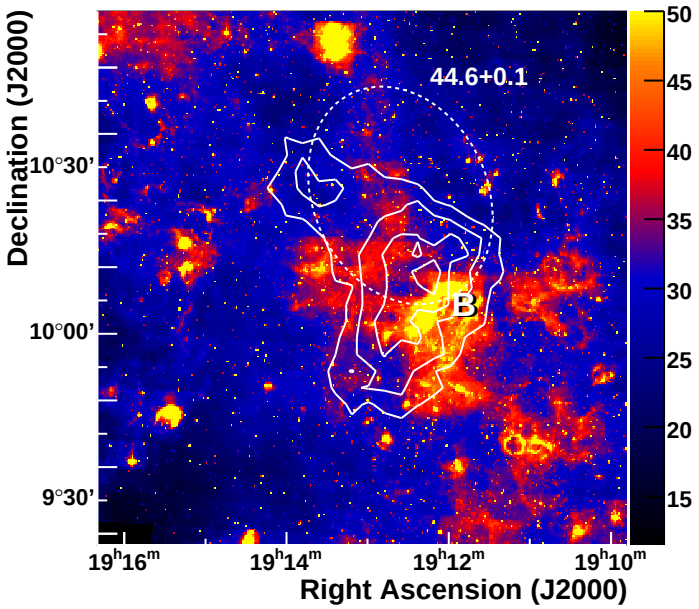

Figure 5.2: Image of the surface brightness (in units of MJy sr^{-1}) measured at $\sim$8.0 μm within the Galactic Legacy Infrared Mid-Plane Survey Extraordinaire (GLIMPSE) using the Spitzer telescope (Benjamin et al., 2003). The white contours indicate the significance of the VHE γ-ray excess. The region marked as "B" is a complex of molecular clouds and HII-regions. The white ellipse illustrates the position and extension of the SNR candidate 44.6+0.1 proposed in the Clark Lake 30.9 MHz Galactic plane survey (Kassim, 1988)

276 excess events were found, corresponding to a statistical significance of 7.5 σ (pre-trials) for the dataset used for spectral analysis. The spectrum shown in Fig. 5.5 can be described by a power law: $\mathrm{d}N/\mathrm{d}E = \Phi_0(E/1\mathrm{TeV})^{-\Gamma}$ with photon index $\Gamma = 2.7 \pm 0.2_{\mathrm{stat}} \pm 0.3_{\mathrm{sys}}$ and flux normalisation $\Phi_0 = (3.5 \pm 0.6_{\mathrm{stat}} \pm 1.0_{\mathrm{sys}}) \times 10^{-12}$ cm^{-2} s^{-1} TeV^{-1} . The fit has a $\chi^2/\mathrm{ndf} = 6.3/4$. The integral flux between 1 and 10 TeV is about 9% of the flux of the Crab Nebula in the same energy range (Aharonian et al. (H.E.S.S. collaboration), 2006g).

5.1.2 Possible Associations

The celestial region around HESS J1912+101 hosts several potential counterparts. While a superposition of two or more is also possible, each of the following objects could individually account for the observed γ-ray emission:

The most plausible counterpart candidate, both in positional and energetic connection to HESS J1912+101 is the pulsar **PSR J1913+1011** (Morris et al., 2002), which is slightly offset from the H.E.S.S. source's best fit position by $\sim$0.15°, spatially consistent at the $\sim 3\sigma$ level. It is a rather energetic pulsar with a spin-down luminosity of 2.9×10^{36} erg s^{-1}, a spin-down age of $\tau_c \approx 1.7 \times 10^5$ years, a spin period of 36 ms and a distance estimated from dispersion measurements of 4.48 kpc (Manchester et al., 2005). The pulsar is sufficiently energetic to power the H.E.S.S. source with an implied conversion efficiency from rotational energy to 1-10 TeV γ-rays of ϵ=0.5%, comparable to the efficiency

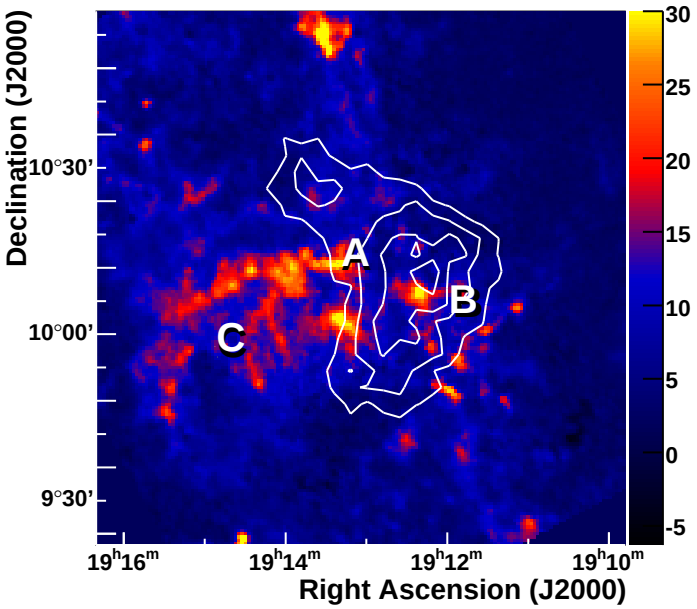

Figure 5.3: GRS ^{13}CO(J=1→0) intensity in units of K km s^{-1}. Intensities are integrated in the velocity range 50 - 70 km s^{-1}, corresponding to a distance of ∼ 5 kpc. The molecular cloud marked as 'A' is coincident with PSR J1913+1011. In region 'C' no significant VHE γ-ray excess was observed so far, even though it contains molecular clouds at a similar distance.

inferred for other VHE PWN candidates such as HESS J1718−385 and HESS J1809−193 (Aharonian et al. (H.E.S.S. collaboration), 2007b). Its distance would result in a projected size of HESS J1912+101 of ∼ 70 pc.

These characteristics suggest an association of the VHE emission with the pulsar's wind nebula, similar to other PWN associations such as Vela X (Aharonian et al. (H.E.S.S. collaboration), 2006f), HESS J1825−137 (Aharonian et al. (H.E.S.S. collaboration), 2006e) and MSH 15−52 (Aharonian et al. (H.E.S.S. collaboration), 2005c). Compared with these examples, HESS J1912+101 would be the oldest candidate for a VHE emitting PWN. In leptonic models of VHE γ-ray production, a PWN is expected to also emit non-thermal X-rays. Two Chandra observations within the region of interest are currently available. The first (Obs. Id 4590) was targeted on EXO 1912+097 (Lu et al., 1996), which is coincident with and possibly the same object as IGR J19140+0951 (Hannikainen et al., 2004). The overlap of this observation with HESS J1912+101 is marginal. The second (Obs. Id 3854) was targeted on the pulsar PSR J1913+1011 and covers a larger fraction of the H.E.S.S. source. No X-ray PWN was reported at the position of PSR J1913+1011 (see Gotthelf, 2004). Existing Chandra observations do not allow for a counterpart search on the same spatial scale as the H.E.S.S. source, and a detailed analysis of the Chandra data is beyond the scope of this paper. Despite considerably less sensitivity, the ASCA satellite with its larger field-of-view seems more suitable for counterpart studies on larger scales. Two ASCA observations coincide with HESS J1912+101. The first (Obs. Id 57005060) covers the whole H.E.S.S. source but suffers strongly from stray light contamination, the second

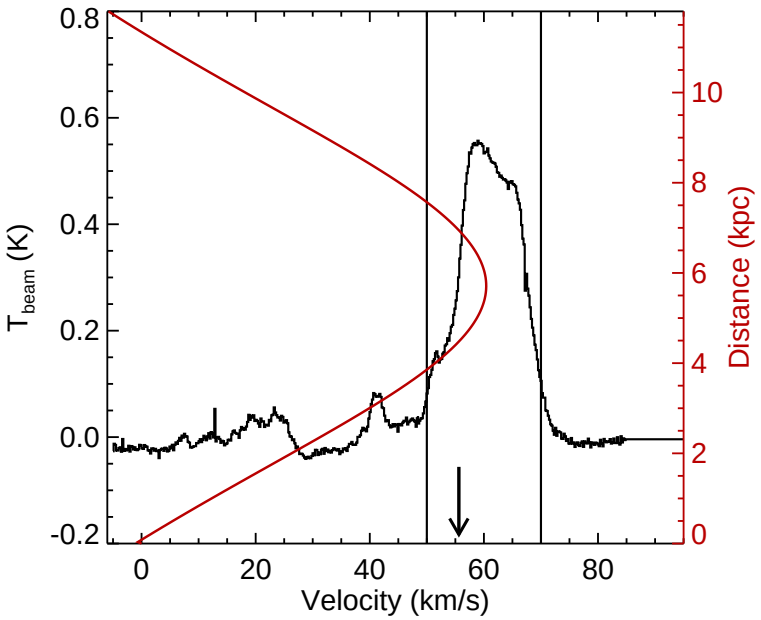

Figure 5.4: Velocity profile of ^{13}CO(J=1→0) intensity at 110.2 GHz from the Galactic Ring Survey (GRS, Jackson et al., 2006), integrated within the dashed circle shown in the Figure 5.1. The velocity resolution is 0.25 km s^{-1}. The distance/velocity correspondence from the Galactic rotation model from Fich et al. (1989) is also shown. The velocity corresponding to the nominal distance of PSR J1913+1011 (4.48 kpc) (Manchester & Taylor, 1977) is marked by an arrow together with the velocity range of the image shown in the Figure 5.3.

(Obs. Id 57005070) barely covers the peak of the VHE emission. Therefore no ASCA data has been analysed for this paper.

In the emerging picture of PWN associations the VHE emission peak is often found offset from the pulsar position (e.g. HESS J1825−137, MSH 15−5*2*, HESS J1718−385 and HESS J1809−193). These offsets can be explained in terms of the proper motion of the pulsar and/or the expansion of the SNR/PWN into an inhomogeneous medium (see e.g. Blondin et al., 2001, and Section 1.3.2). In the case of HESS J1912+101 the observed offset could be explained by proper motion assuming a velocity of ∼60 km s^{-1} (to travel the ∼10 pc from the centroid of the VHE emission to the current pulsar location in 1.7×10^5 years). The hypothesis that the PWN of PSR J1913+1011 (and the associated SNR) is expanding into an inhomogeneous medium seems quite plausible as the ^{13}CO(J=1→0) emission line measurements taken at 110.2 GHz indicate the existence of 'clumpy' molecular material (in particular the area "A" as indicated in Fig. 5.3) at the pulsar position and roughly at its distance. Such a scenario for an asymmetric nebula was also proposed for HESS J1825−137 (Aharonian et al. (H.E.S.S. collaboration), 2006e). HESS J1912+101 and HESS J1825−137 share several similarities: 1) similar offset of the VHE emission region from the pulsar position; 2) similar angular size (rms size of 0.24° for HESS J1825−137 and 0.26° for HESS J1912+101); 3.) similar distances (inferred from dispersion measurements of the corresponding pulsars to be ∼4 kpc). The intrinsic sizes are hence both

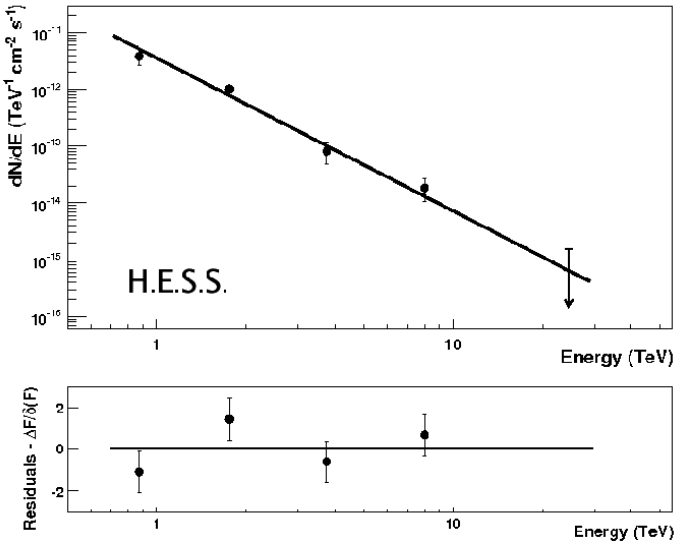

Figure 5.5: Differential energy spectrum of HESS J1912+1011, extracted from the circular region indicated in Fig.5.1. Events with energies between 0.55 and 55 TeV were used in the determination of the spectrum. They were binned with three bins per decade – the resulting number of bins is 6 – and then fitted with a power law (solid line). The two highest energy points of the spectrum were merged and are shown here as a 2σ upper limit.

$\sim 40\,\mathrm{pc}$. In a leptonic scenario, the cooling timescale, in combination with the propagation speed of the lowest energy (and hence longest-lived) electrons which upscattering soft photons to energies detectable by H.E.S.S., limit the extent of the emission region. As argued by Aharonian et al. (H.E.S.S. collaboration) (2006e), synchrotron cooling is likely to be the dominant energy-loss process for magnetic field strengths $\mathrm{B} > 3\,\mu\mathrm{G}$ and multi-TeV electrons. For scattering in the Thomson regime by cosmic microwave background radiation (CMBR) photons, the parent electron population responsible for the VHE γ-rays detected by H.E.S.S. have energies 10–100 TeV (see Equation 1.17). The magnetic field strength within the extended X-ray PWN of PSR B1823−13 suggested by Gaensler et al. (2003) is $\sim 10\,\mu\mathrm{G}$. Considering the different sizes of the X-ray and VHE γ-ray emission regions (5' versus 60') for PSR B1823−13, the magnetic field strength in the outer VHE nebula should be lower than in the more compact X-ray nebula (see de Jager & Djannati-Ataï, 2008). Here we assume similar magnetic field strengths for HESS J1825−137 and HESS J1912+101. The corresponding lifetime due to synchrotron losses of electrons upscattering CMBR photons to energies E_γ is given by

$$\tau_{\mathrm{synch}} \approx 3 \times 10^4 \left(\frac{\mathrm{B}}{5\mu\mathrm{G}}\right)^{-2} \left(\frac{\mathrm{E}_\gamma}{\mathrm{TeV}}\right)^{-1/2} \mathrm{years} \tag{5.1}$$

(combining Equation 1.14 and Equation 1.17). Even for a magnetic field strength of $5\,\mu\mathrm{G}$ – a value similar to the interstellar magnetic field – and 1 TeV γ-rays is the synchrotron cooling time scale for the upscattering electrons a factor ~ 6 lower than the age of PSR J1913+1011 ($\tau_c = 1.7 \times 10^5$ years) and still close to the age of PSR B1823−13

($\tau_c = 2.1 \times 10^4$ years). This provides a natural explanation for the similar sizes of HESS J1825−137 and HESS J1912+101 even though the spin-down ages of the corresponding pulsars are different by a factor of ~ 8. Assuming the transport process to be dominantly advective rather than diffusive, the necessary average flow speed needed to drive electrons from the position of the pulsar to the edge of the γ-ray nebula ($\mathrm{D^{trav}} \approx 40 \frac{\mathrm{d}}{4.5\mathrm{kpc}}\mathrm{pc}$) within the synchrotron loss time is

$$v = \frac{\mathrm{D^{trav}}}{\tau_{\mathrm{synch}}} \approx 1400 \left(\frac{\mathrm{d}}{4.5\mathrm{kpc}}\right)\left(\frac{\mathrm{B}}{5\mu\mathrm{G}}\right)^2\left(\frac{\mathrm{E}_\gamma}{\mathrm{TeV}}\right)^{1/2} \mathrm{kms}^{-1} \ . \tag{5.2}$$

This speed is fairly large, but may not be implausible if the associated SNR expanded at least in part into the low-density phase of the interstellar medium. Assuming an energy-independent advection speed, Equation 5.2 predicts an energy-dependent morphology for the nebula, as was observed for HESS J1825−137, where the photon index changes with distance by $\Delta\,\Gamma \approx 0.6$ (Aharonian et al. (H.E.S.S. collaboration), 2006e). With the available statistics it is not possible to extract position-resolved spectra for HESS J1912+101 to test this hypothesis also in this case. We also note that a possibly significant fraction of the observed VHE emission could also result from IC scattering of higher energy target photons, e.g. emission from the close-by molecular clouds and HII-regions as visible in Fig. 5.2. This component of the VHE emission would probe lower energy electrons with significantly higher cooling times. Its size would therefore be limited not by the cooling time but by the age of the system.

Whilst the spin-down powers of PSR B1823−13 and PSR J1913+1011 are very similar ($\sim 3{\times}10^{36}$ erg s^{-1}), HESS J1825−137 is a more luminous source than HESS J1912+101, resulting in fairly different apparent VHE conversion efficiencies of 3% for the former and 0.5% for the latter. The spectral indices of the VHE sources are, however, compatible within statistical uncertainties ($\Gamma = 2.38{\pm}0.02_{\mathrm{stat}}{\pm}0.15_{\mathrm{sys}}$ and $\Gamma = 2.7{\pm}0.2_{\mathrm{stat}}{\pm}0.3_{\mathrm{sys}}$). Assuming a continous injection of electrons with a power law $dN/dE \approx E^{-\alpha}$ where $\alpha = 2.0$ .. 2.2, α is increased to 3.0 ... 3.2 by radiative cooling, and a VHE γ-ray spectrum with a photon index of 2.0 to 2.1 is expected above a synchrotron break energy of ~ 30 GeV for HESS J1912+101 (see Section 1.1 and Section 1.2). In Aharonian et al. (H.E.S.S. collaboration) (2005b) different scenarios were discussed to explain the observed softer photon index, including the effect of Klein-Nishina corrections to the IC scattering cross-section and the superposition of IC spectra arising from electrons injected in the past. Both these arguments are equally applicable to HESS J1912+101.

Another candidate object for the observed emission is the shell of a hypothetical **supernova remnant** which would be rather old if associated with the birth of PSR J1913+1011 (spin-down age 1.7×10^5 years). In this scenario, the observed γ-ray emission could be explained as the result of the interaction of accelerated particles from the SNR with dense molecular clouds. A candidate for a supernova remnant assocation is 44.6+0.1, an yet unconfirmed SNR candidate proposed in the Clark Lake 30.9 MHz Galactic plane survey (Kassim, 1988) and further investigated by Gorham (1990). The estimated position and size of this object are illustrated by a white ellipse in Figure 5.2. 44.6+0.1 overlaps with the VHE emission region, but the overall match in morphology is rather poor. However, the resolution from the Clark Lake survey is insufficient for a firm conclusion about the morphology and only part of the remnant might be visible at 30.9 MHz. No SNR has been detected in X-rays. The only published keV X-ray sources in this region are the faint ROSAT sources 1RXS J191159.6+100814, 1RXS J191254.3+103807 and 1RXS J191114.8+102102

(Voges et al., 2000). Such a lack of X-ray emission could be explained using for example the model of Yamazaki et al. (2006), in which an age of the SNR of 1.7×10^5 years would imply a rather low X-ray to TeV energy flux ratio of ~ 0.01 (for the energy ranges 2-10 keV and 1-10 TeV). In this scenario the spatial distribution of the VHE emission should then trace the distribution of the molecular clouds which act as target material. Such clouds have been observed in the vicinity of PSR J1913+1011 (indicated as area "B" in Fig.5.2) in infrared at $\sim 8\,\mu$m (Fig.5.2), in the ^{13}CO measurements presented above (Fig.5.3) and in the GRS CS(J=2→1) map of the region. The best distance estimate for G44.3+0.1, an HII region located within this region and coincident with 1RXS J191159.6+100814, is 3.9 kpc (from HI absorption measurements, Kuchar & Bania, 1994), which – given the uncertainties of the two methods – would place it at a distance consistent with that of the pulsar (4.48 kpc, from dispersion measurements). The VHE emission peaks close to this dense region. There is, however, no evidence for an overall spatial correlation of the γ-ray emission with molecular clouds (see e.g. area "C" in Fig.5.3). In summary, we find little evidence to support the scenario of an old SNR causing the observed VHE γ-ray signal, but can not exclude this hypothesis on the basis of the available experimental data.

Other celestial objects in the vicinity of HESS J1912+101 include the microquasar GRS 1915+105 and the Integral source IGR J19140+0951. GRS 1915+105 is $\sim 1^\circ$ away from the centroid of the VHE emission. The suggested distances to GRS 1915+105 (12.5 kpc (Rodriguez et al., 1995) and 6.5 kpc (Kaiser et al., 2005)) would correspond to a projected distance to the centroid of HESS J1912+101 of 110 to 220 pc and the suggested jet termination sites (IRAS 19132+1035, IRAS 19124+1106) are both situated outside the VHE emission region. A possible association of GRS 1915+105 and HESS J1912+101 is therefore considered as unlikely. The relative position of IGR J19140+0951, which is probably a Super Giant X-ray binary (Nespoli et al., 2007), renders a dominant contribution to the VHE emission from this object unlikely as well.

5.1.3 Summary

The continuation of the H.E.S.S. survey of the Galactic plane has resulted in the discovery of a new extended VHE γ-ray source, HESS J1912+101. The complexity of the vicinity of HESSJ 1912+101 at other wavebands does not allow us to make a firm conclusion on the nature of the source yet. The most plausible scenario appears to be that the observed emission is associated with the high spin-down luminosity pulsar PSR J1913+1011, which would make HESS J1912+101 a γ-ray PWN similar to HESS J1825−137 in both the characteristics of the observed γ-ray emission and the energetics of the associated pulsar. Ultimately, an energy-dependent morphology change needs to be established in further H.E.S.S. observations to confirm the similarity with HESS J1825−137 as argued here. Also the PWN needs to be detected in deep X-ray observations. An alternative possibility is the interaction of accelerated particles from an old SNR with molecular material in a dense region in the interstellar medium. Neither of the two scenarios is fully supported by existing multiwavelength data, but the existence of an energetic pulsar within the VHE emission region favours an association with a PWN, although the confirmation of a PWN at other wavebands is currently pending.

5.2 RCW 86

The shell-type supernova remnant RCW 86, possibly associated with the historical supernova SN 185, with its relatively large size (about 40' in diameter) and the presence of non-thermal X-rays is a promising target for γ-ray observations. This chapter is devoted to the detection of this SNR in VHE γ-rays. Morphological and spectral studies will be presented. Possible origins of the very high energy gamma-ray emission, via either Inverse Compton scattering by electrons or the decay of neutral pions produced by proton interactions, are discussed on the basis of spectral features obtained both in the X-ray and γ-ray regimes.

This Chapter is adopted from a paper written in close cooperation by Marianne Lemoine-Goumard and the author on the behalf of the H.E.S.S. collaboration. The paper is intended for a publication in the *Astrophysical Journal*. Ms. Lemoine-Goumard kindly agreed to a presentation of the paper also in the context of this thesis.

5.2.1 Introduction

Shell-type supernova remnants are widely believed to be the prime candidates for accelerating cosmic ray protons and nuclei up to 10^{15}eV (see Section 1.3.1). A promising way of proving the existence of high energy hadrons accelerated in SNR shells is the detection of very high energy (VHE; E > 100 GeV) γ-rays produced in nucleonic interactions with ambient matter. VHE γ-ray emission has been detected recently in several shell-type SNRs, especially from Cassiopeia A (Aharonian et al. (H.E.S.S. collaboration) (2001), Albert et al. (2007)), RX J1713.7-3946 (Aharonian et al. (H.E.S.S. collaboration), 2007d) and RX J0852.0-4622 (Aharonian et al. (H.E.S.S. collaboration), 2007c). These two latest sources both show an extended morphology highly correlated with the structures seen in non-thermal X-rays. Although a hadronic origin is probable in the above cases (Berezhko & Völk, 2006), a leptonic origin can not be ruled out (Porter et al., 2006). Another young shell-type SNR is RCW 86 (also known as G315.4-2.3 and MSH $14-63$). It has a complete shell in radio (Kesteven & Caswell, 1987), optical (Smith, 1997) and X-rays (Pisarski et al., 1984), with a nearly circular shape of 40' diameter. It received substantial attention because of its possible association with SN 185, the first historical Galactic supernova (Clark & Stephenson, 1977). However, conclusive evidence for this connection is still missing: using optical observations, Rosado et al. (1996) found an apparent kinematic distance of 2.8 kpc and an age of $\sim$ 10 000 years, whereas recent observations of the North-East part of the remnant with the Chandra and XMM-Newton satellites strengthen the case that the event recorded by the Chinese in 185 AD was a supernova and that RCW 86 is its remnant (Vink et al., 2006). In this case, a distance to the SNR of $\sim$ 1 kpc can be estimated for a standard Sedov evolution scenario (Bocchino et al., 2000). The X-ray spectrum obtained with the Einstein satellite was first represented by a two-temperature plasma model (Winkler, 1978). Then, RXTE (Petre et al., 1999) and ASCA observations (Bamba et al. (2000), Borkowski et al. (2001)), with a wider spectral coverage, were used to resolve a non-thermal component in the X-ray spectrum which can be well described by a soft power-law with a photon index of ~ 3. The large-scale density gradient across RCW 86 (Pisarski et al. (1984) and Claas et al. (1989)) possibly suggests that the northern part could be the shocked half of a very low-density wind bubble plus dense shell from the progenitor star, and to this extent it could well be similar to RX J1713.7-3946

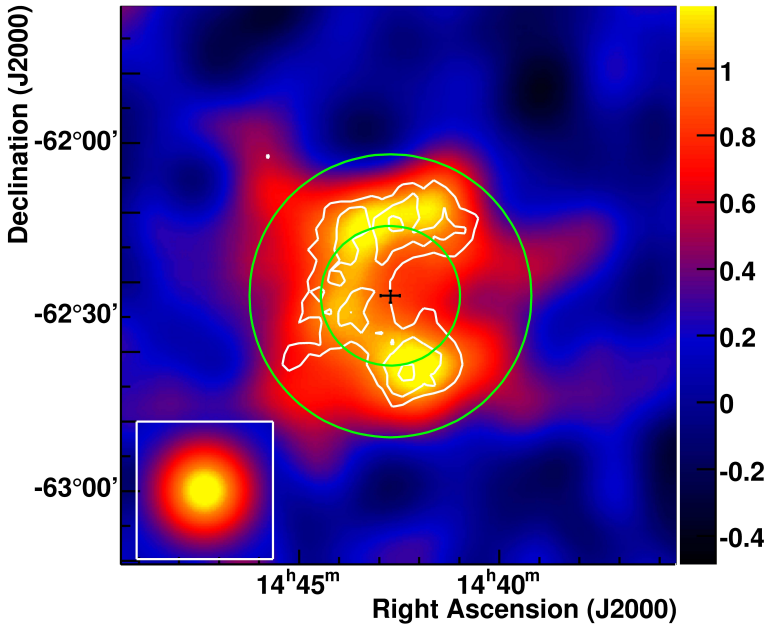

Figure 5.6: H.E.S.S. γ-ray image of RCW 86. The map was smoothed with a Gaussian function with a $\sigma_{\mathrm{smooth}} = 4.8'$ to reduce the effect of statistical fluctuations. The linear color scale is in units of excess counts per arcmin^2. White contours correspond to 4, 5, 6 σ significance, obtained by counting gamma rays within 0.14° from each given location. The image inset in the bottom left corner indicates the size of a point source as seen by H.E.S.S., for an equivalent analysis, smoothing and zenith angles. The centre of the fitted shell, as discussed in the text, is marked by a black cross. The two solid green circles correspond to the inner and outer radii of this shell.

and RX J0852.0-4622. In its southern part, RCW 86 contains an HII region. Apparently, the gas density in this HII region is rather high and spatially extended. Therefore, the SNR shock has swept over an extended high density region in the South, with consequent high radio and thermal X-ray emissions (Bocchino et al., 2000). With a diameter of about 40', RCW 86 is one of the very few non-thermal X-ray emitting SNRs resolvable in VHE γ-rays. H.E.S.S., with its high sensitivity, its good angular resolution and its large field of view is ideally suited for morphology studies of such an extended object.
Evidence for γ-ray emission from RCW 86 was found using the CANGAROO-II instrument, but no firm detection was claimed (Watanabe & Cangaroo Collaboration, 2003). Here, we present data on RCW 86 obtained with the full H.E.S.S. array between 2004 and 2007.

5.2.2 Analysis methods

The shell-type SNR RCW 86 was observed between 2004 and 2007 with the complete H.E.S.S. array. After standard data quality selection and dead time correction, the resulting live time is 31 hours. The observations have been carried out at zenith angles ranging from 38° to 53°. The data were taken using the wobble mode decribed in Section 2.2; the mean offset angle of the data set used in this analysis is 0.7°. The energy threshold of the system

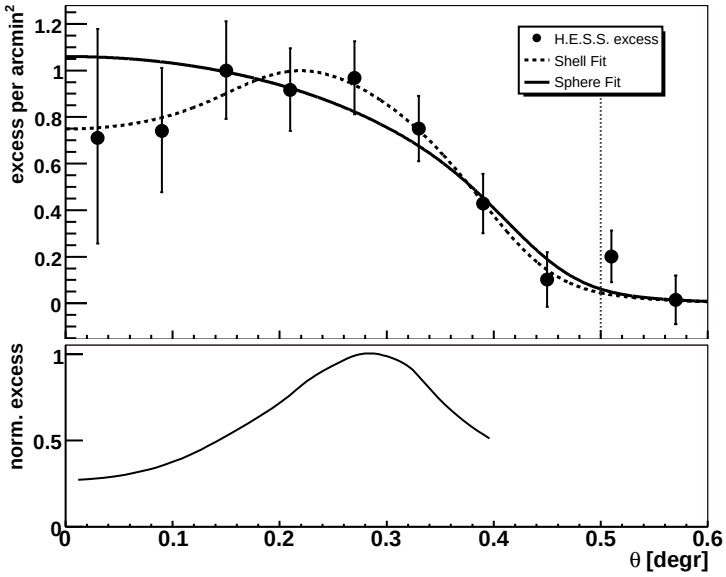

Figure 5.7: **Upper panel:** H.E.S.S. radial profiles around the fitted centre of the SNR ($\alpha_{J2000} = 14^h42^m43^s$, $\delta_{J2000} = -62°26'42"$). The solid line shows the result of a projected uniformly-emitting sphere smoothed with the H.E.S.S. point-spread function and fitted to the H.E.S.S. data. The dashed line corresponds to a projection of a thick and spherically symmetric shell. The dotted vertical line illustrates the extent of the region used for the azimuthal profile and for the spectral analysis. **Lower panel:** Radial profiles of the X-ray data (3-6 keV) from XMM-Newton. These data are background subtracted and smoothed to match the H.E.S.S. angular resolution. Additionally, the obtained excess profile was normalized. The XMM data was kindly provided by Jacco Vink.

increases with zenith angle: for the observations presented here, the average threshold was 480 GeV.
The data were calibrated using standard H.E.S.S. calibration procedures, as discussed by Aharonian et al. (H.E.S.S. collaboration) (2004a). The data were analyzed using a Hillas parameter based method as described in Section 2.4 with *standard* cuts, which include a minimum requirement of 80 photo electrons in each camera image. Two different background estimation procedures were used, as described in Section 2.4. For 2D image generation and morphology studies, the *ring background* method was applied with a mean ring radius of 0.7°. As this method uses an energy averaged radial acceptance correction, the *reflected-region background* method was applied for spectral studies. As a cross-check, a second analysis chain, sharing only the raw data and using the "Combined Model" analysis (de Naurois, 2006), was also applied to the data. The two analysis methods yield consistent results.

5.2.3 Results

A clear VHE γ-ray signal of 8.5σ standard deviation and 1546 ± 183 excess γ-rays is detected from a circular region of 0.45° radius, centered on ($\alpha_{J2000} = 14^h42^m43^s$, $\delta_{J2000} = -62°28'48''$). This integration region was chosen a priori on the basis of the X-ray data

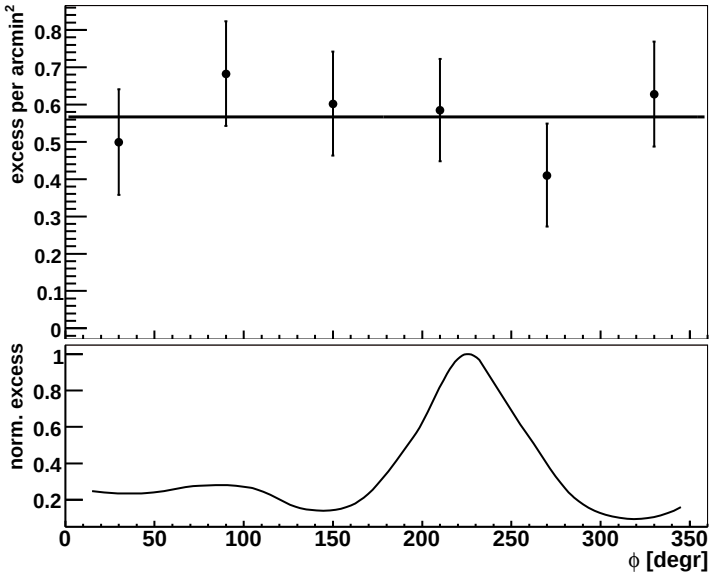

Figure 5.8: **Upper panel:** H.E.S.S. azimuthal profile integrated over a region of 0.5° radius covering the SNR RCW 86. The azimuthal angle is calculated with respect to the fitted shell centre. 0° corresponds to the North part of the source and 90° to the East. The solid line shows the result of a fit of the data to a constant which yields a chi-square of 1.47 for 5 degrees of freedom. **Lower panel:** Azimuthal profiles of the X-ray data (3-6 keV) from XMM-Newton. These data are background subtracted and smoothed to match the H.E.S.S. angular resolution. Additionally, the obtained excess profile was normalized. The XMM data was kindly provided by Jacco Vink.

obtained with the ROSAT satellite and fully encompasses the SNR. Figure 5.6 shows the VHE γ-ray excess map of the $1.6° \times 1.6°$ region around RCW 86. The map has been smoothed with a Gaussian kernel with a σ of $4.8'$ to suppress statistical fluctuations on scales smaller than the H.E.S.S. point-spread function (PSF). The VHE γ-ray excess from RCW 86 is significantly extended beyond the PSF of the instrument, which is illustrated in the bottom left corner of Figure 5.6. Contours of constant significance are superimposed in white at the 4, 5 and 6σ levels. An excess map has also been produced with the so-called "hard cuts" for better gamma hadron separation, which includes a stricter cut of 200 photo electrons on the image size compared to the "standard cuts", and was found to be compatible with Figure 5.6. The VHE emission shown in Figure 5.6 is suggestive of a shell-like morphology. To test this hypothesis, the brightness profile of a thick shell projected along the line of sight and folded with the H.E.S.S. point-spread function was fit to the unsmoothed excess map. The details of this fit will be described in Section 5.2.4. As illustrated in Figure 5.6, the best fit (χ^2/ndf = 233.1/220) is obtained with an outer radius of $24.43' \pm 1.79'_{\rm stat}$, a width of $12.39' \pm 4.22'_{\rm stat}$ and a centre of the shell at (α_{J2000} $= 14^h42^m42.96^s \pm 14.1^s_{\rm stat}$, $\delta_{J2000} = -62°26'41.6'' \pm 66.5''_{\rm stat}$).

Figure 5.7 shows the radial profile of the VHE excess relative to the fitted centre. The fit of the radial profiles to the data points results in a chi-square per degree of freedom of χ^2/ndf = 2.85/7 for a projected shell (determined by outer ring radius, ring width

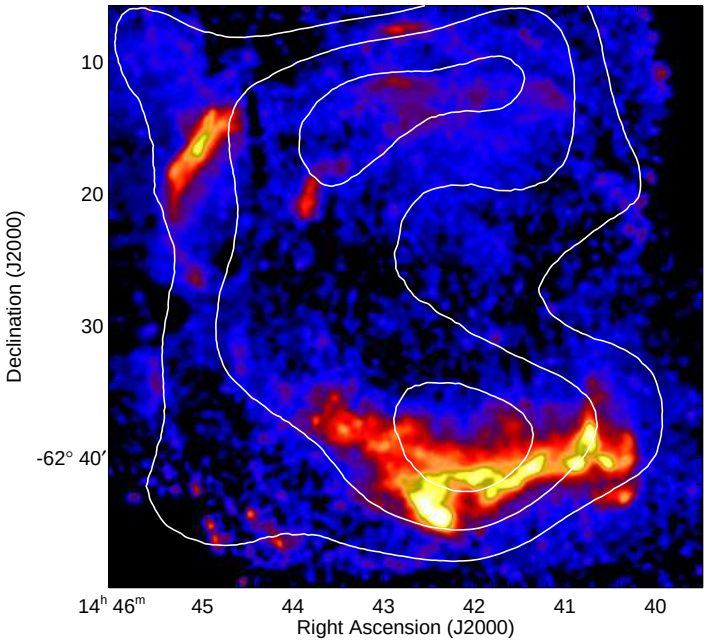

Figure 5.9: Excess contours of γ-ray emission (0.55, 0.8, 1.05 γ-rays per arcmin^2 Gaussian smoothed with $\sigma_{\rm smooth} = 4.8'$) superimposed on the background subtracted XMM-Newton EPIC (MOS/PN) 3-6 keV X-ray image of the remnant (by courtesy of Jacco Vink).

and absolute normalization) which is not significantly better than the fit of a projected uniformly-emitting sphere characterized by a ring radius and a normalization factor (χ^2/ndf = 5.43/8). Also visible in Figure 5.6 is an apparent deficit of γ-rays at the western part of the SNR. However, the azimuthal profile in Figure 5.8 is consistent with a constant and reveals that this dip is not significant (χ^2/ndf = 1.47/5). A more detailed comparison of the γ-ray and X-ray morphologies would require a higher statistics than presently available, and hence will have to await future longer observations.

Figure 5.9 shows the 3-6 keV X-ray map of RCW 86 obtained using six observations of the remnant carried out by the XMM-Newton satellite in 2006 (Vink et al., 2006) and additional observations taken in 2007. The energy range was selected to avoid as much as possible contamination from line emission from the, in general, cool plasma (< 1 keV) of RCW 86. Potentially, the 3 - 4 keV range could contain some contamination from Ar and Ca lines, but no such line emission is seen in the available Chandra, XMM-Newton (Vink et al., 2006) or Suzaku spectra (Ueno et al., 2007). This map was obtained by first automatically cleaning the observations of $> 3\sigma$ excursions to the mean count rate, thus minimizing the background of the maps. Then, for each observation and for each of the three detectors (MOS1, MOS2, and PN), a background count rate in the 3-6 keV band was determined using a relatively empty region of the field of view. In the final stage, the background image was subtracted from the count rate image, and then corrected using the exposure maps obtained with the standard XMM-Newton SAS 7.1.0 software (which includes vignetting correction), in order to obtain the background corrected map displayed in Figure 5.9. An overall positional agreement with the H.E.S.S. contours derived from Figure 5.6 can be

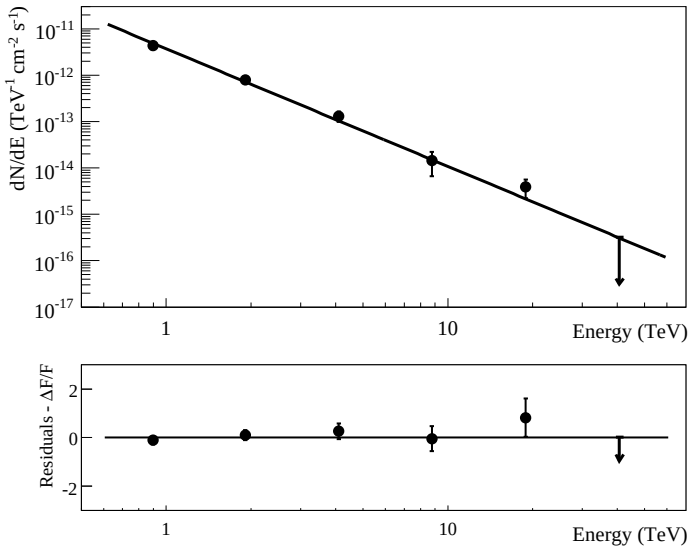

Figure 5.10: Differential energy spectrum of RCW 86, extracted from a circular region of 0.5° radius around the position ($\alpha_{J2000} = 14^h42^m43^s$, $\delta_{J2000} = -62°26'42"$) adjusted to the H.E.S.S. data to enclose the whole source. The solid line shows the result of a pure power-law fit. The error bars denote 1σ statistical errors; the upper limit (arrow) is estimated at the 2σ level. The bottom panel shows the residuals to the power-law fit. Events with energies between 600 GeV and 60 TeV were used in the determination of the spectrum.

observed. However, the γ-ray morphology differs from the X-ray emission, as is apparent in the radial (Figure 5.7) and azimuthal profiles (Figure 5.8).

For the spectral analysis, the source region (ON region) is defined by a circle of 0.5° radius centered on the best fit position of the shell, chosen to fully enclose the whole source. The radius of the extraction region is illustrated in Figure 5.7. The spectrum obtained (see Figure 5.10) is well described by a power-law with a photon index of $2.54 \pm 0.12_{\rm stat} \pm 0.20_{\rm sys}$ and a flux normalisation at 1 TeV of $(3.72 \pm 0.50_{\rm stat} \pm 0.8_{\rm sys}) \times 10^{-12}{\rm cm}^{-2}{\rm s}^{-1}{\rm TeV}^{-1}$ (χ^2/ndf = 6.30/4). The integral flux in the energy range 1 - 10 TeV is $(2.34 \pm 0.3_{\rm stat} \pm 0.5_{\rm sys}) \times 10^{-12}\,{\rm cm}^{-2}{\rm s}^{-1}$, which corresponds to $\sim 10\%$ of the integrated flux of the Crab nebula in the same energy interval. No significant improvement is obtained by fitting a power-law with an exponential cut-off (χ^2/ndf = 2.96/3). If the fit range is restricted to energies below 10 TeV, a photon index of $2.41 \pm 0.16_{\rm stat} \pm 0.20_{\rm sys}$ and a flux normalisation at 1 TeV of $(3.57 \pm 0.5_{\rm stat} \pm 0.8_{\rm sys}) \times 10^{-12}{\rm cm}^{-2}{\rm s}^{-1}{\rm TeV}^{-1}$ are determined (χ^2/ndf = 0.68/2), compatible with the fit of the SNR in the whole energy range.

5.2.4 The Morphology Analysis of RCW 86

The VHE γ-ray excess from RCW 86 appears shell-like in Figure 5.6. To put this hypothesis to a more stringent statistical test the signal was fitted with the intensity profile of a 3-dimensional shell projected along the line of sight. Even though the results of this fit were already used in the paragraphs above, the details of the shell fit necessitate further description. They will be given in the following.

A 3-dimensional symmetric shell with finite thickness is described by 6 parameters: The (x,y,z)-coordinate of its center, its outer radius, its width and its surface brightness. When the intensity profile is projected along the line of sight, the parameter which describes the distance to the object cancels and the result is a 2-dimensional intensity distribution. Due to the radial symmetry of this model distribution, all information is still contained in its 1-dimensional radial profile, which is given by:

$$I(\theta) = N \cdot \left[R_{\text{out}} \cdot \sin\left(\arccos\left(\frac{\theta}{R_{\text{out}}}\right)\right) - (R_{\text{out}} - W) \cdot \sin\left(\arccos\left(\frac{\theta}{R_{\text{out}} - W}\right)\right)\right] , \tag{5.3}$$

where $\theta = \sqrt{[(\alpha_0 - \alpha)a]^2 + [\delta_0 - \delta]^2}$ is the radial distance to the center described by the coordinates α_0 and δ_0 (e.g. RA Dec coordinates), $a = \cos(y)^{-1}$ is a scale factor resulting from the spherical character of the coordinate system on the sky with non-Cartesian metrics, R_{out} is the outer shell radius and W is the thickness of the shell. Figure 5.11 illustrates this radial profile together with its characteristic parameters.

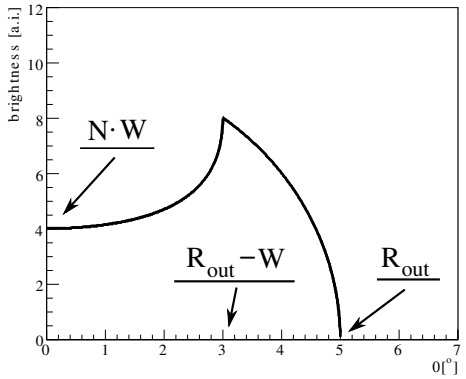

Figure 5.11: Sketch of the radial profile of a 3-dimensional shell integrated along the line of sight.

Before the model intensity distribution can be fit to the observed signal, the limited angular resolution of the instrument has to be taken into account. For that purpose the one-dimensional radial profile described in Equation 5.3 is convolved with the PSF of the instrument. The PSF is approximately described by two Gaussian curves:

$$PSF(\theta) = K_1 \exp\left(-\frac{\theta^2}{2\sigma_1^2}\right) + K_2 \exp\left(-\frac{\theta^2}{2\sigma_2^2}\right) , \tag{5.4}$$

where the parameters K_1, K_2, σ_1 and σ_2 are characteristic of the data set, depending on the zenith and the offset angle of the observations. Figure 2.8(a) illustrates the shape of the PSF. The analytic convolution of Equation 5.3 and 5.4 is not easily possible. Thus, it is performed numerically using GSL[1] routines, which apply the Gauss-Kronrod 21-point integration rule adaptively to avoid any step-like artefacts in the resulting curve which could hinder the minimization later on. The resulting convolved radial profile can be seen in Figure 5.7.

[1] http://www.gnu.org/software/gsl/

The convolved model profile is then fit to the 2-dimensional uncorrelated excess map shown in Figure 5.12(a). Because this excess map does not follow counting statistics, no likelihood fit can be used. Instead a χ^2 minimization is performed using MIGRAT, which is a part of the MINUIT package [2]. The 2-dimensional intensity distribution, obtained by rotating the best fit radial profile around the fitted center, is shown in Figure 5.12(b). The black cross illustrates the best fit center of the putative shell together with its statistical errors, the black circles show the fitted inner and outer radius (with the effect of the PSF removed). The best-fit parameter values are: $\alpha_0 = 14^h42^m42.96^s \pm 14.1^s_{\rm stat}$, $\delta_0 = -62°26'41.6'' \pm 66.5''_{\rm stat}$, $R_{\rm out}$=24.43′ ± 1.79′$_{\rm stat}$ and W=12.39′ ± 4.22′$_{\rm stat}$. The reduced χ^2 is 233.1 for 220 degrees of freedom. Figure 5.12(c) depicts the residuals between the uncorrelated excess map and the model distribution; for illustrational purposes the map has been correlated using a correlation radius of 0.11°.

The error estimates on the best-fit parameter values have also been obtained using MIGRAT. For illustrational purposes, the χ^2 planes spanned by two of them at a time is shown in Figure 5.12(d) to 5.12(f). The paramters not shown in the figures are fixed to their best-fit value. The white contours illustrate the parameter values at which the χ^2 has increased by 1,2 and 3 relative to its minimum. Even though this is the definition of the $1\,\sigma$, $2\,\sigma$ and $3\,\sigma$ errors, the errors on the parameters can not be directly read from Figure 5.12(d) to 5.12(f) since merely projections of the parameter space are shown. As apparent in Figure 5.12(d), the RA- and Dec-coordinate of the shell center are rather independent of each other. The same is true for the thickness and the outer radius, as can be judged from Figure 5.12(e). The normalization and the shell thickness, however, are more strongly correlated, see Figure 5.12(f). This correlation arises from the influence of the shell thickness on the observed surface brightness after a profection along the line of sight, i.e. as stated in Figure 5.11 the intensity at the shell center depends on both the normalization N and the shell thickness w in Equation 5.3.

[2]Part of of PACKLIB: http://cernlib.web.cern.ch/cernlib/packlib.html

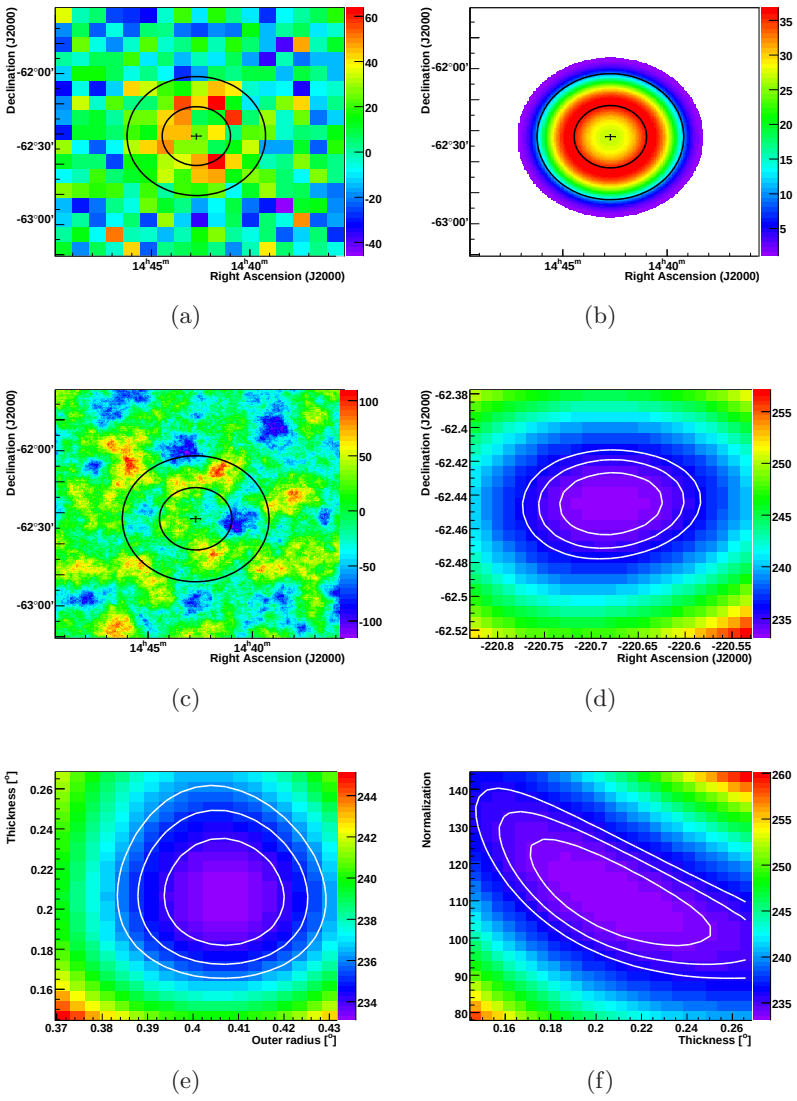

Figure 5.12: RCW 86 shell fit: a.) Uncorrelated excess map of the VHE γ-ray signal detected from the SNR RCW 86. The results of a fit with the intensity distribution of a shell are also shown: the center together with the estimated errors are illustrated by a cross, the inner (outer) circle depicts the inner (outer) radius of the shell taking the PSF of the instrument into account. b.) Intensity distribution of a shell which best fits the VHE γ-ray excess. c.) Correlated residual map: the residuals between the fit result shown in b.) and a fine binned uncorrelated excess map have been correlated with a radius of 0.11°. d.) χ^2 between the uncorrelated excess map shown in Figure 5.12(a) and the shell fit function shown in Figure 5.12(b) for different values of the Right Ascention and Declination of the shell center; e.) Same as d.) but for the outer radius and width of the shell; f.) Same as d.) but for the Width of the shell and total normalization. The fit parameters not shown in the plot have been fixed to their best fit value.

5.2.5 Discussion

As described in Section 1.2 there are two commonly invoked mechanisms for VHE γ-ray production in young supernova remnants, inverse Compton (IC) scattering of high energy electrons off ambient photons (leptonic scenario) and π^0 meson production in inelastic interactions of accelerated protons with ambient gas (hadronic scenario). In such a hadronic scenario, a comparison between the expected thermal X-ray emission and the actually measured thermal emission has to await deeper observations in which one can better determined whether the TeV emission traces the denser, thermal X-ray emitting parts of the SNR, or is more closely correlated with the X-ray synchrotron emission from the remnant. The measured γ-ray spectrum from RCW 86, restricted to energies below 10 TeV, translates into an energy flux between 1 and 10 TeV of $8.6 \times 10^{-12}\,\mathrm{erg\,cm^{-2}\,s^{-1}}$. The X-ray spectrum of the whole remnant is mixed between thermal and non-thermal emission. Assuming that the hard X-ray continuum originates from non-thermal synchrotron emission as reported by Rho et al. (2002), Vink et al. (2006) and Ueno et al. (2007), the measurement made by Petre et al. (1999) using RXTE data provides an estimate of the total amount of non-thermal flux from RCW 86. They find that the spectrum is well fitted by a power-law of index ~ 3 and a flux normalization at 10 keV of $10^{-4}\,\mathrm{cm^{-2}\,s^{-1}\,keV^{-1}}$, which extrapolated down to the 0.7 to 10 keV band leads to an integral flux of $2.1 \times 10^{-10}\,\mathrm{erg\,cm^{-2}\,s^{-1}}$. In a leptonic scenario, assuming that the γ-ray emission is entirely due to the IC process on cosmic microwave background photons, the ratio of the synchrotron power and IC power radiated is often used to constrain the magnetic field. For a power-law distribution of electron energies, $K\gamma^{-p}$, the general equation relating the synchrotron power (P_S) produced by electrons with Lorentz factors between $\gamma_{1,X}$ and $\gamma_{2,X}$ and the IC power (P_{IC}) radiated between $\gamma_{1,IC}$ and $\gamma_{2,IC}$ can be expressed as follow:

$$\frac{P_S}{P_{IC}} = \frac{U_B}{U_{ph}} \frac{(\gamma_{2,X}^{3-p} - \gamma_{1,X}^{3-p})}{(\gamma_{2,IC}^{3-p} - \gamma_{1,IC}^{3-p})} \tag{5.5}$$

where U_{ph} and U_B are the energy density of the photon field and the energy density of the magnetic field, respectively. It should be noted here that, for a fixed X-ray energy, $\gamma_{1,X}$ and $\gamma_{2,X}$ are inversely proportional to the square root of the magnetic field. If X-rays and γ-rays probe the same region of the electron spectrum, one finds the standard relation between the synchrotron and IC power $\frac{P_S}{P_{IC}} = \frac{U_B}{U_{ph}}$ (see Equation 1.19). Assuming that the target photon field is the cosmic microwave background, a magnetic field of $30\,\mu$G can be estimated using Equation 5.5 and the synchrotron photon index of ~ 3, independent of the distance and age of the SNR. This estimate is compatible with that of Vink et al. (2006) based on thin filaments resolved by Chandra (assuming a distance of 2.5 kpc) in which the authors also deduce a high speed of the blast wave ($\sim 2700\,\mathrm{km\,s^{-1}}$); their estimated value would increase to $\sim 50\,\mu$G for a distance of 1 kpc. However, it is still a factor of 2 lower than the magnetic field determined by Völk et al. (2005) using a lower shock velocity of $800\,\mathrm{km\,s^{-1}}$ as suggested by optical data in the Southern region of the SNR (Rosado et al., 1996). The difference between the field amplification estimated by Vink et al. (2006) and that of Völk et al. (2005) lies in the fact that Völk et al. obtained a higher result when they de-projected the measured filament width, as for an ideal spherical shock, whereas Vink et al. did not. Without de-projection the two results remarkably agree, even though they were obtained for the southern side and the northern side, respectively. A discussion

of de-projection for RCW 86 is given in Völk et al. (2005). With similar data, Bamba et al. (2005) deduced a significantly lower magnetic field strength of $\sim 4-12\,\mu$G. However, their analysis is based on rather different assumptions on the nature of filament formation.

In a hadronic scenario, one can estimate the total energy in accelerated protons W_p in the range $10-100$ TeV required to produce the γ-ray luminosity L_γ observed by H.E.S.S. using the relation $W_p(10-100\,\mathrm{TeV}) \approx \tau_\gamma \times \mathrm{L}_\gamma(1-10\,\mathrm{TeV})$, in which $\tau_\gamma \approx 4.9\times10^{15}\left(\frac{n}{1\,\mathrm{cm}^{-3}}\right)^{-1}$ s is the characteristic cooling time of protons through the π^0 production channel (Kelner et al., 2006). The total energy injected in protons is calculated by extrapolating the proton spectrum down to 1 GeV. Because of this extrapolation over 4 decades in energy, the uncertainty of the estimate can be as large as a factor of 10. Assuming that the relatively steep slope of the proton spectrum (as inferred from the observed γ-ray spectrum), is the result of an energy cut-off (somewhere around several tens of TeV in proton energy), and that at lower energies the proton spectrum has a E^{-2} type spectrum representative of those predicted by the diffusive shock acceleration theory, the total energy budget in all protons for the distance of 2.5 kpc and the ambient gas density between $0.3\,\mathrm{cm}^{-3}$ and $0.7\,\mathrm{cm}^{-3}$ (Bocchino et al., 2000), would be $(2-4)\times10^{50}$ erg. This estimate is in reasonable agreement with theoretical expectations that a significant fraction of the explosion energy of 10^{51} erg is released in relativistic protons. On the other hand, if the power-law spectrum of protons continues to GeV energies with the spectral index $\Gamma = 2.4$ (i.e. similar to the gamma-ray spectrum below 10 TeV), the total budget in protons would exceed few times 10^{51} erg for a distance of 2.5 kpc. This would exclude the hadronic origin of TeV γ-rays, unless the SNR is nearby ($\sim$ 1 kpc), or if the γ-rays are produced in very dense regions. Indeed, Pisarski et al. (1984) and Claas et al. (1989) reported that there is a large density contrast across the remnant, e.g. in the South, where the density could be as high as $10\,\mathrm{cm}^{-3}$; with such a dense medium, a larger distance for the remnant could still be compatible with the observed γ-ray flux.

5.2.6 Conclusions

H.E.S.S. observations have led to the discovery of the shell-type SNR RCW 86 in VHE γ-rays. The γ-ray signal is significantly more extended than the H.E.S.S. point-spread function. The possibility of a shell-like morphology was addressed, but cannot be settled on the basis of the limited statistics available at the moment. The flux from the remnant is $\sim$10% of that from the Crab nebula, with a photon index of about 2.5. The question of the nature of the particles producing the γ-ray signal observed by H.E.S.S. is also discussed. In a leptonic scenario, assuming that the γ-ray emission is entirely due to the IC process on cosmic microwave background photons and that the synchrotron and IC photons are produced by the same electrons, the ratio of the γ-ray energy flux and the X-ray flux determines the magnetic field to be close to $30\,\mu$G. In the hadronic scenario, the lack of information about the low-energy γ-ray spectrum results in large uncertainties on the total energy budget in protons. If below several tens of TeV, the proton spectrum has a E^{-2} type spectrum, the total energy in protons would be in reasonable agreement with theoretical expectations. On the other hand, if we assume that the proton spectrum continues down to GeV energies with the observed spectral index $\Gamma = 2.4$, energetics would rule out a hadronic origin for the TeV γ-rays unless the SNR is nearby, or if the γ-rays are produced in a very dense medium as reported in the South part of the remnant.

5.3 HESS J1708-442

The high spin-down lumniosity pulsar PSR B1706-44 has been observed by H.E.S.S. in dedicated observations in the year 2007. A new and extended VHE γ-ray source, HESS J1708-442, was discovered in its vicinity with a statistical significance of 8 standard deviations. In this chapter, the morphological and spectral analysis of HESS J1708-442 is presented. Additional multi-wavelength data was drawn on to discuss its possible associations with the pulsar wind nebula of PSR B1706-44 and/or with the broad-scale radio structure of the SNR candidate G343.1−2.3. This chapter is a adopted from a paper draft, which the author has written on behalf of the H.E.S.S. collaboration. It is intended for publication in *Astronomy and Astrophysics*.

5.3.1 Introduction

The pulsar PSR B1706−44 was first detected in a high frequency radio survey by Johnston et al. (1992). With a spin period of 102 ms, a characteristic age of 17,500 years and a spin-down luminosity of $3.4{\cdot}10^{36}\,\mathrm{erg\,s^{-1}}$, it belongs to the class of relatively young and very energetic pulsars of which the Vela pulsar is the most prominent example. Its distance estimate ranges from 1.8 kpc (Johnston et al., 1992; Taylor & Cordes, 1993) to 3.2 kpc (Koribalski et al., 1995). The bright gamma-ray source 2CG342−02, originally discovered by the COS B satellite (Swanenburg et al., 1981) and positionally coincident with the pulsar, was firmly identified with PSR B1706−44 when the EGRET instrument observed pulsation matching the period seen in the radio waveband (Thompson et al., 1992). PSR B1706−44 is therefore one of the very few pulsars from which pulsed emission is discovered not only in radio (Johnston et al., 1992) and X-rays (Gotthelf et al., 2002), but also in high-energy gamma-rays.

Radio observations by Frail et al. (1994b) and Giacani et al. (2001) revealed a synchrotron nebula with an extension of 3' surrounding the pulsar. The observed polarization and the flat spectrum with a photon index of 0.3 suggest a pulsar wind nebula (PWN) origin. However, the implied conversion efficiency from spin-down energy to radio flux of $2{\cdot}10^{-6}$ is the lowest of any radio PWN (Giacani et al., 2001). The synchrotron nebula is also visible in X-rays, first reported by Finley et al. (1998) using the ROSAT instrument. The morphology of the PWN could be mapped in detail by Romani et al. (2005) employing the superior resolution of the Chandra instrument. Their findings suggest a diffuse PWN extending as far as 110" from the pulsar with a spectral index of 1.77 surrounding a more complex structure of torus, inner and outer jets. The existence of undeformed X-ray jets supports the low scintillation velocity of the pulsar of less than 100 km/s as reported by Johnston et al. (1998).

PSR B1706−44 is located at the south east end of an incomplete arc of radio emission (McAdam et al., 1993) suggested to be the shell of a faint SNR (G343.1−2.3, see Figure 5.13). The arc itself is embedded in weak broad-scale radio emission (Frail et al., 1994b). Polarization measurements suggest an association of this diffuse emission with synchrotron radiation from the SNR (Dodson & Golap, 2002). The SNR has not been detected in any other waveband (see e.g. Becker et al., 1995; Aharonian et al. (H.E.S.S. collaboration), 2005e). The possible association of PSR B1706−44 and G 343.1−2.3 has been questioned based on the differing age and distance estimates for SNR and pulsar, the lack of visible interaction and the high implied

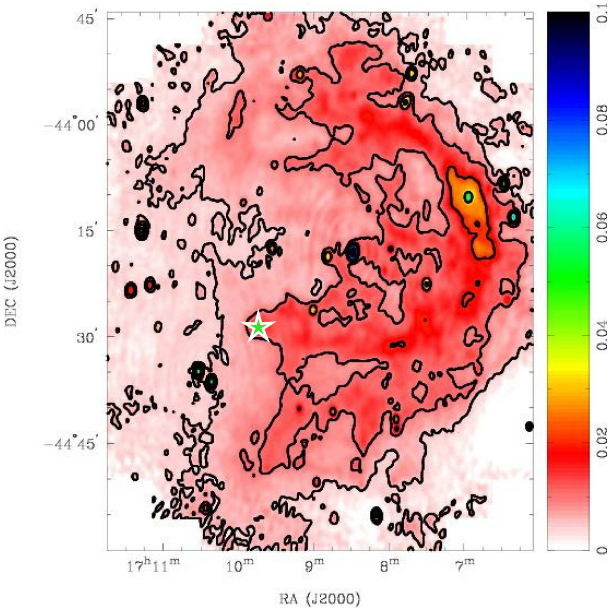

Figure 5.13: SNR G343.1−2.3 as seen by the Australia Telecope Compact Array (ATCA) at 1384 MHz. The Figure was taken from Dodson & Golap (2002). The pulsar position is marked by a green star.

velocity of the pulsar (∼700 km/s) which is incompatible with the measured scintillation velocity. Recent changes in the electron distribution model by Cordes & Lazio (2002) have resulted in a revised dispersion distance for the SNR of 2.3 kpc (Romani et al., 2005, and references therein) which is now compatible with the pulsar distance. Bock & Gvaramadze (2002) suggested a scenario of an off-centered cavity explosion which would release the restrictions on the implied velocity and invalidate the age estimate for the SNR of 5000 years (McAdam et al., 1993), which is based on a Sedov-Taylor model (see Figure 5.14. In this scenario PSR B1706−44 and G 343.1−2.3 are associated, the radio arc, however, is not identified with the SNR shell but with the former boundary of the wind blown cavity that was overtaken and compressed by the expanding SNR. The diffuse broad-scale radio emission is interpreted as resulting from the interaction of the SNR with the parent molecular cloud.

At very-high energies (VHE; > 100 GeV) the pulsar and the SNR were observed using ground based air-Cherenkov instruments. The findings of the different instruments are, however, inconsistent. The Cangaroo experiment detected a steady emission coincident with the pulsar at the level of 50% of the Crab flux (Kifune et al., 1995; Kushida & Cangaroo Collaboration, 2003). The result was supported by the Durham Mark 6 collaboration (Chadwick et al., 1998) which reported a significant excess from the pulsar above 300 GeV. The H.E.S.S. collaboration, however, did not confirm the detection of the pulsar and reported an upper limit as low as 1% of the Crab flux above 350 GeV in clear disagreement with the previous findings (Aharonian et al. (H.E.S.S. collaboration), 2005e). Here we present data on PSR B1706−44 and G 343.1−2.3 obtained with the full H.E.S.S. array in the year 2007.

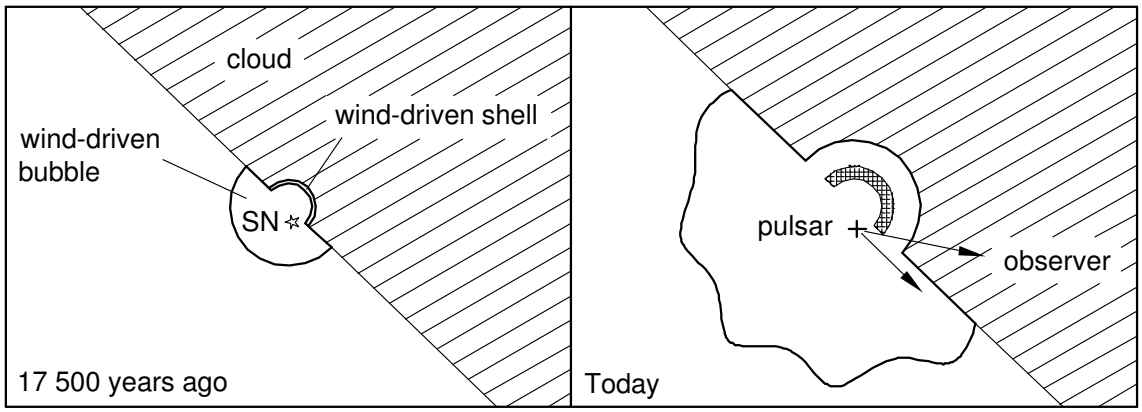

Figure 5.14: Schematic illustrating the scenario of an off-centered cavity explosion and the association of the radio shell with the former boundary of the wind-blown cavity. The Figure was taken from Bock & Gvaramadze (2002).

5.3.2 H.E.S.S. observations and analysis methods

The data

The region of interest which includes PSR B1706−44 and SNR G 343.1−2.3 was observed with the full H.E.S.S. array in the year 2007. The observations were dedicated to search for VHE γ-ray emission from the pulsar and have therefore been taken in wobble mode (see Section 2.2) centered around its radio position (α_{2000}=$17^h9^m42.73^s$, δ_{2000}=$-44°29'8.2''$, Wang et al. (2000)). After standard quality selection to remove data affected by unstable weather conditions or hardware issues, the total live time of the data set is 15 hours. The zenith angle of the observations ranges from 20° to 30° with a mean of 24°. The average offset from the pulsar position is 0.7°.

The analysis method

The data set was analyzed using the Hillas second moment method as described in Section 2.4. For gamma-hadron separation, the so-called *hard cuts* were used, which require a minimum of 200 photon electrons (p.e.) recorded per shower image. Compared to *std cuts* (80 p.e.), this relatively hard requirement results in better background rejection and an improved angular resolution, but also in a slightly increased energy threshold of 560 GeV for this data set. Three different background estimation procedures described in Section 2.4 were applied in this analysis. For 2D image generation the ring-background method was used with a mean ring radius of 0.7°. As this method includes an energy averaged model for the camera acceptance to account for the different offsets of signal and background regions from the camera center, it was not used for spectral extraction. Instead the reflected-region method was applied to measure the flux from the pulsar position. For the spectral extraction from very extended regions, which also enclose the pointing positions of the instrument, the background was estimated from off-source data taken in the years 2006 and 2007. The normalization between on- and off-source observations was deduced from the total event number in the two runs, excluding regions with significant VHE γ-ray signals.

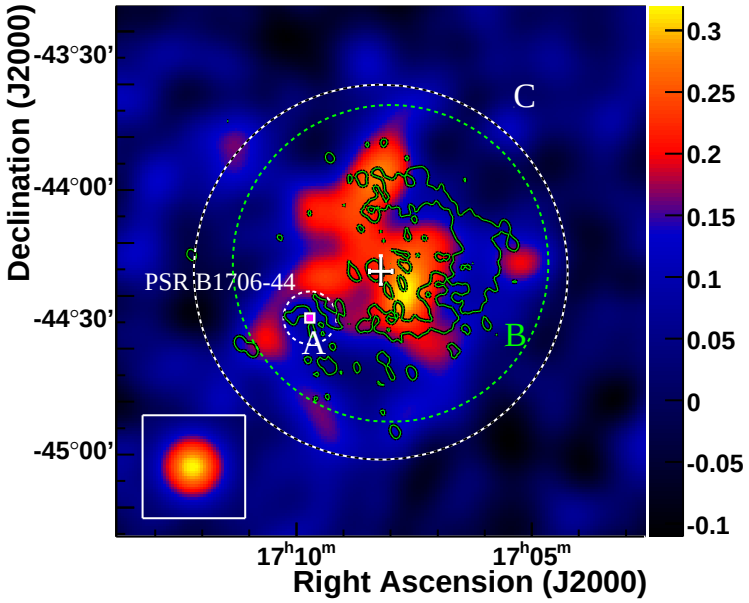

Figure 5.15: Image of the VHE γ-ray excess from HESS J1708−443, smoothed with a Gaussian profile of σ=0.075° along each axis. The white cross indicates the best fit position of the center-of-gravity of the emission together with its statistical errors. The small and the large white circles illustrate regions A and C, respectively, which were used for spectral analysis. Region B, from which the detection significance was calculated, is marked by a green circle. The three regions are summarized in Table 5.1. The position of the pulsar PSR B1706−44 is marked by a square. The inset in the bottom left corner shows the point-spread function of the instrument for this particular data set smoothed in the same way as the excess map. Contours of constant intensity as seen at 330 MHz with the VLA instrument are shown in green (by courtesy of Gloria Dubner and Elisabeth Giacani).The radio data were smoothed with the same Gaussian profile as the H.E.S.S. data to match the angular resolution.

The time-dependent optical response of the system was estimated from the Cherenkov light of single muons passing close to the telescopes (Bolz, 2004).

5.3.3 Results

To reduce the number of trials, two different regions were defined a priori to search for VHE γ-ray emission. As other Cherenkov instruments have reported a point-like emission from the pulsar location, one is centered at its position and has a radius of 0.1°, which is usually used to detect point sources in the H.E.S.S. standard analysis scheme (Section 2.4). This region will be denoted as region A in the following, see Figure 5.15. The other region, denoted as region B, is centered at the apparent center of the radio arc (α_{2000}=17^h8^m and δ_{2000}=$-44°16'48''$) and has a radius of 0.6° to enclose the whole structure. No emission is observed from the pulsar position (region A). An upper limit of 18 excess events is detected from this direction at a confidence level of 99% following the unified approach of

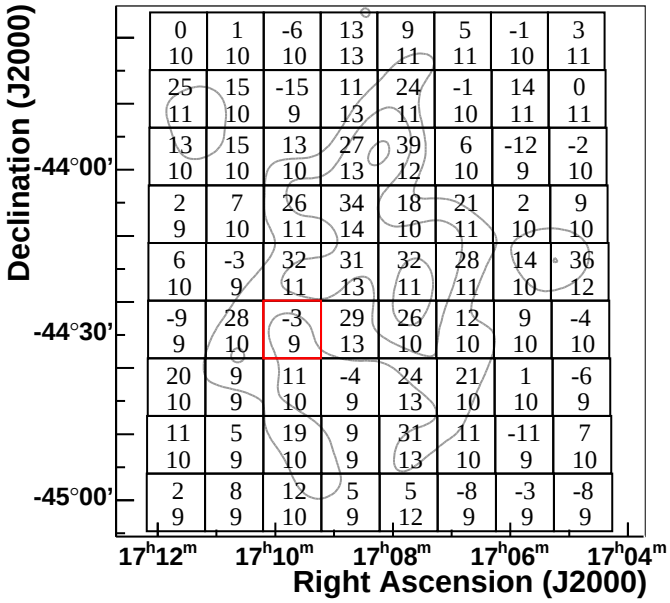

Figure 5.16: Uncorrelated excess in quadratic bins of 0.175° width. The upper number in each bin is the uncorrelated excess summed within this bin, the lower number is the corresponding statistical error. The gray contours correspond to a smoothed excess of 0.12, 0.2 and 0.28 events per arc min^2 taken from the Figure 5.15. The red rimmed bin is centered on the pulsar position. Note the different scale used in Figure 5.15 and Figure 5.16.

Feldman & Cousins (1998). From region B, however, a clear signal of 618 VHE γ-rays at a statisitical significance of 8 standard deviations is detected. Table 5.1 summarizes the event statistics for region A and B.

In order to investigate the morphology of the VHE γ-ray emission from region B, Figure 5.15 shows the excess count map of the $1^\circ \times 1^\circ$ region around the H.E.S.S. source, smoothed with Gaussian brightness profile of width 0.075° to reduce statistical fluctuations. The smoothing radius is chosen to be of the same scale as the point-spread function of the instrument. The extension of the emission region clearly exceeds beyond the point-spread function depicted in the lower left inlay. Figure 5.16 depicts the number of excess events within the emission region together with their statistical errors in quadratic bins of 0.175° width. For this representation no smoothing was applied. The lack of VHE γ-rays in the vicinity of the pulsar is apparent in both figures.

Fitting the fine-binned and unsmoothed excess map with a radially symmetric Gaussian profile ($\phi = \phi_0 e^{-r^2/(2\sigma^2)}$) convolved with the point-spread function of the instrument leads to a best fit position of α_{2000}=$17^h 8^m 12.46^s$ and δ_{2000}=$-44^\circ 18' 46.6''$, with a statistical error of $3'$ on each axis, as indicated by the white cross in Figure 5.15. Consequently the new VHE γ-ray source is called HESS J1708−443. The fit results in an intrinsic Gaussian width of σ =$0.27^\circ \pm 0.03^\circ{}_{\rm stat}$.

Spectral analyses were performed within two regions, region A, as already introduced above, and region C, which is centered on the best fit position and has a radius of 0.71°

Reg.	Center		R	N_{on}	N_{off}	α	Excess	Sign.
	$\alpha_{2000}[^\circ]$	$\delta_{2000}[^\circ]$	$[^\circ]$					$[\sigma]$
A	$17^h9^m42.73^s$	$-44°29'8.2''$	0.1	75	1125	$7.2{\cdot}10^{-2}$	$-6.0^{+9.3}_{-8.7}$	-0.65
B	17^h8^m	$-44°16'48''$	0.6	3200	2432	1.06	619^{+77}_{-77}	8
C	$17^h8^m12.46^s$	$-44°18'46.6''$	0.71	4310	3325	1.06	779^{+90}_{-90}	8.7

Table 5.1: Event statistics for region A,B and C. The center and the radius of the circular ON region is stated. For region A the background was extracted from OFF regions in the same field of view, for region B and C it was estimated from off-source observations. Due to the smaller extent of region A, more OFF regions could be used, which results in a smaller normalization factor α than for region B and C. N_{on} and N_{off} are the event numbers in the ON and OFF regions. The significance was calculated following the approach of Li & Ma (1983).

chosen to fully include the observed γ-ray emission (see Table 5.1). Both regions are indicated by dashed circles in Figure 5.15. From region A, a limit of $3.6{\cdot}10^{-13}\mathrm{cm}^{-2}\mathrm{s}^{-1}$ on the integral flux above 605 GeV was derived at a confidence level of 99% using the unified approach of Feldman & Cousins (1998). The upper limit corresponds to 0.7% of the flux of the Crab Nebula in the same energy range. The associated differential upper limits are shown in Figure 5.21. The underlying γ-ray spectrum is assumed to follow a power law with a photon index of 2.5, an index in the same range as most of the indices of the Galactic VHE γ-ray sources (see Section 4.4.3). The energy spectrum of the whole source is extracted from region C. Within the large integration circle 779 excess events were found, corresponding to a statistical significance of $8.7\,\sigma$ (pre-trials). The spectrum is well described by a power law $\phi = \phi_{1\mathrm{TeV}} \cdot \mathrm{E}^{-\Gamma}$ with a spectral index of $\Gamma{=}2.1{\pm}0.1_{\mathrm{stat}} \pm 0.2_{\mathrm{sys}}$ and a flux normalization at 1 TeV of $\phi_{1\mathrm{TeV}}{=}(5.2{\pm}0.8_{\mathrm{stat}} \pm 1.0_{\mathrm{sys}}){\cdot}10^{-12}\,\mathrm{cm}^{-2}\mathrm{s}^{-1}\mathrm{TeV}^{-1}$. The integral flux between 1 and 10 TeV is about 19% of the Crab Nebula flux in the same energy range. The extracted flux points from the extended emission and the fit result are shown in Figure 5.17.

5.3.4 Possible Counterparts

While a superposition of PSR B1706−44 and SNR G 343.1−1.3 cannot be excluded, each of them could account individually for the observed VHE γ-ray emission. The possible associations of HESS J1708−443 will be discussed in the following.

PSR B1706−44

The pulsar PSR B1706−44, with its high spin-down luminosity of $3.4{\cdot}10^{36}\,\mathrm{erg\,s}^{-1}$, is energetic enough to power the observed VHE γ-ray emission. Assuming a distance of 2.5 kpc for the pulsar, the energy flux from the H.E.S.S. source between 1 and 10 TeV is $1.2{\cdot}10^{34}\,\mathrm{erg\,s}^{-1}$. The implied effective conversion efficiency from rotational energy to γ-rays in this energy range is then ∼0.4%, comparable to the efficiency of 0.8% inferred for PSR J1420-6048 (Aharonian et al. (H.E.S.S. collaboration), 2006c). At this distance, the inferred projected size of HESS J1708−443 is 11 pc (68% containment radius).

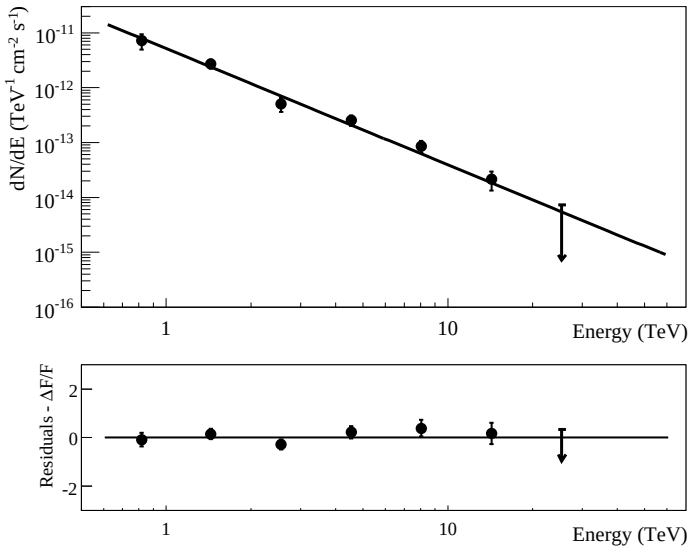

Figure 5.17: Differential energy spectrum of HESS J1708−443, extracted from Region C, see Table 5.1. The solid line shows the result of a pure power-law fit. The error bars denote 1σ statistical errors; the upper limit (arrow) is estimated at the 2σ level. The bottom panel shows the residuals to the power-law fit. Events with energies between 600 GeV and 34 TeV were used in the determination of the spectrum.

These characteristics suggest an association of the VHE γ-ray emission with the pulsar's wind nebula, similar to other PWN associations such as Vela X (Aharonian et al. (H.E.S.S. collaboration), 2006f) and MSH 15−52 (Aharonian et al. (H.E.S.S. collaboration), 2005c). In this scenario, the VHE γ-radiation originates from accelerated electrons which up-scatter ambient photons to VHE energies (leptonic scenario, Section 1.2).

Compared to the size of the PWN as seen in radio (radius $\sim 1.5'$) (Giacani et al., 2001) and X-rays (radius $\sim 110''$) (Romani et al., 2005), the implied TeV PWN is a factor of $\sim$10 larger. Such differences in size have been observed in other PWN associations such as HESS J1825−137 (Aharonian et al. (H.E.S.S. collaboration), 2006e), and can be explained by the different energies, and hence cooling times, of X-ray emitting and VHE γ-ray emitting electrons; Aharonian et al. (H.E.S.S. collaboration) (2005b) estimate the ratio of sizes to:

$$\frac{R_\gamma}{R_\mathrm{X}} = 2.8 \left(\frac{\mathrm{B}}{10\mu\mathrm{G}} \right)^{-\frac{1}{2}} \left(\frac{E_\mathrm{keV}}{E_\mathrm{TeV}} \right)^{\frac{1}{2}} \tag{5.6}$$

with a mean of 2 keV at X-ray energies and a mean energy of 0.9 TeV in VHE γ-rays. However, in contrast to the PWN of PSR J1826−1334, where a magnetic field strength of 10μG was inferred from X-ray observations (Gaensler et al., 2003), Romani et al. (2005) estimated a magnetic field as strong as $140\,\mu$G within the extended X-ray PWN of PSR B1706−44. In such high magnetic fields, electrons that emit keV X-rays and those that emit TeV γ-rays have comparable energies and hence comparable cooling times (see Equation 1.18). Thus, the TeV PWN should appear almost point-like on the 5' scale of

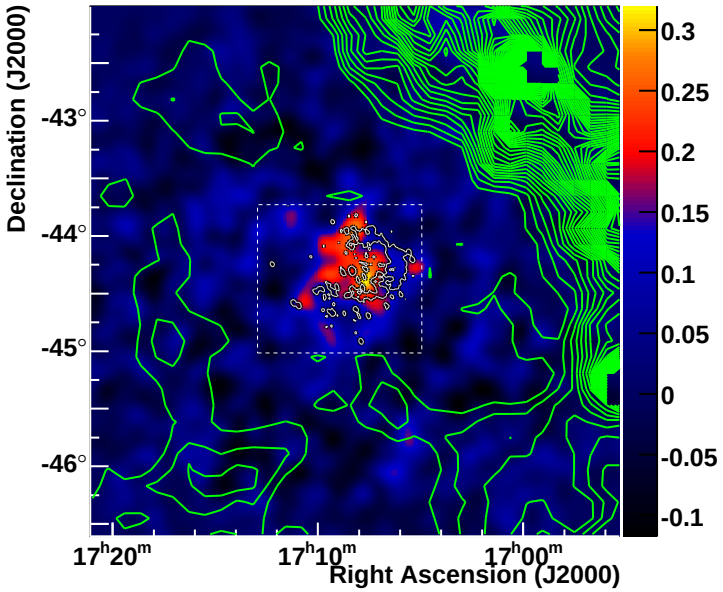

Figure 5.18: 4.6°×4.6° overview map of the region containing HESS J1708−443. The Gaussian (σ=0.075°) smoothed VHE γ-ray excess from Figure 5.15 is shown in color coding. The white contours indicate the intensity of the 330 MHz radio emission detected in VLA observations (see also contours in Figure 5.15, by courtesy of Gloria Dubner and Elisabeth Giacani). The white box illustrates the field-of-view covered by the VLA observations. Outside of this region the lower resolution 2.4 GHz radio continuum data (Duncan et al., 1995) taken with the Parkes telescope with a resolution of 10.4' is shown as green contours.

the point-spread-function of the H.E.S.S. instrument. Furthermore, given that the ratio of X-ray to VHE γ-ray energy flux is determined by the energy density in magnetic fields and IC target photon fields (Equation 1.19), the predicted γ-ray flux is well below the observed level (see red curve in Figure 5.21). This is true even if the local target radiation fields are enlarged by a factor of 10 compared to the average Galactic values for the far-infrared radiation and by a factor of 2 for starlight, as used in Aharonian et al. (1997).

One way to reconcile the difference in size of the emission regions and the high flux level of the VHE emission is to assume that the size of the X-ray PWN is essentially governed by the extent of the high-field region, and that the magnetic field falls off by a large factor outside the X-ray PWN. Then, electrons can escape from the high-field region and – by accumulation over a significant fraction of the lifetime of the pulsar – form a larger nebula only visible in VHE γ-rays. The synchrotron cooling time of electrons up-scattering CMBR photons to energies E_γ is given by

$$\tau_{\rm synch} \approx 40 \left(\frac{\rm B}{140\mu{\rm G}}\right)^{-2} \left(\frac{\rm E_\gamma}{\rm TeV}\right)^{-1/2} {\rm years} \qquad (5.7)$$

In the 140 μG field inside the X-ray PWN, the cooling time of up-scattering electrons producing 1 TeV γ-rays is ∼40 years. Assuming a dominantly advective rather than diffusive

transport process, the necessary average flow speed needed to drive electrons from the pulsar position to the edge of the X-ray PWN ($r \sim 110''$) within 40 years is $\sim 0.1\,c$, a reasonable value following the arguments of Kennel & Coroniti (1984) (see also Figure 1.11). In the low-field region outside the X-ray PWN, the synchrotron lifetime increases. Even for a magnetic field strength of $10\,\mu G$, a value about three times as large as the interstellar magnetic field, the cooling time of the aforementioned electrons is about 8,000 years and thereby almost half of the spin-down age of the pulsar (17,500 years).

This scenario still does not explain the asymmetry of the VHE γ-ray nebula with respect to the pulsar location, or the lack of detectable radiation from the location of the pulsar. Such asymmetries were observed before in other TeV PWNs, e.g. HESS J1718−385, HESS J1809−193 (Aharonian et al. (H.E.S.S. collaboration), 2007b) and HESS J1825-137 (Aharonian et al. (H.E.S.S. collaboration), 2005b, 2006e). They were explained either by the proper motion of the pulsar or by a density gradient within the ambient medium that either causes an asymmetry in the reverse shock of the original supernova or different expansion velocities of the TeV emitting electrons (Blondin et al., 2001; van der Swaluw et al., 2001); in some of the simulations of van der Swaluw et al. (2001) the displaced PWN is well separated from its pulsar. Both explanations are in principle applicable in this situation, however, the measured scintillation velocity of less than 100 km/s for the pulsar renders the former explanation unlikely. The latter explanation would favor an offset of the TeV PWN towards a low density region, contrary to the observed offset, which brings the PWN closer to the giant molecular cloud visible in Figure 5.18. It should be noted that a local density gradient, e.g. directly at the position of the pulsar, could affect the spatial distribution of the TeV PWN and might not be visible in the Parkes data.

Another problem for leptonic PWN scenarios arises from the fact that the VHE γ-ray spectrum extends up to at least 20 TeV. While synchrotron radiation from TeV electrons is well below the keV range and escapes detection, the higher-energy electrons responsible for these VHE γ-rays should create detectable X-ray emission, even for magnetic fields as low as $5\,\mu$G. The upper limit of $9{\cdot}10^{-13}\,\mathrm{erg\,s^{-1}\,cm^{-2}}$ on the 0.1-2.4 keV unabsorbed X-ray flux (Becker et al., 1995) from the bright radio arc, a region partially coincident with the putative TeV PWN (see Fig. 5.15), limits the cut-off energy of the electron spectrum to $\sim$7 TeV, at variance with the unusually extended and flat VHE γ-ray spectrum.

In this discussion it was assumed that the pulsar dominantly accelerates electrons. If a considerable fraction of the accelerated particles are hadrons, as discussed by Horns et al. (2007), the constraints imposed by the large magnetic field within the X-ray PWN are removed. The TeV emission would then originate from π^0 meson decay produced in inelastic interactions of accelerated protons with ambient gas (hadronic scenario, see Section 1.2.1), and the VHE γ-ray emission would trace the distribution of the target material. The bright radio arc, which was interpreted by Bock & Gvaramadze (2002) as the compressed outer boundary of the former wind blown bubble, could act as such a region of enhanced target material density, which would explain its coincidence with the H.E.S.S. source.

SNR G 343.1−1.3

The H.E.S.S. source is partially coincident with the bright radio arc and the surrounding diffuse emission of the SNR visible in the 1.4 GHz observations taken with the ATCA instrument (see Figure 5.15). The best fit position of the H.E.S.S. source is consistent with the apparent center of the bright radio arc (α_{2000}=17^h8^m and δ_{2000}=$-44°16'48''$). However,

due to low statistics in the VHE data, no conclusions can be made about morphological similarities. No significant VHE emission was detected from the broad-scale/diffuse emission visible further to the East of the bright radio arc, as seen in the low resolution 2.4 GHz continuum radio data (Duncan et al., 1995) (Figure 5.18). This diffuse radio emission was interpreted by Bock & Gvaramadze (2002) as originating from the eastern half of the expanding SNR shell, propagating into a low-density region.

Similar to the potential association with the PWN of PSR B1706−44, again both, leptonic and hadronic scenarios for VHE γ-ray production have to be considered. The leptonic scenario suffers from the same difficulties mentioned in the discussion of the PWN association: the non-detection of the SNR at X-ray energies implies a low energy cut-off in the injected electron spectrum below roughly 7 TeV for a magnetic field strength of 5 μG, which is difficult to reconcile with the hard γ-ray spectrum reaching up to at least 20 TeV (see Figure 5.21, black solid curve). A *free* fit of a simple leptonic model to the available multi-wavelength data results in a cut-off in the electron spectrum at ∼50 TeV, but with an unreasonably low magnetic field of ∼1 μG. Even this optimized scenario does not fully describe the hard VHE γ-ray spectrum (Figure 5.21, black dashed curve).

In the hadronic scenario, where synchrotron radiation is expected only from secondary electrons, the lack of X-ray detection can easily be accounted for. In this scenario, the total energy in accelerated protons $W_{\rm p}$ in the energy range 10-100 TeV necessary to produce the observed γ-ray luminosity L_γ can be estimated from Relation 1.28:

$$W_{\rm p}(10-100\,{\rm TeV}) \approx \tau_\gamma \times L_\gamma(1-10\,{\rm TeV}) \tag{5.8}$$

where $\tau_\gamma \approx 4.9 \cdot 10^{15} \left(\frac{\rm n}{\rm cm^{-3}}\right)^{-1}$ s is the characteristic cooling time of protons through the π^0 production channel. The total energy within the whole proton population $W_{\rm P}({\rm tot}) \approx 8.4 \times 10^{49}{\rm erg} \left(\frac{\rm n}{\rm cm^{-3}}\right)^{-1} \left(\frac{\rm D}{\rm kpc}\right)^2$ is then estimated by extrapolating the proton spectrum down to 1 GeV assuming the same spectral shape as the γ-ray spectrum. For a total energy of 10^{51} erg released in the supernova explosion, an acceleration efficiency of ϵ=0.15 and a distance of 2.5 kpc, the necessary average proton density is n≈3.5 cm^{-3}, only slightly larger than the average Galactic ambient density.

The measured VHE γ-ray spectrum reaches up to at least 20 TeV. The spectral energy distribution of γ-rays produced in the decay of mono-energetic protons drops sharply beyond roughly 15% of the original proton energy (see e.g. Kelner et al., 2006). Therefore, the parent proton population giving rise to the detected VHE γ-ray emission has to extend up to at least 130 TeV, a limit which is increasingly difficult to explain as the age of the system becomes larger. An association of SNR G 343.1−2.3 with the pulsar PSR B1706−44, a scenario controversely discussed in the community, (see e.g. Bock & Gvaramadze, 2002; Romani et al., 2005), would make the SNR rather old (∼ 17,000 years) and place it in the late Sedov-Taylor, or more likely, in the radiative phase (Section 1.3.1). However, the γ-ray emitting SNR shells unambiguously identified so far, such as RX J1713.7−3946 (Aharonian et al. (H.E.S.S. collaboration), 2007d) and RX J0852.0−4622 (Aharonian et al. (H.E.S.S. collaboration), 2007c), are much younger (∼2000 years). In case of an old SNR, a rather low ambient density is necessary to maintain the high shock velocity required for proton acceleration beyond 100 TeV. Following the approach of Truelove & McKee (1999) presented in Section 1.3.1 and assuming a very low ambient density of n≈0.001 cm^{-3}, a 10 solar mass progenitor star, and an energy release of 10^{51} erg, the resulting shock velocity for a 17,000 year old SNR is approximately

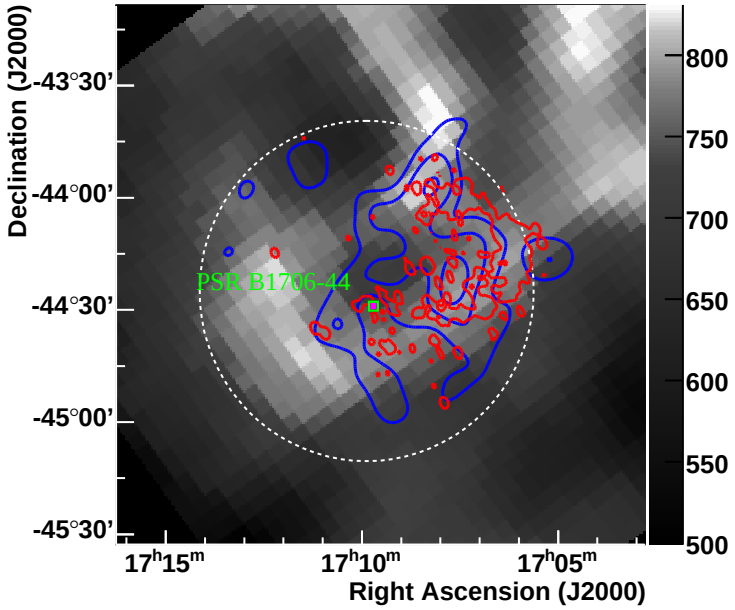

Figure 5.19: HI line emission intensity in units of $\mathrm{K\,km\,s^{-1}}$, as measured by the Parkes telescope during the Southern Galactic Plane Survey (SGPS) (McClure-Griffiths et al., 2005). The intensities are integrated in the velocity range from -13.79 $\mathrm{km\,s^{-1}}$ to -21.21 $\mathrm{km\,s^{-1}}$, corresponding to a distance of 1.6-2.3 kpc or 13.7-13.0 kpc. Contours of the Gaussian ($\sigma_{\mathrm{smooth}} = 0.075°$) smoothed VHE γ-ray excess are shown in blue. The red contours depict the intensity of the radio emission measured by the VLA instrument at 330 MHz, see also Figure 5.15 (by courtesy of Gloria Dubner and Elisabeth Giacani). The radio data has been smoothed with the same Gaussian brightness profile as the HESS data. The white circle illustrates the integration region for the velocity profile shown on the right.

1800 km/s. Following Ptuskin & Zirakashvili (2005), the maximally reached proton energy is then as high as 92 TeV (using Equation 1.44). However, to explain the observed γ-ray flux, the average density must exceed $3.5\,\mathrm{cm^{-3}}$. A constant ambient density of $3.5\,\mathrm{cm^{-3}}$ would result in a shock velocity of $\sim$200 km/s and a maximum proton energy of a few TeV. To reconcile both requirements the SNR shell had to enter a higher density region in the recent past. Such a scenario was used by Bock & Gvaramadze (2002) to explain the diffuse radio emission outside the bright radio arc.

If the SNR is in the radiative phase, the ambient material swept up by the SNR should be visible in CO or HI data. Unfortunately, no high resolution CO data are available at the moment, but a ring-like structure is visible in the HI line emission survey of the Parkes telescope, as shown in Figure 5.19. The structure is best visible in the velocity range -13.79 km/s to -21.21 km/s corresponding to a distance of either 1.6-2.3 kpc or 13.7-13.0 kpc, seen in Figure 5.20. The closer distance is compatible with the distance estimate of 2.3 kpc for the SNR extracted from dispersion measurements (Romani et al., 2005, and references therein). A rough estimate of the mass of the HI structure extracted from the radial region illustrated by the white dashed circle in Figure 5.19 is of the order

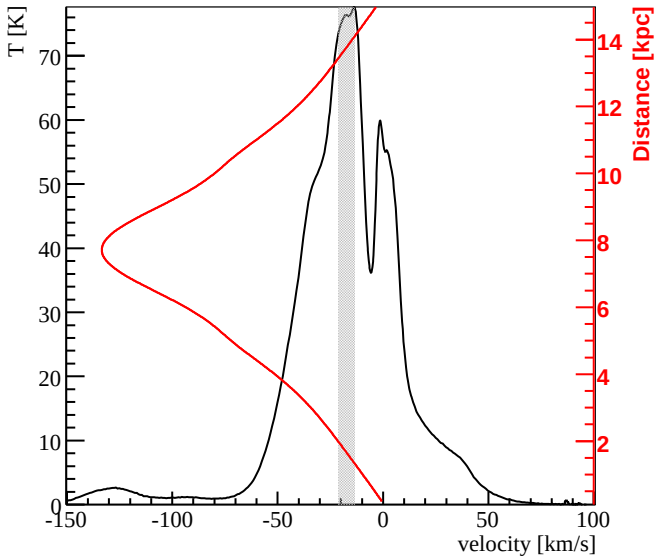

Figure 5.20: Velocity profile of HI line emission intensity, integrated within the dashed circle shown on the left. The velocity resolution is $0.08\,\mathrm{km\,s^{-1}}$. The distance/velocity correspondence from the Galactic rotation model from Fich et al. (1989) is also shown.

of 6,000 solar masses. Assuming radial symmetry, this corresponds to an original density of the swept up mass of a few protons per cm^3, comparable to the density requirements inflected by the observed γ-ray flux. The bright radio arc and the VHE γ-ray emission coincide spatially with only one half of the HI shell-like structure. This situation can be explained by the additional dependence of the radio and γ-ray emission on the target density which is probably higher closer to the parent molecular cloud. It should be noted that since the shell-like structure is nearly complete and the pulsar lies close to its center, the scenario of an off-center cavity explosion as suggested by Bock & Gvaramadze (2002) would be disfavored.

So far, the discussion of a putative association of HESS J1708−443 with the SNR G 343.1−2.3 was based on the assumption that the SNR and the pulsar PSR B1706−44 were created at the same time. If this assumption proves to be wrong, very little is known about the SNR. The age estimate using a Sedov-Taylor model is about 5,000 years (McAdam et al., 1993; Nicastro et al., 1996). The younger age would further ease the proton acceleration to energies beyond 100 TeV.

5.3.5 Summary

H.E.S.S. observations have led to the discovery of a new extended VHE γ-ray source HESS J1708−443. The possible associations of HESS J1708−443 with the energetic pulsar PSR B1706−44 and the SNR G 343.1−2.3 have been discussed using radio and HI line data. No γ-ray emission was detected at the position of the pulsar, in clear disagreement with the measurement reported by other Cherenkov instruments. The depletion of γ-rays in its vicinity renders the association of the pulsar to the H.E.S.S. source less likely even

though offset TeV PWN have been observed before. The diffuse broad scale radio emission, proposed to originate from the interaction of the SNR with an ambient molecular cloud, is positionally coincident with HESS J1708−443, suggesting an association. However, the possible connection of the SNR to PSR B1706−44 or to a shell-like structure discovered in HI line emission data suggests the SNR is in a later evolutionary stage than other previously detected VHE SNRs.

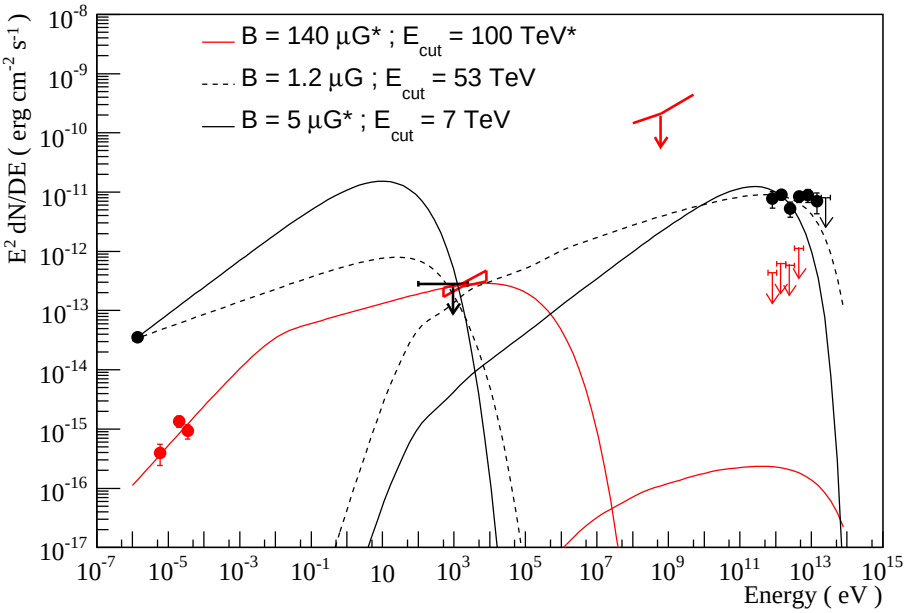

Figure 5.21: Spectral energy distribution of the PWN of PSR B1706−44 (red data points) and of the broad scale emission around G 343.1−2.3 (black data points). At very high energies the differential H.E.S.S. upper limits from region A (red) and the H.E.S.S. spectrum extracted from region C (black) are shown. At γ-ray energies, the time averaged flux detected by the EGRET satelite (Thompson et al., 1992) from the vicinity of the pulsar is shown as an upper limit to the unpulsed emission from the PWN. At X-ray energies the flux measured from the equatorial PWN by Romani et al. (2005) using the Chandra satelite (red) and the upper limit from the bright radio arc measured by Becker et al. (1995) with the ROSAT satelite (black) are depicted. At radio energies the flux points measured by Frail et al. (1994b) for the broad scale radio emission (black) and by Giacani et al. (2001) for the pulsar (red) are given. A simple Synchrotron/Inverse Compton model was fit to the data. Only Inverse Compton scattering in the Thompson regime on the Cosmic Microwave Background Radiation and on photons from dust and starlight is considered. Following Aharonian et al. (1997), the energy density of the dust far-infrared radiation is fixed to $0.5\,\mathrm{eV/cm^3}$. The local star light density is set to $1\,\mathrm{eV/cm^3}$. The red curve is the best fit to the pulsar region emission data points assuming a magnetic field of $140\,\mu$G as suggested by Romani et al. (2005). The black dashed curve represents a free fit to the broad scale emission, resulting in a magnetic field of $\sim 1\mu$G, the black solid curve marks the best fit with a fixed magnetic field of 5μG. Parameters labeled with a (*) have been fixed in the corresponding fit.

Chapter 6

Conclusions and Outlook

Eighteen years after the discovery of the Crab nebula by the Whipple collaboration, Imaging Atmospheric Cherenkov telescopes have detected 52 VHE γ-ray sources within our Galaxy. When H.E.S.S. started operation in the year 2003, only $\sim$10 such sources were known including some false detection claimed by the Cangaroo collaboration such as PSR B1706-44 and SN 1006. The H.E.S.S. Galactic plane survey, the results of which have been presented within this work, was remarkably successful in detecting new sources, adding further $\sim$35 previously unknown VHE γ-ray emitters to the Galactic γ-ray club. The increasing number of these sources allows one now – for the first time – to look for common properties among them: most cluster closely along the Galactic plane hinting at large distances on the order of kilo parsecs rather than local objects; their energy spectra follow power laws, with a rather hard spectral indices $< \Gamma > \approx 2.3$, well compatible with the predictions of diffusive and/or relativistic shock acceleration.

Extensive multi-wavelength studies have been performed to identify the individual astrophysical objects giving rise to the observed VHE γ-ray emission. So far three distinct classes of counterparts have been established with confidence: supernova remnants, pulsar wind nebulae and binary systems. Up to now, shell-like VHE morphology has been unambiguously resolved in only two shell-type supernova remnants: RX J1713.7-3946 and Vela Jr. Hopefully, RCW 86 will join them in the near future when more data is taken on this source. The nature of the energetic particles within the expanding shocks of these objects is still not settled. A hadronic origin could be established by a spatial correlation of the γ-ray emission with available target material. Such a correlation might have already been found with the detection of HESS J1800-240 and HESS J1801-233 in the old SNR W 28.

Pulsar wind nebulae provide the largest population of identified VHE γ-ray emitters. HESS J1912+101 and HESS J1708-442, the discovery of which was presented in this work, might also belong to this class. Given the large number of extended VHE γ-ray sources within the Galaxy, the probability of a chance coincidence with a pulsar is not negligible. Carrigan et al. (2007) performed a statistical study of PWN associations and found a clear excess of positional coincidences with high spin-down luminosity pulsars beyond the expectations for chance coincidences. The implied conversion efficiencies from rotational energy to VHE γ-rays is of the order of 1%.

Binary systems of a compact object and a massive star constitute the third class of well established Galactic VHE γ-ray sources. Three of them have been identified so far:

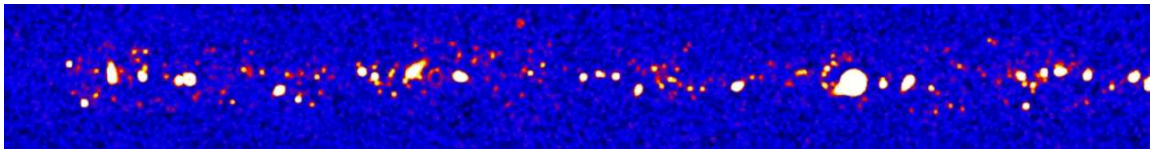

Figure 6.1: Simulated view of the Galactic plane with an Imaging Cherenkov instrument with 10 times the effective area of the H.E.S.S.-I experiment; assumed was an angular resolution and a background rejection improved by a factor 2 with respect to H.E.S.S.-I, the resultant sensitivity improvement is approximately by a factor of 9. By courtesy of German Herman.

PSR B1259−63, LS 5039 and LSI+61 303, which was discovered by the MAGIC collaboration. They appear to be either microquasars or binary PWN. The association with the later seems certain only for PSR B1259−63, in the other two cases the orbiting compact objects could be black holes. Beyond these established source classes, indications of a new emerging class have been found through the detection of HESS J1023-575, which is positionally coincident with a cluster of massive stars. The proposed association of the VHE emission to their collective winds, however, needs to be strengthened by further discoveries of such kind. Despite the ongoing effort, many of the currently known Galactic sources remain unidentified, paying tribute to the difficulties involved in identifying extended sources without clear substructure in a region as crowded as the Galactic plane.

The first phase of the H.E.S.S. Galactic plane survey is now complete, the survey region spans from l=280° to l=60° covering a strip of ∼6° width centered along the Galactic Plane. A further extension of the survey region is hardly possible due to the disadvantageous zenith angles and the rainy season in Namibia. Future observations with the H.E.S.S. phase-I array will most likely concentrate on individual sources and on deep surveys of selected regions within the Galactic plane. This will naturally change when the second stage of extension of the H.E.S.S. experiment becomes operative. HESS phase-II consists of the original HESS-I array upgraded by a fifth telescope which is considerably larger (600 m^2) than any of the other four telescopes and will be placed in the center of the array. The additional telescope will decrease the energy threshold down to ∼20 GeV and additionally improve its sensitivity in the current HESS-I energy range. The improved performance of the HESS-II experiment will probably lead to the detection of even more Galactic VHE γ-ray sources. Furthermore, the reconstruction of a wider spectrum in energy can give useful information on the γ-ray production mechanisms in SNRs and will help to distinguish leptonic and hadronic scenarios. In the case of pulsars, low-energy measurements might allow to distinguish between the two basic model classes, the pulsar cap and the outer gap model.

The construction of the large H.E.S.S.-II telescope has already begun and will be finished in the year 2009. A project a bit further in future is the Cherenkov Telescope Array (CTA), which is being designed as the next generation ground-based γ-ray instrument. CTA is supposed to serve as an open observatory in contrast to the current instruments which are operated by collaborations. The aim of this project is to improve the sensitivity by a factor of 5-10 in the current HESS-I energy range and extend the accessible energy

domain to well below 100 GeV and to above 100 TeV. The project is currently in the stage of design studies and simulations. Figure 6.1 shows a possible view of the Galactic plane observed with a CTA-like instrument, suggesting a bright future for VHE γ-ray astronomy.

Appendix A

The H.E.S.S. Galactic Plane Survey: More Details

In this section additional information will be given on the H.E.S.S. Galactic plane survey. The two additional significance maps which are used in the blind search for unknown VHE γ-ray sources within the Galactic plane are shown. The maps are equivalent to Figure 4.5 but are produced with different correlation radii. Furthermore, additional flux maps of the Galactic plane will be presented. At the end a table is given summarizing all publications concerning Galactic VHE γ-ray sources observed with the H.E.S.S. experiment.

A.1 Additional Significance and Flux Maps

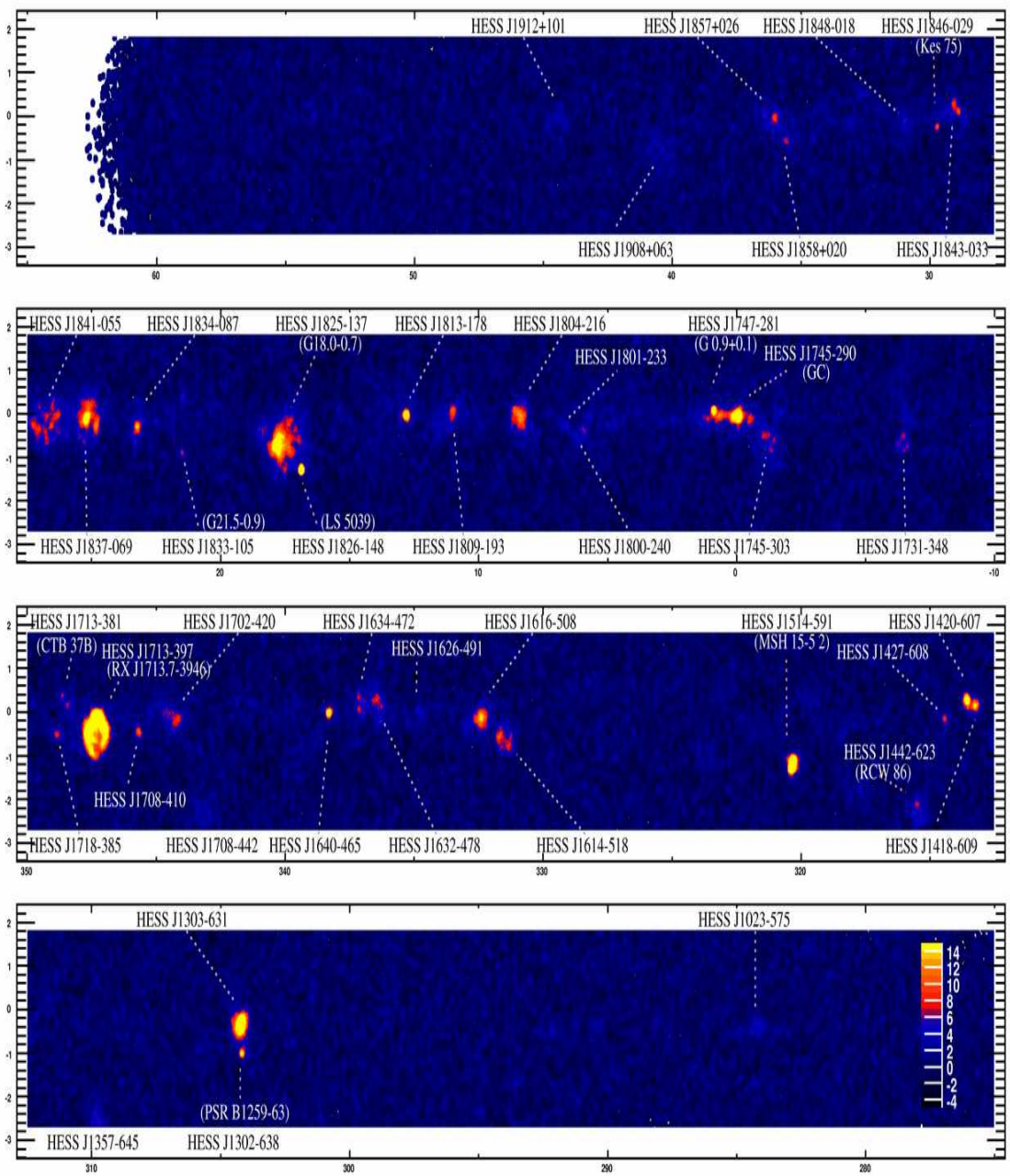

Figure A.1: Additional significance map of the H.E.S.S. Galactic plane survey region used to search for new VHE γ-ray sources. The maps was created using the parameter set 1 summarized in Table 4.2. All VHE γ-ray source from Table 4.4 and 4.5 are labeled. The color scale is truncated at 15 σ for visibility.

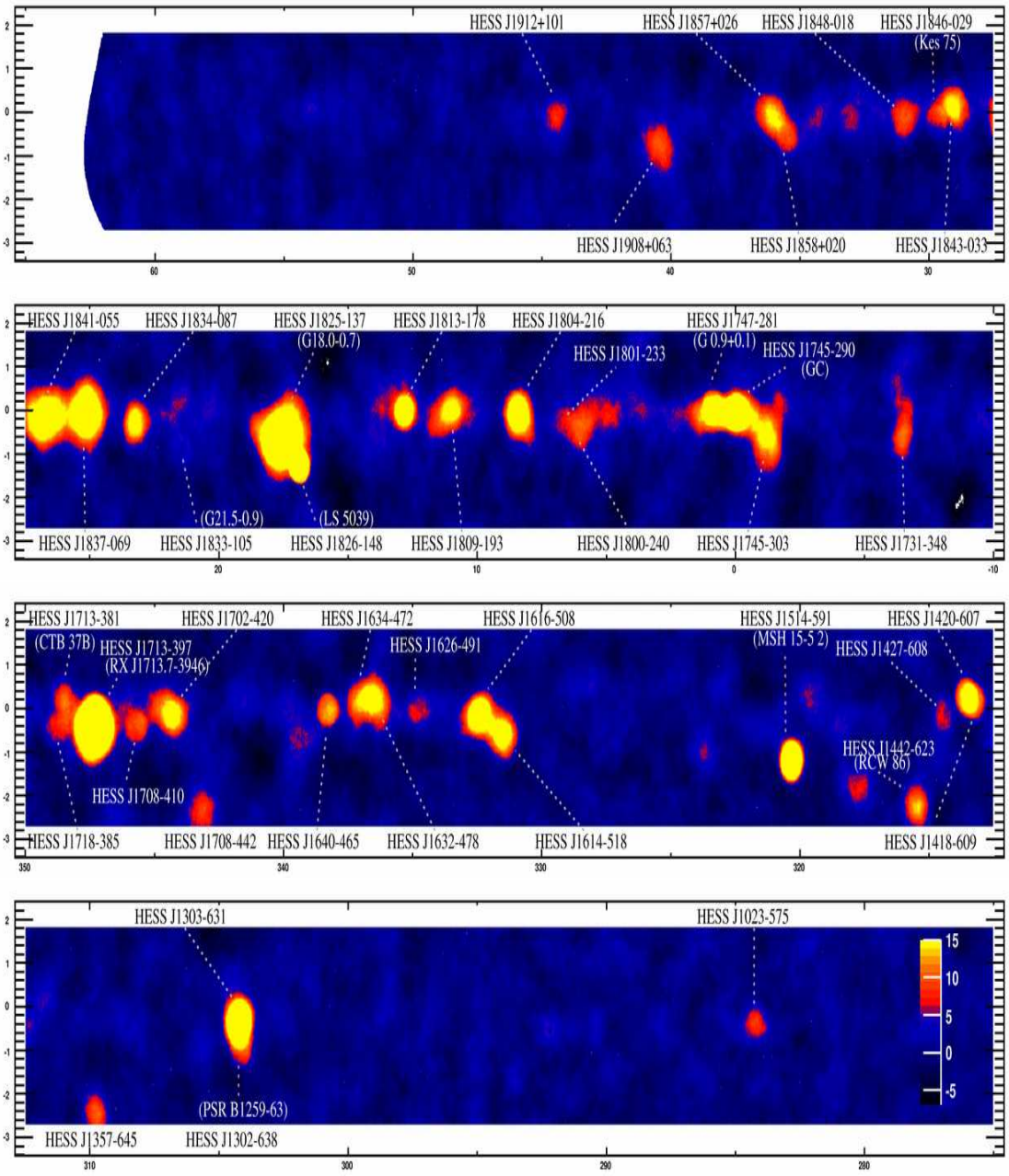

Figure A.2: Third significance map of the H.E.S.S. Galactic plane survey region produced using parameter set 3 given in Table 4.2. The color scale is truncated at 15 σ for visibility.

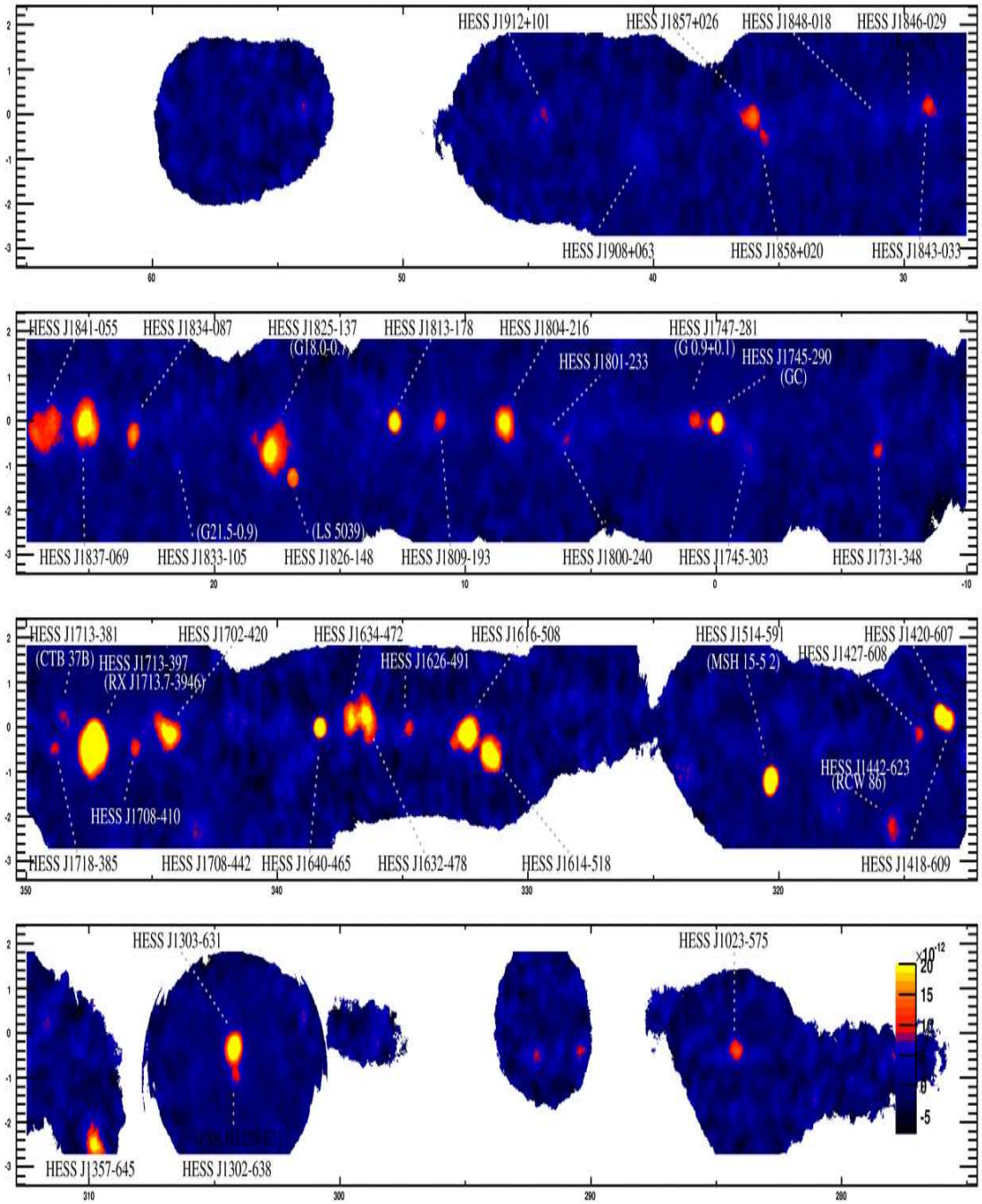

Figure A.3: Flux map of the H.E.S.S. Galactic plane survey region in units of $\mathrm{cm}^{-2}\ \mathrm{s}^{-1}$. The map is equivalent to Figure 4.7 with the exception that no requirement on the significance of signal is made. Only regions with a point-source sensitivity of better then 2.5% of the Crab nebula flux are shown.

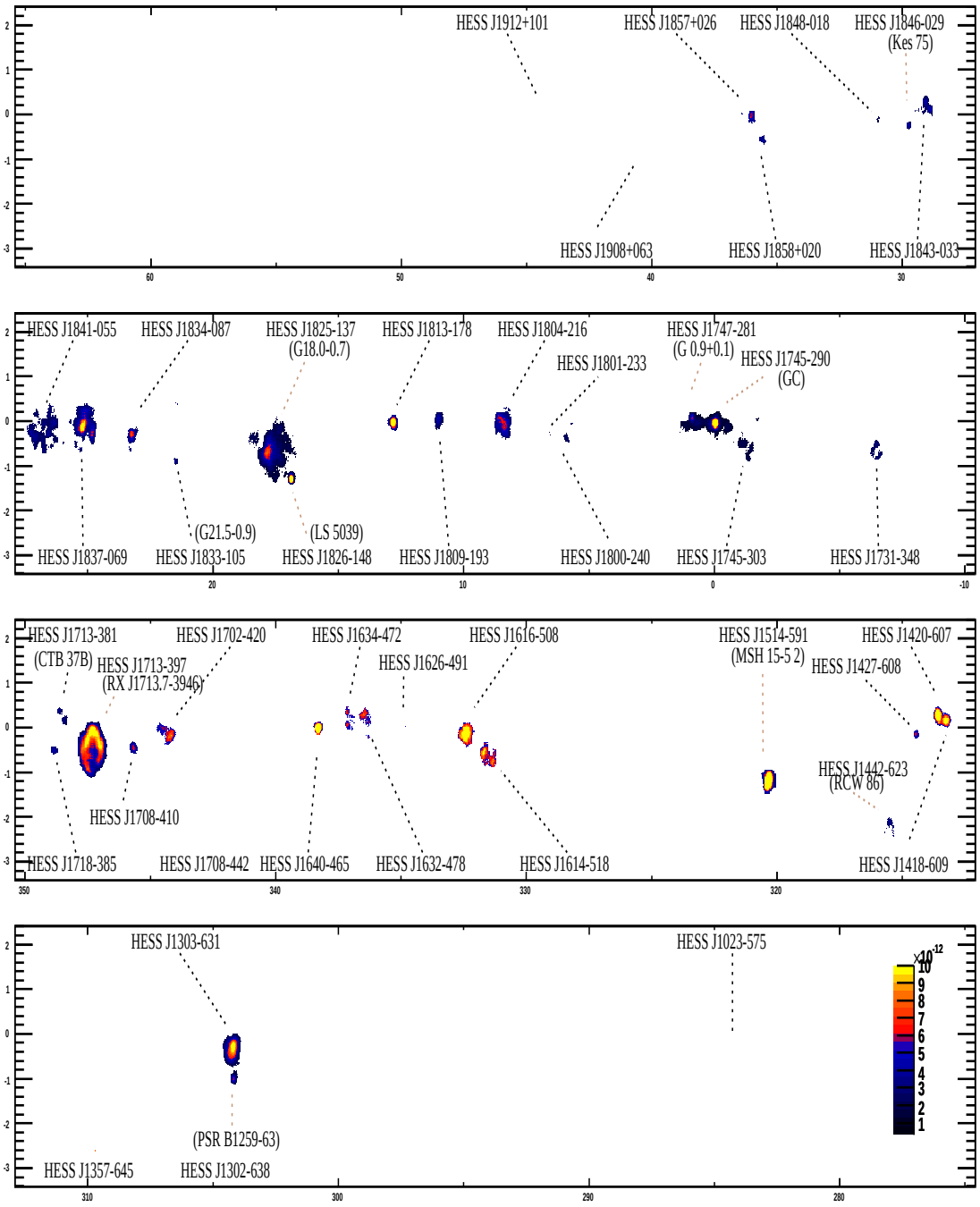

Figure A.4: Flux map of the H.E.S.S. Galactic plane survey region in units of $\mathrm{cm}^{-2}\ \mathrm{s}^{-1}$. The map is equivalent to Figure 4.7, only the correlation radius has been changed to 0.1°.

A.2 Sources and their References

Source	Reference
HESS J1023-575	Aharonian et al. (H.E.S.S. collaboration) (2007a)
HESS J1303-638	Aharonian et al. (H.E.S.S. collaboration) (2005f)
HESS J1303-631	Aharonian et al. (H.E.S.S. collaboration) (2005f)
HESS J1356-645	Aharonian et al. (H.E.S.S. collaboration) (2008e)
HESS J1418-609	Aharonian et al. (H.E.S.S. collaboration) (2006d)
HESS J1420-607	Aharonian et al. (H.E.S.S. collaboration) (2006d)
HESS J1427-608	Aharonian et al. (H.E.S.S. collaboration) (2008g)
HESS J1442-623	Hoppe et al. (2007b)
HESS J1507-622	not published
HESS J1514-591	Aharonian et al. (H.E.S.S. collaboration) (2005c)
HESS J1614-518	Aharonian et al. (H.E.S.S. collaboration) (2005a)
HESS J1616-508	Aharonian et al. (H.E.S.S. collaboration) (2005a)
HESS J1626-491	Aharonian et al. (H.E.S.S. collaboration) (2008g)
HESS J1632-478	Aharonian et al. (H.E.S.S. collaboration) (2006h)
HESS J1634-472	Aharonian et al. (H.E.S.S. collaboration) (2006h)
HESS J1640-465	Aharonian et al. (H.E.S.S. collaboration) (2005a)
HESS J1708-442	not published
HESS J1702-420	Aharonian et al. (H.E.S.S. collaboration) (2006h, 2008g)
HESS J1708-410	Aharonian et al. (H.E.S.S. collaboration) (2006h, 2008g)
HESS J1713-397	Aharonian et al. (H.E.S.S. collaboration) (2004b, 2006b, 2007d)
HESS J1714-385	Aharonian et al. (H.E.S.S. collaboration) (2008b)
HESS J1713-381	Aharonian et al. (H.E.S.S. collaboration) (2006h, 2008a)
HESS J1718-385	Aharonian et al. (H.E.S.S. collaboration) (2007b)
HESS J1731-347	Aharonian et al. (H.E.S.S. collaboration) (2008g)
HESS J1745-303	Aharonian et al. (H.E.S.S. collaboration) (2006h, 2008f)
HESS J1745-290	Aharonian et al. (H.E.S.S. collaboration) (2004c)
HESS J1747-281	Aharonian et al. (H.E.S.S. collaboration) (2005g)
HESS J1800-240	Aharonian et al. (H.E.S.S. collaboration) (2008c)
HESS J1801-233	Aharonian et al. (H.E.S.S. collaboration) (2008c)
HESS J1804-216	Aharonian et al. (H.E.S.S. collaboration) (2005a, 2006h)
HESS J1809-193	Aharonian et al. (H.E.S.S. collaboration) (2007b)
HESS J1813-178	Aharonian et al. (H.E.S.S. collaboration) (2005a, 2006h)
HESS J1826-148	Aharonian et al. (H.E.S.S. collaboration) (2005d, 2006a)
HESS J1825-137	Aharonian et al. (H.E.S.S. collaboration) (2005a,b, 2006e)
HESS J1833-105	Djannati-Atai et al. (2007a)
HESS J1834-087	Aharonian et al. (H.E.S.S. collaboration) (2005a, 2006h)
HESS J1837-069	Aharonian et al. (H.E.S.S. collaboration) (2005a, 2006h)
HESS J1841-055	Aharonian et al. (H.E.S.S. collaboration) (2008g)
HESS J1843-033	Hoppe et al. (2007a)
HESS J1846-029	Djannati-Atai et al. (2007a)
HESS J1848-018	not published
HESS J1858+020	Aharonian et al. (H.E.S.S. collaboration) (2008g)
HESS J1857+026	Aharonian et al. (H.E.S.S. collaboration) (2008g)
HESS J1908+062	Djannati-Atai et al. (2007b)
HESS J1912+101	Aharonian et al. (H.E.S.S. collaboration) (2008d)

Table A.1: Table of references for all Galactic VHE γ-ray sources

Bibliography

Abdo, A. A., Allen, B., Berley, D., et al. 2007, ApJ, 664, L91

Achterberg, A., Gallant, Y. A., Kirk, J. G., & Guthmann, A. W. 2001, MNRAS, 328, 393

Aharonian, F. A., Atoyan, A. M., & Kifune, T. 1997, MNRAS, 291, 162

Aharonian, F. A. & Bogovalov, S. V. 2003, New Astronomy, 8, 85

Aharonian et al. (HEGRA collaboration). 2002, A&A, 395, 803

Aharonian et al. (H.E.S.S. collaboration). 2001, A&A, 370, 112

Aharonian et al. (H.E.S.S. collaboration). 2004a, Astroparticle Physics, 22, 109

Aharonian et al. (H.E.S.S. collaboration). 2004b, Nature, 432, 75

Aharonian et al. (H.E.S.S. collaboration). 2004c, A&A, 425, L13

Aharonian et al. (H.E.S.S. collaboration). 2005a, Science, 307, 1938

Aharonian et al. (H.E.S.S. collaboration). 2005b, A&A, 442, L25

Aharonian et al. (H.E.S.S. collaboration). 2005c, A&A, 435, L17

Aharonian et al. (H.E.S.S. collaboration). 2005d, Science, 309, 746

Aharonian et al. (H.E.S.S. collaboration). 2005e, A&A, 432, L9

Aharonian et al. (H.E.S.S. collaboration). 2005f, A&A, 439, 1013

Aharonian et al. (H.E.S.S. collaboration). 2005g, A&A, 432, L25

Aharonian et al. (H.E.S.S. collaboration). 2006a, A&A, 460, 743

Aharonian et al. (H.E.S.S. collaboration). 2006b, A&A, 449, 223

Aharonian et al. (H.E.S.S. collaboration). 2006c, A&A, 456, 245

Aharonian et al. (H.E.S.S. collaboration). 2006d, A&A, 456, 245

Aharonian et al. (H.E.S.S. collaboration). 2006e, A&A, 460, 365

Aharonian et al. (H.E.S.S. collaboration). 2006f, A&A, 448, L43

Aharonian et al. (H.E.S.S. collaboration). 2006g, A&A, 457, 899

Aharonian et al. (H.E.S.S. collaboration). 2006h, ApJ, 636, 777

Aharonian et al. (H.E.S.S. collaboration). 2007a, A&A, 467, 1075

Aharonian et al. (H.E.S.S. collaboration). 2007b, ArXiv e-prints, 705

Aharonian et al. (H.E.S.S. collaboration). 2007c, ApJ, 661, 236

Aharonian et al. (H.E.S.S. collaboration). 2007d, A&A, 464, 235

Aharonian et al. (H.E.S.S. collaboration). 2008a, A&A, 486, 829

Aharonian et al. (H.E.S.S. collaboration). 2008b, ArXiv e-prints, 803

Aharonian et al. (H.E.S.S. collaboration). 2008c, ArXiv e-prints, 801

Aharonian et al. (H.E.S.S. collaboration). 2008d, A&A, 484, 435

Aharonian et al. (H.E.S.S. collaboration). 2008e, A&Ain preparation

Aharonian et al. (H.E.S.S. collaboration). 2008f, A&A, 483, 509

Aharonian et al. (H.E.S.S. collaboration). 2008g, A&A, 477, 353

Albert, J., Aliu, E., Anderhub, H., et al. 2007, A&A, 474, 937

Amato, E. & Arons, J. 2006, ApJ, 653, 325

Anderson, G. P., Kneizys, F. X., Chetwynd, J. H., et al. 1996, in Presented at the Society of Photo-Optical Instrumentation Engineers (SPIE) Conference, Vol. 2830, Proc. SPIE Vol. 2830, p. 82-93, Optical Spectroscopic Techniques and Instrumentation for Atmospheric and Space Research II, Paul B. Hays; Jinxue Wang; Eds., ed. P. B. Hays & J. Wang, 82–93

Arikawa, Y., Tatematsu, K., Sekimoto, Y., & Takahashi, T. 1999, PASJ, 51, L7

Axford, W. I., Leer, E., & Skadron, G. 1978, in International Cosmic Ray Conference, Vol. 11, International Cosmic Ray Conference, 132–137

Bamba, A., Koyama, K., & Tomida, H. 2000, PASJ, 52, 1157

Bamba, A., Ueno, M., Koyama, K., & Yamauchi, S. 2003a, ApJ, 589, 253

Bamba, A., Yamazaki, R., Ueno, M., & Koyama, K. 2003b, ApJ, 589, 827

Bamba, A., Yamazaki, R., Yoshida, T., Terasawa, T., & Koyama, K. 2005, ApJ, 621, 793

Becker, R. H. & Helfand, D. J. 1984, ApJ, 283, 154

Becker, W., Brazier, K. T. S., & Truemper, J. 1995, A&A, 298, 528

Bednarek, W. 2005, MNRAS, 363, L46

Bednarz, J. & Ostrowski, M. 1998, Physical Review Letters, 80, 3911

Bell, A. R. 1978a, MNRAS, 182, 147

Bell, A. R. 1978b, MNRAS, 182, 443

Benbow, W. (for the H.E.S.S. Collaboration). 2005, in American Institute of Physics Conference Series, Vol. 745, High Energy Gamma-Ray Astronomy, ed. F. A. Aharonian, H. J. Völk, & D. Horns, 611–616

Benjamin, R. A., Churchwell, E., Babler, B. L., et al. 2003, PASP, 115, 953

Berezhko, E. G. & Ellison, D. C. 1999, ApJ, 526, 385

Berezhko, E. G., Elshin, V. K., & Ksenofontov, L. T. 1996, Soviet Journal of Experimental and Theoretical Physics, 82, 1

Berezhko, E. G., Ksenofontov, L. T., & Völk, H. J. 2002, A&A, 395, 943

Berezhko, E. G. & Völk, H. J. 2000, Astroparticle Physics, 14, 201

Berezhko, E. G. & Völk, H. J. 2004, A&A, 427, 525

Berezhko, E. G. & Völk, H. J. 2006, A&A, 451, 981

Blandford, R. D. & Ostriker, J. P. 1978, ApJ, 221, L29

Blondin, J. M., Chevalier, R. A., & Frierson, D. M. 2001, ApJ, 563, 806

Blum, R. D., Damineli, A., & Conti, P. S. 1999, AJ, 117, 1392

Blumenthal, G. R. & Gould, R. J. 1970, Reviews of Modern Physics, 42, 237

Bocchino, F., van der Swaluw, E., Chevalier, R., & Bandiera, R. 2005, A&A, 442, 539

Bocchino, F., Vink, J., Favata, F., Maggio, A., & Sciortino, S. 2000, A&A, 360, 671

Bock, D. C.-J. & Gvaramadze, V. V. 2002, A&A, 394, 533

Bolz, O. 2004, PhD in Pysics, Ruprecht-Karls-Universität Heidelberg

Bolz, O. 2004, Universität Heidelberg

Bonanos, A. Z., Stanek, K. Z., Udalski, A., et al. 2004, ApJ, 611, L33

Borkowski, K. J., Rho, J., Reynolds, S. P., & Dyer, K. K. 2001, ApJ, 550, 334

Brogan, C. L., Devine, K. E., Lazio, T. J., et al. 2004, AJ, 127, 355

Brogan, C. L., Gelfand, J. D., Gaensler, B. M., Kassim, N. E., & Lazio, T. J. W. 2006, ApJ, 639, L25

Camilo, F., Manchester, R. N., Lyne, A. G., et al. 2004, ApJ, 611, L25

Camilo, F., Ransom, S. M., Gaensler, B. M., et al. 2006, ApJ, 637, 456

Cappellaro, E. 2001, Memorie della Societa Astronomica Italiana, 72, 863

Carrigan, S., Hinton, J. A., Hofmann, W., et al. 2007, ArXiv e-prints, 709

Chadwick, P. M., Dickinson, M. R., Dipper, N. A., et al. 1998, Astroparticle Physics, 9, 131

Chevalier, R. A. 1982, ApJ, 258, 790

Chevalier, R. A. & Fransson, C. 1994, ApJ, 420, 268

Cioffi, D. F., McKee, C. F., & Bertschinger, E. 1988, ApJ, 334, 252

Claas, J. J., Kaastra, J. S., Smith, A., Peacock, A., & de Korte, P. A. J. 1989, ApJ, 337, 399

Clark, D. H. & Stephenson, F. R. 1977, The historical supernovae (Oxford [Eng.] ; New York : Pergamon Press, 1977. 1st ed.)

Claussen, M. J., Frail, D. A., Goss, W. M., & Gaume, R. A. 1997, ApJ, 489, 143

Claussen, M. J., Goss, W. M., Frail, D. A., & Desai, K. 1999, ApJ, 522, 349

Cordes, J. M. & Lazio, T. J. W. 2002, ArXiv Astrophysics e-prints

Cortina, J. 2005, Ap&SS, 297, 245

de Jager, O. C. & Djannati-Ataï, A. 2008, ArXiv e-prints, 803

de Jager, O. C., Harding, A. K., Michelson, P. F., et al. 1996, ApJ, 457, 253

de Naurois, M. 2006, ArXiv Astrophysics e-prints

Djannati-Atai, A., De Jager, O. C., Terrier, R., et al. 2007a, ArXiv e-prints, 710

Djannati-Atai, A., Ona-Wilhelmi, E., Renaud, M., Hoppe, S., & for the H. E. S. S. Collaboration. 2007b, ArXiv e-prints, 710

Dodson, R. & Golap, K. 2002, MNRAS, 334, L1

Drury, L. O. 1983, Reports of Progress in Physics, 46, 973

Drury, L. O., Aharonian, F. A., & Voelk, H. J. 1994, A&A, 287, 959

Dubner, G. M., Velázquez, P. F., Goss, W. M., & Holdaway, M. A. 2000, AJ, 120, 1933

Duncan, A. R., Stewart, R. T., Haynes, R. F., & Jones, K. L. 1995, MNRAS, 277, 36

Ellison, D. C., Decourchelle, A., & Ballet, J. 2004, A&A, 413, 189

Esposito, P., Tiengo, A., de Luca, A., & Mattana, F. 2007, A&A, 467, L45

Fedorenko, V. N., Ostriakov, V. M., Poliudov, A. N., & Shapiro, V. D. 1990, Soviet Journal of Plasma Physics, 16, 443

Feldman, G. J. & Cousins, R. D. 1998, Phys. Rev. D, 57, 3873

Fermi, E. 1949, Physical Review, 75, 1169

Fich, M., Blitz, L., & Stark, A. A. 1989, ApJ, 342, 272

Fields, B. D., Olive, K. A., Cassé, M., & Vangioni-Flam, E. 2001, A&A, 370, 623

Finley, J. P., Srinivasan, R., Saito, Y., et al. 1998, ApJ, 493, 884

Fonseca, V. 1998, Ap&SS, 263, 377

Frail, D. A., Goss, W. M., & Slysh, V. I. 1994a, ApJ, 424, L111

Frail, D. A., Goss, W. M., & Whiteoak, J. B. Z. 1994b, ApJ, 437, 781

Gaensler, B. M., Schulz, N. S., Kaspi, V. M., Pivovaroff, M. J., & Becker, W. E. 2003, ApJ, 588, 441

Gaensler, B. M. & Slane, P. O. 2006, ARA&A, 44, 17

Giacani, E. B., Frail, D. A., Goss, W. M., & Vieytes, M. 2001, AJ, 121, 3133

Ginzburg, V. L. 1979, Theoretical physics and astrophysics (International Series in Natural Philosophy, Oxford: Pergamon, 1979)

Goebel. 2007, ArXiv e-prints, 709

Gorham, P. W. 1990, ApJ, 364, 187

Gotthelf, E. V. 2004, in IAU Symposium, Vol. 218, Young Neutron Stars and Their Environments, ed. F. Camilo & B. M. Gaensler, 225

Gotthelf, E. V., Halpern, J. P., & Dodson, R. 2002, ApJ, 567, L125

Gotthelf, E. V., Vasisht, G., Boylan-Kolchin, M., & Torii, K. 2000, ApJ, 542, L37

Goudis, C. 1976, Ap&SS, 40, 91

Green, A. J., Cram, L. E., Large, M. I., & Ye, T. 1999, ApJS, 122, 207

Green, D. A. 2004, Bulletin of the Astronomical Society of India, 32, 335

Gupta, Y., Mitra, D., Green, D. A., & Acharyya, A. 2005, Current Science, 89, 853

Hannikainen, D. C., Rodriguez, J., Cabanac, C., et al. 2004, A&A, 423, L17

Harding, A. K. 2001, in American Institute of Physics Conference Series, Vol. 558, American Institute of Physics Conference Series, ed. F. A. Aharonian & H. J. Völk, 115–+

Harding, A. K. & Gaisser, T. K. 1990, ApJ, 358, 561

Harris, D. E. & Roberts, J. A. 1960, PASP, 72, 237

Hartman, R. C., Bertsch, D. L., Bloom, S. D., et al. 1999, VizieR Online Data Catalog, 212, 30079

Haverkorn, M., Gaensler, B. M., McClure-Griffiths, N. M., Dickey, J. M., & Green, A. J. 2006, ApJS, 167, 230

Heck, D., Knapp, J., Capdievelle, J. D., Schatz, G., & Thouw, T. 1998, Forschungszentrum Karlsruhe Technical Report, Report FZKA 6019

Helfand, D. J., Becker, R. H., White, R. L., Fallon, A., & Tuttle, S. 2006, AJ, 131, 2525

Helfand, D. J., Collins, B. F., & Gotthelf, E. V. 2003, ApJ, 582, 783

HESS Collaboration: F. Aharonian. 2008, ArXiv e-prints, 803

HESS Collaboration: F Aharonian. 2008, ArXiv e-prints, 803

Hessels, J. W. T., Nice, D. J., Gaensler, B. M., et al. 2008, ApJ, 682, L41

Hewish, A., Bell, S. J., Pilkington, J. D., Scott, P. F., & Collins, R. A. 1968, Nature, 217, 709

Hinton, J. A. 2004, New Astronomy Review, 48, 331

Hoppe, S., , & for the H. E. S. S. Collaboration. 2007a, ArXiv e-prints, 710

Hoppe, S., Lemoine-Goumard, M., & for the H. E. S. S. Collaboration. 2007b, ArXiv e-prints, 709

Horns, D., Aharonian, F., Hoffmann, A. I. D., & Santangelo, A. 2007, Ap&SS, 309, 189

Hoshino, M., Arons, J., Gallant, Y. A., & Langdon, A. B. 1992, ApJ, 390, 454

Jackson, J. M., Rathborne, J. M., Shah, R. Y., et al. 2006, ApJS, 163, 145

Johnston, S., Lyne, A. G., Manchester, R. N., et al. 1992, MNRAS, 255, 401

Johnston, S., Nicastro, L., & Koribalski, B. 1998, MNRAS, 297, 108

Kaiser, C. R., Sokoloski, J. L., Gunn, K. F., & Brocksopp, C. 2005, Ap&SS, 300, 283

Kaspi, V. M., Lyne, A. G., Manchester, R. N., et al. 1993, ApJ, 409, L57

Kassim, N. E. 1988, ApJ, 328, L55

Kelner, S. R., Aharonian, F. A., & Bugayov, V. V. 2006, Phys. Rev. D, 74, 034018

Kennel, C. F. & Coroniti, F. V. 1984, ApJ, 283, 694

Kesteven, M. J. & Caswell, J. L. 1987, A&A, 183, 118

Kifune, T., Tanimori, T., Ogio, S., et al. 1995, ApJ, 438, L91

Kirk, J. G., Guthmann, A. W., Gallant, Y. A., & Achterberg, A. 2000, ApJ, 542, 235

Kirk, J. G., Lyubarsky, Y., & Petri, J. 2007, ArXiv Astrophysics e-prints

Koribalski, B., Johnston, S., Weisberg, J. M., & Wilson, W. 1995, ApJ, 441, 756

Koyama, K., Petre, R., Gotthelf, E. V., et al. 1995, Nature, 378, 255

Krymskii, G. F. 1977, Akademiia Nauk SSSR Doklady, 234, 1306

Kubo, H., Asahara, A., Bicknell, G. V., et al. 2004, New Astronomy Review, 48, 323

Kubo, H., Dazeley, S. A., Edwards, P. G., et al. 2000, in American Institute of Physics Conference Series, Vol. 515, American Institute of Physics Conference Series, ed. B. L. Dingus, M. H. Salamon, & D. B. Kieda, 313–+

Kuchar, T. A. & Bania, T. M. 1994, ApJ, 436, 117

Kulsrud, R. M. & Cesarsky, C. J. 1971, Astrophys. Lett., 8, 189

Kushida, J. & Cangaroo Collaboration. 2003, in International Cosmic Ray Conference, Vol. 4, International Cosmic Ray Conference, 2493–+

Lafferty, G. D. & Wyatt, T. R. 1995, Nuclear Instruments and Methods in Physics Research A, 355, 541

Lagage, P. O. & Cesarsky, C. J. 1983a, A&A, 118, 223

Lagage, P. O. & Cesarsky, C. J. 1983b, A&A, 125, 249

Leahy, D. A. & Tian, W. W. 2008, A&A, 480, L25

Li, T.-P. & Ma, Y.-Q. 1983, ApJ, 272, 317

Lozinskaya, T. A. 1981, Soviet Astronomy Letters, 7, 17

Lu, F. J., Li, T. P., Sun, X. J., Wu, M., & Page, C. G. 1996, A&AS, 115, 395

Lucek, S. G. & Bell, A. R. 2000, MNRAS, 314, 65

Malkov, M. A. & O'C Drury, L. 2001, Reports on Progress in Physics, 64, 429

Manchester, R. N., Hobbs, G. B., Teoh, A., & Hobbs, M. 2005, AJ, 129, 1993

Manchester, R. N. & Taylor, J. H. 1977, Pulsars (San Francisco : W. H. Freeman, c1977.), 36–+

Mathis, J. S., Mezger, P. G., & Panagia, N. 1983, A&A, 128, 212

McAdam, W. B., Osborne, J. L., & Parkinson, M. L. 1993, Nature, 361, 516

McClure-Griffiths, N. M., Dickey, J. M., Gaensler, B. M., et al. 2005, ApJS, 158, 178

McKee, C. F. 1974, ApJ, 188, 335

McKenzie, J. F. & Völk, H. J. 1982, A&A, 116, 191

Migliazzo, J. M., Gaensler, B. M., Backer, D. C., et al. 2002, ApJ, 567, L141

Morris, D. J., Hobbs, G., Lyne, A. G., et al. 2002, MNRAS, 335, 275

Nespoli, E., Fabregat, J., & Mennickent, R. 2007, The Astronomer's Telegram, 983, 1

Nicastro, L., Johnston, S., & Koribalski, B. 1996, A&A, 306, L49+

Nomoto, K., Shigeyama, T., Kumagai, S., Yamaoka, H., & Suzuki, T. 1994, in Supernovae, ed. S. A. Bludman, R. Mochkovitch, & J. Zinn-Justin, 489–+

Nomoto, K., Tanaka, M., Tominaga, N., Maeda, K., & Mazzali, P. A. 2007, ArXiv e-prints, 707

O'C Drury, L., Duffy, P., & Kirk, J. G. 1996, A&A, 309, 1002

Parizot, E., Marcowith, A., Ballet, J., & Gallant, Y. A. 2006, A&A, 453, 387

Peacock, J. A. 1981, MNRAS, 196, 135

Petre, R., Allen, G. E., & Hwang, U. 1999, Astronomische Nachrichten, 320, 199

Pisarski, R. L., Helfand, D. J., & Kahn, S. M. 1984, ApJ, 277, 710

Porter, T. A., Moskalenko, I. V., & Strong, A. W. 2006, ApJ, 648, L29

Ptuskin, V. S. & Zirakashvili, V. N. 2003, A&A, 403, 1

Ptuskin, V. S. & Zirakashvili, V. N. 2005, A&A, 429, 755

Rauw, G., De Becker, M., Nazé, Y., et al. 2004, A&A, 420, L9

Rho, J., Dyer, K. K., Borkowski, K. J., & Reynolds, S. P. 2002, ApJ, 581, 1116

Ritz, S. M., Michelson, P. F., Meegan, C., Grindlay, J., & GLAST Mission Team. 2007, in Bulletin of the American Astronomical Society, Vol. 38, Bulletin of the American Astronomical Society, 909–+

Rodgers, A. W., Campbell, C. T., & Whiteoak, J. B. 1960, MNRAS, 121, 103

Rodriguez, L. F., Gerard, E., Mirabel, I. F., Gomez, Y., & Velazquez, A. 1995, ApJS, 101, 173

Romani, R. W., Ng, C.-Y., Dodson, R., & Brisken, W. 2005, ApJ, 631, 480

Rosado, M., Ambrocio-Cruz, P., Le Coarer, E., & Marcelin, M. 1996, A&A, 315, 243

Russeil, D. 2003, A&A, 397, 133

Sanwal, D., Pavlov, G. G., & Garmire, G. P. 2005, in Bulletin of the American Astronomical Society, Vol. 37, Bulletin of the American Astronomical Society, 497–+

Shara, M. M., Smith, L. F., Potter, M., & Moffat, A. F. J. 1991, AJ, 102, 716

Smith, R. C. 1997, AJ, 114, 2664

Sugizaki, M., Mitsuda, K., Kaneda, H., et al. 2001, ApJS, 134, 77

Swanenburg, B. N., Bennett, K., Bignami, G. F., et al. 1981, ApJ, 243, L69

Taylor, J. H. & Cordes, J. M. 1993, ApJ, 411, 674

Teshima, M. 2008, The Astronomer's Telegram, 1491, 1

Thompson, D. J., Arzoumanian, Z., Bertsch, D. L., et al. 1992, Nature, 359, 615

Tian, W. W., Leahy, D. A., Haverkorn, M., & Jiang, B. 2008, ApJ, 679, L85

Truelove, J. K. & McKee, C. F. 1999, ApJS, 120, 299

Ueno, M., Sato, R., Kataoka, J., et al. 2007, PASJ, 59, 171

van der Hucht, K. A. 2001, New Astronomy Review, 45, 135

van der Swaluw, E., Achterberg, A., Gallant, Y. A., & Tóth, G. 2001, A&A, 380, 309

van der Swaluw, E., Downes, T. P., & Keegan, R. 2004, A&A, 420, 937

Vink, J., Bleeker, J., van der Heyden, K., et al. 2006, ApJ, 648, L33

Vink, J. & Laming, J. M. 2003, ApJ, 584, 758

Voelk, H. J., Zank, L. A., & Zank, G. P. 1988, A&A, 198, 274

Voges, W., Aschenbach, B., Boller, T., et al. 2000, VizieR Online Data Catalog, 9029, 0

Voges, W., Boller, T., Englhauser, J., Freyberg, M., & Supper, R. 2001, in Astronomical Society of the Pacific Conference Series, Vol. 225, Virtual Observatories of the Future, ed. R. J. Brunner, S. G. Djorgovski, & A. S. Szalay, 234–+

Völk, H. J., Berezhko, E. G., & Ksenofontov, L. T. 2005, A&A, 433, 229

Wang, N., Manchester, R. N., Pace, R. T., et al. 2000, MNRAS, 317, 843

Watanabe, S. & Cangaroo Collaboration. 2003, in International Cosmic Ray Conference, Vol. 4, International Cosmic Ray Conference, 2397–+

Weekes, T. C. 2005, in Bulletin of the American Astronomical Society, Vol. 37, Bulletin of the American Astronomical Society, 1402–+

Weekes, T. C., Cawley, M. F., Fegan, D. J., et al. 1989, ApJ, 342, 379

Weisskopf, M. C., Hester, J. J., Tennant, A. F., et al. 2000, ApJ, 536, L81

Westerlund, B. 1961, Arkiv for Astronomi, 2, 419

Whiteoak, J. B. Z. & Uchida, K. I. 1997, A&A, 317, 563

Wiedner, C. A. 1998, H.E.S.S. internal note

Winkler, C., Courvoisier, T. J.-L., Di Cocco, G., et al. 2003, A&A, 411, L1

Winkler, Jr., P. F. 1978, ApJ, 221, 220

Woltjer, L. 1972, ARA&A, 10, 129

Yamazaki, R., Kohri, K., Bamba, A., et al. 2006, MNRAS, 371, 1975

Zavlin, V. E. 2007, ApJ, 665, L143

Danksagung

An dieser Stelle möchte ich mich nochmals bei den vielen Menschen bedanken, die zur Entstehung dieser Arbeit beigetragen haben, jeder auf seine Weise. Im Besonderen möchte ich mich bedanken bei:

- Herrn Professor Werner Hofmann, der mir erst die Gelegenheit gegeben hat, am H.E.S.S. Experiment zu promovieren. Besonders dankbar bin ich für die interessante Aufgabe, die Durchmusterung der Galaktischen Ebene zu begleiten, für die gewährten Freiräume und das damit verbundene Vertrauen, sowie die Möglichkeit Erfahrungen auf internationalen Konferenzen zu sammeln.
- Herrn Professor Heinz Völk, dafür dass er das Koreferat übernommen hat und für die wertvolle Unterstützung bei der Veröffentlichung der RCW 86 Analyse.
- Karl Kosack und Christopher van Eldik für die Beantwortung aller Fragen, die sich in den drei Jahren ergeben haben (denn davon gab und gibt es viele), für die interessante Zeit während und nach den Konferenzen und natüerlich für die unermüdliche Hilfe während des Zusammenschreibens dieser Promotionsschrift.
- Conor Masterson, der sich meiner angenommen hat, in der ersten Zeit bei H.E.S.S. als es mehr Arbeit als Nutzen bedeutet hat, mit mir zusammenzuarbeiten.
- Meinen Mitdoktoranden Rolf Bühler, Kathrin Egberts, Stefan Ohm und Dalibor Nedbal für die schöne Zeit, das gemeinsame Klettern, die vielen Gespräche und für ein offenes Ohr, wenn ich mal Dampf ablassen musste. Und natürlich Wilfried Domainko für die vielen Stunden, die wir mit schlechten Filmen verbracht haben.
- Matthieu Renaud für die häufige Hilfe mit dem FITS-Format (was wären wir ohne IDL), für die unermüdliche Beantwortung von Fragen und vor allem für seine Begeisterung für unsere Arbeit, mit der er mich immer wieder angesteckt hat.
- der gesamten Heidelberger Gruppe, es war eine schöne Zeit mit Euch.
- Marianne Lemoine-Goumard für die gute Zusammenarbeit an der Veröffentlichung der RCW 86 Analyse und dafür, dass Sie mir in der Zeit des Zusammenschreibens den Rücken freigehalten hat.
- der H.E.S.S. Kollaboration, besonders zu nennen dabei sind: Jim Hinton, Olaf Reimer, Yves Gallant, Okkie de Jager, Gerard Fontaine und Dieter Horns.

Und natürlich gilt meine größte Dankbarkeit meiner Familie: ohne meine Mutter Monika hätte ich es niemals bis zur Promotion geschafft und ohne meine Verlobte Friederike, ihre Liebe, ihr Verständnis und ihre Geduld wäre die letzte Zeit wohl um einiges schwerer gewesen.